Explicit Exchange Interaction and Decoherence Dynamics in One-Dimensional Quantum Systems

Dissertation

zur
Erlangung des Doktorgrades
der Naturwissenschaften
(Dr. rer. nat.)

dem
Fachbereich Physik
der Philipps-Universität Marburg
vorgelegt von

Xiaoxuan Huang

aus Zhejiang (China)

Marburg/Lahn, März 2011

Vom Fachbereich Physik der Philipps-Universität Marburg
als Dissertation angenommen am: 02.05.2011

Erstgutachter: Prof. Dr. R. M. Noack
Zweitgutachter: Prof. Dr. Bruno Eckhardt

Tag der mündlichen Prüfung am: 12.05.2011

Zusammenfassung

In dieser Arbeit werden zwei Aspekte eindimensionaler wechselwirkender Quantenvielteilchensystemen untersucht. Das erste Thema ist die Auswirkung expliziter antiferromagnetischer Austauschwechselwirkungen auf die Quantenphasenübergänge eines eindimensionalen itineranten Elektronensystems. Das zweite Thema ist die Untersuchung des Dekohärenzverhaltens eines an ein eindimensionalen Quantenspinsystem gekoppeltes Quantenbits (Qubit).

Quantenphasenübergänge entstehen als Folge der Konkurrenz zwischen verschiedenen Arten von Wechselwirkungen in Vielteilchensystemen. Sie spielen eine zentrale Rolle in der Physik kondensierter Materie und stehen im Zusammenhang mit wesentlichen Mechanismen vieler neuartiger Phänomene, die in niedrig-dimensionalen Systemen der kondensierten Materie wie zum Beispiel Hochtemperatursupraleitung erscheinen. Eindimendionale Quantensysteme bieten eine ideale Spielwiese für die Untersuchung von Quantenphasenübergänge. Dies liegt daran, dass der Effekt der Wechselwirkung eine wesentlich größere Rolle als in ihren hörerdimensionalen Pendants spielt. In eindimensionalen Systemen sind nur Kollektivanregungen möglich, im Gegensatz zu zwei-und dreidimensionalen Systemen, wo sowohl kollektive wie Quasiteilchen-Anregungen erscheinen können. Noch wichtiger ist es, dass die kollektiven Anregungen von eindimensionalen Systeme in zwei verschiedene Zweige aufgeteilt werden können: ein nur Spin und keine Ladung trägt (Spinon), der zweite trägt nur Ladung und kein Spin trägt (Holon). Dieses Phänomen wird Spin-Ladungs-Trennung genannt. Bekannte analytische Methoden, die Bethe Ansatz und die Bosonisierung, sowie eine leistungsfähige numerische Methode, die Dichtematrix-Renormierungsgruppe (DMRG), ermöglichen detaillierte Untersuchungen verschiedener eindimensionalen Modelle. Das Mustermodell eines eindimensionalen wechselwirkenden Elektronensystems ist das eindimensionale Hubbard-Modell (auch t - U-Modell genannt), das aus einem mit t parametrierten kinetischen Energie-Beitrag und einer mit U parameterisierten Elektron-Elektron-Coulomb-Wechselwirkung U besteht. Bei halber Bandfüllung befindet sich der Grundzustand des eindimensionalen Hubbard-Modells in einer Spindichtewellen-Phase für alle positiven Werte der Wechselwirkung

U. Dieses einfache Modell kann in vielen möglichen Weisen, die das Grundzustandphasendiagramm beeinflussen, erweitert werden. Einen Satz von Wechselwirkungen, die interessant sind, sind explizit antiferromagnetische Austauschwechselwirkungen der nächsten Nachbarn, J_1 und der übernächsten Nachbarn, J_2. Ein auf diese Weise erweitertes Hubbard-Modell, das als t-U-J_1-J_2-Modell bezeichnet wird, wird ausführlich in dieser Arbeit untersucht. Es wird allgemein vermutet, dass die J_1-Wechselwirkung die Stärke der Supraleitung in zweidimensionalen Systemen wesentlich steigern kann. Zudem wird vorhergesagt, dass sie eine Bond-Ordnungswellen-Phase im halbgefüllten System induziert. Allerdings zeigen unsere DMRG-Rechnungen der Spin- und Ladungslücken und des Bond-Ordnungsparameters, die auf endlichen Gittern berechnet und anschliessend zum thermodynamischen Limes extrapoliert wurden, dass die J_1-Wechselwirkung nicht zu einer Frustration des Nächst-Nachbar-Austausches führt. Das heißt, dass der Grundzustand des halbgefüllten t-U-J_1-Modells aus einer Spindichtewelle-Phase ohne jeglicher Phasenübergang besteht. Zudem zeigt eine Bosonisierungsrechnung, die im Schwachkopplungsbereich gültig ist, dass der Grundzustand in einer Spin-Dichte-Wellen-Phase ist. Dieses Ergebnis motivierte uns, eine zusätzliche frustrierte J_2-Wechselwirkung hinzuzufügen. Weitere numerische und analytische Rechnungen für einen endlichen J_2 zeigen uns, dass eine Bond-Ordnungs-Wellen-Phase für einen positiven kritischen Wert von J_2 erscheint, der von den Werten von U und J_1 abhängt. Für bestimmte größere Werte von J_2 finden wir eine metallische Luther-Emery-Phase, das heißt, eine Spinlücke öffnet sich.

Ein weitere grundlegende Fragestellung in Quantensystemen beschäftigt sich mit dem klassischen Grenzfall: wie entwickelt sich die klassische Mechanik aus der Quantenmechanik? In den frühen Tagen der Entwicklung der Quantenmechanik, hat man versucht diesen, Übergang durch Anwendung des Ehrenfest-Theorems und des Bohrschen Korrespondenzprinzips zu erklären. Allerdings stoßen solche Zugänge auf fundamentale Grenzen und liefern kein eindeutiges Bild. Ein weiterer Ausgangspunkt ist es, das System nicht als isoliert zu betrachten, sondern als an seine Umgebung, d.h. an ein Bad, gekoppelt. Die Zeitentwicklung des Systems mitsamt Umgebung, d.h. ein Gesamtsystem in einem reinen Zustand, wird von der Schrödinger-Gleichung beschrieben. Der zeitentwickelte Zustand kann durch eine Entwicklung in klassischen Konfigurationen der Subsysteme dargestellt werden. Man kann System und Bad in unterschiedlichen Weisen konfigurieren, um das Dekohärenzverhalten zu untersuchen. Der offensichtliche erste Schritt, die Dekohärenz zu untersuchen, ist der Fall eines an ein Bad gekoppelten einzelnen Qubits zu betrachten. Vorherige Arbeiten haben die Fälle eines nicht wechselwirkenden Bads und eines wechselwikendes Bads, das sich anfangs in seinem

Grundzustand befindet, betrachtet. In dieser Arbeit behandeln wir den realistischeren Fall, wo das Bad durch einen Quantenquench präpariert wird. Solche Systeme können durch die zeitabhängige DMRG und in einigen Fällen auch analytisch behandelt werden. Hier wenden wir die adaptive zeitabhängige DMRG mit einer Suzuki-Trotter Zerlegung zweiter Ordnung an, um die Dekohärenz eines mit einem eindimensionalen XXZ-Spinbad gekoppelten Qubits (mittels des sogenannten “Loschmidt-Echos”) zu berechnen. Als Vergleich betrachtet wir auch ein Bad, das aus einem Ising-Modell in einem transversalen Feld besteht. Für dieses System kann die vollständige Zeitentwicklung analytisch berechnet werden. Wir betrachten sowohl den Fall eines Grundzustandes als Anfangszustand des Bads, was eine Nachprüfung vorherigerer Arbeiten entspricht, wie den Fall eines durch einen Quantenquench präparierten Anfangszustands. Wir finden, dass das Kurzzeitverhalten des Loschmidt-Echos für beide Fälle einer Gaußfunktion folgt. Ob das Langzeitverhalten zur vollständigen Dekoheränz des Zustands des Qubits folgt oder nicht, hängt hingegen von der Art des Anfangszustands des Bads ab: ein durch einen Quantenquench präpariertes Bad führt allgemein zu vollständiger Dekohärenz, für einen Grundzustand ist dies aber für die meisten Werte der Parameter des Bad-Hamiltonoperators nicht der Fall.

Abstract

In this thesis, we investigate two aspects of one-dimensional interacting quantum systems. The first one is the effect of explicit antiferromagnetic exchange interactions on the quantum phase transitions of a one-dimensional itinerant electron system. The second one is the decoherence of a qubit coupled to a one-dimensional quantum spin system.

Quantum phase transitions arise as a result of competition between different types of interactions in many-particle systems. They play a central role in condensed matter physics and are related to the essential mechanisms of many novel phenomena that appear in low-dimensional condensed matter systems such as high-T_c superconductivity. One-dimensional systems are ideal playgrounds for studying quantum phase transitions because the effects of the interactions play a more major role than their higher-dimensional counterparts. In one-dimensional systems, the excitations are collective ones, in contrast to two- and three-dimensional systems when single-particle and collective excitations are both possible. More importantly, the collective excitations of one-dimensional systems can be split into two different branches: one carrying only spin without charge (spinon) and the other carrying only charge without spin (holon). This phenomena is termed spin-charge separation. Well-established analytic methods, the Bethe ansatz and bosonization, as well as a powerful numerical method, the density matrix renormalization group (DMRG), make possible detailed studies of various one-dimensional models. The prototype of a one-dimensional interacting electron system is the one-dimensional Hubbard (t-U) model, which consists of a kinetic energy parameterized by t and an on-site electron-electron Coulomb interaction U. At half-filling, the ground state of the one-dimensional Hubbard model is in a spin-density-wave phase. This simple model has many possible extensions which influence the ground-state phase diagram. One interesting set of interactions to consider are explicit antiferromagnetic exchange interactions of nearest-neighbors, J_1, and next-nearest-neighbors, J_2. A Hubbard model extended in this way is called the t-U-J_1-J_2 model. This model has been extensively studied in this thesis. The J_1 term is thought to significantly enhance the superconductivity in a two-dimensional system.

It was predicted to induce a bond-order-wave phase in a half-filled system. However, our DMRG calculations of the spin gap, the charge gap, and the bond-order-wave parameter on finite lattices when extrapolated to the thermodynamic limit indicate that J_1 does not frustrate U. Thus, the ground-state phase diagram of the half-filled t-U-J_1 model consists of a spin-density-wave phase without any phase transitions. We have also carried out a bosonization calculation in the weak-coupling region of this model, which also confirms that there is only a spin-density-wave phase. This result motivated us to consider an additional frustrating J_2 term. Additional numerical and analytical calculations for nonzero J_2 ascertain that a bond-order-wave phase appears at a positive critical value of J_2 related to the values of U and J_1. For some specific larger values of J_2, we find a spin-gapped, metallic Luther-Emery phase.

Another fundamental problem in quantum systems is how the classical limit emerges in quantum systems. In other words, how does classical mechanics arise from quantum mechanics? In the early days of quantum mechanics, applications of the Ehrenfest theorem and the Bohr correspondence principle try to explain how classical mechanics arises from quantum mechanics. However, such attempts have intrinsic limitations and are ambiguous. Another idea is to consider the fact that a system, in general, is not isolated, but interacts with its surroundings, i.e. a bath. In fact, by including the system and a bath and considering the composite system to evolve through the Schrödinger equation, we find that the initial wave function of the whole composite system will evolve into a wave function expanded by a classical configuration of subsystems. We can choose different configurations of the system and the bath to study decoherence. Clearly, the first step to study decoherence is to consider the decoherence of a single qubit coupled to a bath. Previous work has considered the cases of a noninteracting bath and an interacting bath initially in a ground state. We consider here a more realistic bath, a quantum quenched bath. These system can be treated by the time-dependent DMRG and, in some cases, can be treated analytically. In this study, we apply the adaptive time-dependent DMRG with a second-order Suzuki-Trotter decomposition to calculate the decoherence (by means of the Loschmidt echo) of a qubit coupled to a one-dimensional XXZ spin bath. For comparison, we also treat a bath that is a one-dimensional transverse-field Ising model analytically. The initial state of the spin bath is taken to be either a ground state (reexamining previous work) or a quantum quenched state. The results for these two models confirm that the short-time behaviour of the Loschmidt echo is a Gaussian for a bath that is initially in a ground state or a quantum quenched state. We find that an initial quantum quenched bath state always leads to more generic behavior, i.e., complete decoherence of the

qubit, whereas complete decoherence of the state of the qubit does not occur in general when the bath is initially in a ground state.

Contents

Introduction

Interacting electron systems have been extensively studied since the 1950s. For about 30 years, the main method of this area was dominated by the Landau Fermi liquid theory [1, 2], which describes the normal low-energy behavior of a two- or three-dimensional interacting electron system that is continuously connected with the free electron system, i.e. consists of free quasi-particles. Starting from the 1980s, a number of novel phenomena were discovered in the interacting electron systems in the low-energy and low-dimension limit, such as the integer and fractional quantum Hall effects and high-temperature superconductivity. Accompanying new concepts have emerged to describe interacting electron systems, such as Luttinger liquid theory [3, 4, 5] of one-dimensional systems, edge states, and composite fermions [6] in quantum Hall states, and high-T_c superconductivity of two-dimensional systems. These concepts are beyond the scope of Landau Fermi liquid theory, and make the study of these kinds of interacting electron systems (strongly correlated systems) one of the frontiers in physics. In particular, Landau Fermi liquid theory is no longer suitable for describing the low-energy properties of one-dimensional systems simply because the low-energy excitations in a one-dimensional system are collective excitations rather than weakly interacting quasi-particle excitations. It is also known that one-dimensional electron systems are closely related to one-dimensional quantum spin systems.

In strongly correlated systems, a system in which all the interactions between electrons are considered is impossible to solve. Only some simplified models, such as the one-dimensional Hubbard model (considering only the on-site electron interaction U) [7] and the one-dimensional $t-J$ model (strong-coupling limit of the Hubbard model) at the supersymmetric point [8, 9], are exactly solvable. When additional electron-electron interaction are present, these models cannot be solved exactly no matter how weak the interactions are. Fortunately, a comprehensive picture of one-dimensional strongly correlated systems can be obtained within the frameworks of bosonization [10] and the density-matrix renormalization group (DMRG) [11, 12, 13]. One-dimensional strongly correlated systems undergo quantum phase transitions [14],

such as metal-insulator transitions, which are driven by quantum fluctuations at zero temperature, rather than normal phase transitions caused by thermodynamic fluctuations. In particular, one-dimensional extended Hubbard models undergo various quantum phase transitions. In Chapter 2, we investigate the ground-state phase diagram of a half-filled Hubbard chain with explicit antiferromagnetic exchange interactions between nearest neighbors, and between next-nearest neighbors by bosonization and DMRG. As a result, we find that the ground state of this model has three different phases: spin-density-wave, bond-order-wave, and metallic Luther-Emery phase.

In recent years, the number of experimental studies of nonequilibrium properties in low-dimensional systems has increased rapidly. In particular, in the scope of quantum optical experiments, developments in the technology of ultra-cold atomic gases has made it possible to construct low-dimension strongly correlated systems [15]. One can artificially manipulate the strength of the electron-electron interaction in these constructed systems. This feature of ultra-cold atomic gases has made possible the investigation of many nonequilibrium problems in strongly correlated systems in which the interactions are time-dependent. A particular example of these kinds of nonequilibrium phenomena is that of quantum quenches [15, 16, 17, 18, 19, 20], in which the strength of interactions of the system is suddenly changed. From the theoretical point of view, the recently developed time-dependent DMRG [21, 22] is well-suited to investigate nonequilibrium phenomena in one-dimensional systems, especially quantum quench problems. These developments, in both experiment and in theory, allow us to study one of the most fundamental problems in quantum mechanics, decoherence [23, 24, 25]. The theory of decoherence describes the loss of intrinsic entanglement of a quantum system when it is coupled to a bath. In Chapter 3, we investigate the decoherence of a qubit induced by coupling to the ground state or to a quenched state of a one-dimensional spin bath. In the cases we treat in this chapter, we find that a quenched initial bath state always leads to more generic behavior, i.e., to complete decoherence of the qubit. For quenched states of the transverse-field Ising chain, the short-time Gaussian decay parameter $\alpha(T_0)$ always slowly oscillates around a time-averaged value $\bar{\alpha}$ after a long waiting time T_0 after which the bath becomes quasi-stationary. For quenched states of an XXZ chain, $\alpha(T_0)$ tends to a maximum value of 0.01 for the qubit-bath coupling strength $\epsilon = 0.2$ for the majority of quenches.

Structure of the Thesis

The thesis is structured into two main parts. The first part, contained in Chapter 1, focuses on the description of the static DMRG and the time-dependent DMRG. The second part, consisting of Chapters 2 and 3, describes our results.

In Chapter 1, we describe the density matrix renormalization group method, which is our main numerical tool including a description of the static DMRG, at the beginning of the chapter followed by descriptions of the various different kinds of time-dependent DMRG. The adaptive time-dependent DMRG with the second-order Suzuki-Trotter decomposition, which is the main method used in this thesis, is discussed in detail.

Chapter 2 describes an application of the static DMRG. We investigate the effect of two additional interaction terms on the phase diagram of the half-filled Hubbard (t-U) chain, namely, explicit antiferromagnetic exchange interactions between nearest neighbors, J_1, and between next-nearest neighbors, J_2. We describe bosonization calculations for the weak-coupling region at the beginning and then present our DMRG results. Both bosonization and the DMRG calculations indicate that a bond-order-wave phase is not present for $J_2 = 0$; the system is in a spin-density-wave phase for *all* positive J_1 and U. We show that a bond-order-wave phase can be induced by turning on J_2 positively, with the critical value required depending on U and J_1. At larger values of J_2, we find additional phases, including a spin-gapped metallic phase which we identify as a Luther-Emery phase.

In Chapter 3, we describe an application of the the second-order Suzuki-Trotter adaptive time-dependent DMRG. We first revisit the decoherence (in terms of the Loschmidt echo) of a qubit coupled to a ground state bath (a XXZ chain) with two types of qubit-bath interactions: an Ising coupling and a Heisenberg coupling. We then consider the case where the initial state of the bath (treated as an XXZ chain and as a transverse-field Ising chain) is out of equilibrium: a quenched state. After a waiting time T_0, the qubit is coupled to the quenched bath after the quench with an Ising coupling. For comparison, we also show some analytical results for the transverse-field Ising chain bath. In Appendix A, we give the details of the analytical method used to calculate the Loschmidt echo for the transverse-field Ising chain. In Appendix B, we analyse the numerical error in the adaptive time-dependent using second-order Suzuki-Trotter decomposition DMRG calculations of the Loschmidt echo. In Appendix C, we analyse the finite-size effects in the results for the Loschmidt echo.

Publications

Some parts of this thesis were already published or are being prepared for publication. The chapters related to each publication are:

Chapter 2
Phase diagram of the t-U-J_1-J_2 chain at half filling
Xiao-Xuan Huang, Edina Szirmai, Florian Gebhard, Jenö Sólyom, and Reinhard M. Noack,
Phys. Rev. B 78, 085128 (2008).

Chapter 3
Decoherence of a qubit coupled to a spin-1/2 chain following a quantum quench
Xiao-Xuan Huang, Salvatore Manmana, and Reinhard M. Noack,
in preparation.

Chapter 1

Density matrix renormalization group

This chapter is devoted exclusively to the introduction of the real-space density matrix renormalization group (DMRG). It is organized as follows: First, the numerical renormalization group algorithm (NRG) will be introduced by analyzing its success in treating quantum impurity systems and its breakdown when treating other strongly correlated systems (such as the Heisenberg, Hubbard and $t-J$ models). Second, the standard DMRG, which overcomes the above-mentioned difficulties encountered in the NRG, will be discussed, explaining its breakthrough ideas (i.e., the density matrix projection) and details of the algorithm (the infinite-system and finite-system DMRG algorithms). The standard DMRG currently provides the most powerful, accurate, and effective simulations of one-dimensional strongly correlated quantum lattice systems. In particular, the static properties of the ground state and a few low-lying excited states can be very accurately evaluated. Third, we will briefly discuss how to apply a variety of extensions of the DMRG method to study time-dependent phenomena in strongly correlated systems. Some of the early extensions were were proven to be incomplete or lack efficiency. The schemes in which the Hilbert space is adaptively adjusted are the most practical and applicable. Finally, in the last section, the most efficient method, the Suzuki-Trotter adaptive time-dependent DMRG (t-DMRG), will be presented. We will introduce the most frequently-used scheme based on the second-order Suzuki-Trotter decomposition and make a short discussion of useful schemes based on first- and fourth-order Suzuki-Trotter decompositions.

1.1 Standard renormalization-group approach

Impurity models, spin lattice models and itinerant-electronic models have been long central, important subjects in theoretical condensed matter physics. On the one hand, some relatively simple models, such as the one-dimensional Heisenberg model and the one-dimensional Hubbard model were exactly solved using the Bethe ansatz by the 1970s. On the other hand, in the early 1970's, Wilson invented a nonperturbative method (the NRG) to give a quantitative solution of the Kondo model [26], which was later extended to the Anderson model by Krishna-murthy, Wilkins, and Wilson [27].

Here we describe the main points of the NRG. By discretizing the conduction band logarithmically using the discretization parameter Λ ($\Lambda > 1$), Wilson mapped the Kondo model to a semi-infinite fermionic chain H, with fermion operators f'_n and f_n which create and annihilate electrons at the n-th site of chain. This discretization procedure allows one to take all the conduction-band energies into account and leads to an exponential decay of the typical hopping energy scale at the n-th site ($t_n \propto \Lambda^{-n/2}$).

To proceed with the iterative renormalization group calculations below, the semi-infinite chain H can be regarded as the limit of a finite size lattice H_N when $N \to \infty$. One defines

$$H = \Lambda^{-(N-1)/2} H_N \longleftrightarrow H_N = \Lambda^{(N-1)/2} H, \quad (N \to \infty). \tag{1.1}$$

The factor $\Lambda^{(N-1)/2}$ cancels the Λ dependence of t_{N-1} in the limit of large N and facilitates the renormalization group analysis. The remaining task is to construct the semi-infinite chain H_N by iteratively adding a site and reducing the Hilbert space through a renormalization group procedure, see Fig. 1.1. The first step is to construct a finite initial block A with Hamiltonian H_N, which contains N sites, including a impurity at the first site, and which is small enough to be exactly diagonalized numerically. The fermion operators $f^\dagger_{n\sigma}$, $f_{n\sigma}$, and other related operators must be represented in the basis of H_N. The second step is to employ full exact diagonalization method to obtain the full energy spectrum of H_N. In the third step, we truncate the high-energy eigenstates, keeping the low-energy eigenstates to form a basis transformation operator O (the rows of O are the eigenstates kept, $|m_s\rangle$). The initial block Hamiltonian H_N is then transformed to a new Hamiltonian H'_N in the reduced basis using the transformation $H'_N = OH_NO^\dagger$. The Hamiltonian H'_N is diagonal in the reduced basis. The fermion operators $f^\dagger_{n\sigma}$ and $f_{n\sigma}$ can be transformed into the same reduced basis using the transformation $f'^\dagger_{n\sigma} = Of^\dagger_{n\sigma}O^\dagger$. This procedure is called the renormalization group transformation. The last step is adding a site to the block A to form a new larger block $A + S$. The enlarged block Hamiltonian H_{N+1}

is represented in the new basis $\{|m_s\rangle|s\rangle\}$. The recursion relation between these two successive Hamiltonians is

$$H_{N+1} = \Lambda^{1/2} H'_N + \Lambda^{N/2} H_{t_N}, \tag{1.2}$$

where

$$H_{t_N} = t_N \sum_{\sigma} (f^{\dagger}_{N\sigma} f_{N+1\sigma} + H.c.). \tag{1.3}$$

Here H_{N+1} contains the rescaled Hamiltonian $\Lambda^{1/2} H'_N$ of the old block A and the rescaled Hamiltonian of the hopping terms $\Lambda^{N/2} H_{t_N}$ between the last site N of old block A and the new added site. The typical energy scale is decreased by a factor $\Lambda^{1/2}$ at each step in this procedure ($t_{N-1} \rightarrow t_N$). We then repeat the second step, starting by replacing H_N with H_{N+1}, until the system approaches a fixed point.

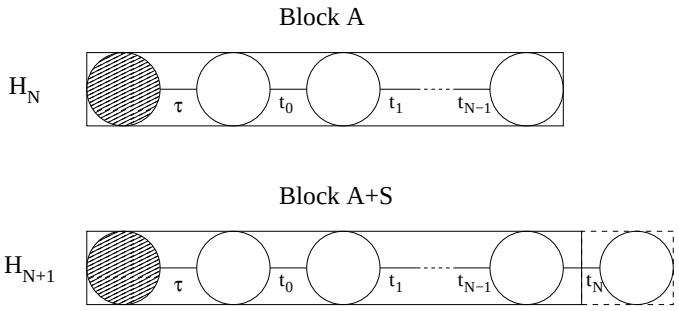

Figure 1.1: Enlarging the chain by adding one site in one step of the numerical renormalization group iteration. The fist circle (shaded) is the impurity site of the chain. The amplitude of the hopping term between the impurity site and the next site is τ.

The success of the NRG in the Kondo and Anderson models encouraged people to study other models. However, all attempts to apply the idea of truncating the eigenstate space in NRG to other models failed. For example, people applied the NRG idea to calculating the ground state of the one-dimensional Hubbard model, enlarging the system through doubling its size at each step [28], and also to the one-dimensional Heisenberg model, enlarging the system by adding a site at each step [29]. In these calculations, the results are not numerically exact even when hundreds of states are kept on very small lattice sizes (less than 20 sites),

One should note that, in the NRG calculation for the Kondo model, the exponential decay of the hopping amplitude $t_N \propto \Lambda^{-N/2}$ ensures that the energy scales of different iterations can be well separated. Thus, the Kondo model can be solved by keeping only a few hundred low-lying eigenstates. However, in the Heisenberg model and the Hubbard model, the amplitude of the coupling strength between different sites is a constant. The energy scales of different

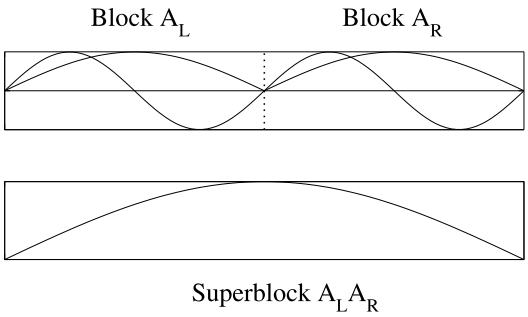

Figure 1.2: A schematic diagram of a superblock $A_L A_R$ assembled from two smaller blocks A_L and A_R for the one-dimensional single-particle tight-binding model. Simply keeping several lowest energy eigenstates (curves) of the block A_L and A_R to form the ground state (the curve) or other low-lying states of the superblock $A_L A_R$ leads to large inaccuracies.

iterations cannot be separated well. Because of this, one must keep almost all the eigenstates of the Hamiltonian in every iteration to get good results.

Even for the simplest model, the one-dimensional single-particle tight-binding model, the NRG cannot be applied directly. The Hamiltonian of the model is

$$H = -\sum_i (|i\rangle\langle i+1| + H.c.), \tag{1.4}$$

where c_i is a fermion operator. White and Noack [30] illustrated the difficulties in this model in a simple way, see Fig. 1.2. For the limit of continuum model, this is just a particle-in-a-box problem. Starting with a small block A_L, one enlarges the system by adding a reflected block A_R, and one finds that all states of the block $A_L A_R$ constructed from the smaller blocks A_L and A_R have a kink in the middle, as the open boundary conditions cause the wave functions of the smaller blocks to vanish at the boundaries, see Fig. 1.2. But actually, the ground state of the larger system has a maximum amplitude in the middle, the large curve in block $A_L A_R$ in Fig. 1.2. Therefore, any truncation in the small block A_L or A_R leads to an incomplete basis.

To solve this problem, one needs to generalize the boundary of the small blocks. One can apply a combination of boundary conditions to each boundary of the blocks A_L and A_R. For example, one can apply fixed and free boundary conditions to either boundary of block

A_L and A_R to get a set of Hamiltonians. Then, following the standard renormalization group approach, one keeps a proportion of the low energy eigenstates of each of these Hamiltonians after diagonalizing them. These states are generally not mutually orthogonal. However, one can orthonormalize them explicitly and use the new basis obtained to form an enlarged system. This scheme works much better than the other attempts mentioned above; it calculates the ground state and low-lying states with high accuracy. However, this scheme cannot be easily extended to interacting systems, such as the Heisenberg model and the Hubbard model. In the many-particle system, the behavior of an individual particle within the many-particle wave function is complicated. Therefore, a mixed set of boundary conditions does not lead to general boundary conditions for every particle. Another method introduced in Ref. [30], called the superblock method, avoids the difficulties of choosing the set of boundary conditions. The idea is to consider the block A_L as the system block that we are interested in, to be surrounded by the extra several blocks, called environment blocks, such as the block A_R. (If the A_R is the only surrounding block, this method reduces to the original Wilson approach.). The extra blocks form the environment of the block A_L. Together with the block A_L, all these blocks compose a "superblock", i.e., $A_L \ldots A_R$. The accuracy becomes better and better as more blocks are added to the superblock. As we will see, the DMRG applies a variant of the superblock scheme, projecting out unimportant density matrix states in order to get an appropriate and effective basis.

1.2 Static DMRG

The first applications of DMRG were to the calculation of the ground-state properties of some typical one-dimensional interacting lattice models. The prototype of these methods is the original DMRG papers of White [11], which calculates the ground state energies and ground state spin-spin correlations of the Heisenberg model for both spin-1/2 and spin-1. In order to distinguish from the DMRG methods used for solving the time dependent problem in one-dimensional systems, (see Sec. 1.3), we call the original DMRG method for the ground state property calculations "Static DMRG".

1.2.1 Density matrix projection

From a mathematical point of view, a natural way to decompose a quantum system in a pure state is the Schmidt decomposition, which expresses the wave function of the whole system as

tensor products of density matrix eigenvectors of two subsystems. This mathematical idea was introduced into the superblock method [30] to implement more reasonable relations between the system block and the environment block. From the renormalization group viewpoint, an effective cut-off of most unrelated states is the essence of getting the ground state or some low-lying exited states.

A pure-state wave function $|\psi\rangle$, such as the ground state of a closed system, can be expressed as a tensor product of states $|i\rangle$ and $|j\rangle$, where $\{|i\rangle\}$ and $\{|j\rangle\}$ are arbitrary orthonormal bases of the system block S and the environment block E, respectively. The general expression for the state $|\psi\rangle$ is

$$|\psi\rangle = \sum_{i,j} \psi_{ij}|i\rangle|j\rangle, \tag{1.5}$$

where the ψ_{ij} are elements of the matrix ψ, i.e., a representation of the wave function $|\psi\rangle$. The singular value decomposition (SVD) of a matrix ψ is given by

$$\psi = \mathbf{u}\boldsymbol{\sigma}\mathbf{v}^{\mathbf{T}}, \tag{1.6}$$

where the matrix $\boldsymbol{\sigma}$ is diagonal with m singular values ($\sum_m \sigma_{mm}^2 = 1$ and $\sigma_{mm} > 0$). Here the dimension of $\boldsymbol{\sigma}$, say m, cannot be larger than the number of states either of the system block S or of the environment block E. The matrices $\mathbf{u}$ and $\mathbf{v}$ are orthogonal ($\mathbf{u}\mathbf{u}^{\mathbf{T}} = \mathbf{1}, \mathbf{v}\mathbf{v}^{\mathbf{T}} = \mathbf{1}$). Rewriting Eq. (1.5), one obtains

$$|\psi\rangle = \sum_{ijm} u_{im}\sigma_{mm}v_{mj}|i\rangle|j\rangle. \tag{1.7}$$

We set

$$|m^S\rangle = \sum_i u_{im}|i\rangle, \tag{1.8}$$

$$|m^R\rangle = \sum_j v_{mj}|j\rangle, \tag{1.9}$$

and

$$\lambda_m = \sigma_{mm}, \tag{1.10}$$

Eq. (1.7) can then be written as

$$|\psi\rangle = \sum_m \lambda_m |m^S\rangle|m^E\rangle \tag{1.11}$$

(the Schmidt decomposition), where the number of states in the sets $\{|m^S\rangle\}$ and $\{|m^R\rangle\}$ are the same, $m^S = m^E = m$.

It is easy to obtain the reduced density matrix of the system block S and the environment block E from Eq. (1.11). The reduced density matrix of the system block S is

$$\rho_S = tr_E|\psi\rangle\langle\psi| = \sum_m \lambda_m^2 |m^S\rangle\langle m^S|, \tag{1.12}$$

and, similarly, the reduced density matrix of the environment block E is

$$\rho_E = tr_S|\psi\rangle\langle\psi| = \sum_m \lambda_m^2 |m^E\rangle\langle m^E|. \tag{1.13}$$

where tr_E and tr_S denote the trace over the degree of freedom of the environment block S and the system block S, respectively. Obviously, the vectors $|m^S\rangle$ and $|m^E\rangle$ are eigenvectors of the reduced density matrix of the system block S and the environment block E, respectively. The reduced density matrices ρ_S and ρ_E have the same eigenvalues, λ_m^2. One can also show that, in general, $tr(\rho_S^2) = tr(\rho_E^2) \leqslant 1$, when $tr(\rho_S^2) < 1$, the states of block S and block E are mixed states. Now we can see a more physical meaning for the orthogonal matrices **u** and **v**. The columns of the two matrices **u** and **v** are the eigenvectors ($|m^S\rangle$ and $|m^E\rangle$) of the reduced density matrices ρ_S and ρ_E, respectively.

The essential task here is to find an effective approximation, say $|\tilde{\psi}\rangle$, to the exact wave function $|\psi\rangle$. It requires a minimization of the quadratic deviation between them,

$$\mathcal{S} = ||\tilde{\psi}\rangle - |\psi\rangle|^2. \tag{1.14}$$

The key to the approximation in the DMRG is to keep the m' ($m' < m$) density matrix eigenstates with the largest reduced density matrix eigenvalues within the set of $\{|m^S\rangle\}$. This procedure results a reduced basis $\{|m'^S\rangle\}$. Note that, the same number (m') of the states will be kept in the set of $\{|m^E\rangle\}$, $m'^S = m'^E = m'$. Therefore, the effective wave function $|\tilde{\psi}\rangle$ is given by

$$|\psi\rangle \approx |\tilde{\psi}\rangle = \sum_{m'} \lambda_{m'} |m'^S\rangle|m'^E\rangle. \tag{1.15}$$

This procedure is essentially different in the DMRG and in the NRG. In the DMRG, the most relevant states are identified by the biggest eigenvalues of the reduced density matrix of one state (or the reduced matrices of a set of states, which are called target states). In the NRG, however, the truncation criterion is to keep the energy eigenstates of the Hamiltonian

with the lowest eigenvalues. In the DMRG, the truncated basis $\{|m'^S\rangle\}$, which contains m' wave vectors, will be used to construct the new basis of the next enlarged system, see below. The truncation of the space of the reduced density matrix in the DMRG is more general and can also be used to generalize the NRG [31].

We will represent $|\tilde{\psi}\rangle$ as a matrix represented in the reduced basis. Similar to the Eq. (1.6), it is

$$\tilde{\psi} = \tilde{\mathbf{u}}\tilde{\boldsymbol{\sigma}}\tilde{\mathbf{v}}^{\mathbf{T}} \tag{1.16}$$

with the matrix elements

$$\tilde{\psi}_{ij} = \sum_{m'} \tilde{u}_{im'}\tilde{\sigma}_{m'm'}\tilde{v}_{m'j}. \tag{1.17}$$

Here $\tilde{\mathbf{u}}$, $\tilde{\boldsymbol{\sigma}}$, and $\tilde{\mathbf{v}}$ are truncated matrices represented in the reduced bases. The matrices $\tilde{\mathbf{u}}$ and $\tilde{\mathbf{v}}$ are still orthogonal ($\tilde{\mathbf{u}}\tilde{\mathbf{u}}^{\mathbf{T}} = \mathbf{1}, \tilde{\mathbf{v}}\tilde{\mathbf{v}}^{\mathbf{T}} = \mathbf{1}$). In this case, the reduced density matrix $\boldsymbol{\rho}_S$ of the system block S can be rewritten as

$$[\tilde{\rho}_S]_{ii'} = \sum_j \tilde{\psi}_{ij}\tilde{\psi}_{i'j}. \tag{1.18}$$

This expression can be simplified to

$$\tilde{\rho}_{\mathbf{S}} = \tilde{\mathbf{u}}\tilde{\sigma}\tilde{\mathbf{v}}^{\mathbf{T}}\tilde{\mathbf{v}}\tilde{\boldsymbol{\sigma}}^{\mathbf{T}}\tilde{\mathbf{u}}^{\mathbf{T}} = \tilde{\mathbf{u}}\tilde{\boldsymbol{\sigma}}^{\mathbf{2}}\tilde{\mathbf{u}}^{\mathbf{T}}, \tag{1.19}$$

clearly showing that the eigenvalues of $\tilde{\rho}_S$ are $\lambda^2_{m'}$. The set of density-matrix eigenvalues $\{\lambda^2_{m'}\}$ corresponds to the probability distribution of the states $|m'_S\rangle$ in the system block S.

Since $\sum_m \lambda^2_m = 1$, a measure of the truncation error is the truncated weight

$$P = 1 - \sum_{m=1}^{m'} \lambda^2_m. \tag{1.20}$$

While the truncated weight P is a good measurement of truncation errors in one step of the DMRG iteration, it is not a good criterion for analyzing the total DMRG error because accumulated truncation errors from previous DMRG steps are neglected. The performance of the truncation is related to the decay of the eigenvalue spectrum $\{\lambda^2_m\}$. For example, $\{\lambda^2_m\}$ decays more slowly in the one-dimensional Hubbard model than in the one-dimensional Heisenberg model. To obtain a given small truncated weight, one must keep hundreds of states in a one-dimensional Hubbard lattice with one hundred lattice sites, while one only needs to keep dozens of states on an one-dimensional Heisenberg lattice of the same size. Moreover, the

decay of $\{\lambda_m^2\}$ generally behaves differently in the different phases of a model. In order to get an accurate solution, one must carefully control the number of the states kept m'.

It is necessary to mention that the DMRG cannot be applied to d-dimensional strongly correlated systems with $d > 1$. The brief explanation is that the eigenvalue spectrum $\{\lambda_m^2\}$ of the reduced density matrix decays very slowly in such models. Keeping only few states could lead to a large truncation error. Thus, one may need to keep many states in the calculation. When the lattice is large, the truncation error becomes very large, and the DMRG simulation becomes inaccurate. From the view point of quantum information theory, this behavior is related to the entanglement, which can be characterized by the von Neumann entropy of the system block (which is the same as that of the environment block),

$$S(\rho_S) = -Tr_E(\rho_S \log \rho_S) = -\sum_m \lambda_m^2 \log \lambda_m^2. \tag{1.21}$$

Typically, the ground state of strongly correlated system is entangled. The behaviour of the block entanglement entropy of spin lattice models was extensively studied [32, 33, 34, 35]. If the one-dimensional system is in a noncritical phase, the entropy $S(\rho_S)$ is proportional to the logarithm of the correlation length ξ, ($S(\rho_S) \propto \log \xi$). Because of the short correlation length ξ in the gapped region, $S(\rho_S)$ will grow logarithmically for small block size L ($L < \xi$) and then saturate to a constant finite value ($\propto \log \xi$) above a certain size L ($L > \xi$), even when the block size tends to thermodynamic limit ($L \to \infty$). If the one-dimensional system is in the critical phase, $S(\rho_S)$ will grow logarithmically with L, $S(\rho_S) \propto \log L$. Thus the DMRG has the ability to treat systems with a small entropy $S(\rho_S)$ for a big lattice size accurately. For this reason, the DMRG works better in the noncritical region than in the critical region. For a d-dimensional system with $d > 1$, calculation of the entropy $S(\rho_S)$ shows it diverges like L^{d-1} (area law [36, 37]). For a two-dimensional model, one must keep many more states as L becomes larger. Thus, the DMRG calculation loses its efficiency and the accuracy breaks down in such cases.

Consider the case of calculating the n lowest-lying states of the lattice. By summing over the reduced density matrices of all of the n energy eigenstates with equal probability, the resulting block basis, obtained from the total reduced density matrix, will also be a good representation of each state. In this case, the total reduced density matrix is given by

$$[\rho_S]_{ii'} = \sum_n W_n \sum_j \tilde{\psi}_{ij}^n \tilde{\psi}_{i'j}^n, \tag{1.22}$$

with

$$\lambda_m^2 = \sum_n W_n (\lambda_m^n)^2, \tag{1.23}$$

where W_n is the probability of each state, $W_n = 1/n$. Note that this choice of the values of W_n ensures that $tr_E(\rho_S) = 1$.

In formulating the DMRG algorithm, another important issue is how to enlarge the superblock. In the traditional DMRG algorithm, two sites, say the site blocks l and $l+1$, are inserted at the positions l and $l+1$, respectively, between the system block and environment block to construct a superblock $m_{l-1}^S \bullet \bullet m_{l+2}^E$, where the symbol $\bullet$ denotes a single site, see Fig. 1.3. For this reason, the DMRG wave function, typically the ground-state wave function, is expressed as

$$|\psi\rangle = \sum_{m_{l-1}^S \sigma_l \sigma_{l+1} m_{l+2}^E} \psi_{m_{l-1}^S \sigma_l \sigma_{l+1} m_{l+2}^E} |m_{l-1}^S\rangle |\sigma_l\rangle |\sigma_{l+1}\rangle |m_{l+2}^E\rangle, \tag{1.24}$$

where the density matrix eigenstates $|m_{l-1}^S\rangle$ and $|m_{l+2}^E\rangle$ denote the bases of the system block and the environment block, respectively, and the $|\sigma_l\rangle$ are the σ_l local states of site block l. The product states $\{|m_{l-1}^S\rangle|\sigma_l\rangle\}$ are the bases of the block $m_{l-1}^S \bullet$ composed of the system block S and the site block l. Similarly, the product states $\{|\sigma_{l+1}\rangle|m_{l+2}^E\rangle\}$ represent the block $\bullet m_{l+1}^E$. In the procedure for calculating the reduced density matrices for the next DMRG step, one should consider the superblock to be still constructed out of two blocks, $m_{l-1}^S \bullet$ and $\bullet m_{l+2}^E$. This means one should trace over the degrees of freedom of the environment block together with the site block $l+1$ ($|\sigma_{l+1}\rangle|m_{l+2}^E\rangle$) to obtain the reduced density matrix of new system $m_{l-1}^S \bullet$, and vice versa for $\bullet m_{l+2}^E$. In this intermediate step, the wave function is given by

$$|\psi\rangle = \sum_{m_l^S, (\sigma_{l+1} m_{l+2}^E)} \psi_{m_l^S, (\sigma_{l+1} m_{l+2}^E)} |m_l^S\rangle |m_{l+2}^E \sigma_{l+1}\rangle, \tag{1.25}$$

where

$$\psi_{m_l^S, (\sigma_{l+1} m_{l+2}^E)} = \sum_{m_{l-1}^S \sigma_l} \psi_{m_{l-1}^S \sigma_l \sigma_{l+1} m_{l+2}^E} \langle m_l^S | m_{l-1}^S \sigma_l\rangle. \tag{1.26}$$

Notice that in Eq. (1.25) and (1.26), $(\sigma_{l+1} m_{l+2}^E)$ is the index of the product states $|m_{l+2}^E \sigma_{l+1}\rangle$.

Similarly, one can get

$$\begin{aligned} |\psi\rangle &= \sum_{m_l^S m_{l+1}^E} \psi_{m_l^S m_{l+1}^E} |m_l^S\rangle |m_{l+1}^E\rangle, \\ &= \sum_m \lambda_m |m_l^S\rangle |m_{l+1}^E\rangle, \end{aligned} \tag{1.27}$$

where

$$\psi_{m_l^S m_{l+1}^E} = \sum_{\sigma_{l+1} m_{l+2}^E} \psi_{m_l^S,(\sigma_{l+1} m_{l+2}^E)} \langle m_{l+1}^E | m_{l+2}^E \sigma_{l+1}\rangle = \lambda_m. \tag{1.28}$$

Here we have defined

$$|m_{l-1}^S \sigma_l\rangle \equiv |m_{l-1}^S\rangle |\sigma_l\rangle, \qquad |m_{l+2}^E \sigma_{l+1}\rangle \equiv |\sigma_{l+1}\rangle |m_{l+2}^E\rangle. \tag{1.29}$$

For a more detailed description, one can replace $|i\rangle$ and $|j\rangle$ in Eq. (1.5) by $|m_{l-1}^S \sigma_l\rangle$ and $|\sigma_{l+1} m_{l+2}^E\rangle$, respectively, and replace the matrix form of the wave function ψ_{ij} by $\psi_{m_{l-1}^S \sigma_l \sigma_{l+1} m_{l+2}^E}$ ($m_{l-1}^S \sigma_l$ by i and $\sigma_{l+1} m_{l+2}^E$ by j). By following the discussion above [starting from Eq. (1.5)], the detailed DMRG procedure can be worked out. However, in practical DMRG algorithms, one does not need to directly carry out the SVD on the matrix form of the wave function, ψ. Instead, one diagonalizes the reduced density matrix $\boldsymbol{\rho}_S$ of the system, which is in the basis $\{|m_{l-1}^S \sigma_l\rangle\}$, to obtain the eigenvectors $|m_l^S\rangle$ and the eigenvalues λ_m^2 directly. It is not necessary to diagonalize the reduced density matrix $\rho_{\mathbf{E}}$ of the environment or to truncate the corresponding basis $\{|m_l^E\rangle\}$. In practical DMRG algorithms, one does not actually calculate the reduced density matrix $\boldsymbol{\rho}_E$ in general. The environment block can be just a reflection the system block (in the infinite-system DMRG algorithm, Sec. 1.2.2), or it can be obtained from previous DMRG iterations by exchanging the status of the system and the environment (in the finite-system DMRG algorithm, Sec. 1.2.3). These special methods are employed to avoid doing this extra work, see below.

1.2.2 Infinite-system DMRG algorithm

The infinite-system DMRG algorithm is devised to build up the initial quantum lattice with a desired size of L. The lattice grows by adding sites in the middle, usually two sites at a time, see Fig. 1.3. The lattice size will grow step by step. In iteration $l-1$ (assume $l \geq 2$), one adds two sites at l and $l+1$ between the system block S (with the Hamiltonian H_S^{l-1}) and the environment block E (with the Hamiltonian H_E^{l+2}) to form the superblock in the basis

$\{|m^S_{l-1}\rangle|\sigma_l\rangle|\sigma_{l+1}\rangle|m^E_{l+2}\rangle\}$. The formal superblock Hamiltonian is constructed using H^{l-1}_S, H^{l+1}_E, and all terms connecting these two blocks. In the Heisenberg model, for example, it is given by *

$$\begin{aligned}
&[H]_{(m^S_{l-1}\sigma_l\sigma_{l+1}m^E_{l+2}),(m'^S_{l-1}\sigma'_l\sigma'_{l+1}m'^E_{l+2})} \\
&\quad = \left[[H^{l-1}_S]_{m^S_{l-1}m'^S_{l-1}}\delta_{\sigma_l\sigma'_l} + [\hat{\sigma}_{l-1}]_{m^S_{l-1}m'^S_{l-1}}\cdot[\hat{\sigma}_l]_{\sigma_l\sigma'_l}\right]\delta_{\sigma_{l+1}\sigma'_{l+1}}\delta_{m^E_{l+2}m'^E_{l+2}} \\
&\quad + \delta_{m^S_{l-1}m'^S_{l-1}}\delta_{\sigma_l\sigma'_l}\left[[\hat{\sigma}_{l+1}]_{\sigma_{l+1}\sigma'_{l+1}}\cdot[\hat{\sigma}_{l+2}]_{m^E_{l+2}m'^E_{l+2}} + [H^{l+1}_E]_{m^E_{l+2}m'^E_{l+2}}\delta_{\sigma_l\sigma'_l}\right] \\
&\quad + \delta_{m^S_{l-1}m'^S_{l-1}}\left[[\hat{\sigma}_l]_{\sigma_l\sigma'_l}\cdot[\hat{\sigma}_{l+1}]_{\sigma_{l+1}\sigma'_{l+1}}\right]\delta_{m^E_{l+2}m'^E_{l+2}},
\end{aligned} \tag{1.30}$$

where the system Hamiltonian H^{l-1}_S and the operator $\hat{\sigma}_{l-1}$ are represented in the reduced basis $\{|m^S_{l-1}\rangle\}$, while the environment Hamiltonian H^{l+1}_E and the first site operator $\hat{\sigma}_{l+2}$ are in the reduced basis $\{|m^E_{l+1}\rangle\}$. The operators $\hat{\sigma}_l$ and $\hat{\sigma}_{l+1}$ are exactly represented in the basis $\{|\sigma_l\rangle\}$ and $\{|\sigma_{l+1}\rangle\}$. The resulting Hamiltonian is represented in the superblock basis $\{|m^S_{l-1}\rangle|\sigma_l\rangle|\sigma_{l+1}\rangle|m^E_{l+2}\rangle\}$.

It is important to describe how to multiply the Hamiltonian by the wave function in the DMRG. For the sake of convenience, we rewrite Eq. (1.30) by replacing $m^S_{l-1}\sigma_l$ and $\sigma_{l+1}m^E_{l+2}$ with i and j respectively, yielding

$$[H]_{ij,i'j'} = [H^l_S]_{ii'}\delta_{jj'} + \delta_{ii'}[H^{l+1}_E]_{jj'} + [\hat{\sigma}_l]_{ii'}\cdot[\hat{\sigma}_{l+1}]_{jj'}, \tag{1.31}$$

where $H^l_S = H^{l-1}_S + \hat{\sigma}_{l-1}\cdot\hat{\sigma}_l$ and $H^{l+1}_E = \hat{\sigma}_{l+1}\cdot\hat{\sigma}_{l+2} + H^{l+2}_E$. Multiplication with the wave function in the current superblock basis can be carried out using

$$\begin{aligned}
[H\psi]_{ij} &= \sum_{i'j'}[H]_{ij,i'j'}\psi_{i'j'} \\
&= \sum_{i'j'}([H^l_S]_{ii'}\psi_{i'j} + \psi_{ij'}[H^{l+1}_E]_{jj'} + [\hat{\sigma}_l]_{ii'}\psi_{i'j'}[\hat{\sigma}_{l+1}]_{jj'}) \\
&= \mathbf{H}^l_S\psi + \psi[\mathbf{H}^{l+1}_E]^T + [\hat{\sigma}_l]\psi[\hat{\sigma}_{l+1}]^T.
\end{aligned} \tag{1.32}$$

Note that we transpose the Hamiltonian rather than transposing the wave function. This multiplication is carried out at every DMRG iteration to obtain the eigenstates. It can be applied to any DMRG algorithm as a standard procedure.

*For simplicity, we only consider spin models, such as the Heisenberg model here. For itinerant electron models, such as the Hubbard model, one needs to consider the signs of the resulting Hamiltonian elements, which are due to the anti-commutation relations of the electrons.

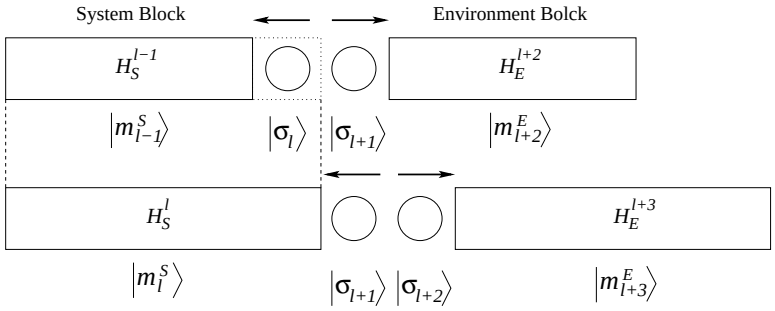

Figure 1.3: Diagrammatic sketch of one iteration of the infinite-system DMRG algorithm.

Assuming the lattice has reflection symmetry, one can form the environment block by reflecting the system block. Notice that the assumption of reflection symmetry is not necessary; it is possible to generalize the infinite-system DMRG algorithm to lattices with no reflection symmetry by building up the system and the environment block in turn.

The infinite-system DMRG algorithm for a reflection symmetric lattice consists of the following steps:

1. Construct a superblock of $L = 4$ from four initial site blocks within the basis $\{|m_1^S \sigma_2\rangle|\sigma_3 m_4^E\rangle\}$ representing the block Hamiltonian H_S^1, H_E^4, and other related operators, such as $\hat{\sigma}_2$ and $\hat{\sigma}_2$, in matrix form.

2. Diagonalize the superblock Hamiltonian using Davidson or Lanczos exact diagonalization to find the target state $\psi_{m_{l-1}^S \sigma_l, \sigma_{l+1} m_{l+2}^E}$, where $l = L/2$. Usually, $\psi_{m_{l-1}^S \sigma_l, \sigma_{l+1} m_{l+2}^E}$ is the ground state. Carry out measurements, such as the expectation values of local spins $\left\langle S_z^i \right\rangle$. If the desired final size is reached, stop the iteration here.

3. Form the reduced density matrix ρ_S of the system block $\{|m_{l-1}^S \sigma_l\rangle\}$ using $[\rho_s]_{(m_{l-1}^S \sigma_l),(m_{l-1}'^S \sigma_l')} = \sum_{\sigma_{l+1} m_{l+2}^E} \psi_{m_{l-1}^S \sigma_l, \sigma_{l+1} m_{l+2}^E} \psi_{m_{l-1}'^S \sigma_l', \sigma_{l+1} m_{l+2}^E}$, see also Eq. (1.18). Diagonalize the reduced density matrix ρ_S using full diagonalization. One can obtain at most $m_{l-1}^S \sigma_l$ eigenvectors $|m_l^S\rangle$. Keep m_l^S eigenvectors $|m_l^S\rangle$ corresponding to the largest eigenvalues. The basis of the new system block is now $\{|m_l^S\rangle\}$.

4. Form the truncated new system block Hamiltonian $H_l'^S$ from the transformation $H_l'^S = O H_l O^\dagger$, where the columns of the matrix O $(m_{l-1}^S \sigma_l \times m_l^S)$ are the eigenvectors of the reduced density matrix $\boldsymbol{\rho_S}$. Also carry out the same transformation on other needed operators of the new system block, such as the site operator $\hat{\sigma}_l' = O \hat{\sigma}_l O^\dagger$ on the boundary site l.

5. Replace the old environment block $\{|m^E_{l+2}\sigma_{l+1}\rangle\}$ with the reflection of new system block $\{|m^S_l\rangle\}$. Rename the environment block $\{|m^E_{l+3}\rangle\}$.

6. Insert two new site blocks between the new system block $\{|m^S_l\rangle\}$ and the new environment block $\{|m^E_{l+3}\rangle\}$ on sites $l+1$ and $l+2$, respectively, see Fig. 1.3. Construct a new superblock of size $L+2$. Represent the new superblock Hamiltonian in the new basis $\{|m^S_l\sigma_{l+1}\sigma_{l+2}m^E_{l+3}\rangle\}$, see Eq. (1.30).

7. Rename $L+2$ to L. Go to step 2.

Even if the lattice is not reflection symmetric, one can still apply the main parts of above infinite-system DMRG steps. One possible way to do this efficiently is to construct an environment block of fixed size instead of using the reflection of the system block in step 5. Only the system block then grows at every DMRG step. Another way to do this is to carry out the RG blocking on the environment block as well as on the system block. The system block and the environment can then have unequal sizes.

The ground state (or some low-lying exited states) that are approximately calculated in the infinite-system DMRG algorithm are usually not numerically exact. Aside from the effects of truncation errors accumulated in every infinite-system DMRG iteration step, the inaccuracy of this algorithm originates in the poor representation of the block basis. The basis of a small system block, constructed in an earlier infinite-system DMRG iteration, does not get updated in later steps when the lattice has been enlarged. Equivalently, one can consider the actual environment of a small system block to be enlarged. Therefore, in general, the previously constructed blocks are not consistent with the current wave function. This problem comes about primarily when one state or only a few states are targeted. Thus, high-energy states of a small system cannot contribute to the basis of a larger system. One possible way to overcome this difficulty is to target many energy eigenstates, taking, e.g., $\rho = \sum_i \rho_i = tr_E \sum_i^n (1/n)\, |\psi_i\rangle\langle\psi_i|$, Clearly this is not efficient. The solution to this problem is the finite-system DMRG algorithm, in which every block basis is updated by sweeping through superblocks of fixed size. In other words, the sweeping procedure improves the self-consistency between the wave function and each block basis by picking up contributions from previously discarded states.

1.2.3 Finite-system DMRG algorithm

After obtaining the approximate block representations for a lattice of desired size L built up by the infinite-system DMRG algorithm, application of the finite-system DMRG algorithm

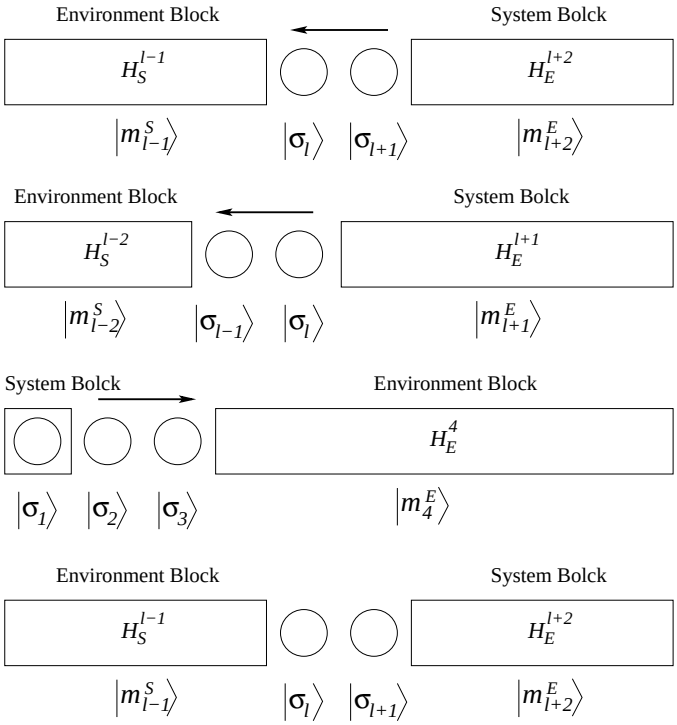

Figure 1.4: Depiction of the finite-system DMRG algorithm.

provides high accuracy results. Each block basis is optimized by sweeping two exactly represented site blocks through a lattice of fixed size L. Because the size of the lattice is fixed, the system block grows, while the environment block shrinks (see Fig. 1.3). The reduced transformation only takes place on the system block, while the environment block is transformed by using previously stored environment blocks. In each step of a particular sweep, the basis of the system block is optimized.

For the consistency with the discussion of the infinite-system DMRG algorithm, Sec. 1.2.2, we assume that the lattice has reflection symmetry. One then only needs to do sweeps through a half of the lattice. The finite-system DMRG algorithm of a reflection symmetric lattice consists of the following steps:

1. After the desired lattice size L is reached in the second step of the infinite-system DMRG algorithm, one has obtained the superblock basis $\{|m_{l-1}^S \sigma_l \sigma_{l+1} m_{l+2}^E\rangle\}$.

2. Switch the roles of system block and the environment, see Fig. 1.4 and steps 2-4 in the infinite-system DMRG algorithm. Construct the new reduced basis $\{|m_{l+1}^E\rangle\}$ of the system block.

3. Use a stored block of appropriate size as an environment block to form the new superblock in the basis $\{|m^S_{l-2}\sigma_{l-1}\sigma_l m^E_{l+1}\rangle\}$, see Fig. 1.4.

4. Repeat steps 2-3 above until the environment block shrinks to only one site. The superblock is now in the basis $\{|\sigma_1\sigma_2\sigma_3 m^E_4\rangle\}$. Note that every system block is stored at each step above. Here a right-to-left half-sweep is finished.

5. Switch the roles of system block and the environment. Repeat steps 2-3 above, until the starting point superblock with the basis $\{|m^S_{l-1}\sigma_l\sigma_{l+1}m^E_{l+2}\rangle\}$ is reached. Here a left-to-right half-sweep is finished. These two half-sweeps make up one sweep in finite-system DMRG algorithm.

6. Repeat steps 2-5, until convergence of the ground state energy is obtained.

7. Carry out the measurements.

Notice that the assumption of reflection symmetry is not necessary; it is possible to generalize the finite-system DMRG algorithm to lattices with no reflection symmetry by sweeping through the whole lattice. In addition, in some cases, simultaneously targeting a few of energy eigenstates may improve the convergence of the ground state.

To improve the efficiency of the calculations, one usually fixes the quantum number of the superblock, drastically shrinking the basis. For example, the z-component of total spin S_z is fixed in the calculation of the ground state of the Heisenberg model; the z-component of total spin S_z and the total electron number are fixed in the calculation of the ground state of the Hubbard model. Besides using $U(1)$ symmetry of the Hamiltonian, other symmetries are also can be applied in the DMRG calculations, e.g., $SU(2)$ symmetry [38].

The measurements are usually performed after several finite-system DMRG sweeps have been carried out. By representing the operator A in the superblock basis, the expectation value of the operator A, $\langle\psi|A|\psi\rangle$, can be directly calculated, where the current wave function has the representation $|\psi\rangle \equiv \psi_{m^S_{l-1}\sigma_l\sigma_{l+1}m^E_{l+2}}$. We take the Heisenberg model as an example. For a local operator S^z_j, the expectation value is given by

$$\langle\psi|S^z_j|\psi\rangle = \sum_{m^S_{l-1}\sigma_l\sigma_{l+1}m^E_{l+2},\sigma'_l} \psi^*_{m^S_{l-1}\sigma_l\sigma_{l+1}m^E_{l+2}}[S^z_j]_{\sigma_l\sigma'_l}\psi_{m^S_{l-1}\sigma'_l\sigma_{l+1}m^E_{l+2}} \tag{1.33}$$

and similarly for other local operators. This formula gives a exact evaluation of $\langle\psi|A|\psi\rangle$ with the approximate wave function $\psi_{m^S_{l-1}\sigma_l\sigma_{l+1}m^E_{l+2}}$. The only error comes from the reduced basis.

For the expectation value of two operators on two different sites, such as the spin-spin correlation function $\langle\psi|S^z_j S^z_k|\psi\rangle$, how to keep track of these two operators depends on whether j and k are located on the different block or not. If j and k are on different blocks, $\langle\psi|S^z_j S^z_k|\psi\rangle$ can be evaluated using

$$\langle\psi|S^z_j S^z_k|\psi\rangle = \sum_{m^S_{l-1}\sigma_l\sigma_{l+1}m^E_{l+2},m'^S_{l-1}m'^E_{l+2}} \psi^*_{m^S_{l-1}\sigma_l\sigma_{l+1}m^E_{l+2}}[S^z_j]_{m^S_{l-1}m'^S_{l-1}}[S^z_k]_{m^E_{l+2}m'^E_{l+2}}\psi_{m'^S_{l-1}\sigma_l\sigma_{l+1}m'^E_{l+2}}, \tag{1.34}$$

where one keeps track of $[S^z_j]_{m^S_{l-1}m'^S_{l-1}}$ and $[S^z_k]_{m^E_{l+2}m'^E_{l+2}}$ independently. If j and k are on the same block, $\langle\psi|S^z_j S^z_k|\psi\rangle$ should be evaluated using

$$\langle\psi|S^z_j S^z_k|\psi\rangle = \sum_{m^S_{l-1}\sigma_l\sigma_{l+1}m^E_{l+2},m'^S_{l-1}} \psi^*_{m^S_{l-1}\sigma_l\sigma_{l+1}m^E_{l+2}}[S^z_j S^z_k]_{m^S_{l-1}m'^S_{l-1}}\psi_{m'^S_{l-1}\sigma_l\sigma_{l+1}m^E_{l+2}}, \tag{1.35}$$

where one does not keep track of $[S^z_j]_{m^S_{l-1}m''^S_{l-1}}$ and $[S^z_j]_{m''^S_{l-1}m'^S_{l-1}}$ separately. The reason is that $\sum_{m''^S_{l-1}}[S^z_j]_{m^S_{l-1}m''^S_{l-1}}[S^z_j]_{m''^S_{l-1}m'^S_{l-1}} \approx [S^z_j S^z_j]_{m^S_{l-1}m'^S_{l-1}}$, where $\sum_{m''^S_{l-1}}|m''^S_{l-1}\rangle\langle m''^S_{l-1}| \approx 1$ for the truncated basis $\{|m''^S_{l-1}\rangle\}$.

The other important operator that must be evaluated is the Hamiltonian operator. By multiplying Eq. (1.32) by ψ^*_{ij} from the left, one obtains the expression for the expected value of the energy,

$$\begin{aligned}\langle\psi|H|\psi\rangle &= \sum_{iji'j'} \psi^*_{ij}[H]_{ij,i'j'}\psi_{i'j'} \\ &= \sum_{iji'j'}(\psi^*_{ij}[H^l_S]_{ii'}\psi_{i'j} + \psi^*_{ij}\psi_{ij'}[H^{l+1}_E]_{jj'} + \psi^*_{ij}[\hat{\sigma}_l]_{ii'}\psi_{i'j'}[\hat{\sigma}_{l+1}]_{jj'}).\end{aligned} \tag{1.36}$$

One can also increase the efficiency by applying the so-called wave function transformation in the finite-system DMRG algorithm [39]. A approximate wave function generated from the previous sweep step using the wave function transformation can reduce the number of Davidson steps or Lanczos steps substantially. For the sake of simplicity, we will not include any truncations in the basis transformation procedure, which means $\sum_m |m\rangle\langle m| = 1$. We begin with the wave function of the superblock

$$|\psi\rangle = \sum_{m^S_{l-1}\sigma_l\sigma_{l+1}m^E_{l+2}} \psi_{m^S_{l-1}\sigma_l\sigma_{l+1}m^E_{l+2}}|m^S_{l-1}\rangle|\sigma_l\rangle|\sigma_{l+1}\rangle|m^E_{l+2}\rangle. \tag{1.37}$$

In step 2 of the finite-system DMRG algorithm, Eq. (1.37) is transformed to

$$|\psi\rangle = \sum_{m^S_{l-1}\sigma_l m^E_{l+1}} \psi_{m^S_{l-1}\sigma_l m^E_{l+1}} |m^S_{l-1}\rangle|\sigma_l\rangle|m^E_{l+1}\rangle, \tag{1.38}$$

where

$$\psi_{m^S_{l-1}\sigma_l m^E_{l+1}} = \sum_{\sigma_{l+1} m^E_{l+2}} \psi_{m^S_{l-1}\sigma_l\sigma_{l+1} m^E_{l+2}} \langle m^E_{l+1}|m^E_{l+2}\sigma_{l+1}\rangle, \tag{1.39}$$

by inserting $\sum_{m^E_{l+1}} |m^E_{l+1}\rangle\langle m^E_{l+1}| = 1$ into Eq. (1.37). Step 3 of the finite-system DMRG algorithm further transforms Eq. (1.38) to

$$|\psi\rangle = \sum_{m^S_{l-2}\sigma_{l-1}\sigma_l m^E_{l+1}} \psi_{m^S_{l-2}\sigma_{l-1}\sigma_l m^E_{l+2}} |m^S_{l-2}\rangle|\sigma_{l-1}\rangle|\sigma_l\rangle|m^E_{l+1}\rangle, \tag{1.40}$$

where

$$\psi_{m^S_{l-2}\sigma_{l-1}\sigma_l m^E_{l+2}} = \sum_{m^S_{l-1}} \psi_{m^S_{l-1}\sigma_l m^E_{l+1}} \langle m^S_{l-2}\sigma_{l-1}|m^S_{l-1}\rangle. \tag{1.41}$$

These two steps shift the positions of the single sites one place from right to left.

The wave function transformation can be generized to the MPS algorithm, which was introduced by by Östlund and Rommer [40]. One can define

$$\langle m^S_{l-2}\sigma_{l-1}|m^S_{l-1}\rangle = A^{m^S_{l-2},m^S_{l-1}}_{l-1}[\sigma_{l-1}], \tag{1.42}$$

$$\langle m^E_{l+3}\sigma_{l+2}|m^E_{l+2}\rangle = A^{m^E_{l+2},m^E_{l+3}}_{l+2}[\sigma_{l+2}], \tag{1.43}$$

where the matrix $A_l[\sigma_l]$ was used to treat the fixed point (i.e., a site independent $A[\sigma]$) to which the DMRG eventually converges. From Eq. (1.42), one then obtains

$$|m^S_{l-1}\rangle = \sum_{m^S_{l-2}\sigma_{l-1}} A^{m^S_{l-2},m^S_{l-1}}_{l-1}[\sigma_{l-1}]|m^S_{l-2}\rangle|\sigma_{l-1}\rangle, \tag{1.44}$$

where

$$\sum_{\sigma_l} A^{S\dagger}_l[\sigma_l]A^S_l[\sigma_l] = 1, \tag{1.45}$$

$$|m^E_{l+2}\rangle = \sum_{m^E_{l+3}\sigma_{l+2}} A^{m^E_{l+2},m^E_{l+3}}_{l+2}[\sigma_{l+2}]|\sigma_{l+2}\rangle|m^E_{l+3}\rangle, \tag{1.46}$$

and

$$\sum_{\sigma_l} A_l^E[\sigma_l] A_l^{E\dagger}[\sigma_l] = 1. \tag{1.47}$$

One can carry out a recursion step to obtain $|m_{l-2}^S\rangle$ expressed in terms of $|m_{l-3}^S\rangle$ using Eq. (1.44). One stops the recursion at site N when the left block basis $|m_N^S\rangle = |\sigma_1 \dots \sigma_N\rangle$ in the dimension D. One then obtains

$$\begin{aligned} |m_{l-1}^S\rangle &= \sum_{m_N^S,\dots m_{l-2}^S \sigma_{N+1}\dots\sigma_{l-1}} A_{N+1}^{m_N^S, m_{N+1}^S}[\sigma_{N+1}] \dots A_{l-1}^{m_{l-2}^S, m_{l-1}^S}[\sigma_{l-1}] |m_N^S\rangle |\sigma_{N+1} \dots \sigma_{l-1}\rangle \\ &= \sum_{m_{N+1}^S,\dots m_{l-2}^S \sigma_1\dots\sigma_{l-1}} A_{N+1}^{m_N^S, m_{N+1}^S}[\sigma_{N+1}] \dots A_{l-1}^{m_{l-2}^S, m_{l-1}^S}[\sigma_{l-1}] |\sigma_1 \dots \sigma_{l-1}\rangle. \end{aligned} \tag{1.48}$$

Similarly, one can expand $|m_{l+1}^E\rangle$ as

$$\begin{aligned} |m_{l+2}^E\rangle &= \sum_{m_{l+3}^E \dots m_R^E \sigma_l \dots \sigma_{M-1}} A_{l+2}^{m_{l+2}^E, m_{l+3}^E}[\sigma_{l+2}] \dots A_{M-1}^{m_{M-1}^E, m_M^E}[\sigma_{M-1}] |\sigma_l \dots \sigma_{M-1}\rangle |m_M^E\rangle \\ &= \sum_{m_{l+3}^E \dots m_{M-1}^E \sigma_{l+2} \dots \sigma_L} A_{l+2}^{m_{l+2}^E, m_{l+3}^E}[\sigma_{l+2}] \dots A_{M-1}^{m_{M-1}^E, m_M^E}[\sigma_{M-1}] |\sigma_{l+2} \dots \sigma_L\rangle, \end{aligned} \tag{1.49}$$

where the recursion is stpped at site M, and the small right block M has the basis $\{|m_M^E\rangle\}$ of the dimension of D, where $|m_M^E\rangle = |\sigma_M \dots \sigma_L\rangle$.

Substituting Eqs. (1.48) and (1.49) into Eq. (1.37), and rewriting $\psi_{m_{l-1}^S \sigma_l \sigma_{l+1} m_{l+2}^E}$ in the form $\psi^{m_{l-1}^S m_{l+2}^E}[\sigma_l \sigma_{l+1}]$, one obtains a $D \times D$ wave function,

$$|\psi\rangle = \sum_{\sigma_1 \dots \sigma_N} [A_{N+1}[\sigma_{N+1}] \dots A_{l-1}[\sigma_{l-1}] \psi[\sigma_l \sigma_{l+1}] A_{l+2}[\sigma_{l+2}] \dots A_{M-1}[\sigma_{M-1}]]^{m_N^S m_M^E} |\sigma_1 \dots \sigma_L\rangle. \tag{1.50}$$

The procedure in the finite-system DMRG sweeps can be recognized again in Eq. (1.50). The wave function coefficients $\psi[\sigma_l \sigma_{l+1}]$ are updated at every step in a right to left sweep. Furthermore, a new optimized matrix $A_{l+2}[\sigma_{l+2}]$ is obtained by using the updated wave function to form the reduced density matrix ρ_E^{l+2}. Note that, the matrices $A_l[\sigma_l]$ and $A_{l+1}[\sigma_{l+1}]$ are not needed to represent the current DMRG wave function. However, they will be generated in the next steps. From this view of point, the DMRG can be viewed as an optimization procedure for a variational matrix-product wave function.

The finite-system DMRG algorithm is also important for the Suzuki-Trotter adaptive time-dependent DMRG (see sec.1.3.2). In the Suzuki-Trotter adaptive time-dependent DMRG, one

directly applies the time-evolution operator to the two site blocks l and $l+1$ in a finite-system sweeping procedure to advance the wave function one time step.

1.3 Time-dependent DMRG

The density matrix renormalization group (DMRG) currently provides one of the most powerful, accurate, and effective simulations of one-dimensional correlated quantum lattice systems for calculating the static properties of the ground state and a few low-lying excited states. It has also been generalized to calculate frequency-dependent spectral functions via the correction vector method [41] or the more efficient "dynamical DMRG" method [42]. However, the most significant recent development in extending the DMRG is the stimulation of the real-time evolution of a quantum system. It allows us to evaluate a number of dynamic properties of a system, such as transport properties, nonequilibrium behavior after a perturbation, and frequency-dependent spectral functions via Fourier transformation.

Let us revisit the time-dependent problem in quantum mechanics. The evolution of a system is determined by the time-dependent Schrödinger equation

$$i\frac{\partial}{\partial t}|\psi(t)\rangle = H(t)|\psi(t)\rangle, \tag{1.51}$$

where $H(t)$ is the (in general time-dependent) Hamiltonian, and $|\psi(t)\rangle$ is the time-dependent wave vector of the system at time t. The basic task is to study the time evolution of the wave vector:

$$|\psi(t_0)\rangle \longrightarrow |\psi(t)\rangle. \tag{1.52}$$

Here $|\psi(t_0)\rangle$ is the wave function at initial time t_0. At first glance, one might try to integrate the Schrödinger equation (1.51) directly. In most cases, it is very difficult construct explicit solutions analytically. Here we will construct a formal solution of the Schrödinger equation. We assert that the wave vector $|\psi(t)\rangle$ is propagated from $|\psi(t_0)\rangle$ by a unitary operator which is called the time evolution operator $U(t,t_0)$:

$$|\psi(t)\rangle = U(t,t_0)|\psi(t_0)\rangle, \tag{1.53}$$

where

$$U^\dagger(t,t_0)U(t,t_0) = 1, \quad U^\dagger(t,t_0) = U^{-1}(t,t_0) = U(t_0,t). \tag{1.54}$$

For an intermediate time t_1, we have

$$U(t,t_1) = U(t,t_1)U(t_1,t_0), \quad (t > t_1 > t_0). \tag{1.55}$$

Substituting Eq. (1.53) into the Schrödinger equation, Eq. (1.51), we can write the Schrödinger equation as

$$i\frac{\partial}{\partial t}U(t,t_0)|\psi(t_0)\rangle = H(t)U(t,t_0)|\psi(t_0)\rangle. \tag{1.56}$$

Since the initial wave vector $|\psi(t_0)\rangle$ is not dependent on Eq. (1.56), Eq. (1.56) can be written as

$$i\frac{\partial}{\partial t}U(t,t_0) = H(t)U(t,t_0). \tag{1.57}$$

This is the Schrödinger equation for the time evolution operator $U(t,t_0)$. The formal solution of Eq. (1.57) is

$$U(t,t_0) = T\left[\exp\left(-i\int_{t_0}^{t} H(t')dt'\right)\right], \tag{1.58}$$

where T is the time-ordering operator. We consider three different cases of the behavior of the system Hamiltonian $H(t)$. If $H(t)$ is independent of time, i.e, $H(t)$ remains unchanged for all time t, the time evolution operator $U(t,t_0)$ can be simplified to

$$U(t,t_0) = \exp\left[-iH(t)(t-t_0)\right]. \tag{1.59}$$

It is easy to check that solution (1.59) satisfies the Schrödinger equation (1.51). If the system Hamiltonian $H(t)$ is time-dependent and the Hamiltonians at different times $\{H(t_i)\}$ all commute, then the time evolution operator $U(t,t_0)$ is given by

$$U(t,t_0) = \exp\left[-i\int_{t_0}^{t} H(t')dt'\right]. \tag{1.60}$$

The time-ordering operator dose not appear.

If the system Hamiltonian set $\{H(t_i)\}$ at different time do not commute, we must expend the time evolution operator in a Dyson series,

$$\begin{aligned} U(t,t_0) = 1 - i\int_{t_0}^{t} dt_1 H(t_1) - \int_{t_0}^{t} dt_1 \int_{t_0}^{t_1} dt_2 H(t_1)H(t_2) \\ + (-i)^n \int_{t_0}^{t} dt_1 \int_{t_0}^{t_1} dt_2 \cdots \int_{t_0}^{t_{n-1}} dt_n H(t_1)H(t_2)\cdots H(t_n) + \cdots . \end{aligned} \tag{1.61}$$

which has the form of time-dependent perturbation theory. Obviously Eq. (1.60) is a special case of Eq. (1.61).

However, from a numerical viewpoint, if the time-dependent Hamiltonian $H(t)$ does not drastically change over time and $H(t_i)$ at different time all commute, one can directly integrate the Schrödinger equation (1.51) by treating the instantaneous Hamiltonian $H(t + \Delta t)$ as a constant value in a very small time interval Δt around time t. This scheme was applied within the DMRG to treat transport problem [21, 43].

We will focus on time operators $U(t, t_0)$ (1.59) in which $H(t)$ only changes at time $t_0 = 0$ and keeps in a constant value H^Q at time $t > 0$. The time evolution wave function $|\psi(t)\rangle$ will then be fully determined by the time evolution operator $U(t, t_0) = \mathrm{e}^{-iH^Q t}$. Thus, one can write down the formal solution of the time-dependent Schrödinger equation (1.51) as

$$|\psi(t)\rangle = \mathrm{e}^{-iH^Q t}|\psi(0)\rangle = \sum_n d_n \mathrm{e}^{-iE_n t}|n\rangle, \tag{1.62}$$

where the coefficients $d_n = \langle n|\psi(0)\rangle$ are time-independent, and the complete basis $\{|n\rangle\}$ and the eigenvalues E_n are solutions of the eigenvalue problem

$$H^Q|n\rangle = E_n|n\rangle. \tag{1.63}$$

In the cases below, the initial wave function $|\psi(0)\rangle$ is given by

$$H(0)|\psi(0)\rangle = E|\psi(0)\rangle \tag{1.64}$$

where $H(0)$ is the initial Hamiltonian at time $t = 0$, and E is the corresponding eigenvalue. In DMRG simulation, $|\psi(0)\rangle$ is typically calculated as the ground state of the Hamiltonian $H(0)$. More general, the initial wave function $|\psi(0)\rangle$ can be an arbitrary known state.

A time-dependent observable $O(t)$ can be evaluated as

$$\langle O(t)\rangle = \langle\psi(t)|O|\psi(t)\rangle = \sum_n |d_n|^2\langle n|O|n\rangle + \sum_{m\neq n} e^{-i(E_n-E_m)t} d_m^* d_n \langle m|O|n\rangle. \tag{1.65}$$

The form on the right-hand side of Eq. (1.65), however, is of limited usefulness because it is hard to obtain all the exited states of the Hamiltonian H^Q. Except for the overlap between two ground states $d_0 = \langle 0|\psi(0)\rangle$, the state overlaps d_n ($n > 0$) in Eq. (1.62) are not easy to obtain. Thus this method can only be applied to very small systems within full exact diagonalization methods which can calculate all the excited states. One way to overcome this difficulty is to

construct an effective approximation to the Hilbert space $\{|n\rangle\}$ at an arbitrary time t. In the last several years, There has been much progress in finding such an effective approximate Hilbert space in the DMRG simulation of time-dependent problems. Several different time-dependent DMRG methods have been developed that can simulate systems for a relatively long time before the accumulated numerical errors become significant.

1.3.1 Historical development of algorithms

The first DMRG approach to time-dependent quantum many-body problems was formulated by Cazalilla and Marston [43]. They studied quantum tunneling through a quantum dot in the Kondo regime and quantum tunneling effects at the junction between two Luttinger liquids. They first calculate the ground state $|\psi(0)\rangle$ of the initial Hamiltonian $H(0)$ using the static infinite-system DMRG algorithm. The initial Hamiltonian $H(0)$ is then represented in the truncated DMRG space as $H'(0)$, and the additional time-dependent perturbation $h(t)$ is represented in the truncated space as $h'(t)$, resulting in the time-dependent Hamiltonian $H'(t) = H'(0) + h'(t)$. The time-dependent Schrödinger equation is then

$$i\frac{\partial}{\partial t}|\psi(t)\rangle = (H'(t) - E_0)|\psi(0)\rangle = \tilde{H}(t)|\psi(0)\rangle, \tag{1.66}$$

where E_0 is the ground-state energy of the initial state. It is important to reduce the value of the diagonal elements of $H'(t)$ in order to weaken the amplitude of the transport current oscillations. Cazalilla and Marston numerically integrated the time-dependent Schrödinger equation (1.66) using the fourth-order Runge-Kutta algorithm [44], [†] which is compactly written in terms of the four vectors

$$\begin{aligned}
|k_1\rangle &= -i\Delta t\tilde{H}(t)|\psi(t)\rangle, \\
|k_2\rangle &= -i\Delta t\tilde{H}(t + \Delta t/2)(|\psi(t)\rangle + 1/2|k_1\rangle), \\
|k_3\rangle &= -i\Delta t\tilde{H}(t + \Delta t/2)(|\psi(t)\rangle + 1/2|k_2\rangle), \\
|k_4\rangle &= -i\Delta t\tilde{H}(t + \Delta t)(|\psi(t)\rangle + |k_3\rangle).
\end{aligned} \tag{1.67}$$

[†]The Runge-Kutta algorithm violates the unitarity of the time evolution. This shortfull can be avoided by using the Crank-Nicholson algorithm [44], which can be implemented by writing the time evolution operator $e^{-iH\Delta t}$ in Cayley form:

$$e^{-i\tilde{H}(t)\Delta t} \simeq \frac{1 - i\tilde{H}(t)\Delta t/2}{1 + i\tilde{H}(t)\Delta t/2}.$$

It is a unitary and second-order method for the time evolution.

The wave function $|\psi(t+\Delta t)\rangle$ at time $t+\Delta t$ is then given by

$$|\psi(t+\Delta t)\rangle \approx |\psi(t)\rangle + \frac{1}{6}|k_1\rangle + \frac{1}{3}|k_2\rangle + \frac{1}{3}|k_3\rangle + \frac{1}{6}|k_4\rangle + O(\Delta t^5). \tag{1.68}$$

Their calculations showed that this method works well for relatively short times ($t \lesssim 20$). However, for a longer time evolution, they found that the transport current deviated from the exact solution with a systematic oscillation even when 500 states were kept. This numerical error is due to the fact that, during the time evolution, the state $|\psi(t)\rangle$ is constrained to be in the static ground-state Hilbert space of $|\psi(0)\rangle$. The overlap between the effective Hilbert space of $|\psi(t)\rangle$ and that of $|\psi(0)\rangle$ is large only for short times. For a longer time evolution, the effective Hilbert space of $|\psi(t)\rangle$ deviates from the ground state space, introducing large numerical errors in some measurements.

An improved method was introduced by Luo, Xiang, and Wang [45]. In principle, in a small time interval Δt, $|\psi(t+2\Delta t)\rangle \approx c_1|\psi(t)\rangle + c_2|\psi(t+\Delta t)\rangle$, with an error less than $O(\Delta t^2)$. This means that $|\psi(t+2\Delta t)\rangle$ has an effective space which is the linear combination of the space of $|\psi(t)\rangle$ and $|\psi(t+\Delta t)\rangle$. This fact motivated the authors to use multiple target states in the DMRG calculation to retain as many relevant states as possible in the time evolution. They proposed simultaneously targeting time-evolved wave functions at several different times t_i. Thus, the reduced density matrix is formed as $\rho_S = \mathrm{tr}_E \sum_{i=0}^{N} p_i|\psi(t_i)\rangle\langle\psi(t_i)|$ with $\sum_{i=0}^{n} p_i = 1$, so that $\mathrm{tr}(\rho_S) = 1$. The final time t_n is equally divided into n intervals $(t_0, t_1, \ldots, t_n)$. They applied the infinite-system DMRG algorithm to construct the system. For the first step of infinite-system DMRG algorithm, they evaluated every $|\psi(t_i)\rangle$ (in their calculations $n \geq 6$) of a small system of size L_0 using a Hamiltonian that contains the time-dependent perturbation $h(t_i)$. Simultaneously, they constructed a larger system using the basis obtained in the first DMRG step from the reduced density matrix $\rho_S^{L_0}$. Every $|\psi(t_i)\rangle$ and ρ_S was treated in every DMRG iteration. This method overcomes the problem with erroneous oscillations in transport current. Cazalilla and Marston's method, which only targets the initial state, i.e., the ground state wave function $|\psi(t_0)\rangle$, is a limiting case of Luo et al.'s method. However, Luo et al.'s method is very time consuming, because every $|\psi_i\rangle$ and density matrix ρ_S must be calculated in every DMRG step.

Alternately to directly solving the time-dependent Schrödinger equation as above, another approach is to directly treat the formal solution $|\psi(t)\rangle = \mathrm{e}^{-iHt}|\psi(0)\rangle$, assuming H does not depend on time explicitly. Schmitteckert calculated the time evolution of a Gaussian wave packet on a spinless Fermi chain by directly computing $\mathrm{e}^{-iH\Delta t}|\psi(0)\rangle$ by mapping it onto the Krylov space expanded by $\{|\psi(0)\rangle, H|\psi(0)\rangle, H^2|\psi(0)\rangle, \ldots, H^n|\psi(0)\rangle\}$ [46]. Here the initial state

$|\psi(0)\rangle$ is the ground state of the perturbed Hamiltonian consisting of H plus a Gaussian potential δH. Moreover, rather than applying the infinite-system DMRG algorithm to construct the approximation solution, the initial state $|\psi(0)\rangle$ is improved using the finite-system DMRG algorithm. As in Lanczos diagonalization, the Hermitian Hamiltonian H is tridiagonalized using a Gram-schmidt orthonormalization process:

$$|v_{i+1}\rangle = H|v_i\rangle - \alpha_i|v_i\rangle - \beta_i^2|v_{i-1}\rangle, \tag{1.69}$$

where the coefficients are given by

$$\alpha_i = \frac{\langle v_i|H|v_i\rangle}{\langle v_i|v_i\rangle}, \qquad \beta_i^2 = \frac{\langle v_{i-1}|H|v_i\rangle}{\langle v_{i-1}|v_{i-1}\rangle} = \frac{\langle v_i|v_i\rangle}{\langle v_{i-1}|v_{i-1}\rangle}, \tag{1.70}$$

$\beta_0 = 0$, and the Lanczos vectors $|v_{-1}\rangle = 0$ and $|v_0\rangle = |\psi(0)\rangle$. Here $|v_n\rangle$ is constructed to be orthogonal to all of the previous vectors $|v_0\rangle, |v_1\rangle, \ldots, |v_{n-1}\rangle$. Notice that $|v_0\rangle$ can be taken to be normalized or unnormalized. In the above iteration, $|v_n\rangle$ ($n > 1$) are unnormalized. At step n, one can stop the recursion using the criterion $\sum_{i=1}^{2}\langle v_{n+i}|v_{n+i}\rangle < 10^{-9}$. The Hamiltonian H is then in tridiagonal form

$$\mathbf{T} = \begin{pmatrix} \alpha_0 & \beta_1 & & & & \\ \beta_1 & \alpha_1 & \beta_2 & & & \\ & \beta_2 & \alpha_2 & \ddots & & \\ & & \ddots & \ddots & \ddots & \\ & & & \ddots & \alpha_{n-1} & \beta_n \\ & & & & \beta_n & \alpha_n \end{pmatrix} \tag{1.71}$$

Thus, the time-evolution operator $e^{-iH\Delta t}$ can be represented as $e^{-i\mathbf{V}\mathbf{T}\mathbf{V}^T\Delta t}$, where $\mathbf{V}$ is a column-orthonormal matrix whose columns are the Lanczos vectors $|v_i\rangle$. One small time evolution step $e^{-iH\Delta t}|\psi(0)\rangle$ is given by the first column of $e^{-i\mathbf{V}\mathbf{T}\mathbf{V}^T\Delta t}\mathbf{V} = \mathbf{V}e^{-i\mathbf{T}\Delta t}$. As in Luo et al's [45] method, the whole time interval is targeted. In order to get the wave function $\psi(t + \Delta t)$, one applies

$$\psi(t + \Delta t) = e^{-iH\Delta t}\psi(t). \tag{1.72}$$

When there is only a small perturbation, the author also targets the ground and low-lying

excited states $|\psi_m\rangle$ of H. The reduced density matrix is formed by targeting all of these states,

$$\rho_S = \mathrm{tr}_E \left(\sum_m \frac{1}{2m} |\psi_m\rangle\langle\psi_m| + \sum_{i=0}^{N} \frac{1}{2n} |\psi(t_i)\rangle\langle\psi(t_i)| \right). \tag{1.73}$$

A few finite-system DMRG sweeps are needed to build up the self-consistency between the reduced density matrix ρ_S and the targeted states. The resulting truncated Hilbert space is thus a good approximation for the whole time evolution. Here the error is mainly determined by the DMRG truncation error ϵ. Since the method forms a Hilbert space for the whole time evolution, it is quite time-consuming.

More efficient methods to treat time evolution adapt the Hilbert space as the procedure is carried out. We will first describe the adaptive method developed by Feiguin and White [47], which is related to the above methods except that it targets several states at different time intervals within the fourth-order Runge-Kutta algorithm. The adaptive scheme can be used with a number of time propagation methods such as the Lanczos-vector-based time evolution or Schmitteckert's method introduced above. We will discuss a more efficient adaptive method, the adaptive time-dependent DMRG using a Suzuki-Trotter decomposition, in the next section.

By targeting a small number of time intervals around a particular time rather than targeting the whole evolution time, Feiguin and White's method [47] shows better performance, consuming less CPU time and memory. They applied the fourth-order Runge-Kutta algorithm to calculate wave fuctions at four targeted times, $|\psi(t)\rangle$, $|\psi(t + \Delta t/3)\rangle$, $|\psi(t + 2\Delta t/3)\rangle$, $|\psi(t + \Delta t)\rangle$. Using Eqs. (1.67), one can obtain the wave functions at time $t + \Delta t/3$ and $t + 2\Delta t/3$:

$$|\psi(t + \Delta t/3)\rangle \approx |\psi(t)\rangle + \frac{1}{162} (31|k_1\rangle + 14(|k_2\rangle + |k_3\rangle) - 5|k_4\rangle) + O(\Delta t^4), \tag{1.74}$$

$$|\psi(t + \Delta 2t/3)\rangle \approx |\psi(t)\rangle + \frac{1}{81} (16|k_1\rangle + 20(|k_2\rangle + |k_3\rangle) - 2|k_4\rangle) + O(\Delta t^4). \tag{1.75}$$

The reduced density matrix of the system block is then formed by targeting these four wave functions: $\rho_S = \mathrm{tr}_E \sum_{j=0}^{3} 1/4\, |\psi(t + j\Delta t/3)\rangle\langle\psi(t + j\Delta t/3)|$. This procedure applies to every step of the finite-system DMRG sweep. Generally, for every Runge-Kutta iteration, the four targeted wave functions and the corresponding reduced density matrix ρ_S are not self-consistent. Therefore, some sweeps are needed to build up the self-consistency between the four targeted wave functions and the reduced density matrix ρ_S in order to get a well-adapted reduced Hilbert space. In practice, they updated $|\psi(t + \Delta t/3)\rangle$, $|\psi(t + 2\Delta t/3)\rangle$, $|\psi(t + \Delta t)\rangle$ using four renewed Runge-Kutta vectors $|k_1\rangle$, $|k_2\rangle$, $|k_3\rangle$, $|k_4\rangle$ obtained from $|\psi(t)\rangle$ (see Eq. (1.67)) at every

step of a finite-system DMRG half-sweep without advancing the time. In a standard DMRG truncation procedure, the Hilbert space of these wave functions at four different time intervals is updated at every step of a half-sweep. A half-sweep is usually sufficient to obtain the self-consistency between wave functions and the reduced density matrix ρ_S. At the last step of a half-sweep, one obtains an effective wave function $|\psi(t+\Delta t)\rangle$ and can then move to the next time step. If necessary, additional sweeps can be carried out in order to further converge the reduced Hilbert space before evolving to the next time step. Except for the error from the Runge-Kutta iterations, the truncation error P from every step in the finite-system DMRG sweeps should accumulate gradually. Because of the adaptive adjustment of the Hilbert space, this method is generally more effective than full Hilbert space time-evolution methods. However, the sweeps needed to build the self-consistancy between the wave functions and the density matrix still costs a lot of additional time, especially for a very large reduced Hilbert Space.

In the context of quantum information physics, Vidal introduced a method called the time-evolving block decimation (TEDB) [48, 49], which is formulated in terms of a matrix product state (MPS), to simulate time-dependent problems of one-dimensional systems with near-neighbor interactions. As the TEDB and the DMRG both use the Schmidt decomposition and an identical truncation procedure, White et al. [21] and Daley et al. [22] were able to express a TEDB-like algorithm in the traditional DMRG language. The new algorithm in the DMRG context is called the "Suzuki-Trotter adaptive time-dependent DMRG".

1.3.2 Suzuki-Trotter adaptive time-dependent DMRG

The key to this algorithm is the Suzuki-Trotter decomposition of the time-evolution operator $e^{-iH\Delta t}$. The Suzuki-Trotter decomposition has been extensively used in the area of quantum Monte Carlo simulations. A Hamiltonian H only containing nearest-neighbor interactions can be split into two parts

$$H = H_A + H_B, \tag{1.76}$$

$$H_{A(B)} = \sum_{i\,odd\,(even)} H_{i,i+1}, \tag{1.77}$$

where $H_{i,i+1}$ are the two-site local bond Hamiltonians operating on the odd bonds connecting the sites i and $i+1$ (i odd), or on the even bonds connecting the sites i and $i+1$ (i even). Although, in general, H_A does not commute with H_B, all the local bond Hamiltonians $H_{i,i+1}$

within each sum H_A or H_B commute with each other. Therefore, the corresponding time-evolution operator $e^{-iH_A\Delta t}$ or $e^{-iH_B\Delta t}$ can be rewritten as a product of local time evolution operators,

$$e^{-iH_A\Delta t} = \prod_{i\,odd} e^{-iH_{i,i+1}\Delta t} = e^{-iH_{1,2}\Delta t} e^{-iH_{3,4}\Delta t} e^{-iH_{5,6}\Delta t} \ldots, \tag{1.78}$$

$$e^{-iH_B\Delta t} = \prod_{i\,even} e^{-iH_{i,i+1}\Delta t} = e^{-iH_{2,3}\Delta t} e^{-iH_{4,5}\Delta t} e^{-iH_{6,7}\Delta t} \ldots. \tag{1.79}$$

For a small time interval Δt, the time-evolution operator $e^{-iH\Delta t}$ can be expanded in the second-order Suzuki-Trotter decomposition as

$$e^{-iH\Delta t} = e^{-iH_A\Delta t/2} e^{-iH_B\Delta t} e^{-iH_A\Delta t/2} + O(\Delta t^3). \tag{1.80}$$

Thus, all the local time-evolution operators $e^{-iH_{i,i+1}\Delta t}$ in $e^{-iH_A\Delta t}$ or $e^{-iH_B\Delta t}$ can be directly applied to the wave function simultaneously, or repeatedly applied to the wave function one by one. After performing this procedure $t/\Delta t$ times to evolve a total time t, the error is of the order of $t\Delta t^2$. The first scheme, introduced by Vidal [49], constructs the wave function in MPS form. It can be made very efficient by applying all the local time-evolution operators on the wave function simultaneously. However, here we will only discuss the second scheme [21, 22], which is much easier to implement in the framework of the standard DMRG algorithm by applying a corresponding local time-evolution operator to the wave function at each step of a finite-system DMRG sweep.

As we know, in the finite-system DMRG algorithm, see Sec. (1.2.3), a initial wave function $|\psi(0)\rangle$, which is the ground state of a specific Hamiltonian, can be expressed in the superblock basis, which is a product of the system block, two single sites, and the environment block. At a particular step l, it reads

$$|\psi(0)\rangle = \sum_{m_{l-1}\sigma_l\sigma_{l+1}m_{l+2}} \psi_{m_{l-1}\sigma_l\sigma_{l+1}m_{l+2}} |m^S_{l-1}\rangle|\sigma_l\rangle|\sigma_{l+1}\rangle|m^E_{l+2}\rangle, \tag{1.81}$$

where $|m^S_{l-1}\rangle$ is the basis of the system block, $|\sigma_l\rangle$ and $|\sigma_{l+1}\rangle$ are the states of the site l and $l+1$, respectively, and $|m^E_{l+2}\rangle$ is the basis of the environment block. After some finite-system sweeps, the wave function $|\psi(0)\rangle$ becomes a good approximation to the true wave function, and all the blocks become self-consistent with the wave function $|\psi(0)\rangle$. We can then apply the time-evolution operator $e^{-iH\Delta t}$ to the wave function $|\psi\rangle$ iteratively.

Since the Hilbert spaces of the two sites l and $l+1$ are usually quite small, one can apply

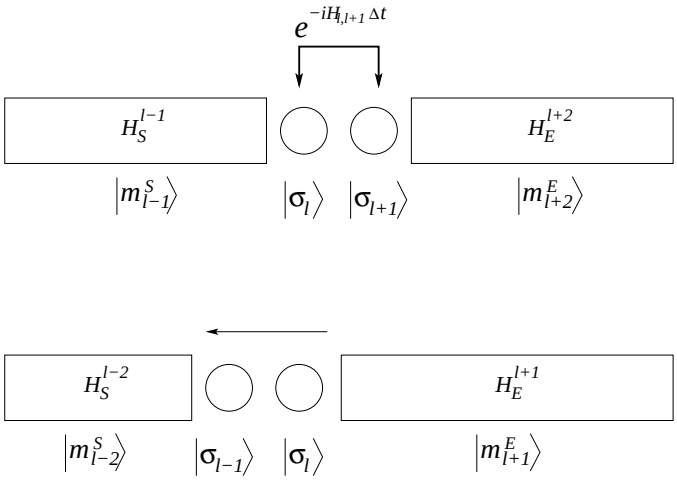

Figure 1.5: A typical sweep in the Suzuki-Trotter time-dependent DMRG

the local time-evolution operators $\mathrm{e}^{-iH_{i,i+1}\Delta t}$ to the wave function $|\psi\rangle$ exactly in one step of the finite-system DMRG sweep to get the updated wave function, see Fig. (1.5). The updated wave function is given by

$$\mathrm{e}^{-iH_{l,l+1}\Delta t}|\psi\rangle = \sum_{m_{l-1}\sigma_l\sigma_{l+1}m_{l+2}} \psi'_{m_{l-1}\sigma_l\sigma_{l+1}m_{l+2}}|m_{l-1}^S\rangle|\sigma_l\rangle|\sigma_{l+1}\rangle|m_{l+2}^E\rangle \tag{1.82}$$

where

$$\psi'_{m_{l-1}\sigma_l\sigma_{l+1}m_{l+2}} = \sum_{\sigma'_l\sigma'_{l+1}} \left[\mathrm{e}^{-iH_{l,l+1}\Delta t}\right]_{\sigma_l\sigma_{l+1},\sigma'_l\sigma'_{l+1}} \psi_{m_{l-1}\sigma_l\sigma_{l+1}m_{l+2}}. \tag{1.83}$$

Here the matrix of the local time evolution operator $\left[\mathrm{e}^{-iH_{l,l+1}\Delta t}\right]$ is represented in the $|\sigma_l\sigma_{l+1}\rangle$ basis. For obtaining $\left[\mathrm{e}^{-iH_{l,l+1}\Delta t}\right]$, one can diagonalize the local Hamiltonian $H_{l,l+1}$ to first get a diagonal matrix representation of the exponent $\mathrm{e}^{-iH_{l,l+1}\Delta t}$,

$$\left[\mathrm{e}^{-iH_{l,l+1}\Delta t}\right]_{\mathrm{diag}} = \begin{pmatrix} \mathrm{e}^{-iE_0\Delta t} & \cdots & 0 \\ \vdots & \ddots & \vdots \\ 0 & \cdots & \mathrm{e}^{-iE_n\Delta t} \end{pmatrix}, \tag{1.84}$$

where $E_0, \ldots, E_n$ are the eigenvalues of $H_{l,l+1}$. The diagonal matrix (1.84) can then be transformed to the $|\sigma_l\sigma_{l+1}\rangle$ basis using the unitary transformation

$$\left[\mathrm{e}^{-iH_{l,l+1}\Delta t}\right] = \mathbf{V}\left[\mathrm{e}^{-iH_{l,l+1}\Delta t}\right]_{\mathrm{diag}}\mathbf{V}^T, \tag{1.85}$$

where the columns of **V** (a column orthogonal matrix) are the eigenvectors of $H_{l,l+1}$.

As in the standard DMRG finite-system sweeps for calculating the ground state, both of these two active single sites l and $l+1$ should be moved to the next site by transforming the updated wave function $e^{-iH_{l,l+1}\Delta t}|\psi\rangle$. For example, we can shift these two sites leftwards, yielding the transformed wave function

$$e^{-iH_{l,l+1}\Delta t}|\psi\rangle = \sum_{m_{l-2}\sigma_{l-1}\sigma_l m_{l+1}} \psi'_{m_{l-2}\sigma_{l-1}\sigma_l m_{l+1}} |m^S_{l-2}\rangle|\sigma_{l-1}\rangle|\sigma_l\rangle|m^E_{l+1}\rangle, \tag{1.86}$$

where

$$\psi'_{m_{l-2}\sigma_{l-1}\sigma_l m_{l+1}} = \sum_{m_{l+2}\sigma_{l+1}m_{l-1}} \psi'_{m_{l-1}\sigma_l\sigma_{l+1}m_{l+2}} \langle m^E_{l+1}|m^E_{l+2}\sigma_{l+1}\rangle\langle m^S_{l-2}\sigma_{l-1}|m^S_{l-1}\rangle. \tag{1.87}$$

Afterwards, the next local time-evolution operator $e^{-iH_{l-1,l}\Delta t}$ can be applied and so forth until all the local time-evolution operators have been applied. In order to evolve through a total time t, this procedure must be performed $t/\Delta t$ times. The error is quadratic, of the order of $t\Delta t^2$. The difference here to the standard finite-system DMRG sweep is that the Hamiltonian diagonalization for getting the eigenstates does not need to be performed. In addition, since the application of $e^{-iH_{l-1,l}\Delta t}$ to the wave function is exact, one does not need to make additional sweeps to improve the basis as in other adaptive time-dependent DMRG methods [47, 50]. It is important to mention that the time evolution is sensitive to the accuracy of the initial state in some problems. Thus, before one carries out the time evolution, one should perform enough finite-system DMRG sweeps to get an initial state, usually a ground state, which is as accurate as possible.

Using the second-order Suzuki-Trotter decomposition, Eq. (1.80), one can apply the bond time-evolution operators $e^{-iH_A\Delta t/2}$ on the odd-numbered bonds during the first half-sweep, keeping the even-numbered bonds unperturbed and then apply the even-numbered bond time-evolution operators $e^{-iH_B\Delta t}$ during the reversed second half-sweep. During the third half-sweep, for the sake of efficiency, one can apply $e^{-iH_A\Delta t}$, which merges the $e^{-iH_A\Delta t/2}$ of the next time step, instead of applying $e^{-iH_A\Delta t/2}$. Then $e^{-iH_B\Delta t}$ and $e^{-iH_A\Delta t/2}$ can be applied to complete the second time step. Finally, measurements can be performed. Thus, the wave function is calculated every two time steps. This method, however, is not as efficient as possible because an average of 2.5 sweeps are needed to advance one time interval Δt.

An alternate way to perform the second-order Suzuki-Trotter decomposition time evolu-

tion is to modify it to adapt to the DMRG sweeps, i.e., to use

$$\mathrm{e}^{-iH\Delta t} = \mathrm{e}^{-iH_{1,2}\Delta t/2}\mathrm{e}^{-iH_{2,3}\Delta t/2}\ldots\mathrm{e}^{-iH_{2,3}\Delta t/2}\mathrm{e}^{-iH_{1,2}\Delta t/2} + O(\Delta t^3). \tag{1.88}$$

This form gives the same order of error $O(\Delta t^3)$ as the usual second-order Suzuki-Trotter decomposition (1.80) and is more efficient because it evolves every bond (even and odd) with the corresponding local time-evolution operator $\mathrm{e}^{-iH_{i,i+1}\Delta t/2}$ at the first sweep and every bond again at the second, reversed half-sweep. The error is of the order of $t\Delta t^2$ for evolving a time t after performing this procedure $t/\Delta t$ times. This means that observables can be measured at every time step, and only two sweeps are needed to advance one time interval Δt. Here one does not need to carry out additional sweeps to achieve the self-consistancy between the wave function and the reduced density matrix because every application of $\mathrm{e}^{-iH_{i,i+1}\Delta t/2}$ to the wave function is exact.

It is also useful to mention two other often-used Suzuki-Trotter decompositions. The first-order Suzuki-Trotter decomposition of the time evolution operator $\mathrm{e}^{-iH\Delta t}$ is

$$\mathrm{e}^{-iH\Delta t} = \mathrm{e}^{-iH_A\Delta t}\mathrm{e}^{-iH_B\Delta t} + O(\Delta t^2). \tag{1.89}$$

By applying $\mathrm{e}^{-iH_B\Delta t}$ to the wave function during first half-sweep and $\mathrm{e}^{-iH_A\Delta t}$ during the second half-sweep, the wave function evolves by the time interval Δt. For evolving a total time t, it requires performing this procedure $t/\Delta t$ times. The error is of the order of $t\Delta t$ rather than the quadratic error in the second-order Suzuki-Trotter decomposition. Therefore, about $1/\Delta t$ times more half-sweeps (or time steps) are necessary to get the required accuracy.

A more precise method can be implemented by making use of the fourth-order Suzuki-Trotter decomposition [51, 52, 53],

$$\begin{aligned}\mathrm{e}^{-iH\Delta t} =& e^{-iH_A\lambda\frac{\Delta t}{2}}e^{-iH_B\lambda\Delta t}e^{-iH_A(1-\lambda)\frac{\Delta t}{2}} \\ & e^{-iH_B(1-2\lambda)\Delta t}e^{-iH_A(1-\lambda)\frac{\Delta t}{2}}e^{-iH_B\lambda\Delta t}e^{-iH_A\lambda\frac{\Delta t}{2}} + O(\Delta t^5),\end{aligned} \tag{1.90}$$

with $\lambda = 1/(2-2^{1/3}) \approx 1.35120719$. Here, seven half-sweeps must be performed to evolve by a time interval Δt. The error is of the order of $t\Delta t^4$ for evolving a time t after performing this procedure $t/\Delta t$ times. Since the error decreases as the fourth power, Δt^4, the number of time steps required to reach a given accuracy is reduced by about $1/\Delta t$ times compared to the second-order Suzuki-Trotter decomposition.

Chapter 2

Ground-state phase diagram of the one-dimensional t-U-J_1-J_2 model at half-filling

2.1 Introduction

The Hubbard chain is the archetype of one-dimensional strongly correlated electron systems. At half-filling and for all values of the Hubbard interaction U, it exhibits insulating spin-density-wave (SDW) behavior, marked by a critical behavior of the spin correlations. In a weak-coupling picture, this insulating behavior is generated by Umklapp scattering, while in strong coupling, the opening of the Mott-Hubbard gap leads to behavior of the spin degrees of freedom governed by an effective Heisenberg chain. These perturbative results are reinforced by the exact Bethe ansatz solution [54]. Hubbard-type models are relevant to a wide variety of one-dimensional materials, such as polymers [55], cuprates [56], or TTF-TCNQ [57].

One important experimental question is to what extent the spin correlations remain critical when additional interactions are present. It is well known that a nearest-neighbor Coulomb repulsion [58, 59], an alternating local potential [60, 61], or a second-neighbor hopping [62, 63] can lead to a spin gap.

The Hubbard model with a nearest-neighbor antiferromagnetic exchange in two dimensions is of interest in the context of the high-T_c cuprates. In particular, spin liquid states [64] and superconductivity [65] at and near half-filling have been proposed as necessary precursors to high-temperature superconductivity at higher doping. Since it is not clear whether such states are present in sufficient strength and for sufficiently wide parameter regimes in

the pure Hubbard or t-J models, additional interactions, including a spin exchange, have been proposed to be relevant [66].

In this chapter, we investigate the effect of two additional terms on the phase diagram of the half-filled (average electron occupation $\langle n \rangle = 1$) Hubbard chain, namely explicit antiferromagnetic exchange interactions between nearest neighbors and between next-nearest neighbors. The Hamiltonian is given by

$$H = -t \sum_{i,\sigma} \left(c^{\dagger}_{i,\sigma} c_{i,\sigma} + h.c. \right) + U \sum_{i} n_{i,\uparrow} n_{i,\downarrow} + J_1 \sum_{i} \boldsymbol{S}_i \boldsymbol{S}_{i+1} + J_2 \sum_{i} \boldsymbol{S}_i \boldsymbol{S}_{i+2}, \tag{2.1}$$

where $c^{\dagger}_{i,\sigma}$ ($c_{i,\sigma}$) creates (annihilates) an electron with spin σ at site i, $n_{i,\sigma} = c^{\dagger}_{i,\sigma} c_{i,\sigma}$, and $\boldsymbol{S}_i$ is the spin operator on site i: $S^{\alpha}_i = \frac{1}{2} \sum_{\sigma,\sigma'} c^{\dagger}_{i,\sigma} \hat{\sigma}^{\alpha}_{\sigma,\sigma'} c_{i,\sigma'}$. The index $\alpha = x, y, z$, and $\hat{\sigma}^{\alpha}_{\sigma,\sigma'}$ are the Pauli matrices. Here t is the hopping amplitude (we set $t = 1$ for simplicity in the remainder of this chapter) and U the strength of the on-site Coulomb interaction. The antiferromagnetic Heisenberg parameters J_1 and J_2 correspond to nearest- and next-nearest-neighbor exchange, respectively.

The unfrustrated ($J_2 = 0$) version of this model has previously been investigated both analytically and numerically. In particular, a generalized model with an anisotropic Heisenberg coupling was investigated in Ref. [67] using bosonization. While this work concentrated primarily on the case of ferromagnetic exchange, isotropic antiferromagnetic exchange was included in a phase that is marked as 'dimer long-range order', which corresponds to a bond-order-wave (BOW) in our notation; see below. The phase diagram from bosonization of the isotropic antiferromagnetic exchange was considered explicitly in Refs. [68] and [69], supported by numerical calculations using the transfer-matrix renormalization group (TMRG) [68] and exact diagonalization [69]. The phase diagram found contains two phases: a BOW phase at sufficiently small U for all J_1, and a SDW at larger U. The critical value of U_c goes to zero at small and large J_1 and reaches a maximum value $U_c/t \approx 0.35$ at intermediate J_1.

The above picture of the effects of an antiferromagnetic J_1 disagrees with the mechanism in which J_1 originates from the Coulomb repulsion U in the strong-coupling limit ($U \gg t$). Therefore, high-precision numerical DMRG calculations, which allow us to explore the phase diagram numerically are needed to verify the correctness of previous studies. However, our DMRG results show that there is no bond-order phase for any positive U and J_1 for the t-U-J_1 model. This intimated a reexamination of the bosonization treatment of this model in the

weak-coupling regime, carried out in collaboration with E. Szirmai F. Gebhard, J. Sólyom, and R. Noack [70]. This reexamination includes the renormalization of the coupling constants within the mean-field approximation, which was not considered previously. The revised analytical results conclude that there is no bond-order phase. In this chapter, we first give a detailed discussion (Sec. 2.2) of the revised bosonization treatment, also considering the effect of an additional frustrating exchange J_2, which allows us to explicitly induce the bond-order phase and to make contact with the known phase diagram of the frustrated Heisenberg chain at large U. We then present the results of the DMRG calculations, (see Sec. 2.3). Both the revised bosonization and the DMRG calculations indicate that a BOW phase is not present for $J_2 = 0$; the system is in a SDW phase for *all* positive J_1 and U. We show that a BOW phase can be induced by turning on J_2 positively, with the critical value required depending on U and J_1. At larger values of J_2, we find additional phases, including a spin-gapped metallic phase which we identify as a Luther-Emery phase. Finally, we conclude in Sec. 2.4.

2.2 Weak-coupling theory: bosonization, renormalization group analysis and mean-field approximation

We start our investigation with an analytical treatment of our model for small couplings, $U, J_1, J_2 \ll t$. In one dimension, the Fermi surface consists only of two points, $k = \pm k_F$. Around the Fermi points, the spectrum can be linearized and one can introduce left-moving and right-moving fermions corresponding to the states near $-k_F$ and $+k_F$, respectively, For the half-filled system, $k_F = \pi/2a$, where a is the lattice constant. We utilize the standard weak-coupling g-ology approach [71, 72] to get the scattering matrix elements: $g_{1\perp} = U - J_1/2 - 3J_2/2$,$g_{2\perp} = U + J_1/2 - 3J_2/2$, $g_{3\perp} = U + 3J_1/2 - 3J_2/2$, $g_{4\perp} = U - 3J_1/2 - 3J_2/2$, $g_{1\parallel} = -J_1/2 + J_2/2$, $g_{2\parallel} = J_1/2 + J_2/2$, $g_{3\parallel} = -J_1/2 + J_2/2$, and $g_{4\parallel} = J_1/2 + J_2/2$. We then apply the bosonization method by introducing the continuous chiral fermion fields $\psi_{\sigma,\pm}(x)$ by making the replacement $c_{i,\sigma}/\sqrt{a} \to \psi_{\sigma,\pm}(x)$ in the Hamiltonian (2.1). The bosonization of the on-site interaction is straightforward. Using Abelian bosonization, we introduce the chiral boson phase fields $\phi_{\sigma,\pm}(x)$ via

$$\psi_{\sigma,\pm}(x) = \frac{1}{\sqrt{2\pi a}} F_{\pm} \mathrm{e}^{\pm \mathrm{i} k_F x \pm \mathrm{i}\phi_{\sigma,\pm}(x)}, \tag{2.2}$$

where $F_{\pm}$ are the so-called Klein factors which ensure the anti-commutation relations of the fermion fields. The symmetric and antisymmetric combination of the spin-dependent boson

fields, $\phi_{c,\pm} = (\phi_{\uparrow,\pm} + \phi_{\downarrow,\pm})/2$ and $\phi_{s,\pm} = (\phi_{\uparrow,\pm} - \phi_{\downarrow,\pm})/2$, correspond to the collective charge and spin modes, respectively. In order to bosonize the non-local processes, one must expand the fermion fields with respect to the lattice constant. The bosonized form of the g-ology Hamiltonian density corresponding to Hamiltonian (2.1), up to first order in the expansion with respect to the lattice constant, is

$$\begin{aligned}\mathcal{H}(x) = \frac{1}{2\pi}\sum_{r=\pm}\left[v_\rho(\partial_x\phi_{c,r})^2 + v_\sigma(\partial_x\phi_{s,r})^2\right] + \frac{g_\rho}{2\pi^2}(\partial_x\phi_{c,+})(\partial_x\phi_{c,-}) - \frac{g_c}{2\pi^2}\cos(2\phi_c) \\ - \frac{g_\sigma}{2\pi^2}(\partial_x\phi_{s,+})(\partial_x\phi_{s,-}) + \frac{g_s}{2\pi^2}\cos(2\phi_s) - \frac{g_{cs}}{2\pi^2}\cos(2\phi_c)\cos(2\phi_s) \\ + \frac{g_{c\sigma}}{2\pi^2}(\partial_x\phi_{s,+})(\partial_x\phi_{s,-})\cos(2\phi_c) - \frac{g_{\rho s}}{2\pi^2}(\partial_x\phi_{c,+})(\partial_x\phi_{c,-})\cos(2\phi_s) \\ + \frac{g_{\rho\sigma}}{2\pi^2}(\partial_x\phi_{c,+})(\partial_x\phi_{c,-})(\partial_x\phi_{s,+})(\partial_x\phi_{s,-}),\end{aligned} \tag{2.3}$$

where $\phi_{c/s} = \phi_{c/s,+} + \phi_{c/s,-}$ are the total phase fields. The renormalized velocities are $v_\rho = 2t + (g_{4\parallel} + g_{4\perp} - g_{1\parallel})/2\pi$ and $v_\sigma = 2t + (g_{4\parallel} - g_{4\perp} - g_{1\parallel})/2\pi$. The Luttinger couplings of the charge and spin sectors are given by $g_\rho = g_{2\perp} + g_{2\parallel} - g_{1\parallel}$ and $g_\sigma = g_{2\perp} - g_{2\parallel} + g_{1\parallel}$, respectively. The couplings g_c and g_s correspond to the Umklapp and the backward scattering of opposite spins, respectively, given by $g_c = g_{3\perp}$ and $g_s = g_{1\perp}$, while the coupling g_{cs} is also Umklapp scattering, but of parallel spins, given by $g_{cs} = g_{3\parallel}$. The other coupling constants are given by $g_{c\sigma} = g_{\rho s} = g_{\rho\sigma} = -J_1/2 + J_2/2$. The coupling $g_{\rho s}$ and $g_{\rho\sigma}$ come from the backward scattering with opposite and parallel spins, respectively, while the coupling $g_{c\sigma}$ is related to Umklapp scattering with opposite spins. Here and in the following, we use the lattice constant as the unit for the coupling constants as well as for the Fermi velocities. The SU(2) symmetry of the spin sector assures $g_s = g_\sigma$, $g_{cs} = g_{c\sigma}$, and $g_{\rho s} = g_{\rho\sigma}$. Therefore, there are five independent couplings which we choose to be g_ρ, g_c, g_s, g_{cs}, and $g_{\rho s}$. We note that the renormalization of the Fermi velocities, which is a secondary effect, will not be taken into account in the following.

The Hamiltonian $\mathcal{H}(x)$ (2.3) cannot be solved exactly. However, a renormalization group (RG) analysis permits the investigation of the relative importance of the various couplings. In the RG procedure, the couplings are considered to be a function of some scaling parameter y, e.g., the logarithm of the effective bandwidth. As the scaling parameter is taken to infinity, the flow of the couplings shows which of them are important and which can be ignored, depending on whether or not they tend to zero, to a finite value, or to infinity. For example, when all couplings but the forward scattering terms tend to zero, the Hamiltonian H describes a Luttinger liquid with freely propagating charge and spin degrees of freedom.

The one-loop RG equations for our five dimensionless running coupling constants $\tilde{g}_x(y) \equiv g_x(y)/4\pi t$ read [68, 73]

$$\frac{\mathrm{d}\tilde{g}_\rho(y)}{\mathrm{d}y} = 2\tilde{g}_c^2 + \tilde{g}_{cs}^2 + \tilde{g}_s\tilde{g}_{\rho s}, \tag{2.4a}$$

$$\frac{\mathrm{d}\tilde{g}_c(y)}{\mathrm{d}y} = 2\tilde{g}_\rho\tilde{g}_c - \tilde{g}_s\tilde{g}_{cs} - \tilde{g}_{cs}\tilde{g}_{\rho s}, \tag{2.4b}$$

$$\frac{\mathrm{d}\tilde{g}_s(y)}{\mathrm{d}y} = -2\tilde{g}_s^2 - \tilde{g}_c\tilde{g}_{cs} - \tilde{g}_{cs}^2, \tag{2.4c}$$

$$\frac{\mathrm{d}\tilde{g}_{cs}(y)}{\mathrm{d}y} = -2\tilde{g}_{cs} + 2\tilde{g}_\rho\tilde{g}_{cs} - 4\tilde{g}_s\tilde{g}_{cs} - 2\tilde{g}_c\tilde{g}_s - 2\tilde{g}_c\tilde{g}_{\rho s} - 4\tilde{g}_{cs}\tilde{g}_{\rho s}, \tag{2.4d}$$

$$\frac{\mathrm{d}\tilde{g}_{\rho s}(y)}{\mathrm{d}y} = -2\tilde{g}_{\rho s} + 2\tilde{g}_\rho\tilde{g}_s - 4\tilde{g}_c\tilde{g}_{cs} - 4\tilde{g}_{cs}^2 - 4\tilde{g}_s\tilde{g}_{\rho s}\,, \tag{2.4e}$$

with initial values $\tilde{g}_x(y = 0) = g_x/4\pi t$. From these equations, it follows that there is only a single line of weak-coupling fixed points, namely $\overline{g}_c = \overline{g}_s = \overline{g}_{cs} = \overline{g}_{\rho s} = 0$. In order to show this, we note that we have started our analysis assuming that there is neither a charge gap nor a spin gap. This implies that a weak-coupling fixed point corresponds to $\overline{g}_c = \overline{g}_s = 0$. Equations (2.4) immediately imply that $\overline{g}_{cs} = \overline{g}_{\rho s} = 0$ also, and that only $\overline{g}_\rho$ remains undetermined.

A linear stability analysis of the fixed-point line shows that it is stable against small perturbations g_{cs} and $g_{\rho s}$, that it is marginally stable against small perturbations g_s and g_ρ, and that its stability with respect to perturbations g_c depends on the sign of the fixed-point value $\overline{g}_\rho$ (stable for $\overline{g}_\rho < 0$, unstable for $\overline{g}_\rho > 0$). Therefore, in order to determine the weak-coupling regime, it is convenient and sufficient to consider the RG equations without the spin-charge coupling terms, i.e., we may consider the RG equations for $\tilde{g}_{cs} = \tilde{g}_{\rho s} = 0$. We thus arrive at

$$\frac{\mathrm{d}\tilde{g}_\rho(y)}{\mathrm{d}y} = 2\tilde{g}_c^2, \tag{2.5a}$$

$$\frac{\mathrm{d}\tilde{g}_c(y)}{\mathrm{d}y} = 2\tilde{g}_\rho\tilde{g}_c, \tag{2.5b}$$

$$\frac{\mathrm{d}\tilde{g}_s(y)}{\mathrm{d}y} = -2\tilde{g}_s^2 \tag{2.5c}$$

in the vicinity of the weak-coupling fixed-point line.

This simpler problem is readily analyzed. The trajectory for the spin coupling $\tilde{g}_s(y)$ flows to infinity if $g_s < 0$. In this case, a gap opens in the spin spectrum. If $g_s > 0$, this coupling is marginally irrelevant, i.e., the spin mode remains soft. In the charge sector, $g_\rho = g_c$ initially, and this relation remains valid under the RG flow. Therefore, it is sufficient to consider Eq. (2.5a). It is seen that for $g_c > 0$ the charge mode becomes gapped because $\tilde{g}_c(y)$ flows to infinity, otherwise the charge excitations remain gapless.

The simplified equations show that a fully gapless Luttinger-liquid phase, $\overline{g}_c = \overline{g}_s = 0$, is not possible for our model. The initial couplings would have to fulfill $g_c < 0$ and $g_s > 0$ which requires $J_2 > 2U/3 + J_1$ for $g_c < 0$ and $J_2 < (2U - J_1)/3$ for $g_s > 0$. These two conditions cannot be fulfilled simultaneously with positive bare couplings U, J_1, and J_2. Consequently, we must redo our RG analysis under the assumption that at least one of the two modes is gapped.

When one of the fields is gapped, the spin-charge coupling processes become relevant [10, 73]. Their contribution will be considered on the mean-field level. In this picture, the gapped field is locked to a value which optimizes the interaction energy.

When there is a gap in the charge sector, the charge field ϕ_c is locked at $\overline{\phi}_c = 0 \bmod \pi$ because the initial value of the coupling g_c is positive. Neglecting the fluctuations of the field ϕ_c in the $g_{c\sigma}$ term of the Hamiltonian (2.3), the terms proportional to $g_{\rho s}$ and $g_{\rho\sigma}$ do not contribute, and $\cos(2\phi_c)$ can be replaced by its weak-coupling mean-field value, $\overline{\cos(2\phi_c)} = 1$. Due to this substitution, the interaction terms proportional to g_{cs} and $g_{c\sigma}$ become marginal because their scaling dimensions reduce to $\overline{x}_{cs} = \overline{x}_{c\sigma} = 2$. On the mean-field level, the spin-coupling term proportional to g_{cs} is of the same form as the interaction term proportional to g_s. Therefore, the spin field ϕ_s fluctuates in the modified potential $g_s^* \cos(2\phi_s)$ with the new coupling g_s^*,

$$g_s^* = g_s - g_{cs} = U - 2J_2. \tag{2.6}$$

Analogously, the interaction term proportional to $g_{c\sigma}$ combines with the interaction term proportional to g_σ to produce the new coupling g_σ^*, with

$$g_\sigma^* = g_\sigma - g_{c\sigma} = U - 2J_2. \tag{2.7}$$

This equation shows that the SU(2) spin symmetry is preserved on the mean-field level.

In the presence of a charge gap and the SU(2) spin symmetry, we only have to analyze a

single equation for $\tilde{g}_s$ instead of the five RG equations (2.4), namely

$$\frac{\mathrm{d}\tilde{g}_s(y)}{\mathrm{d}y} = -2\tilde{g}_s^2\,, \tag{2.8}$$

with the initial value $\tilde{g}_s(y=0) = g_s^*/4\pi t$. It is readily seen that the spin mode becomes gapped if $g_s^* < 0$, i.e., $J_2 > U/2$, independently of the value of the nearest-neighbor interaction J_1.

When there is a gap in the spin sector, the spin field ϕ_s is locked at $\overline{\phi}_s = 0 \bmod \pi$ because the initial value of the coupling g_s is negative. Neglecting the fluctuations of the field ϕ_s in the $g_{\rho s}$ term of the Hamiltonian (2.3), the terms proportional to $g_{\rho\sigma}$ and $g_{c\sigma}$ do not contribute and $\cos(2\phi_s)$ can be substituted by its weak-coupling mean-field value, $\overline{\cos(2\phi_s)} = 1$. Due to this substitution, the interaction terms proportional to g_{cs} and $g_{\rho s}$ become marginal because their scaling dimensions reduce to $\overline{x}_{cs} = \overline{x}_{\rho s} = 2$. On the mean-field level, the charge-coupling term proportional to g_{cs} is of the same form as the interaction term proportional to g_c. Therefore, the charge field ϕ_c fluctuates in the modified potential $g_c^* \cos(2\phi_c)$ with the new coupling g_c^*,

$$g_c^* = g_c + g_{cs} = U + J_1 - J_2. \tag{2.9}$$

Using similar reasoning, the new coupling g_ρ^* becomes

$$g_\rho^* = g_\rho - g_{\rho s} = U + 2J_1 - 2J_2. \tag{2.10}$$

Note that these new initial couplings are *not* equal, so we must analyze the two-dimensional scaling curves defined by the equations

$$\frac{\mathrm{d}\tilde{g}_\rho(y)}{\mathrm{d}y} = 2\tilde{g}_c^2, \tag{2.11a}$$

$$\frac{\mathrm{d}\tilde{g}_c(y)}{\mathrm{d}y} = 2\tilde{g}_\rho\tilde{g}_c\,, \tag{2.11b}$$

given the initial values $\tilde{g}_c(y=0) = g_c^*/4\pi t$ and $\tilde{g}_\rho(y=0) = g_\rho^*/4\pi t$. The flow diagram is shown in Fig. 2.1. The conditions for a gapped charge mode are either $g_\rho^* > 0$ or ($g_\rho^* < 0$ and $|g_c^*| > |g_\rho^*|$). This leads to the result that a gapped charge mode exists if $J_2 < 2U/3 + J_1$.

In general, we find three regions where either the charge gap or the spin gap or both are finite. It is interesting to analyze the dominant correlations in the various gapped phases. The order parameters for density waves in the charge (CDW), spin (SDW), bond-charge (BCDW),

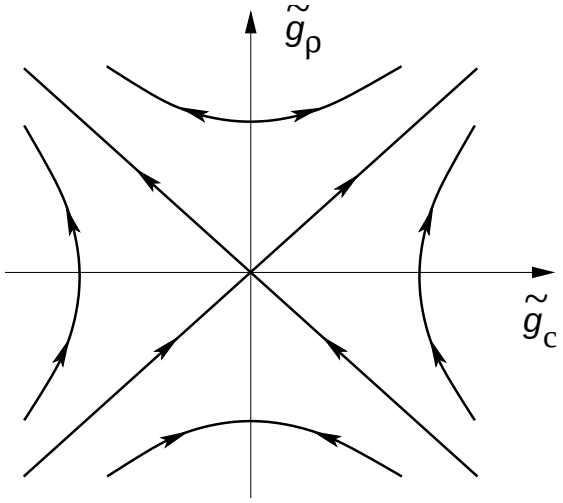

Figure 2.1: Scaling curves for the charge-coupling parameters $\tilde{g}_c$ and $\tilde{g}_\rho$ in the presence of a spin gap.

and bond-spin (BSDW) require the calculation of correlation functions using the operators

$$O_{i,\mathrm{CDW}} = (-1)^i(n_{i,\uparrow} + n_{i,\downarrow}), \tag{2.12a}$$

$$O_{i,\mathrm{SDW}} = (-1)^i(n_{i,\uparrow} - n_{i,\downarrow}), \tag{2.12b}$$

$$O_{i,\mathrm{BCDW}} = (-1)^i(c^\dagger_{i,\uparrow}c_{i+1,\uparrow} + c^\dagger_{i,\downarrow}c_{i+1,\downarrow} + h.c.), \tag{2.12c}$$

$$O_{i,\mathrm{BSDW}} = (-1)^i(c^\dagger_{i,\uparrow}c_{i+1,\uparrow} - c^\dagger_{i,\downarrow}c_{i+1,\downarrow} + h.c.)\,, \tag{2.12d}$$

written in terms of the lattice fermions. These order parameters become

$$O_{\mathrm{CDW}}(x) \propto \sin\phi_c(x)\cos\phi_s(x), \tag{2.13a}$$

$$O_{\mathrm{SDW}}(x) \propto \cos\phi_c(x)\sin\phi_s(x), \tag{2.13b}$$

$$O_{\mathrm{BCDW}}(x) \propto \cos\phi_c(x)\cos\phi_s(x), \tag{2.13c}$$

$$O_{\mathrm{BSDW}}(x) \propto \sin\phi_c(x)\sin\phi_s(x) \tag{2.13d}$$

in bosonized form. When the charge mode is gapped, the field ϕ_c is locked at $\overline{\phi}_c = 0 \bmod \pi$. When the spin mode is gapped, the field ϕ_s is locked at $\overline{\phi}_s = 0 \bmod \pi$. Therefore, in the regime where both of the fields are gapped, we find that the BCDW order parameter is maximal. The model thus describes a phase with bond ordering (BOW) for $\Delta_c \neq 0$ and $\Delta_s \neq 0$.

When only the charge mode is gapped, the spin field is a free field. However, upon increasing the scaling parameter (y) of the renormalization group procedure, the initially neg-

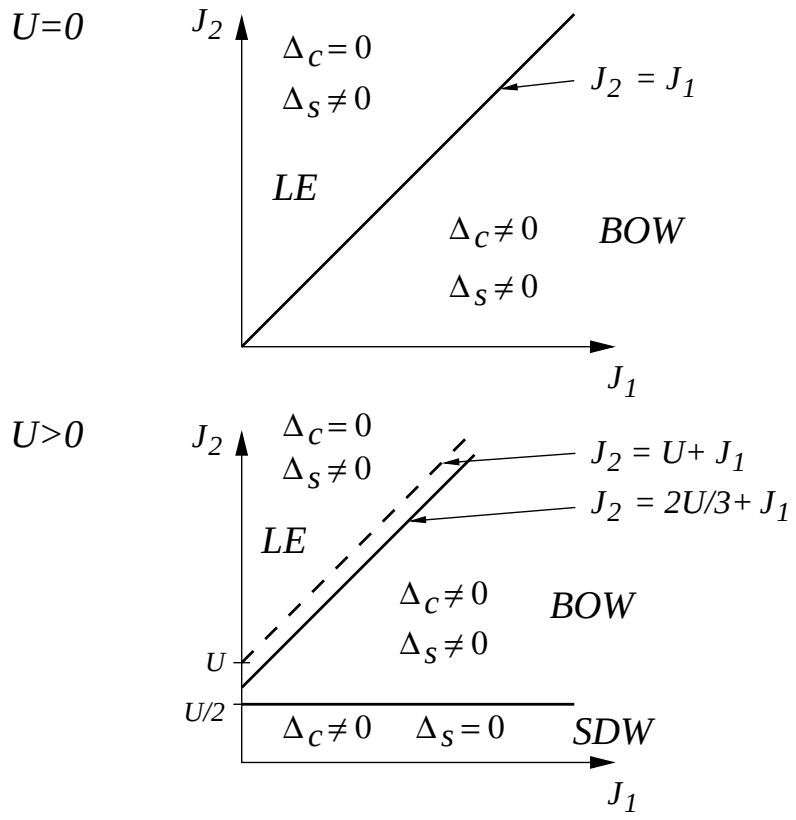

Figure 2.2: Field-theory prediction for the half-filled t-U-J_1-J_2 model. The solid lines give the phase boundaries between the fully gapped regime (bond-order-wave, BOW) and the semi-gapped regimes (spin-density wave, SDW; Luther-Emery, LE). The dashed line shows the border between dominantly charge-density-wave and bond-order-wave correlations in the Luther-Emery phase.

ative spin coupling grows and tends to zero, and the spin field oscillates around $\pi/2$ (mod π). Therefore, for small couplings, the dominating ordering is SDW for $\Delta_c \neq 0$ and $\Delta_s = 0$. Note that the SU(2) spin symmetry is not spontaneously broken, i.e., the spin correlations are critical without true long-range order.

Similarly, when the spin mode is gapped and the charge mode is gapless, there is no true long-range charge order. Therefore, we call this phase the Luther-Emery (LE) phase. The charge coupling g_c tends to zero, either from positive values or from negative values. Depending on the sign of the charge coupling, ϕ_c fluctuates around $\pi/2$ or around zero. Correspondingly, the dominating correlations are either CDW or BCDW for $\Delta_c = 0$ and $\Delta_s \neq 0$. The line which separates the dominant BCDW critical correlation and the dominant CDW correlations in the LE phase is indicated in Fig. 2.2 by a dashed line.

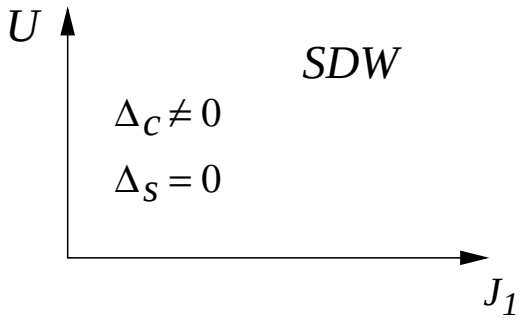

Figure 2.3: Field-theory prediction for the half-filled t-U-J_1 model. For all $J_1 > 0$, the ground state is a spin-density-wave (SDW) phase with a finite charge gap, zero spin gap and critical spin correlations.

The resulting phase diagram of the t-U-J_1-J_2 model at weak coupling is shown in Fig. 2.2. For $U = 0$, the spin gap is always finite for $J_2 > 0$. For $J_2 < J_1$, the charge gap is also finite, and the ground state is characterized by a bond-order wave. The charge gap closes at $J_2 = J_1$ and the system goes into a LE phase with no long-range charge or spin ordering but critical charge-density-wave correlations.

For $U > 0$, $J_1 > 0$, and $J_2 < U/2$, the ground state is analogous to the spin-density-wave (SDW) phase of the one-dimensional Hubbard model, i.e., the charge gap is finite, the spin gap is zero, and the spin correlations are critical. For $2U/3 + J_1 > J_2 > U/2$, both the spin gap and the charge gap are finite. The ground state is a BOW with long-range order in the bond-charge-density-wave correlations. For $J_2 > 2U/3 + J_1$, the charge gap closes and the system goes over to the LE phase with a finite spin gap but no charge long-range order. For $2U/3 + J_1 < J_2 < U + J_1$, the bond-charge-density-wave fluctuations dominate, whereas, for $J_2 > U + J_1$, the fluctuations in the charge-density-wave order parameter are maximal.

In order to make contact with earlier work, we display the phase diagram of the t-U-J_1 model separately in Fig. 2.3. In contrast to previous results [67, 68, 69], we do not find any signature of a BOW phase. For all $J_1 > 0$, the ground state is SDW, just as is the ground state of the half-filled Hubbard model for $U > 0$. This result is corroborated by our numerical DMRG data, which we present in the next section.

2.3 Numerical results

In order to explore the phase diagram of the Hamiltonian (2.1) and to test the predictions of bosonization, we carry out extensive, high-precision, ground-state DMRG calculations [11,

12, 13]. Relatively high sensitivity is required to resolve the phases, especially in the weak-coupling regimes in which one would expect bosonization to be valid. In order to differentiate the possible phases, we calculate the spin gap Δ_s, the charge gap Δ_c, and the bond-order-wave parameter $\langle B\rangle$ of the one-dimensional t-U-J_1-J_2 model on lattices with open boundary conditions and up to $L = 256$ sites. The weight of the discarded density-matrix eigenstates is held below a maximum of 10^{-9}.

For finite systems, the spin gap $\Delta_s(L)$ is defined as

$$\Delta_s(L) = E_0(L, N, S = 1) - E_0(L, N, S = 0). \tag{2.14}$$

Accordingly, the charge gap $\Delta_c(L)$ is determined using

$$\begin{aligned}\Delta_c(L) &= [E_0(L, N+2, S = 0) + E_0(L, N-2, S = 0) \\ &\quad -2E_0(L, N, S = 0)]/2,\end{aligned} \tag{2.15}$$

where $E_0(L, N, S)$ is the ground-state energy for an L-site system with N electrons and total spin S. We extrapolate using second-order polynomials in $1/L$ to determine the spin gap Δ_s and the charge gap Δ_c in the thermodynamic limit,

$$\begin{aligned}\Delta_s(L) &= \Delta_s^\infty + A_s/L + B_s/L^2, \\ \Delta_c(L) &= \Delta_c^\infty + A_c/L + B_c/L^2,\end{aligned} \tag{2.16}$$

where $\Delta_{c,s}^\infty$, $A_{c,s}$, and $B_{c,s}$ are fitting parameters. The staggered bond order parameter is defined as

$$\langle B\rangle(L) = \frac{1}{2(L-1)} \sum_{i=1}^{L} \sum_{\sigma} (-1)^{i+1} \langle c_{i\sigma}^\dagger c_{i+1,\sigma} + h.c\rangle. \tag{2.17}$$

The bond order parameter $\langle B\rangle$ is extrapolated using finite-size corrections of the form $1/L^\gamma$, without considering higher corrections,

$$\langle B\rangle(L) = \langle B^\infty\rangle + A_B/L^\gamma\,, \tag{2.18}$$

where $\langle B^\infty\rangle$, A_B, and γ are fitting parameters. We find that adding higher-order terms, which increases the number of fit parameters, tends to make the fits less stable.

In the following, we first treat the t-U-J_1 model, i.e., $J_2 = 0$ in Hamiltonian (2.1), then study finite positive J_2, first with $U = 0$, then with nonzero U. For simplicity, in the remainder

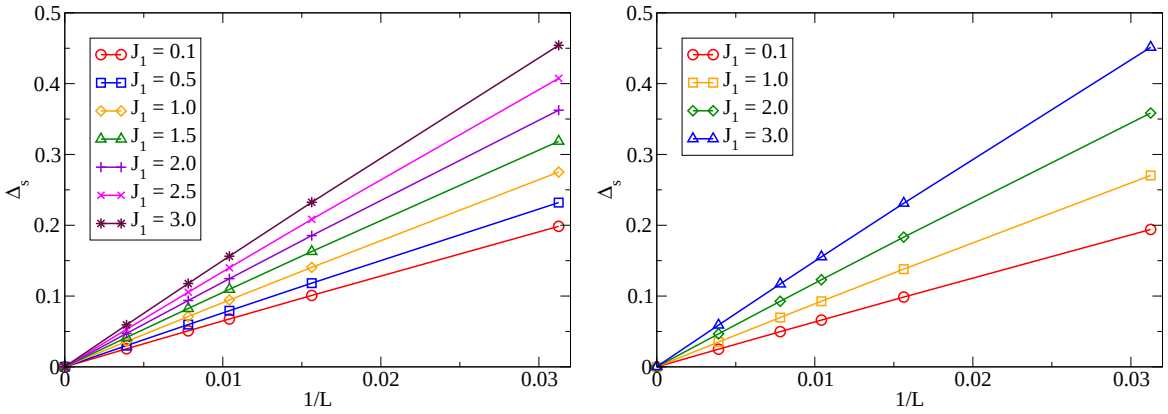

Figure 2.4: Finite-size extrapolation of the spin gap as a function of $1/L$ for the t-U-J_1 model at (a) $U = 0$ and (b) $U = 0.1$.

of this chapter, the energy scale is set by taking $t = 1$, and so U, J_1, and J_2 are dimensionless quantities.

2.3.1 Results for $J_2 = 0$

For the unfrustrated case ($J_2 = 0$), our bosonization procedure of Sec. 2.2 predicts a SDW phase with a finite charge gap and critical gapless spin excitations, $\Delta_c > 0$ and $\Delta_s = 0$. In the SDW phase, the bond order parameter vanishes.

The finite-size extrapolation of the spin gap, plotted as a function of $1/L$ for $U = 0$ and $U = 0.1$ is shown in Fig. 2.4. As can be clearly seen, the scaling behavior is predominantly linear in $1/L$, and the $1/L \to 0$ extrapolated value, Δ_s^∞, is zero on the scale of the plot for all values of J_1 for both values of U. A fit of the data with a second-order polynomial in $1/L$, as discussed above, yields a value of Δ_s that is less than 2×10^{-4} in all cases. This puts a rather stringent constraint on bond ordering in this case; the spin excitations are gapless to a very high numerical accuracy.

The system-size behavior of the charge gap is displayed in Fig. 2.5. As can be seen, the $1/L \to 0$ extrapolated value, Δ_c^∞, is nonzero in general, with the scaling going from being predominantly linear in $1/L$ (with a small negative $(1/L)^2$ term) when Δ_c is small, to having a substantial positive $(1/L)^2$ term when Δ_c is significantly different from zero. Such finite-size behavior is typical for gaps in one-dimensional systems with open boundary conditions.

The behavior of the extrapolated gaps as a function of J_1 is shown in Fig. 2.6. As discussed above, the spin gap is numerically indistinguishable from zero for all values of J_1 for both $U = 0$ and $U = 0.1$. The extrapolated charge gap is small on the scale of the plot for $J_1 \lesssim 0.8$, and

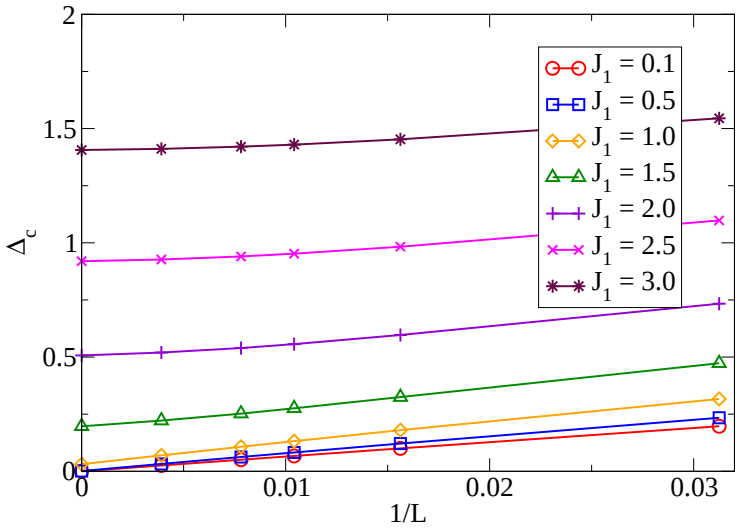

Figure 2.5: Finite-size extrapolation of the charge gap as a function of $1/L$ for the t-U-J_1 model at $U = 0$.

then increases, crossing over to a linear increase for larger values of J_1. From bosonization, we would expect an exponential opening of the gap with J_1, similar to the exponential opening of the charge gap with U in the $J_1 = 0$ case [74]. The J_1-dependence of Δ_c^∞ in Fig. 2.6 is qualitatively consistent with such a behavior. We have not carried out an explicit fit because the detailed form of the exponential opening is not known from bosonization; to determine the specifics of a general exponential form via fitting to finite-size extrapolated data is difficult.

We now turn to the BOW order parameter, displayed as a function of J_1 for various system sizes and $L = \infty$ in Fig. 2.7. At each system size, $\langle B \rangle(L)$ has an appreciable positive finite value which varies significantly as a function of J_1. The $L \to \infty$ extrapolated value $\langle B^\infty \rangle$ is small, but still shows some variation with J_1. Note, however, that the extrapolated value is negative at small and large J_1 and is positive only for intermediate J_1. Taking the largest negative value ($\langle B^\infty \rangle \approx -0.003$) as a rough estimate of the extrapolation error, the largest positive value, $\langle B^\infty \rangle \approx 0.007$, is not distinguishable from zero to within our accuracy. Moreover the fit to Eq. (2.18) yields an exponent γ which varies between 0.47 and 0.77. All this underlines the uncertainty in carrying out extrapolations using this analytic form and the sensitivity of $\langle B^\infty \rangle$ to the details of the fit. On the other hand, as discussed above, Δ_s^∞ vanishes to a high accuracy for all J_1, precluding a BOW phase. Thus, within the numerical methods applied here, the spin gap seems to be a significantly more sensitive probe for the existence of a bond order wave phase than the bond order parameter $\langle B \rangle$ itself.

Our DMRG calculations for $J_2 = 0$ are thus in agreement with the predictions of the

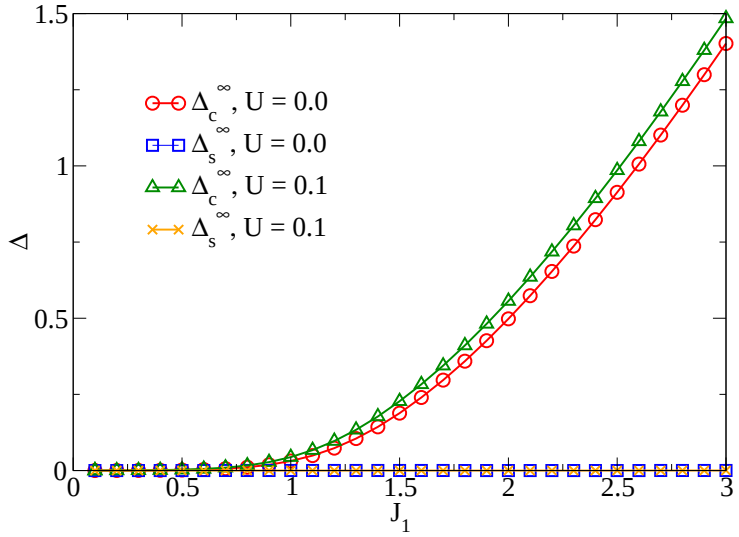

Figure 2.6: Extrapolated spin and charge gaps for the t-U-J_1 model at $U = 0$ and 0.1 as functions of J_1.

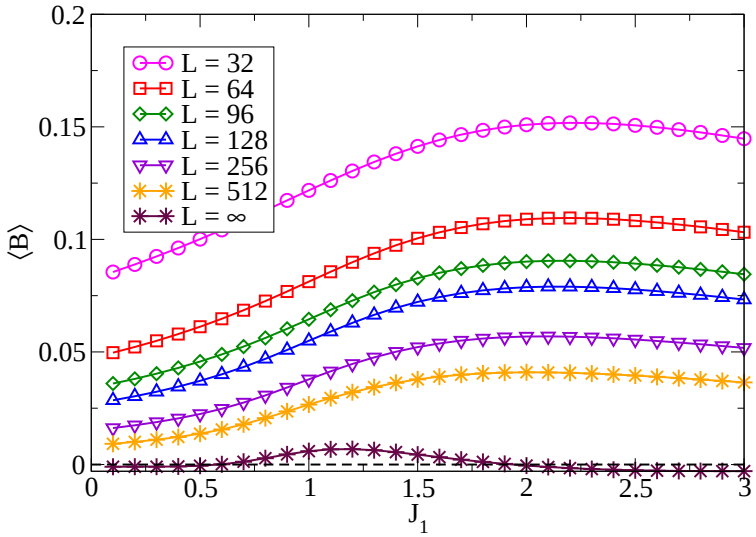

Figure 2.7: Bond order parameter $\langle B\rangle(L)$ for $L = 32, 64, 96, 128, 256, 512$ and extrapolated bond order parameter $\langle B^{\infty}\rangle$ as a function of J_1 for the t-U-J_1 model at $U = 0$.

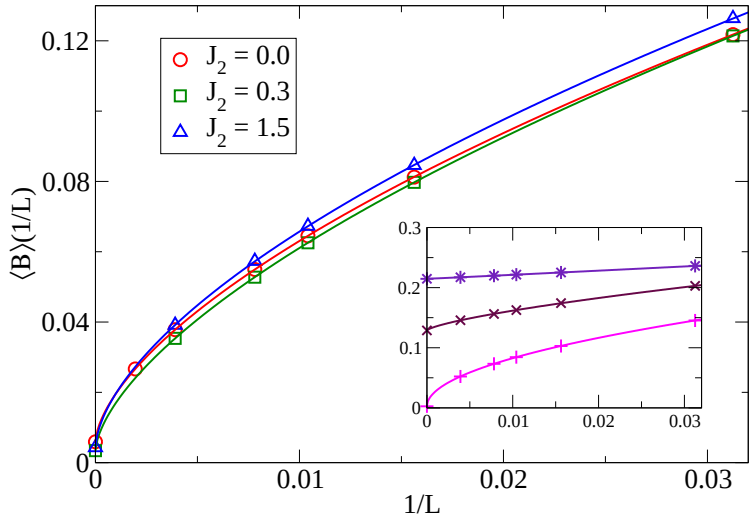

Figure 2.8: Finite-size scaling analysis for $\langle B\rangle(L)$ for different J_2 when $U = 0$ and $J_1 = 1$. The inset shows the finite-size scaling analysis for $J_2 = 2.0$, 2.5, and 3.0, from bottom to top.

bosonization calculations of Sec. 2.2; see Fig. 2.3: the ground-state phase is a SDW with gapless spin excitations for all positive U and J_1. While we have treated explicitly only two values of the interaction strength, $U = 0$ and $U = 0.1$, we have chosen these values in accordance with the phase diagrams of Refs. [68] and [69] which predict the appearance of a BOW phase only for $U \lesssim 0.35$. At larger values of U, the behavior should be that of the ordinary half-filled Hubbard chain and one would not expect a BOW phase to occur.

2.3.2 Results for $U = 0$ and nonzero J_2

We now include the explicit frustration J_2 while setting the on-site Coulomb interaction to zero. Fig. 2.9 shows the system-size extrapolated spin and charge gaps, Δ_s^∞ and Δ_c^∞, as functions of J_2 at $U = 0$ and $J_1 = 1$. (We do not show the finite-size extrapolation, which proceeds similarly to that in Figs. 2.4 and 2.5, explicitly.) The spin gap opens slowly at small J_2, but with a form consistent with a critical $J_2^s = 0$ (see the inset in particular). The charge gap decreases rapidly with J_2 at small J_2, reaching zero at $J_2^{c(1)} \approx 1 = J_1$, but then opens again at $J_2^{c(2)} \approx 2$. At weak coupling, this behavior of both gaps is consistent with the predictions of bosonization, but the reopening of the charge gap for larger J_2 is not contained in the bosonization analysis. However, such large values of J_2 are clearly outside its region of validity.

Representative results for the finite-size scaling of the bond order parameter $\langle B\rangle$ are

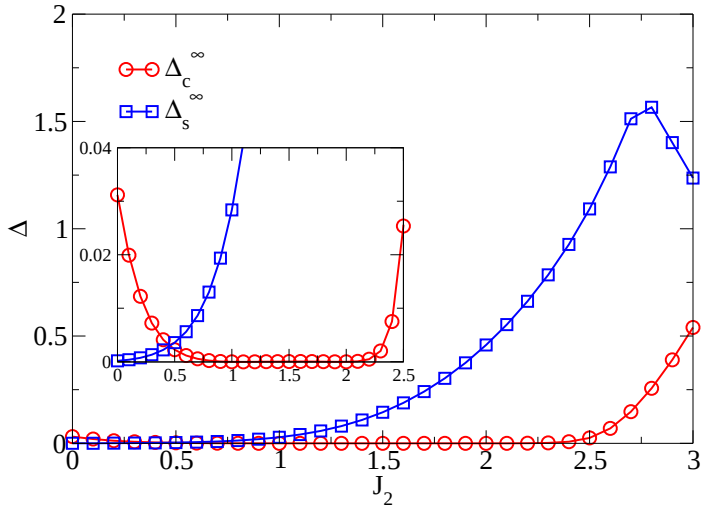

Figure 2.9: Extrapolated spin gap and charge gap as functions of J_2 for $U = 0$, $J_1 = 1$. The inset displays the same data for $J_2 \leq 2.5$ on an enlarged scale.

present in Fig. 2.8. For small J_2, the scaling behavior is similar to that for $J_2 = 0$, yielding an exponent γ that varies between 0.44 and 0.71. However, for large J_2, the data extrapolate almost linearly to finite values. This illustrates that the scaling form (2.18), goes over to a function that might be better fit by a polynomial in $1/L$, as in Eq. (2.16). However, for consistency, we nevertheless always use Eq. (2.18) for the fitting and note that the case of a linear function of $1/L$ is encompassed by Eq. (2.18) with $\gamma = 1$.

The extrapolated results for $\langle B^\infty \rangle$, plotted as a function of J_2, are shown in Fig. 2.10. For $J_2 = 0$ to $J_2^{c(1)}$, $\langle B^\infty \rangle$ is very small, even falling off from the small finite value at $J_2 = 0$, which we have argued to come about due to numerical and extrapolation errors. Note that here, for $J_2 < J_2^{c(1)} \approx 1$, the phase is characterized as bond order wave within bosonization. While this seems to be a contradiction at first glance, note that the charge gap, Fig. 2.9, falls off very rapidly from its small finite value at $J_2 = 0$, whereas the spin gap opens very slowly due to its putative exponential form. In consequence, the value of $\langle B^\infty \rangle$ is very small. Our interpretation, then, is that the BOW order parameter is finite, but numerically unresolvable in this region. For $J_2^{c(1)} < J_2 < J_2^{c(2)}$, the spin gap is clearly non-vanishing, but $\langle B^\infty \rangle$ is numerically zero. This behavior is consistent with the bosonization prediction of a Luther-Emery phase. In other words, the vanishing charge gap indicates a phase in which there is no BOW. When $J_2 > J_2^{c(2)}$, coincident with the reopening of the charge gap in Fig. 2.9, the BOW phase reappears, this time clearly marked by a finite bond order parameter as well as finite spin and charge gaps.

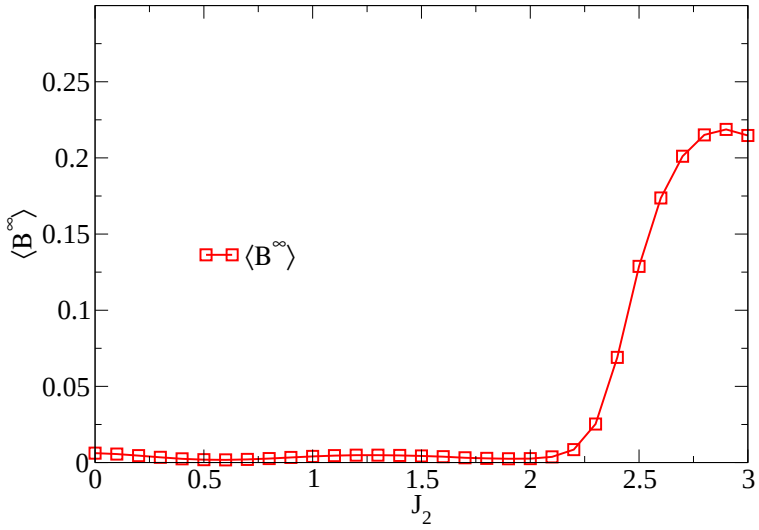

Figure 2.10: The $L = \infty$ extrapolated bond order parameter $\langle B^{\infty} \rangle$ as a function of J_2 for $U = 0$ and $J_1 = 1$.

2.3.3 Results for nonzero U and J_2

We now study the effect of the frustration J_2 when the Coulomb repulsion U is finite. Bosonization predicts that the SDW phase that is present only along the $J_2 = 0$ line at $U = 0$ becomes enlarged to a finite region at finite U. We explore the behavior as a function of J_2 for moderate values of U and J_1, $U = 2$, and $J_1 = 1$. Fig. 2.11 shows the spin and charge gaps, extrapolated to infinite systems size, as a function of J_2. As can be seen, the spin gap opens at a finite $J_2^s \approx 0.6$ and the charge gap, although at first decreasing and reaching a minimum at $J_2 \approx 1.1$, is always finite. As can be seen in Fig. 2.12, the bond order parameter $\langle B^{\infty} \rangle = 0$ when $J_2 < J_2^s$, and opens rapidly to a large, finite value at $J_2 \approx 0.5$. The behavior of all quantities is consistent with a SDW phase for small J_2 and a BOW for large J_2. Bosonization does predict a transition from a SDW phase to a BOW phase at $J_2 = U/2$ (see Fig. 2.2). However, it also predicts a transition to a spin-gapless LE phase at larger J_2, which is not found in the numerical calculations. In our opinion, this is because the values of U, J_1 and J_2 here are large enough so that the regime of validity of bosonization is exceeded. Note that the critical value $J_2^s \approx 0.5$ is far from the weak-coupling prediction of $J_2 = U/2 = 2$, but agrees fairly well with the value expected from the frustrated Heisenberg chain, for which $(J_2^{\rm Heis}/J_1^{\rm Heis})_c \approx 0.241$ [75, 76], if we take $J_1^{\rm Heis} = J_1 + 4t^2/U = 3$, the effective Heisenberg coupling within strong coupling; this yields an estimate $J_2^{c({\rm strong})} \approx 0.72$, in reasonable agreement with the DMRG result.

Fig. 2.13 summarizes the phase diagrams as a function of J_2 obtained from the DMRG

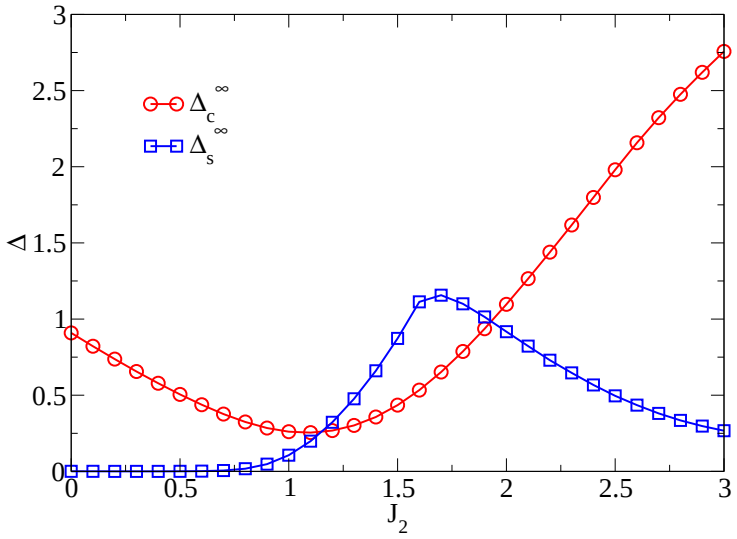

Figure 2.11: The $L = \infty$ extrapolated spin gap and charge gap as functions of J_2 for $U = 2$, $J_1 = 1$.

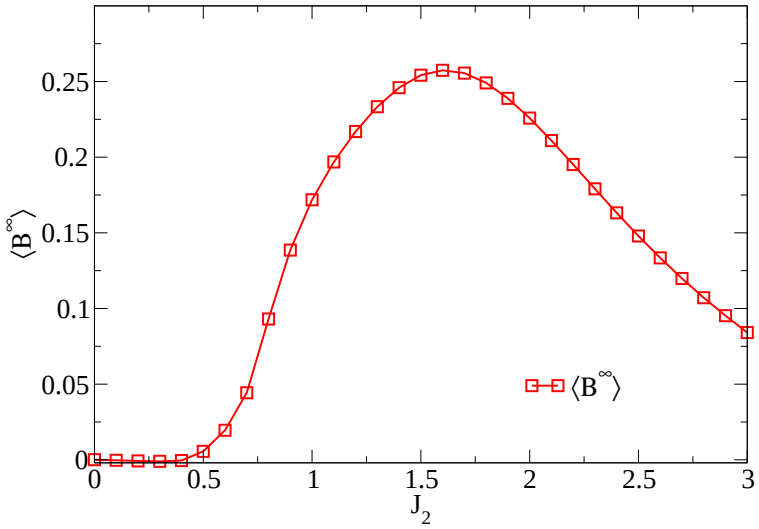

Figure 2.12: The $L = \infty$ extrapolated $\langle B \rangle$ as a function of J_2 for $U = 2$, $J_1 = 1$.

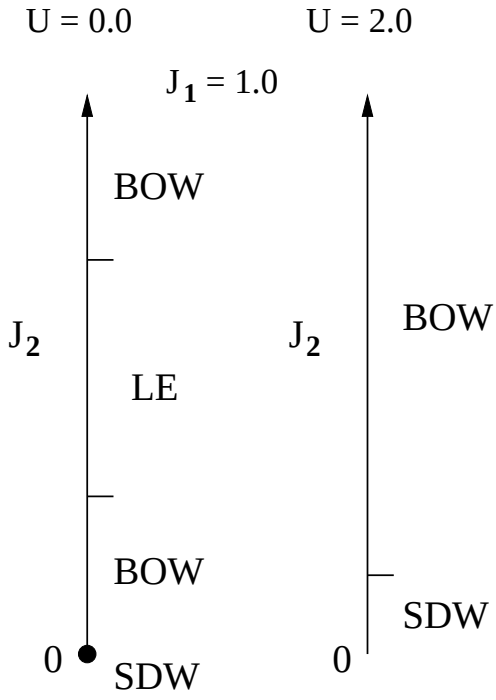

Figure 2.13: A sketch of the ground-state phase diagram of the one-dimensional t-U-J_1-J_2 model at zero and finite U obtained from analysis of the DMRG calculations.

calculations at zero and finite U. For $U = 0$, the SDW phase at $J_2 = 0$ becomes a BOW phase at arbitrarily small, but weak J_2. At intermediate J_2, a metallic, but spin-gapped Luther-Emery phase occurs, and at large J_2 the system reenters the BOW phase. At moderate, finite U, the SDW phase persists when J_2 is small and finite, going over to a BOW at larger J_2.

2.4 Discussion and conclusion

In this chapter, we have investigated the ground-state behavior of the half-filled one-dimensional Hubbard model with antiferromagnetic nearest-neighbor and next-nearest-neighbor Heisenberg interactions. Our field-theoretical analysis for weak couplings indicates that the ground state has a finite gap for either charge excitations (spin-density-wave phase, SDW) or spin excitations (Luther-Emery phase, LE) or both (bond-order-wave phase, BOW). Our extensive numerical DMRG investigations agree very well with the field-theoretical predictions for small interactions. The only exception is the lack of numerical evidence for a finite bond-order parameter in the region $U = 0$, $J_1 = 1$ and $0 < J_2 < J_1$. Here the system sizes are large enough to resolve finite spin and charge gaps but they are still too small to detect the very

small bond order parameter.

For larger interactions, e.g., $U = 2$, the DMRG finds a strong-coupling bond-order-wave phase which eludes the field-theoretical description. Instead, its existence and its properties can be inferred from a strong-coupling expansion of the model where it is seen that the strong-coupling BOW phase results from the frustration of the nearest-neighbor and next-nearest-neighbor Heisenberg couplings. Therefore, the metallic Luther-Emery phase is limited to a narrow weak-coupling region in parameter space where it would be very difficult to justify the strengths of the coupling parameters from microscopic considerations. For moderate interactions, an echo of the weak-coupling Luther-Emery phase can be seen in the behavior of the charge gap as a function of J_2, which displays a minimum at some $J_2 \gtrsim J_1$.

The nearest-neighbor Heisenberg coupling J_1 is *not* a frustrating interaction for the half-filled Hubbard model because the ground state of the t-U-J_1 model is a spin-density wave for all $J_1 \geq 0$. In order to arrive at this conclusion in the field-theoretical analysis, the fact that bosonic phase fields are locked to their mean-field values when excitations are gapped, so that seemingly irrelevant operators become marginal operators, must be taken into account. In numerical calculations one needs to study rather large system sizes in order to extrapolate to a vanishing spin gap and bond-order parameter in the thermodynamic limit. The next-nearest-neighbor Heisenberg interaction J_2, in contrast, truly frustrates the Hubbard model, opening the way to Luther-Emery and bond-charge-ordered phases for $J_2 > 0$. As expected from our experience with the frustrated Heisenberg model, the SDW phase is stable against weak frustration for $U > 0$, i.e., a finite J_2 is required to open the spin gap.

In conclusion, our study demonstrates both analytically and numerically that a nearest-neighbor Heisenberg exchange interaction added to the half-filled Hubbard model does not lead to frustration or to new phases in the ground-state phase diagram, whereas a frustrating next-nearest-neighbor exchange does.

Chapter 3

Decoherence of a qubit coupled to a spin chain bath

One of the fundamental aspects of quantum mechanics is its quantum coherence. Coupling to a bath, however, leads to a rapid reduction of this entanglement and on very short time scales the entangled state evolves to a statistical mixture. This generic phenomenon, known as decoherence, helps in understanding why it is not possible to detect quantum superpositions in our everyday life, which is governed by the rules of classical mechanics. Decoherence is the major obstacle in constructing a quantum computer, which relies on the existence of entangled states. It is therefore of general interest to investigate various scenarios in which qubits are coupled to a bath, hoping that a better understanding of these processes will eventually open the way to reduce or suppress the decoherence on time scales long enough to perform the basic operations of quantum algorithms. In this chapter, we analyze the decoherence behavior in the simplest interacting spin system, in which we consider the coupling of a single qubit to an interacting spin-1/2 chain realized by the XXZ model, one of the fundamental models in quantum many body physics and quantum magnetism. The chapter is organized as follows. In the first section, Sec. 3.1, we make a brief introduction of the basic concept of decoherence and introduce a model Hamiltonian consisting of a system and an environment that will be studied throughout this chapter. We also discuss how to characterize the decoherence by the Loschmidt echo, which is the square of the off-diagonal elements of the reduced density matrix of the system. In the second section, Sec. 3.2, we describe how to compute the Loschmidt echo using the adaptive t-DMRG. In Sec. 3.3, we revisit the decoherence dynamics of a qubit coupled to a interacting spin chain in various ground states as has previously been studied in Refs. [77, 78]. In Sec. 3.4, we then treat the decoherence dynamics of a qubit coupled to a

spin chain in various quantum quenched states. The conclusion is drawn in the last section, Sec. 3.5.

3.1 Decoherence

3.1.1 Introduction

Decoherence [23, 24, 25] is a mechanism in which an initially quantum state system becomes classical. It occurs when a system interacts with another system, to be described as "the bath" below. Basically, when the interaction between the system and the bath is turned on, the initially pure state of the system immediately evolves into a mixed state. This actually means that the superposition of the initially pure state is irreversibly converted into a statistical mixture, i.e. the initially finite off-diagonal elements of the reduced density matrix finally go to zero on a very short time scale which is called decoherence time and is shorter than any other dynamic time scale of the system. After decoherence has occurred, it resembles the reduced density matrix of a classical ensemble with different proportions of stable and einselection states (environment-induced superselection) [23]. However the wave function of the system and the bath does not collapse and the corresponding state of the system plus bath is still a pure state. One can measure the decoherence through a quantity called Loschmidt echo [79], which encodes the decay of the off-diagonal elements of the reduced density matrix of the system.

For a detailed analysis of decoherence, a concrete bath should be chosen. In our studies, we focus on the case of a bath consisting of a spin chain. Other kinds of bath are also interesting, such as the Bose-Hubbard model [80]. Previous papers discussed decoherence due to a bath consisting of non-interacting spins [79] as well as interacting spin models [77, 78, 81, 82]. The simplest nontrivial case of a system for discussing decoherence is a single qubit system [24, 77, 78, 79, 80, 81, 82]. Early works focus on the case of a central spin homogeneously coupled to all of the non-interacting spin-1/2 spins in the bath [79]. A more realistic bath with self-interaction, the quantum Ising model, was also treated [81]. In Ref. [81], the authors emphasize that the decay of the Loschmidt echo is enhanced when the bath is close to the critical point. For more complicated cases, one can introduce more general spin-1/2 spin baths, such as the spin-1/2 XY model and the spin-1/2 Heisenberg model. Also, one should consider more realistic interaction modes between the single qubit system and the bath. A detailed discussion for the cases that a qubit is inhomogeneously coupled to multiple

spins or coupled to a single spin in a one-dimensional quantum spin-1/2 model can be found in Refs. [77] and [78]. In Ref. [77], the authors discuss the decoherence of a single qubit coupled to one spin or a few spins of a general spin bath with an Ising coupling. Additionally, Ref. [78] investigates the case of a Heisenberg coupling between the qubit and the bath. The effect of other other spin-spin interactions in the bath, in particular a Dzyaloshinsky-Moriya interaction, was also considered [83]. In addition to considering eigenstates, especially the ground state, as the initial state of the bath, thermal states and thermal phase transition effects have also been studied [84]. Authors have also treated a two-qubit system coupled to a spin bath [85, 86]. From above studies, it can be concluded that decoherence behavior is affected by the interaction between the system and the bath, and that it is mainly influenced by the properties and quantum phase of the bath. Below, we will focus on a single qubit system interacting with the ground state and with quenched states of the bath.

3.1.2 System plus bath (S + E)

In order to investigate decoherence in detail, let us consider the system S (a spin-1/2 spin) coupled to a bath E that consists of a chain of L spin-1/2 particles, see Fig. 3.1. We will study how the properties of the bath E and the interaction between S and E affects the evolution of the coherence of S. The Hamiltonian of the complete system (system plus bath) is

$$H_{SE} = H_S + H_E + H_{int}, \tag{3.1}$$

where H_S and H_E are the Hamiltonian of the system S and of the bath E, respectively, and H_{int} is the coupling term between the system S and the bath E. The complete system composed of the system S and the bath E will evolve under this Hamiltonian. Regardless of the actual physical makeup of the qubit and without loss of generality, the single-qubit system is assumed to have a simple self-Hamiltonian,

$$H_S = -\omega S_z = -\frac{\omega}{2}(|\uparrow\rangle\langle\uparrow| - |\downarrow\rangle\langle\downarrow|), \tag{3.2}$$

where ω is a constant. States $|\uparrow\rangle$ and $|\downarrow\rangle$, respectively, are the spin-up eigenstate and the spin-down eigenstate of the qubit. In most discussions of the Loschmidt echo, such assumptions are also used. For some simple cases, the self-Hamiltonian of the system S can be set to zero without changing the evolution of the Loschmidt echo. However, in other cases, the pointer states $\{|\uparrow\rangle, |\downarrow\rangle\}$ (the states that is not entangled with the bath) [23] can be changed to

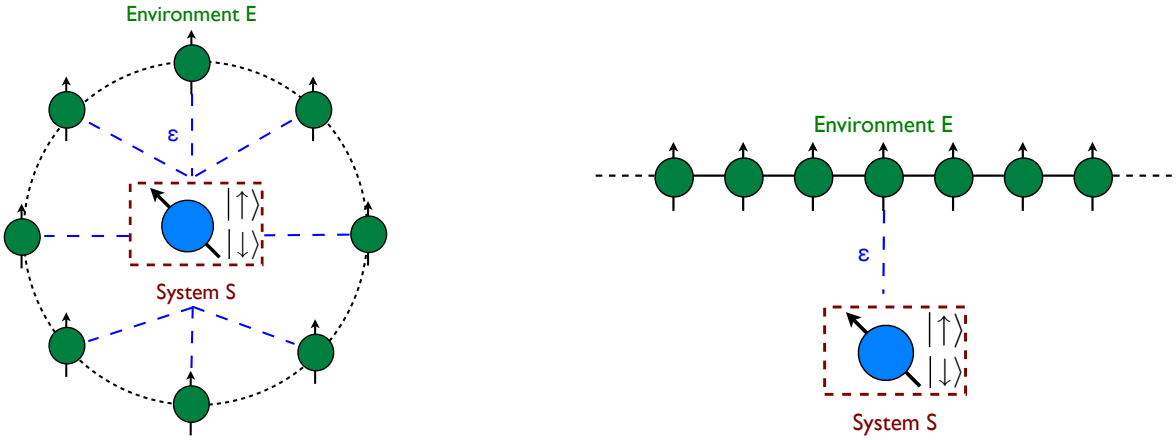

Figure 3.1: Schematic diagram of the coupling schemes between system and bath. The spin chain (bath) can have periodic boundary conditions (PBCs) or open boundary conditions (OBCs). One coupling scheme is that the qubit (system) homogeneously couples to each spin in the spin chain (left). If the spin chain has OBCs, the model will always be called the central spin model. Another coupling scheme is that the qubit couples to only one spin or a few arbitrary spins in the chain (right). The qubit may display different decoherence behaviors in the different coupling schemes.

the eigenstates of some special self-Hamiltonians of the system [24, 25, 79]. For example, H_S could describe a magnetic field in the x-direction or a time-dependent magnetic field. We will assume the bath Hamiltonian H_E is a one-dimensional spin-1/2 chain with the form

$$H_E = -2J \sum_{j=1}^{L} [(1+\gamma) S_j^x S_{j+1}^x + (1-\gamma) S_j^y S_{j+1}^y + \Delta S_j^z S_{j+1}^z + \lambda S_j^z], \tag{3.3}$$

where S_i^x, S_i^y, and S_i^z denote the spin operators of the i-th spin site in the chain. For simplicity, we will use periodic boundary conditions (PBCs) in analytical calculations and open boundary conditions (OBCs) in the DMRG calculations. The parameters J ($J \geq 0$), γ, Δ, and λ, determine the interaction strength in the xy plane between nearest-neighbor spins, the anisotropy in the xy plane and along the z-axis, and a z-direction transverse magnetic field, respectively. We consider the two limiting cases in which $\gamma = \lambda = 0$ (the XXZ chain) and $\gamma = 1, \Delta = 0$ (the transverse-field Ising model). The ground state of the XXZ chain is critical for $-1 \leq \Delta \leq 1$, is in an antiferromagnetic phase for $\Delta < -1$, and is in a ferromagnetic phase for $\Delta > 1$, see Fig. 3.2 (a). For $\lambda > 0$, the ground state of the transverse-field Ising chain has one critical point at $\lambda_c = 1$. For $0 \leq \lambda < 1$, it is in a long-range ordered ferromagnetic phase with a broken Z_2 symmetry, while for $\lambda > 1$, it is in a paramagnetic phase, see Fig. 3.2 (b).

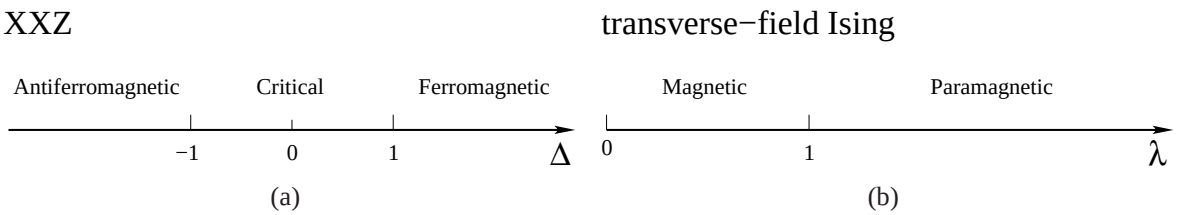

Figure 3.2: Ground-state phase diagram for (a) the XXZ chain and (b) the transverse-field Ising chain.

When the qubit is coupled to a transverse-field Ising chain, the system can be solved exactly for all times so that the long-time behavior can be fully investigated, see Appendix A. For the case of a coupling to an XXZ chain, we compute the time evolution using the adaptive t-DMRG.

We consider two types of coupling Hamiltonians H_{int}: the Ising coupling and the Heisenberg coupling. The general anisotropic Ising couping H_{int}^{Ising} has the form

$$H_{int}^{Ising} = -\epsilon \left|\uparrow\right\rangle \left\langle\uparrow\right| S_j^z + \epsilon' \left|\downarrow\right\rangle \left\langle\downarrow\right| S_j^z, \tag{3.4}$$

where ϵ and ϵ' are the anisotropic Ising coupling constants. The bath site label j indicates that the qubit only couples locally to one bath spin. We will concentrate mainly on the Ising coupling form of H_{int}^{Ising}.

The general Heisenberg couping H_{int}^{Heis} has the form

$$H_{int}^{Heis} = -\sum_{\alpha=x,y,z} \varepsilon^\alpha S_{qubit}^\alpha S_j^\alpha, \tag{3.5}$$

where ε^α ($\alpha = x, y, z$) are the coupling constants along three Cartesian axes, and S_{qubit}^α and S_j^α are the spin operators of the system and the spin operator of the j-th spin in the bath, respectively. Below, we will only consider an isotropic Heisenberg couping in H_{int}^{Heis}, i.e., $\varepsilon^x = \varepsilon^y = \varepsilon^z$.

Notice that, for the Ising coupling form, H_{int}^{Ising}, $[H_S, H_{SE}] = 0$. The interpretation is that the expectation value of the system Hamiltonian H_S is constant, and no energy exchange between the system S and the bath E occurs. This gives rise to a purely dephasing form of the time evolution. The system loses its coherence only. However, for a Heisenberg coupling form H_{int}^{Heis}, $[H_S, H_{SE}] \neq 0$, in general, and the system will undergo both dephasing and energy relaxation. However, if one sets $H_S = 0$, there is also pure dephasing only.

In studying the decoherence of the system S, we assume that the initial state of the com-

plete system (S plus E) is a pure state. That means the wave function of the complete system is a direct product of the state of the system S and the state of the bath E, i.e., it is given by

$$|\Psi_{SE}(t=0)\rangle = |\psi_S(0)\rangle|\psi_E(0)\rangle, \tag{3.6}$$

where $|\psi_S(0)\rangle$ and $|\psi_E(0)\rangle$ are the initial states of the system S and the bath E, respectively. One is relatively free to select an initial state of the system S. Here, in the general case, we choose an arbitrary state $|\psi_S(0)\rangle = c_\uparrow|\uparrow\rangle + c_\downarrow|\downarrow\rangle$, a superposition of the spin-up state $|\uparrow\rangle$ and the spin-down state $|\downarrow\rangle$, where $|c_\uparrow|^2 + |c_\downarrow|^2 = 1$. Consider, however, the limiting case of $|\psi_S(0)\rangle = |\uparrow\rangle$ or $|\downarrow\rangle$. At first glance, the off-diagonal elements of the density matrix of the system S, which characterize the decoherence (Loschmidt echo), will be zero initially and for all times. It seems that this behavior cannot characterize a general decoherence. However, one can rotate $|\uparrow\rangle$ or $|\downarrow\rangle$ through arbitrary angles to obtain a general state $|\psi_S(0)\rangle$ with nonzero off-diagonal elements of the density matrix. Thus, it is still completely general to choose $|\uparrow\rangle$ or $|\downarrow\rangle$ as the initial state for calculating the Loschmidt echo. On the other hand, we can choose the specific initial state of the bath $|\psi_E(0)\rangle$ that we are interested in. Building on previous studies [77, 78] that take the ground state of the bath Hamiltonian H_E, Eq. (3.3), as the initial state, we will make more accurate calculations for this case and then will also consider a quenched initial state, which is evolved from the ground state by carrying out a sudden change of the interaction constant, as the initial state. It is useful to mention that when the bath is an XXZ chain, only the case of the anisotropic parameter $\Delta = 0$ in Eq. (3.3) can be exactly solved. These exact results can be used for checking the accuracy and precision of the DMRG results. We apply the static DMRG to compute the ground state of the XXZ chain and then use the adaptive t-DMRG to compute the Loschmidt echo. We choose OBCs for the spin chain in the DMRG calculations because, as is well-known, the classical DMRG method does not converge well under PBCs. Additionally, for small bath size, i.e., $L \leq 17$, we utilize the exact diagonalization (ED) method.

The complete initial wave function, Eq. (3.6), evolves with the Hamiltonian, Eq. (3.1),

$$|\Psi_{SE}(t)\rangle = e^{-iH_{SE}t}|\Psi_{SE}(t)\rangle = e^{-iH_{SE}t}|\psi_S(0)\rangle|\psi_E(0)\rangle. \tag{3.7}$$

Since the wave function $|\psi_S(0)\rangle$ of the initial state of the system S has two branches, the spin up state $|\uparrow\rangle$ and the spin down state $|\downarrow\rangle$, the complete wave function, Eq. (3.7), also splits into

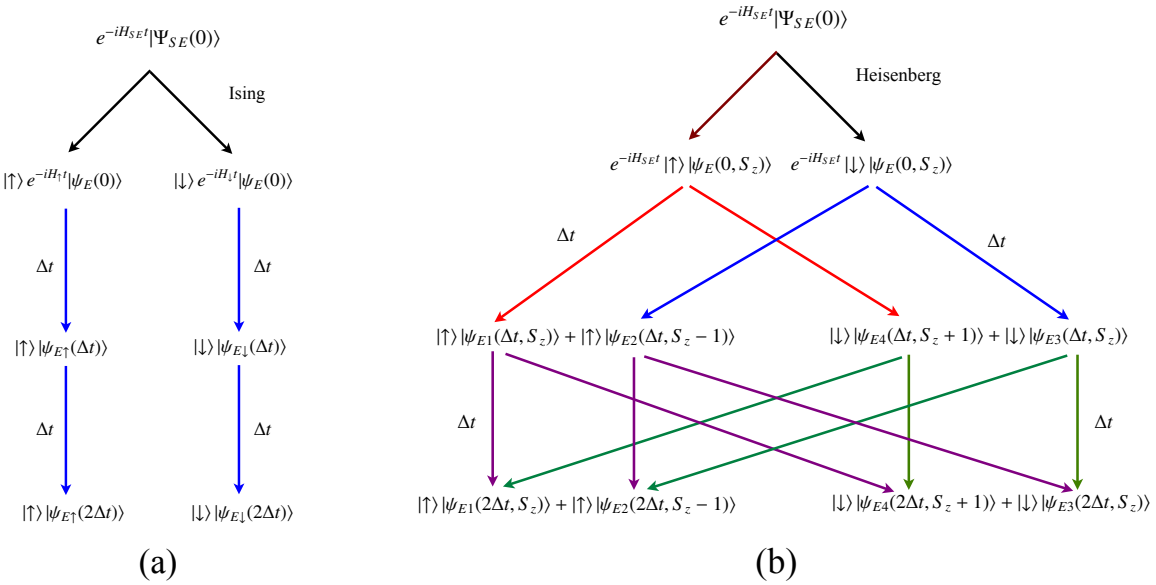

Figure 3.3: Depiction of the manner of the time evolution of the two branch wave functions, $|\uparrow\rangle|\psi_{E\uparrow}(t)\rangle$ and $|\downarrow\rangle|\psi_{E\downarrow}(t)\rangle$ with two different kinds of interactions between the system and the bath: (a) For the Ising coupling between the system and the bath, two branch wave functions evolve independently. (b) For the Heisenberg coupling between the system and the bath, the total spin of the bath wave function in the z-direction varies over S_z, S_z+1 and S_z-1 in different time steps. In this case, the two branches of the wave function evolve in a correlated way.

two branches. The result is

$$\begin{aligned}|\Psi_{SE}(t)\rangle &= e^{-iH_{SE}t}|\Psi_{SE}(0)\rangle \\ &= e^{-iH_{SE}t}(c_\uparrow|\uparrow\rangle + c_\downarrow|\downarrow\rangle)|\psi_E(0)\rangle.\end{aligned} \tag{3.8}$$

For the case of an Ising coupling H_{int}^{Ising}, Eq. (3.4), we can simplify the Eq. (3.8) to

$$\begin{aligned}|\Psi_{SE}(t)\rangle &= c_\uparrow e^{-iH_{SE}t}|\uparrow\rangle|\psi_E(0)\rangle + c_\downarrow e^{-iH_{SE}t}|\downarrow\rangle|\psi_E(0)\rangle \\ &= c_\uparrow e^{i\frac{\omega}{2}t}|\uparrow\rangle e^{-iH_\uparrow t}|\psi_E(0)\rangle + c_\downarrow e^{-i\frac{\omega}{2}t}|\downarrow\rangle e^{-iH_\downarrow t}|\psi_E(0)\rangle \\ &= c_\uparrow e^{i\frac{\omega}{2}t}|\uparrow\rangle|\psi_{E\uparrow}(t)\rangle + c_\downarrow e^{-i\frac{\omega}{2}t}|\downarrow\rangle|\psi_{E\downarrow}(t)\rangle,\end{aligned} \tag{3.9}$$

where the effective Hamitonians $H_\uparrow = -\epsilon S_j^z + H_E$ and $H_\downarrow = \epsilon' S_j^z + H_E$. The problem is changed to that of two independent time evolutions of the wave function of the bath E with these two effective Hamiltonians $H_\uparrow$ and $H_\downarrow$, respectively, see Fig. 3.3 (a). By using the complete wave function $|\Psi_{SE}(t)\rangle$, Eq. (3.9), and by tracing out the degrees of freedom of the bath E, the

time-dependent reduced density matrix of the system S,

$$\begin{aligned}
\rho_S(t) =& \mathrm{Tr}_E|\Psi_{SE}(t)\rangle\langle\Psi_{SE}(t)| \qquad (3.10)\\
=& \sum_n \langle n|\Psi_{SE}(t)\rangle\langle\Psi_{SE}(t)|n\rangle \\
=& \sum_n \langle n|(|c_\uparrow|^2 |\uparrow\rangle |\psi_{E\uparrow}(t)\rangle\langle\psi_{E\uparrow}(t)| \langle\uparrow| + |c_\downarrow|^2 |\downarrow\rangle |\psi_{E\downarrow}(t)\rangle\langle\psi_{E\downarrow}(t)| \langle\downarrow| \\
&+ c_\downarrow^* c_\uparrow e^{i\omega t} |\uparrow\rangle |\psi_{E\uparrow}(t)\rangle\langle\psi_{E\downarrow}(t)| \langle\downarrow| + c_\uparrow^* c_\downarrow e^{-i\omega t} |\downarrow\rangle |\psi_{E\downarrow}(t)\rangle\langle\psi_{E\uparrow}(t)| \langle\uparrow|)|n\rangle \\
=& \sum_n |c_\uparrow|^2 |\uparrow\rangle \langle\uparrow| \langle n|\psi_{E\uparrow}(t)\rangle\langle\psi_{E\uparrow}(t)|n\rangle + |c_\downarrow|^2 |\downarrow\rangle \langle\downarrow| \langle n|\psi_{E\downarrow}(t)\rangle\langle\psi_{E\downarrow}(t)|n\rangle \\
&+ c_\downarrow^* c_\uparrow e^{i\omega t} |\uparrow\rangle \langle\downarrow| \langle n|\psi_{E\uparrow}(t)\rangle\langle\psi_{E\downarrow}(t)|n\rangle + c_\uparrow^* c_\downarrow e^{-i\omega t} |\downarrow\rangle \langle\uparrow| \langle n|\psi_{E\downarrow}(t)\rangle\langle\psi_{E\uparrow}(t)|n\rangle \\
=& |c_\uparrow|^2 |\uparrow\rangle \langle\uparrow| + |c_\downarrow|^2 |\downarrow\rangle \langle\downarrow| \\
&+ c_\downarrow^* c_\uparrow e^{i\omega t} |\uparrow\rangle \langle\downarrow| \langle\psi_{E\downarrow}(t)|\psi_{E\uparrow}(t)\rangle + c_\uparrow^* c_\downarrow e^{-i\omega t} |\downarrow\rangle \langle\uparrow| \langle\psi_{E\uparrow}(t)|\psi_{E\downarrow}(t)\rangle,
\end{aligned}$$

is obtained, where we have taken the states $|n\rangle$ to be a complete basis for the bath E. The off-diagonal elements of the reduced density matrix, Eq. (3.10), represented in the basis of the eigenstates $|\uparrow\rangle$, $|\downarrow\rangle$ of the system S, characterize the decoherence of the system. The matrix form of $\rho_S(t)$ is

$$\rho_S(t) = \begin{bmatrix} \rho_{s,\uparrow\uparrow}(t) & \rho_{s,\uparrow\downarrow}(t) \\ \rho_{s,\downarrow\uparrow}(t) & \rho_{s,\downarrow\downarrow}(t) \end{bmatrix} = \begin{bmatrix} |c_\uparrow|^2 & c_\downarrow^* c_\uparrow e^{i\omega t}\langle\psi_{E\downarrow}(t)|\psi_{E\uparrow}(t)\rangle \\ c_\uparrow^* c_\downarrow e^{-i\omega t}\langle\psi_{E\uparrow}(t)|\psi_{E\downarrow}(t)\rangle & |c_\downarrow|^2 \end{bmatrix}. \qquad (3.11)$$

The off-diagonal element $\rho_{s,\uparrow\downarrow}(t)$ decays as *

$$\rho_{s,\uparrow\downarrow}(t) = c_\downarrow^* c_\uparrow e^{i\omega t}\langle\psi_{E\downarrow}(t)|\psi_{E\uparrow}(t)\rangle. \qquad (3.12)$$

However the diagonal elements $\rho_{s,\uparrow\uparrow}$ and $\rho_{s,\downarrow\downarrow}$ always retain their in the initial values $|c_\uparrow|^2$ and $|c_\downarrow|^2$ and will never decay in the time evolution. The overlap between the two branch states of the bath E, $\langle\psi_{E\downarrow}(t)|\psi_{E\uparrow}(t)\rangle$, characterizes the Loschmidt echo. We can define the Loschmidt echo as a real number,

$$LE(t) = |\langle\psi_{E\downarrow}(t)|\psi_{E\uparrow}(t)\rangle|^2 = |\langle\psi_E(0)|e^{iH_\downarrow t}e^{-iH_\uparrow t}|\psi_E(0)\rangle|^2, \qquad (3.13)$$

where the wave function of the initial state $|\psi_E(0)\rangle$ is the ground state or a quenched state of

*Since, $\rho_{s,\uparrow\downarrow}(t) = \rho^*_{s,\downarrow\uparrow}(t)$, we will only consider $\rho_{s,\uparrow\downarrow}(t)$.

the bath E. It decays exponentially as a Gaussian at short times [77, 78, 79, 86, 87]:

$$LE(t) \sim e^{-\alpha t^2}, \quad t \sim 0. \tag{3.14}$$

We can set one of the coupling constants ϵ, ϵ' to zero (actually, in most studies, $\epsilon' = 0$). If the initial state $|\psi_E(0)\rangle$ is a ground state of the bath E, Eq. (3.13) is identical to

$$LE(t) = |\langle\psi_E(0)|e^{-iH_\uparrow t}|\psi_E(0)\rangle|^2, \tag{3.15}$$

which can also be interpreted as the "survival probability" of the initial state evolved under the effective Hamiltonian $H_\uparrow$. In the time evolution, the Loschmidt echo quickly deviates from the initial value 1 because of the presence of the interaction, and the system state is converted into a statistical mixture. For some cases, the Loschmidt echo even approaches zero, and the reduced density matrix of the system, Eq. (3.10), becomes diagonal. This means that the coherence of the system is strongly suppressed and gradually leaks to the bath, but the complete system still keeps its coherence. Furthermore, if the Loschmidt echo is close to 1, it indicates that the interaction between the system and the bath is very weak. In particular, the case that the Loschmidt echo always remains 1 simply means the initial system state is a eigenstate of the effective Hamiltonian $H_\uparrow$, or, in other words, that there is negligible interaction between the system S and the bath E. All previous studies are based on calculations with a finite-sized bath. Since there is, in general, a bath-size-dependent revival time of the Loschmidt echo, this kind of decoherence behavior is called an "echo". Moreover, the Loschmidt echo can never revive to the full initial value of 1, and the value of the revived Loschmidt echo becomes weaker and weaker with more and more revivals. This is why such decoherence behavior is called a "Loschmidt echo".

Furthermore, for the case of Heisenberg coupling H_{int}^{Heis}, Eq. (3.5), one finds that the two branch wave functions in Eq. (3.8) will evolve correlatively, see Fig. 3.3 (b). Since the Heisenberg coupling will lead to an exchange of quantum numbers between the system S and the bath E, the quantum number of the bath will be changed. In order to facilitate the discussion, we explicitly write down the total spin to identify different states. We assume that the initial state of the bath E, $|\Psi_{SE}(t = 0, S_z)\rangle$, has a total spin S_z. Thus, Eq. (3.8) can be written as

$$\begin{aligned}
|\Psi_{SE}(t)\rangle &= \left[e^{-iH_{SE}t}c_\uparrow|\uparrow\rangle|\psi_E(0, S_z)\rangle\right] + \left[e^{-iH_{SE}t}c_\downarrow|\downarrow\rangle|\psi_E(0, S_z)\rangle\right] \qquad (3.16)\\
&= \left[c_\uparrow|\uparrow\rangle|\psi_{E1}(t, S_z)\rangle + c_\uparrow|\downarrow\rangle|\psi_{E4}(t, S_z + 1)\rangle\right] + \left[c_\downarrow|\downarrow\rangle|\psi_{E3}(t, S_z)\rangle + c_\downarrow|\uparrow\rangle|\psi_{E2}(t, S_z - 1)\rangle\right]\\
&= |\uparrow\rangle\left[c_\uparrow|\psi_{E1}(t, S_z)\rangle + c_\downarrow|\psi_{E2}(t, S_z - 1)\rangle\right] + |\downarrow\rangle\left[c_\downarrow|\psi_{E3}(t, S_z)\rangle + c_\uparrow|\psi_{E4}(t, S_z + 1)\rangle\right],
\end{aligned}$$

where the effective wave function $|\psi_1\rangle = |\uparrow\rangle|\psi_{E1}(t,S_z)\rangle + |\downarrow\rangle|\psi_{E4}(t,S_z+1)\rangle$ evolves from the wave function $e^{-iH_{SE}t}|\uparrow\rangle|\psi_E(0,S_z)\rangle$, and the effective wave function $|\psi_2\rangle = |\downarrow\rangle|\psi_{E3}(t,S_z)\rangle + |\uparrow\rangle|\psi_{E2}(t,S_z-1)\rangle$ evolves from the wave function $e^{-iH_{SE}t}|\downarrow\rangle|\psi_E(0,S_z)\rangle$. The wave functions $|\psi_{E1}(t,S_z)\rangle$, $|\psi_{E2}(t,S_z)\rangle$, $|\psi_{E3}(t,S_z)\rangle$ and $|\psi_{E4}(t,S_z)\rangle$ are not assumed to be normalized. This means that

$$\begin{aligned}\langle\psi_{E1}(t,S_z)|\psi_{E1}(t,S_z)\rangle + \langle\psi_{E4}(t,S_z+1)|\psi_{E4}(t,S_z+1)\rangle &= 1/|c_\uparrow|^2, \\ \langle\psi_{E3}(t,S_z)|\psi_{E3}(t,S_z)\rangle + \langle\psi_{E2}(t,S_z-1)|\psi_{E2}(t,S_z-1)\rangle &= 1/|c_\downarrow|^2.\end{aligned} \tag{3.17}$$

The wave function $|\uparrow\rangle|\psi_{E1}(t,S_z)\rangle$ contributes to the wave function $|\downarrow\rangle|\psi_{E4}(t',S_z+1)\rangle$ at the next time step t', and vice versa. The wave functions $|\downarrow\rangle|\psi_{E3}(t,S_z)\rangle$ and $|\uparrow\rangle|\psi_{E2}(t,S_z-1)\rangle$ behave similarly. This behavior is depicted in Fig. 3.3 (b). All four of these four wave functions do not have simple forms; they must be determined by specific calculations. Notice that we can also write Eq. (3.16) as $|\Psi_{SE}(t)\rangle = c_\uparrow(t)|\uparrow\rangle|\psi_{\uparrow E}(t)\rangle + c_\downarrow(t)|\downarrow\rangle|\psi_{\downarrow E}(t)\rangle$ [78].

We now examine the Loschmidt echo. It is easy to see that the off-diagonal element of the reduced density matrix ρ_s, e.g., $\rho_{s,\uparrow\downarrow}(t)$, is given by

$$\rho_{s,\uparrow\downarrow}(t) = c_\downarrow^* c_\uparrow \langle\psi_{E3}(t,S_z)|\psi_{E1}(t,S_z)\rangle. \tag{3.18}$$

Thus, analogously to Eq. (3.13), the Loschmidt echo can be defined as

$$LE(t) = |\langle\psi_{E3}(t,S_z)|\psi_{E1}(t,S_z)\rangle|^2. \tag{3.19}$$

Here the Loschmidt echo is only related to the overlap between two wave functions that have the same quantum number as the wave function of the initial state.

It is useful to discuss the energy relaxation behavior here. If the Hamiltonian of the system S is still defined by Eq. (3.2), the observable $\langle H_S\rangle$ can be written as

$$\begin{aligned}\langle H_S\rangle(t) &= \mathrm{Tr}(H_S\rho_s(t)) = -\frac{\omega}{2}\rho_{s,\uparrow\uparrow}(t) + \frac{\omega}{2}\rho_{s,\downarrow\downarrow}(t) = \omega\left(\frac{1}{2} - \rho_{s,\uparrow\uparrow}(t)\right) \\ &= \omega\left(\frac{1}{2} - |c_\uparrow|^2\langle\psi_{E1}(t,S_z)|\psi_{E1}(t,S_z)\rangle - |c_\downarrow|^2\langle\psi_{E2}(t,S_z-1)|\psi_{E2}(t,S_z-1)\rangle\right)\end{aligned} \tag{3.20}$$

using Eq. (3.17), where $\rho_{s,\uparrow\uparrow}(t)$ and $\rho_{s,\downarrow\downarrow}$ are diagonal elements of the reduced density matrix ρ_s. The energy relaxation behavior is related to the choice of the initial state of the system S. Different combinations of $c_\uparrow$ and $c_\downarrow$ will lead to different energy relaxation behaviors. To pre-

vent energy relaxation, we can set $H_S = 0$ in our calculations, but it is also easy to generalize to the case of non-zero H_S.

The behavior of the Loschmidt echo (i.e., the decoherence) of the system S (the qubit) could be sensitive to the internal dynamics of the bath (i.e., the quantum phases and the quench time). In the following, we will explore how the time evolution of the Loschmidt echo of the system S is affected by the internal dynamics of the bath E.

3.2 Details of the program

In this section, we discuss the details of how to calculate the Loschmidt echo, Eq. (3.13) and Eq. (3.19), by means of the adaptive t-DMRG with OBCs. The adaptive t-DMRG calculations of the Loschmidt echo are based on the discussion in Sec. 3.1.2

For the Ising coupling case, the Loschmidt echo, Eq. (3.13), is the square of the overlap between the two branch wave functions $|\psi_{E\downarrow}(t)\rangle$ and $|\psi_{E\uparrow}(t)\rangle$. Although these two wave functions evolve independently, see Eq. (3.9), we need to keep track of both wave functions simultaneously so that they are represented in the same computational basis.

As mentioned in Sec. 1.3, we first must apply the static DMRG to evaluate the ground state of the bath E. We then apply the adaptive t-DMRG to simulate the time evolution of the two branch wave functions $|\uparrow\rangle|\psi_{E\uparrow}(t)\rangle$ and $|\downarrow\rangle|\psi_{E\downarrow}(t)\rangle$ independently. Here we use the second-order Trotter-Suzuki adaptive t-DMRG, i.e., the time evolution operators $e^{H_\uparrow}$ and $e^{H_\downarrow}$ are decomposed in a second order Trotter-Suzuki decomposition. We apply the bond time-evolution operators $U_\uparrow = e^{-iH_{\uparrow,ij}\Delta t}$ and $U_\downarrow = e^{-iH_{\downarrow,ij}\Delta t}$ (for the sites i and j of the bath E, respectively) to these two wave functions simultaneously. For the sake of convenience, we set the populations of the initial state of the system all to 1, $c_\uparrow = c_\downarrow = 1$. At each step of the adaptive t-DMRG sweep, the state $|\Psi_{SE}(t)\rangle$, Eq. (3.9), is evolved using

$$\begin{aligned}|\Psi_{SE}(t+\Delta t)\rangle &= e^{-iH_{SE,ij}\Delta t}|\Psi_{SE}(t)\rangle = e^{i\frac{\omega}{2}t}U_\uparrow|\uparrow\rangle|\psi_{E\uparrow}(t)\rangle + e^{-i\frac{\omega}{2}t}U_\downarrow|\downarrow\rangle|\psi_{E\downarrow}(t)\rangle \\ &= e^{i\frac{\omega}{2}t}|\uparrow\rangle|\psi_{E\uparrow}(t+\Delta t)\rangle + e^{-i\frac{\omega}{2}t}|\downarrow\rangle|\psi_{E\downarrow}(t+\Delta t)\rangle, \end{aligned} \tag{3.21}$$

where $|\psi_{E\uparrow}(t+\Delta t)\rangle$ and $|\psi_{E\downarrow}(t+\Delta t)\rangle$ are the states of the current adaptive t-DMRG step. During the time evolution, the basis of the states is changed. The new reduced density matrix is updated by simultaneously targeting $|\psi_{E\uparrow}(t+\Delta t)\rangle$ and $|\psi_{E\downarrow}(t+\Delta t)\rangle$. We set the density matrices of both wave functions to have the weight $1/2$, ensuring that the trace of the total

density matrix is 1. The total reduced density matrix is then given by

$$\rho_{dmrg} = \mathrm{Tr}_e(\frac{1}{2}|\psi_{E\uparrow}(t+\Delta t)\rangle\langle\psi_{E\uparrow}(t+\Delta t)| + \frac{1}{2}|\psi_{E\downarrow}(t+\Delta t)\rangle\langle\psi_{E\downarrow}(t+\Delta t)|). \tag{3.22}$$

Here Tr_e means the trace over the degrees of the freedom of the environment block in the DMRG algorithm. After a standard renormalization step of the DMRG, the new common basis of the two branch wave functions are constructed. These two branch wave functions are thus both represented in a common basis. Thus, it is possible to directly evaluate the overlap between $|\psi_{E\uparrow}(t)\rangle$ and $|\psi_{E\downarrow}(t)\rangle$. After reaching the time we are interested in, the Loschmidt echo, Eq. (3.13), is evaluated.

For the case of Heisenberg coupling between the system S and the bath E, we can still write down each sweep step of the adaptive t-DMRG calculation even though the two branch wave functions evolve in a correlated way. For example, one applies the local bond time evolution operator $e^{-iH_{SE,ij}\Delta t}$ (for the sites i and j of the complete system S+E) to the wave functions obtained from previous sweep step, Eq. (3.16), (setting $c_\uparrow = c_\downarrow = 1$):

$$\begin{aligned}
&|\Psi_{SE}(t+\Delta t)\rangle = e^{-iH_{SE,ij}\Delta t}|\Psi_{SE}(t)\rangle \\
=&e^{-iH_{SE,ij}\Delta t}\{|\uparrow\rangle[|\psi_{E1}(t,S_z)\rangle + |\psi_{E2}(t,S_z-1)\rangle] + |\downarrow\rangle[|\psi_{E3}(t,S_z)\rangle + |\psi_{E4}(t,S_z+1)\rangle]\} \\
=&|\uparrow\rangle|\psi^a_{E1}(t+\Delta t,S_z)\rangle + |\downarrow\rangle|\psi^b_{E1}(t+\Delta t,S_z+1)\rangle + |\uparrow\rangle|\psi^a_{E2}(t+\Delta t,S_z-1)\rangle + |\downarrow\rangle|\psi^b_{E2}(t+\Delta t,S_z)\rangle \\
&+|\downarrow\rangle|\psi^a_{E3}(t+\Delta t,S_z)\rangle + |\uparrow\rangle|\psi^b_{E3}(t+\Delta t,S_z-1)\rangle + |\downarrow\rangle|\psi^a_{E4}(t+\Delta t,S_z+1)\rangle + |\uparrow\rangle|\psi^b_{E4}(t+\Delta t,S_z)\rangle \\
=&|\uparrow\rangle|\psi'_{E1}(t+\Delta t,S_z)\rangle + |\uparrow\rangle|\psi'_{E2}(t+\Delta t,S_z-1)\rangle + |\downarrow\rangle|\psi'_{E3}(t+\Delta t,S_z)\rangle + |\downarrow\rangle|\psi'_{E4}(t+\Delta t,S_z+1)\rangle,
\end{aligned} \tag{3.23}$$

where

$$|\psi'_{E1}(t+\Delta t,S_z)\rangle = |\psi^a_{E1}(t+\Delta t,S_z)\rangle + |\psi^b_{E4}(t+\Delta t,S_z)\rangle, \tag{3.24a}$$

$$|\psi'_{E2}(t+\Delta t,S_z-1)\rangle = |\psi^a_{E2}(t+\Delta t,S_z-1)\rangle + |\psi^b_{E3}(t+\Delta t,S_z-1)\rangle, \tag{3.24b}$$

$$|\psi'_{E3}(t+\Delta t,S_z)\rangle = |\psi^a_{E3}(t+\Delta t,S_z)\rangle + |\psi^b_{E2}(t+\Delta t,S_z)\rangle, \tag{3.24c}$$

and

$$|\psi'_{E4}(t+\Delta t,S_z+1)\rangle = |\psi^a_{E4}(t+\Delta t,S_z+1)\rangle + |\psi^b_{E1}(t+\Delta t,S_z+1)\rangle. \tag{3.24d}$$

Notice that, the local bond time-evolution operator $e^{-iH_{SE,ij}\Delta t}$ is obtained from the second-order Trotter-Suzuki decomposition of the time evolution operator $e^{-iH_{SE}t}$. For every time step of the

adaptive t-DMRG, every sector of the wave function will split into two parts with different quantum numbers, Eq. (3.24). Similarly to the discussion of Ising coupling case, the total reduced density matrix is given by

$$\begin{aligned}\rho_{dmrg} = \mathrm{Tr}_e(&\frac{1}{2}|\psi'_{E1}(t+\Delta t, S_z)\rangle\langle\psi'_{E1}(t+\Delta t, S_z)| + \frac{1}{2}|\psi'_{E2}(t+\Delta t, S_z-1)\rangle\langle\psi'_{E2}(t+\Delta t, S_z-1)| \\ &+\frac{1}{2}|\psi'_{E3}(t+\Delta t, S_z)\rangle\langle\psi'_{E3}(t+\Delta t, S_z)| + \frac{1}{2}|\psi'_{E4}(t+\Delta t, S_z+1)\rangle\langle\psi'_{E4}(t+\Delta t, S_z+1)|).\end{aligned} \tag{3.25}$$

Notice that we do not set the weight of each density matrix to $1/4$ because $|\psi_1\rangle = |\uparrow\rangle|\psi'_{E1}(t+\Delta t, S_z)\rangle + |\downarrow\rangle|\psi'_{E4}(t+\Delta t, S_z+1)\rangle$ and $|\psi_2\rangle = |\downarrow\rangle|\psi'_{E3}(t+\Delta t, S_z)\rangle + |\uparrow\rangle|\psi'_{E2}(t+\Delta t, S_z-1)\rangle$ are actually two independent wave functions. In order to normalize the trace of the total density matrix ρ_{dmrg} to 1, we only need to set the weights of the density matrices of $|\psi_1\rangle$ and $|\psi_2\rangle$ to 1/2. As a result, we get Eq. (3.25).

In addition, the method mentioned above is not the most straightforward method of calculating the Loschmidt echo. Actually, one can calculate the off-diagonal matrix element of the reduced density matrix of the system S, $\rho_{s,\uparrow\downarrow}(t)$, directly in the DMRG. Using Eq. (3.13) and Eq. (3.19), the Loschmidt echo can be easily expressed as

$$LE(t) = \left|\frac{\rho_{s,\uparrow\downarrow}(t)}{c^*_\downarrow c_\uparrow}\right|^2. \tag{3.26}$$

This form is particularly useful when a complex self-Hamiltonian or a complex interaction term to the bath E is present, which may lead to a wave function that cannot be written in the form of a finite number of branches.

3.3 Ground state as initial state

We focus on the long- and short-time behaviors of the Loschmidt echo that occur when the system is coupled to a ground-state bath (XXZ) at the initial time. We will consider the case of Ising coupling, see Eq. (3.4), as well as that of Heisenberg coupling, see Eq. (3.5), between the system and the bath. The bath Hamiltonian is that of the XXZ chain, which is

$$H_E = -2J\sum_{j=1}^{L}[S^x_j S^x_{j+1} + S^y_j S^y_{j+1} + \Delta S^z_j S^z_{j+1}]. \tag{3.27}$$

The ground state of the XXZ chain has three phase with two critical points $\Delta_c = -1$ and $\Delta_c = 1$. It is critical for $-1 \leq \Delta \leq 1$; the critical state, is spanned by $|\uparrow\downarrow\uparrow\downarrow \ldots \uparrow\rangle$, $|\uparrow\uparrow\downarrow\downarrow \ldots \uparrow\rangle$, $\ldots$, and $|\downarrow\uparrow\downarrow\uparrow \ldots \downarrow\rangle$. In the antiferromagnetic phase, $\Delta < -1$, the ground state is doubly degenerate, i.e., $|\uparrow\downarrow\uparrow\downarrow \ldots \downarrow\rangle$ or $|\downarrow\uparrow\downarrow\uparrow \ldots \uparrow\rangle$. In the ferromagnetic phase, $\Delta > 1$, the ground state is $|\uparrow\uparrow\uparrow\uparrow \ldots \uparrow\uparrow\rangle$.

3.3.1 Ising coupling between S and E

In this section, we consider the case of Ising coupling, Eq. (3.4), between the system S and the bath E. Using adaptive t-DMRG calculations with $\Delta t = 0.001$ for the time evolution, discarded weight below 10^{-13}, a typical minimum truncated Hilbert space dimension of $D = 100$ and a typical maximum truncated Hilbert space dimension of $D = 1000$, we treat systems with up to 301 sites with OBCs. We choose an odd number of sites with total spin $S_z = 1/2$ in order to ensure a unique ground state in the antiferromagnetic phase of the XXZ chain. In order to minimize the boundary effects, we consider only the case in which the system is coupled to a spin in the middle of the chain, i.e., $j = 25$ for $L = 49$. The error analysis is shown in Appendix B.

The generic behavior of the Loschmidt echo as a function of time for different values of the anisotropy interaction strength Δ and lattice sizes $L = 49$ and 101 with coupling constant $\epsilon = 0.2$ is depicted in Figs. 3.4 and 3.5. Due to the smaller Hilbert space, our calculations for $L = 49$ can reach a much longer time than those for $L = 101$. In the antiferromagnetic phase, $\Delta < -1$, the decay of the Loschmidt echo is suppressed, i.e, at $\Delta = -3$ and -2, and it is completely suppressed when $\Delta \to -\infty$. In the critical region, the decay of the Loschmidt echo is affected by the values of Δ only at long times. The oscillation of the curve for $\Delta = 0.5$ has a frequency and an amplitude proportional to ϵ that is related to the finite-size effects. In the ferromagnetic phase, the Loschmidt echo does not decay because the ground state is essentially classical. Near or at the critical points, the decay of the Loschmidt echo is strongly enhanced. Already for $L = 49$, the asymptotic behavior of the Loschmidt echo is characterized by a decay to zero close to and at the critical point $\Delta_c = 1$. We choose the state with a spin quantum number $S_z = 1/2$ at the critical point, $\Delta_c = 1$, where the ground state is highly degenerate. At long times, the Loschmidt echo revives due to the finite-size effects. The revival time for this case can be roughly estimated to be $t^* \approx \frac{L}{2v}$, where v is the velocity

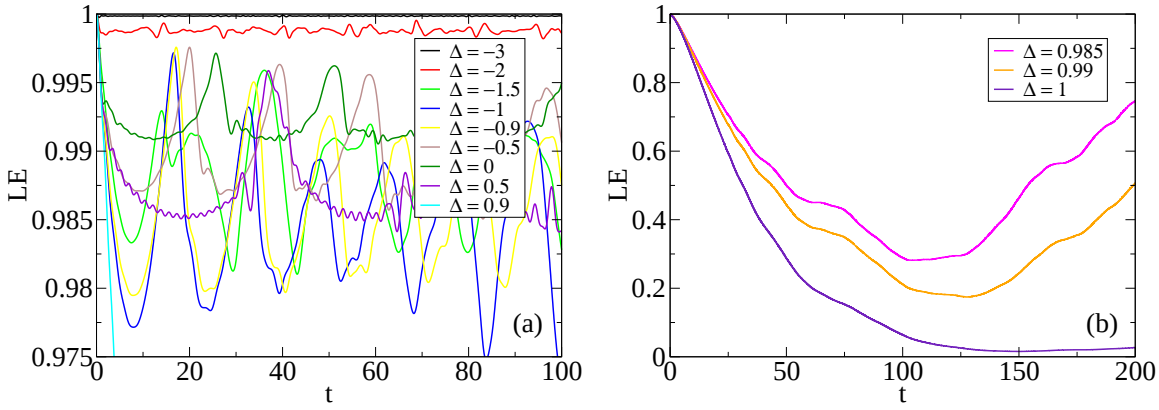

(a) (b)

Figure 3.4: Ising coupling case: Loschmidt echo *LE* as a function of time t for different values of the anisotropy interaction strength: (a) $\Delta = -3$ (black), -2 (red), -1.5 (green), -1 (blue), -0.9 (yellow), -0.5 (brown), 0 (olive), 0.5 (violet), and 0.9 (cyan); (b) $\Delta = 0.985$ (magenta), 0.99 (orange), and 1 (indigo) for a spin-1/2 XXZ chain with lattice size $L = 49$ and OBCs.

of the elementary excitations in the critical region (XXZ), given by [88, 89]

$$v = \frac{\pi\sqrt{1-\Delta^2}}{2\arccos(-\Delta)}. \tag{3.28}$$

For $\Delta \to 1$ and $v \to 0$, the revival time becomes very large, see Fig. 3.4.

The behavior of the Loschmidt echo for short time is depicted in Fig. 3.6 (a), which is a magnification of the curve in Fig. 3.5. We have fit the data points of the Loschmidt echo for time $t \lesssim 0.02$ to a Gaussian decay with parameter α. For time $t \gtrsim 0.04$, the Loschmidt echo does not, in general, decay as a Gaussian deep in the antiferromagnetic phase. The short-time Gaussian decay parameter α is shown in Fig. 3.6 (b) as a function of Δ for the bath lattice sizes $L = 49$, 101, and 301. These are no visible finite-size effects in all phases except at the points close to the critical point $\Delta_c = -1$. For $\Delta \to -\infty$, α asymptotically tends to zero. As Δ moves close to the critical point $\Delta_c = -1$, α increases to the maximal value 0.01 and remains almost constant in the critical region ($-1 < \Delta < 1$). At the critical point $\Delta_c = -1$, α is continuous. However, at the critical point $\Delta_c = 1$, α is completely discontinuous, independent of finite-size effects. In the ferromagnetic phase, α is strictly zero.

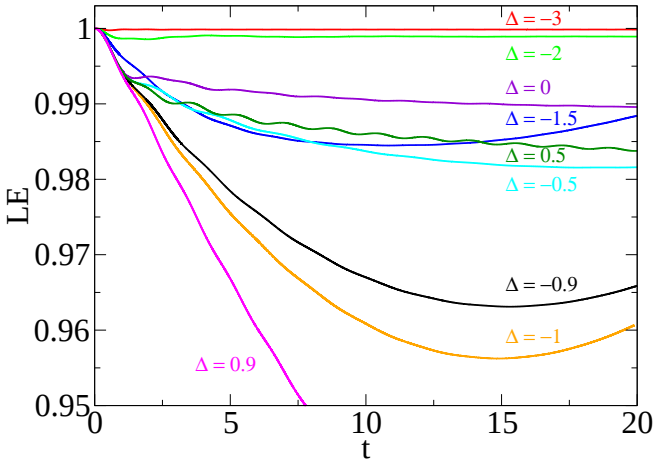

Figure 3.5: Ising coupling case: the Loschmidt echo LE as a function of time t for different values of the anisotropy interaction strength $\Delta = -3$ (red), -2 (green), 0 (violet), -1.5 (blue), 0.5 (olive), -0.5 (cyan), -0.9 (black), -1 (orange), and 0.9 (magenta) of a spin-1/2 XXZ chain with lattice size $L = 101$ and OBCs.

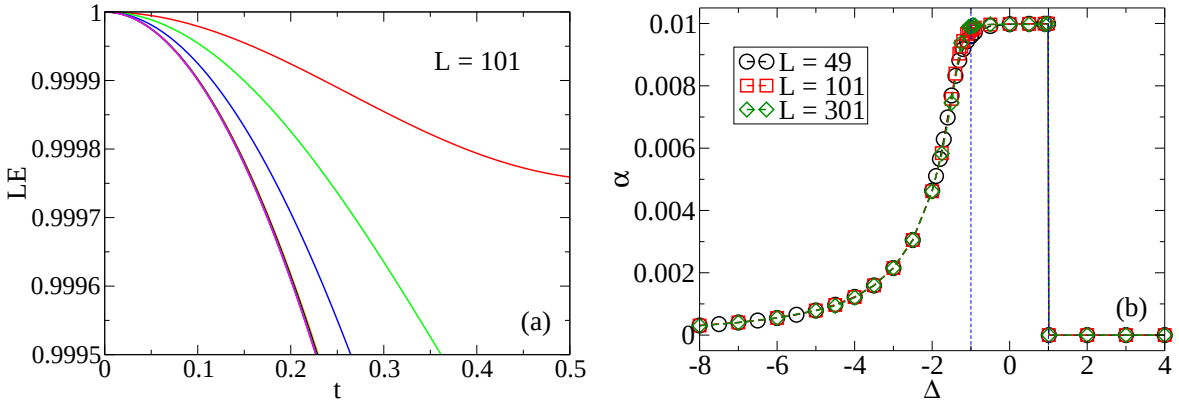

(a) (b)

Figure 3.6: Ising coupling case: (a) short-time behavior of the Loschmidt echo LE with bath lattice sizes $L = 101$ and $t \leq 0.5$, where the LE is fit to a Gaussian decay, $LE(t) \sim e^{-\alpha t^2}$. The plot corresponds to an enlargement of Fig. 3.5 at small times. The various curves are for different values of Δ, from top to bottom: $\Delta = -3$ (red), -2 (green), -1.5 (blue), 0 (violet), 0.5 (olive), -0.5 (cyan), ..., 0.9 (magenta), where the curves overlap for $-1 < \Delta \leq 1$, i.e., in the critical phase of the XXZ chain. (b) Scaling analysis of the decay parameter α as a function of Δ for different bath lattice sizes $L = 49$ (black), $L = 101$ (red), and $L = 301$ (green). Here the coupling constant between the system and bath is kept fixed, $\epsilon = 0.2$.

3.3.2 Heisenberg coupling between S and E

In this section, we consider the case of Heisenberg coupling, Eq. (3.5), between the system S and the bath E. Using the adaptive t-DMRG calculations with a time step of $\Delta t = 0.001$, and keeping the discarded weight below 10^{-13} for $t < 15$ and 10^{-10} for $15 < t < 100$, and the size of the truncated Hilbert space above $D = 100$ and below $D = 1000$, we treat systems with up to 101 sites, OBCs, and an odd number of sites with a spin quantum number $S_z = 1/2$. In order to minimize the boundary effects, we consider only the case in which the system is coupled to a spin in the middle of the chain, i.e., $j = 25$ for $L = 49$.

In Fig. 3.7, we plot the decay of the Loschmidt echo as a function of time for different values of the anisotropy interaction strength Δ for a bath lattice size $L = 49$, with isotropic coupling constant $\varepsilon^x = \varepsilon^y = \varepsilon^z = 0.2$. In the antiferromagnetic phase, $\Delta < -1$, the long-time decay of the Loschmidt echo is strongly suppressed (i.e., $\Delta = -3$ and -2) and is completely suppressed as $\Delta \to -\infty$. In the critical region ($-1 < \Delta < 1$), the decay of the Loschmidt echo is affected by the values of Δ only at long times. For $L = 49$, the Loschmidt echo already decays to zero for all parameters. In the ferromagnetic phase, unlike the case of Ising coupling, decay of the Loschmidt echo takes place because the effects of ε^x and ε^y destroy the fully polarization of the ground state. The decay is also strongly suppressed, with complete suppression occurring when $\Delta \to \infty$. Near or at the critical points, the short-time decay of the Loschmidt echo is strongly enhanced. However, the long-time behavior is more complicated to interpret. We can still see that the Loschmidt echo revives at a long time scale. The revival time is approximately proportional to L. For $\Delta = -1$, -0.9, -0.5, and 0, a kink in the curve of the Loschmidt echo at about $t = 20$ is related to the odd number of the bath lattice size. We cannot find such kinks for the case of even bath lattice size.

The short-time Gaussian decay parameter α is shown in Fig. 3.8 as a function of Δ for the bath lattice size $L = 25, 49$, and 101. We have fit the data points of the Loschmidt echo for times $t \lesssim 0.02$ to obtain the Gaussian decay parameter α. For time $t > 0.04$, the Loschmidt echo does not, in general, decay strictly as a Gaussian deep in the antiferromagnetic phase. As shown in the figure, as for the case of Ising coupling, the finite-size effects are only obvious near the critical point $\Delta_c = -1$. In other regions, the finite-size effects are not noticeable. For $\Delta \to -\infty$, it asymptotically tends to 0 (not shown in the figure) because the effects of the small coupling between the qubit and the bath are negligible for an infinite value of Δ. From $\Delta = -8$ to $\Delta = -1$, α increases from 0.01 to the maximal value 0.02. In the critical region ($-1 < \Delta < 1$) on finite lattices, the decay parameter α depends on Δ. However, as the bath size approaches the thermodynamic limit, the dependence of α on Δ is reduced. In Fig. 3.8,

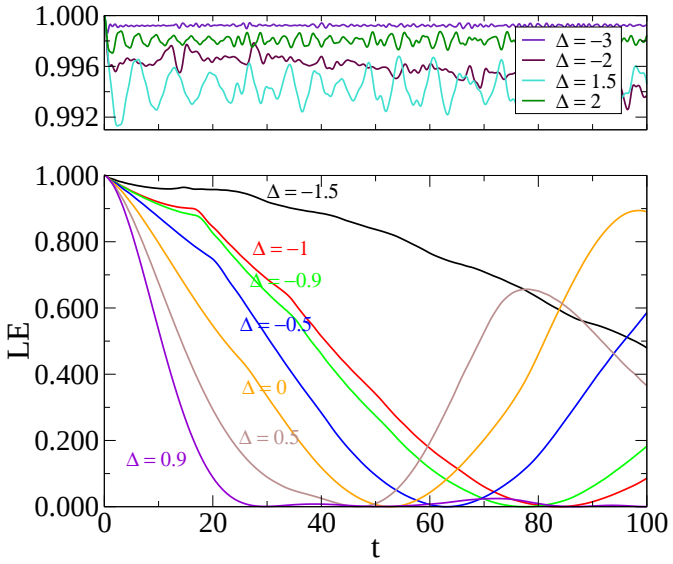

Figure 3.7: Heisenberg coupling case: Loschmidt echo LE as a function of time t for different values of the anisotropy interaction strength: $\Delta = -3$ (indigo), -2 (maroon), 1.5 (turquoise), 2 (olive), -1.5 (black), -1 (red), -0.9 (green), -0.5 (blue), 0 (orange), 0.5 (brown), and 0.9 (violet) of a spin-1/2 XXZ chain with lattice size $L = 49$ and OBCs.

the decay parameter α retains an almost constant value 0.02, as expected in the critical region, already for a lattice size $L = 101$. As in the case of Ising coupling, the curves of α are continuous at the critical point $\Delta_c = -1$. At the critical point $\Delta_c = 1$, they are completely discontinuous, and are also not dependent on L. In the ferromagnetic phase, in contrast to the case of Ising coupling, α remains a constant finite value 0.01 and asymptotically tends to 0 when $\Delta \to \infty$. Since the ferromagnetic ground state is not an eigenvector of the complete Hamiltonian H_{SE}, the effects of the small coupling between the qubit and the bath are negligible for an infinite value of Δ.

3.4 Quantum quenched state as initial state

As shown in Sec. 3.3.1 for the Ising coupling case (the pure dephasing case without energy exchange between S and E), a system in its ground state is not a typical realization of a bath. A more general configuration for the bath would be a mixed state, e.g., a bath at finite temperature. However, such states are hard to treat within the DMRG. One possibility for generating a more general configuration is a system pushed out of equilibrium. This experimental background for this idea is the development of the technology in recent years making it possible to

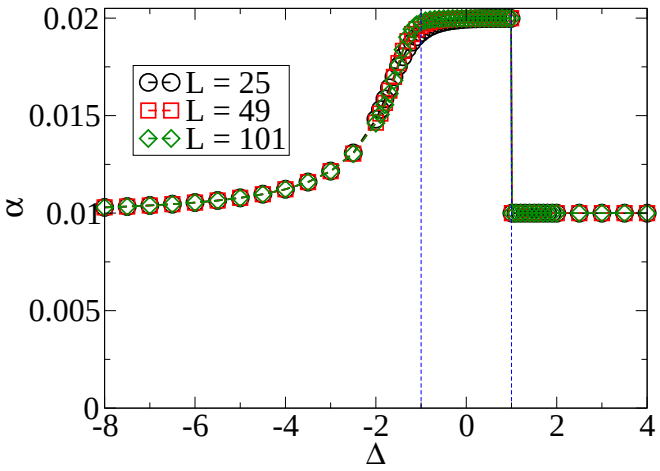

Figure 3.8: Heisenberg coupling case: scaling analysis of the decay parameter α as a function of Δ for different bath lattice sizes $L = 25$ (black), $L = 49$ (red), and $L = 101$ (green). Here the coupling constant between the system and bath is kept fixed, $\varepsilon^x = \varepsilon^y = \varepsilon^z = 0.2$.

form ultra-cold atomic gases. In such experiments, one can tune the strength of interactions of a quantum system using Feshbach resonances [90, 91]. This feature of ultra-cold atomic gases has motivated research into many nonequilibrium problems of quantum systems where the interactions are time-dependent. A particular example of these kinds of nonequilibrium phenomena is that of quantum quenches, in which the strength of interactions of the system is suddenly changed. Even though the system remains in a pure state, recent experimental and theoretical investigations of quantum quenches have revealed that the presence of a huge number of interacting degrees of freedom will lead, after a while, to a quasi-stationary state oscillating weakly around a well-defined time average. This behavior is strongly reminiscent of the typical behavior of a bath. Some examples include the collapse and revival of multiple matter wave interference patterns of a Bose-Einstein condensate [15] and a quantum Newton cradle implemented by arrays of trapped one-dimensional Bose gases [16]. A number of theoretical studies have examined the time-dependent correlation functions [92, 93, 94, 95, 96, 97, 98]. Although correlation functions often display quasi-stationary behavior after sufficiently long times, the underlying distribution does not, in general, correspond to a bath in thermal equilibrium. This opens up the possibility to systematically tune the behavior and to investigate new aspects of nonequilibrium physics. One can form qualitatively very different baths by carrying out different quenches: for situations in which the system is not too far from a thermalized state, we expect generic behavior like that of a qubit coupled to a thermal bath. For situations in which a strongly nonthermal quasi-stationary state is obtained, however, it is less

clear how decoherence will occur.

3.4.1 General expression and behaviors of the Loschmidt echo

For the purpose of preparing a quenched state, we first need to obtain a ground state of the bath Hamiltonian H_E using the static DMRG. Here we need to calculate the ground state of the one-dimensional XXZ model. By a sudden change of the strength of the interaction (quantum quench), we transform the bath Hamiltonian into a new one, which we will name H_Q. At time t, the state of the bath $|\psi_E(t)\rangle$ is given by $|\psi_E(t)\rangle = e^{-iH_Q t}|\psi_E(0)\rangle$, where $|\psi_E(0)\rangle$ is the ground state of the bath. After waiting for a time T_0, we couple the system (qubit) to the bath instantaneously. Only the case of the Ising coupling between the system and the bath is considered here. From now on, the complete system (S+E) will evolve with the new Hamiltonian

$$H_{SEQ} = H_S + H_Q + H_{int}. \tag{3.29}$$

As was discussed in Sec. 3.1.2, the Loschmidt echo is formally given by Eq. (3.13), here with the initial state $|\psi_E(T_0)\rangle$. Thus, the new expression for the Loschmidt echo reads

$$\begin{aligned} LE(t) &= \left|\langle\psi_E(T_0)|e^{-iH_{Q\uparrow}t}|\psi_E(T_0)\rangle\right|^2 \\ &= \left|\langle\psi_E(0)|e^{iH_Q T_0}e^{iH_{Q\downarrow}t}e^{-iH_{Q\uparrow}t}e^{-iH_Q T_0}|\psi_E(0)\right|^2, \end{aligned} \tag{3.30}$$

with the effective Hamiltonians $H_{Q\uparrow} = -\epsilon S^z_j + H_Q$, $H_{Q\downarrow} = \epsilon' S^z_j + H_Q$. For the sake of convenience and without loss of generality, we will set $\epsilon' = 0$ as in Eq. (3.15). Consequently, the Loschmidt echo can be rewritten as

$$LE(t) = \left|\langle\psi_E(0)|e^{iH_Q(T_0+t)}e^{-iH_{Q\uparrow}t}e^{-iH_Q T_0}|\psi_E(0)\rangle\right|^2. \tag{3.31}$$

In addition, it is useful to further evaluate the Loschmidt echo, Eq. (3.31), before we carry out the detailed analysis. Assume $|m\rangle$ and $|n\rangle$ are the eigenstates of H_Q with eigenvalues E_m,E_n, respectively, and $|q\rangle$ is the eigenstates of $H_{Q\uparrow}$ with eigenvalues E'_q. Insert the identities

$\sum_m |m\rangle\langle m| = \mathbf{1}$, $\sum_n |n\rangle\langle n| = \mathbf{1}$ and $\sum_p |q\rangle\langle q| = \mathbf{1}$ into the Eq. (3.31). It can be rewritten as

$$\begin{aligned} LE(t) &= \left| \sum_{mnq} \langle\psi_E(0)|m\rangle\langle m|e^{iE_m(T_0+t)}e^{-iE'_q t}|q\rangle\langle q|e^{-iE_n T_0}|n\rangle\langle n|\psi_E(0)\rangle \right|^2 \\ &= \left| \sum_{nq} \langle\psi_E(0)|n\rangle\langle n|e^{iE_n t}e^{-iE'_q t}|q\rangle\langle q|n\rangle\langle n|\psi_E(0)\rangle + \sum_{m\neq n,q} \langle\psi_E(0)|m\rangle\langle m|q\rangle\langle q|n\rangle\langle n|\psi_E(0)\rangle e^{i(E_m-E_n)T_0}e^{i(E_m-E'_q)t} \right|^2 \\ &= \left| \underbrace{\langle\psi_E(0)|e^{iH_Q t}e^{-iH_Q t}|\psi_E(0)\rangle}_{(a)} + \underbrace{\sum_{m\neq n,q} \langle\psi_E(0)|m\rangle\langle m|q\rangle\langle q|n\rangle\langle n|\psi_E(0)\rangle e^{i(E_m-E'_q)t}(e^{i(E_m-E_n)T_0}-1)}_{(b)} \right|^2, \end{aligned} \tag{3.32}$$

The first term (a) in Eq. (3.32) is the Loschmidt echo for the waiting time $T_0 = 0$. Notice that, in general, $\langle m|q\rangle\langle q|n\rangle$ is a very small quantity if $m \neq n$, and $e^{i(E_m-E_n)T_0} - 1$ is also a small quantity relative to 1. Therefore, the second term (b) has only a small contribution for time t large enough when the Loschmidt echo is much less than 1. This means that for different T_0, the Loschmidt echo should always behave similarly to the Loschmidt echo for $T_0 = 0$ for a long time t. However, the second term (b) is not negligible at short times t, when the Loschmidt echo is only slightly less than 1. In particular, small differences in the Loschmidt echo at short times may lead to a large differences in the short-time decay parameters α.

In addition, for $H_Q = \pm\infty$, the effects of the local perturbation term $-\epsilon S^z_j$ can be omitted; thus no decoherence will occur. For $H_Q \approx H_S$, H_Q is very closed to H_S, the dynamics of the Loschmidt echo is similar to the case of no quench, i.e. $H_S = H_Q$. Without specific mention, we will not consider such cases of quenches below.

3.4.2 The transverse-field Ising chain after a quantum quench

For a simple understanding of this problem, we will first study the decoherence induced by quenched states of the transverse-field Ising bath, which can be exactly evaluated.

The transverse-field Ising model is

$$H_E = -J \sum_{j=1}^{L} (\sigma^x_j \sigma^x_{j+1} + \lambda\sigma^z_j), \tag{3.33}$$

where the σ's are the Pauli matrices, J is the coupling strength between nearest-neighbor

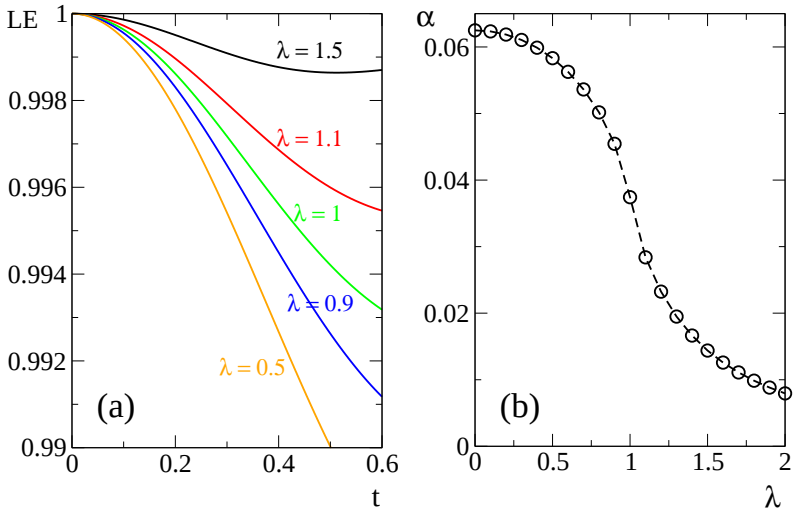

Figure 3.9: Short-time behavior of the Loschmidt echo LE for a ground-state transverse-field Ising bath (the same results as FIG.3 in Ref. [77]) with the lattice size $L = 300$ and PBCs. (a) The Loschmidt echo at short times for different values of λ, where a Gaussian decay $LE \approx e^{-\alpha t^2}$ is visible for time $t \lesssim 0.4$ for all the different values of λ. (b) The Gaussian decay parameter $\alpha(\lambda)$ as a function of λ ($0 \leq \lambda \leq 2$).

spins, and λ is a magnetic field which will drive H across the quantum phase transition. The ground state of the transverse-field Ising chain has one critical point $\lambda_c = 1$ for $\lambda > 0$. For $0 \leq \lambda < 1$, it belongs to a long-range ordered ferromagnetic phase with a broken Z_2 symmetry, i.e., the state spanned by $|\rightarrow\rightarrow\cdots\rightarrow\rangle$ and $|\leftarrow\leftarrow\cdots\leftarrow\rangle$. For $\lambda > 1$, it is in a paramagnetic phase with the state $|\uparrow\uparrow\ldots\uparrow\rangle$. We set $J = 1$ and $\epsilon = 0.5$ in the following discussion (the same parameters as Fig.3 in Ref. [77]). In Fig. 3.9, the short-time behavior of the Loschmidt echo when the initial state of the transverse-field Ising bath is a ground state is shown [77]. The Gaussian decay is fit to data for times $t \lesssim 0.1$. As can be seen in Fig. 3.9 (a), the $\lambda = 1.5$ curve is obviously not Gaussian for time $t \gtrsim 0.2$. The curve for α decays continually from ~ 0.06 to 0.01 as λ varies from 0 to 2. The calculations for this section are carried out with a bath with lattice size $L = 300$ and PBCs. For such a large lattice, the OBCs and the odd size of the lattice, e.g., $L = 301$, do not affect the results of the short-time behavior of the Loschmidt echo shown here either for OBCs or PBCs.

Ferromagnetic phase initial state

We begin our discussion of the results by considering quenches that start from a ferromagnetic ground state, i.e., $H(\lambda_0)$ with $\lambda_0 = 0.5$. In Fig. 3.10, we display the long-time behavior

of the Loschmidt echo after various quench schemes $\lambda_Q = 0.9, 1, 1.5, 2,$ and 20 and for different waiting times, $T_0 = 0, 10, 100$. The quenched Hamiltonians $H(\lambda_Q)$ is taken to be in the ferromagnetic phase ($\lambda_Q = 0.9$), at the quantum critical point ($\lambda_Q = 1$), and in the paramagnetic phase ($\lambda_Q = 1.5, 2, 20$). For completeness we also display quenches in the ferromagnetic phase ($\lambda_0 = 0.9$, $\lambda_Q = 0.5$). For all the different quenches that start from a ferromagnetic ground state, complete decoherence takes place, and the Loschmidt echo decays to 0 after a long enough time for a variety of waiting times, even including $T_0 = 0$. This is completely different from the situation when the bath is a transverse-field Ising chain in its ground state, where the Loschmidt echo decays to 0 only at the critical point [99], while it decays to a finite value in other phases [77, 99]. In the ground-state case, the bath has a single low-energy mode, whereas it simultaneously has low-energy and high-energy modes in the quenched cases, which induce complete decoherence. Notice that when the quench is very small, i.e., $\lambda_0 = 0.5$ and $\lambda_Q = 0.501$, only the lowest energy modes are present. In this case, the Loschmidt echo should be similar to the case of no quench, i.e., $\lambda_0 = \lambda_Q = 0.5$. We find that the quench determines the decoherence behavior and the decoherence time. In Figs. 3.10 (a) and (b), revivals of the Loschmidt echo can be observed. The revival time depends on the lattice size of the bath, see Appendix C. Otherwise, revivals are not visible for quenches with $\lambda_Q > 1$, as can be seen in Figs. 3.10 (c), (d), (e) and (f). For λ_Q far away from λ_0, the decoherence time becomes shorter, see Figs. 3.10 (b), (c), and (d). The length of the waiting time T_0 does not have a large effect on the long-time behavior of the Loschmidt echo, i.e., when it approaches 0. This coincides with our discussion of Eq. (3.32). However, the waiting time T_0 affects the short-time dynamics of the Loschmidt echo.

As in the case of a ground-state bath, the short-time dynamics of the Loschmidt echo are Gaussian. The decay parameter $\alpha(T_0)$ is shown in Fig. 3.11 as a function of T_0. We notice that $\alpha(T_0 = 0)$ has only a very small deviation from $\alpha(\lambda_0)$, for the ground state bath. This is because the short-time behavior of the Loschmidt echo is not seriously affected by the quench dynamics if we quench the bath and connect the system to the bath simultaneously. There is a significant effect only after the bath has evolved by itself for some time $T_0 > 0$, as can been seen in Fig. 3.11. The strong oscillations of $\alpha(T_0)$ for $T_0 \gtrsim 70$ are due to finite-size effects. Similarly to correlation functions that oscillate weakly around a time average for a times sufficiently long after a quench [94, 95, 98], $\alpha(T_0)$ also weakly oscillates around an average value $\bar{\alpha}$ for $T_0 \gtrsim 10$ after strongly oscillating between the values $\alpha(\lambda_0)$ and $\alpha(\lambda_Q)$, for the ground state bath.

In Fig. 3.12, we plot the time-averaged decay parameter $\bar{\alpha}$ as a function of λ_Q for a fixed

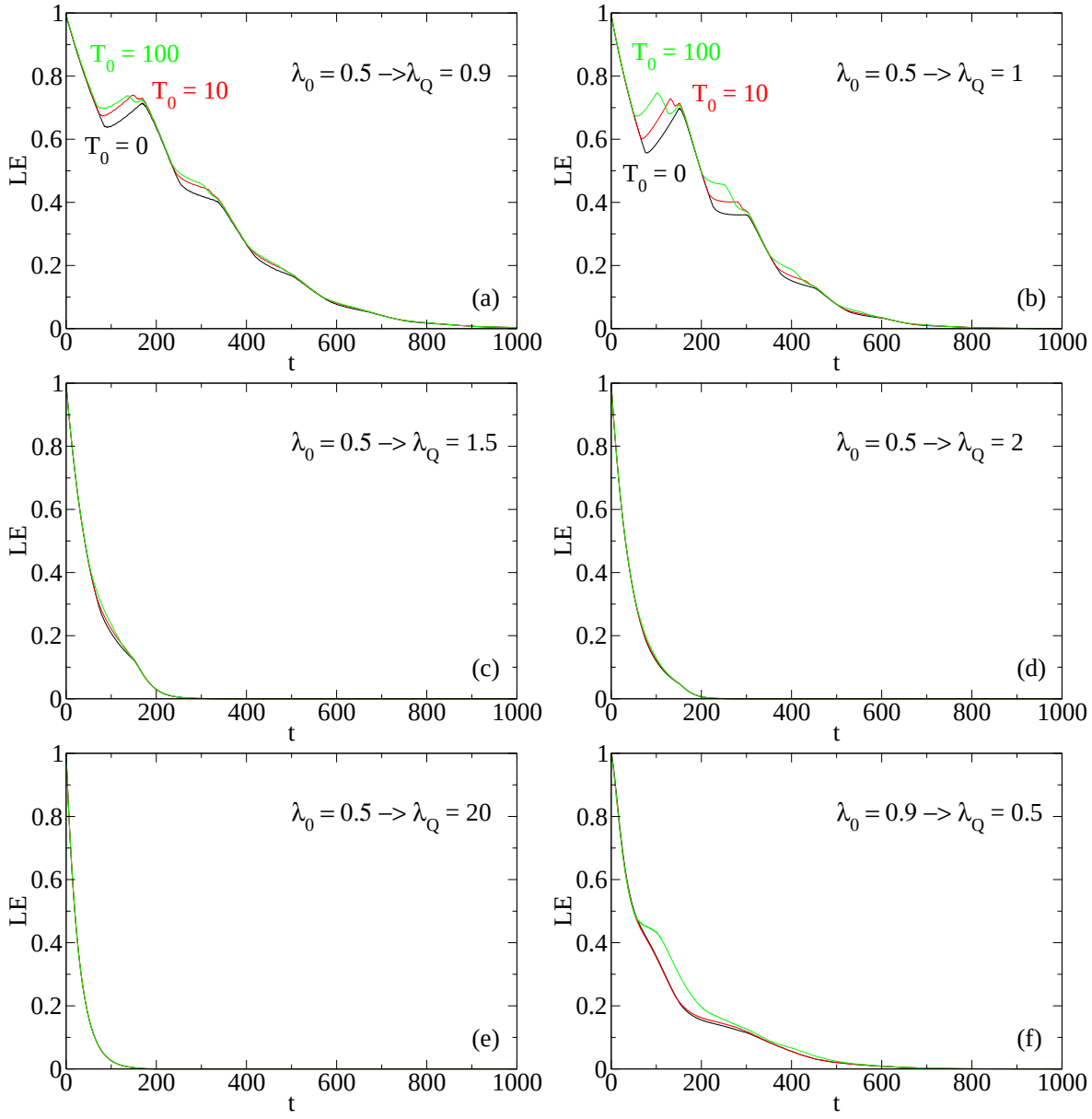

Figure 3.10: Loschmidt echo of a qubit coupled to a transverse-field Ising chain for various quantum quenches from a ferromagnetic ground state and for different waiting times $T_0 = 0$ (black), $T_0 = 10$ (black), $T_0 = 100$ (green). The lattice size of the bath is $L = 300$. The quench parameters are (a) $\lambda_0 = 0.5$, $\lambda_Q = 0.9$; (b) $\lambda_0 = 0.5$, $\lambda_Q = 1$; (c) $\lambda_0 = 0.5$, $\lambda_Q = 1.5$; (d) $\lambda_0 = 0.5$, $\lambda_Q = 2$; (e) $\lambda_0 = 0.5$, $\lambda_Q = 20$; and (f) $\lambda_0 = 0.9$, $\lambda_Q = 0.5$.

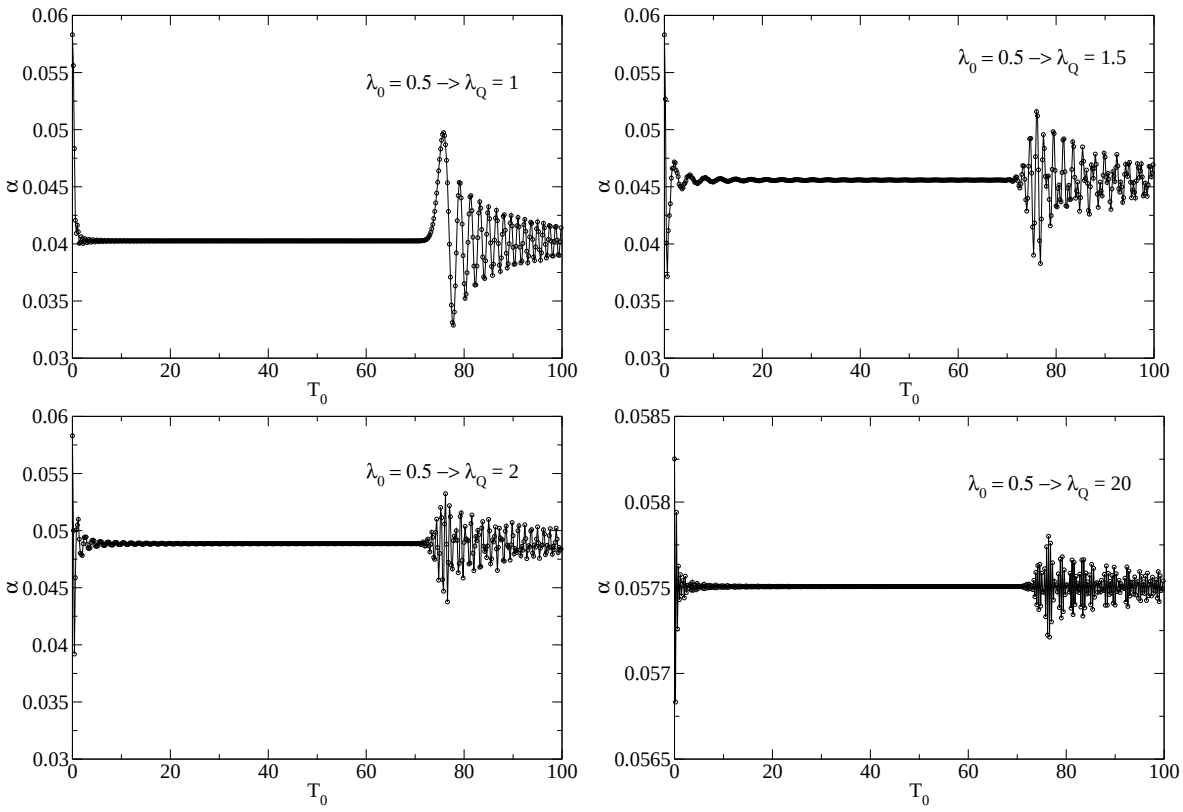

Figure 3.11: Decay parameter α of the Loschmidt echo when coupling a qubit to a transverse-field Ising chain after a quantum quench starting from a ferromagnetic ground state as a function of the waiting time T_0. The lattice size of the bath is $L = 300$ under PBCs. The strong oscillations for $T_0 \gtrsim 70$ are due to finite-size effects.

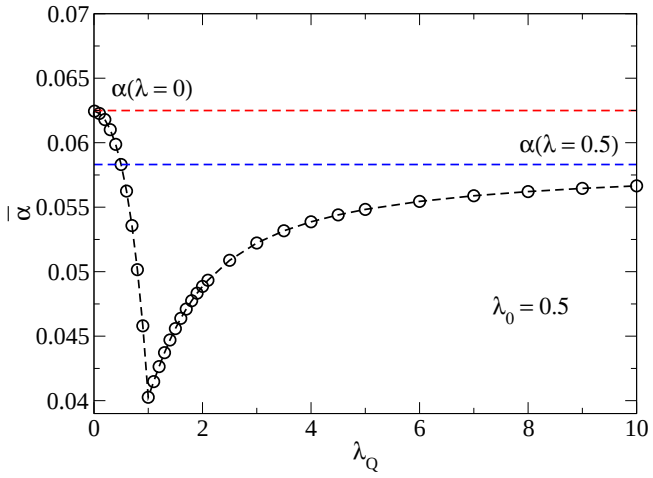

Figure 3.12: The time-averaged decay parameter $\bar{\alpha}$ for the quench starting from ferromagnetic ground state ($\lambda_0 = 0.5$). Red dashed line: $\alpha(\lambda = 0)$, the maximum value for the ground state bath. Blue dashed line: $\alpha(\lambda = 0.5)$ for the bath without any quench.

initial bath state with $H(\lambda_0 = 0.5)$ quenched to various $H(\lambda_Q)$. The time-averaged $\bar{\alpha}$ is obtained by averaging of all the values of α between $T_0 = 20$ and $T_0 = 60$. The curve of $\bar{\alpha}$ is continuous everywhere in the plot. However, its first derivative is discontinuous at the critical point $\lambda_Q = 1$. The average exponent $\bar{\alpha}$ is close to $\alpha(\lambda_Q)$ for $\lambda_Q \in (0, 1]$ and tends to $\alpha(\lambda_0)$ for $\lambda_Q > 1$. When the bath is quenched deeply into the paramagnetic phase ($\lambda_Q \approx 10$) from the ferromagnetic phase ($\lambda_0 = 0.5$), the time-averaged decay parameter $\bar{\alpha}$ is very close to the constant value $\alpha(\lambda = 0.5)$ (blue dashed line in Fig. 3.12), which is the decay parameter for the case when the ground state is the initial state of the bath. This is because when the time t is small enough and λ_Q is large enough, $e^{-i(H_Q - \epsilon S_j^z)t} \approx e^{-iH_Q t} e^{\epsilon S_j^z t}$. Thus Eq. (3.31) can be simplified to

$$LE(t \sim 0) \approx |\langle \psi_E(0)| e^{-\epsilon S_j^z t} |\psi_E(0)\rangle|^2. \tag{3.34}$$

Obviously, Eq. (3.34) is suitable for evaluating the short-time behavior of the Loschmidt echo for the case of the ground state as the initial state of the bath. In addition, for $\lambda_Q = \infty$, the effects of the local perturbation term ϵS_j^z can be omitted; thus, no decoherence will occur. Note that the time-averaged decay parameter $\bar{\alpha}$ does not depend on the lattice size; here the bath lattice size $L = 300$ is large enough for obtaining a quasi-stationary state for $T_0 \lesssim 70$.

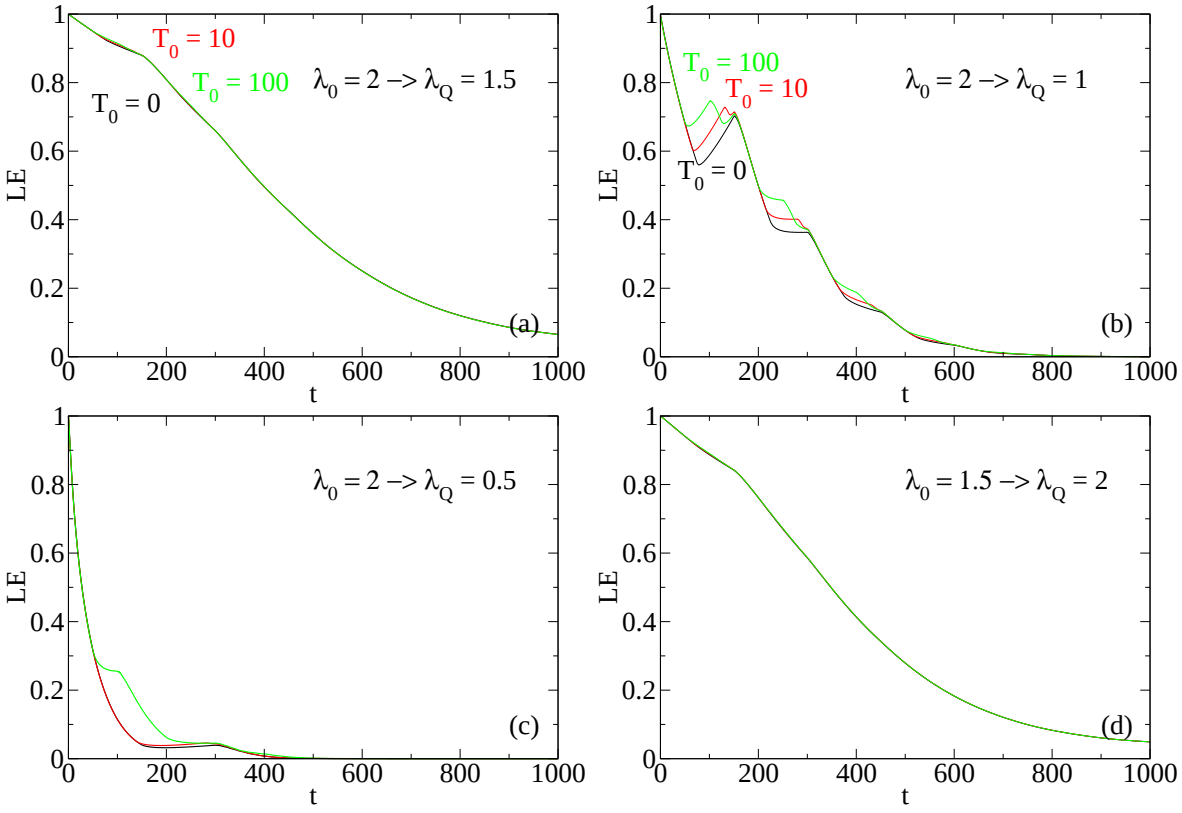

Figure 3.13: Loschmidt echo of a qubit coupled to a transverse-field Ising chain for quantum quenches from a paramagnetic ground state and for waiting times $T_0 = 0$ (black), $T_0 = 10$ (black), and $T_0 = 100$ (green). The lattice size of the bath is $L = 300$. The quench parameters are (a) $\lambda_0 = 2$, $\lambda_Q = 1.5$; (b) $\lambda_0 = 2$, $\lambda_Q = 1$; (c) $\lambda_0 = 2$, $\lambda_Q = 0.5$; and (d) $\lambda_0 = 1.5$, $\lambda_Q = 2$.

Paramagnetic phase initial state

In Fig. 3.13, we show the long-time behavior of the Loschmidt echo for quenches that start from a paramagnetic ground state, i.e., $H(\lambda_0)$ with $\lambda_0 = 2$, with the quench parameters $\lambda_Q = 0.5, 1, 1.5, 2,$ and 20 for different waiting times $T_0 = 0, 10, 100$. Hamiltonian $H(\lambda_Q)$ is taken to be in the ferromagnetic phase ($\lambda_Q = 0.5$), at the quantum critical point ($\lambda_Q = 1$) and in the paramagnetic phase ($\lambda_Q = 1.5$). For completeness, we also show a quench in the paramagnetic phase ($\lambda_0 = 1.5$, $\lambda_Q = 2$). For most of quenches that start from a paramagnetic ground state, complete decoherence is obtained as in the quenches starting from ferromagnetic phase. The Loschmidt echo decays to 0 for a long enough times for all waiting times shown. In these cases, the quenched states contain low-energy as well as high-energy modes. However, if the quench occurs deep in the paramagnetic phase, see Fig. 3.14, the Loschmidt echo retains a finite value of around 0.99 and does not decay to 0. The reason is that a quench deep in

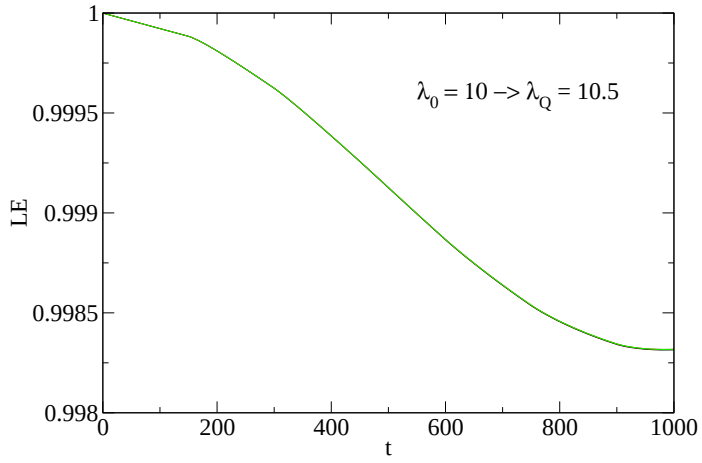

Figure 3.14: Loschmidt echo of a qubit coupled to a transverse-field Ising chain for the quantum quench deep in paramagnetic phase, $\lambda_0 = 10.5$, $\lambda_Q = 10$, and for different waiting times $T_0 = 0$ (black), $T_0 = 10$ (black), $T_0 = 100$ (green). The Loschmidt echo retains a small deviation from 1. Complete decoherence does not occur in this case. The results for different T_0 almost overlap. The lattice size of the bath is $L = 300$.

the paramagnetic phase only contains the lowest energy modes of the states, i.e., $|\uparrow\uparrow \ldots \uparrow\rangle$. Notice that when the quench is small enough, i.e., $\lambda_0 = 2$ and $\lambda_Q = 2.001$, only the lowest energy modes are present. In this case, the Loschmidt echo dynamics should be similar to the case of no quench, i.e., $\lambda_0 = \lambda_Q = 2$. In the figure, the quench still determines the decoherence time. A larger quench leads to a shorter decoherence time, see Fig. 3.14 (a), (b), and (c). The waiting time T_0 does not have a large effect on the long-time behavior of the Loschmidt echo when it approaches 0.

In Fig. 3.15, the Gaussian decay parameter α is plotted as a function of the waiting time T_0. The deviation of $\alpha(T_0 = 0)$ from $\alpha(\lambda_0)$ is negligible, as before. The strong oscillations of $\alpha(T_0)$ for $T_0 \gtrsim 70$ are due to finite-size effects, as before. For long enough times, $\alpha(T_0)$ also weakly oscillates around an average value $\bar{\alpha}$ for $T_0 \gtrsim 20$ after a strong oscillations for $T_0 \lesssim 20$. The behavior for these cases is similar to that for the case of the ferromagnetic initial state.

We plot the time-averaged decay parameter $\bar{\alpha}$ as a function of λ_Q in Fig. 3.16 for a fixed initial bath state with $H(\lambda_0 = 2)$ quenched to various $H(\lambda_Q)$. The time-averaged $\bar{\alpha}$ is obtained by averaging of all the values of α between $T_0 = 20$ and $T_0 = 60$, as before. The curve of $\bar{\alpha}$ is continuous and the first derivative of $\bar{\alpha}$ is discontinuous at the critical point $\lambda_Q = 1$. $\bar{\alpha}$ tends to $\alpha(\lambda_Q)$ for $\lambda_Q \in (0, 2]$ and $\alpha(\lambda_0)$ for $\lambda_Q > 1$. In the figure, the value of $\bar{\alpha}$ is very close to the constant value $\alpha(\lambda = 2)$ (blue dashed line in Fig. 3.16) when $\lambda_Q \approx 10$. The reason is given

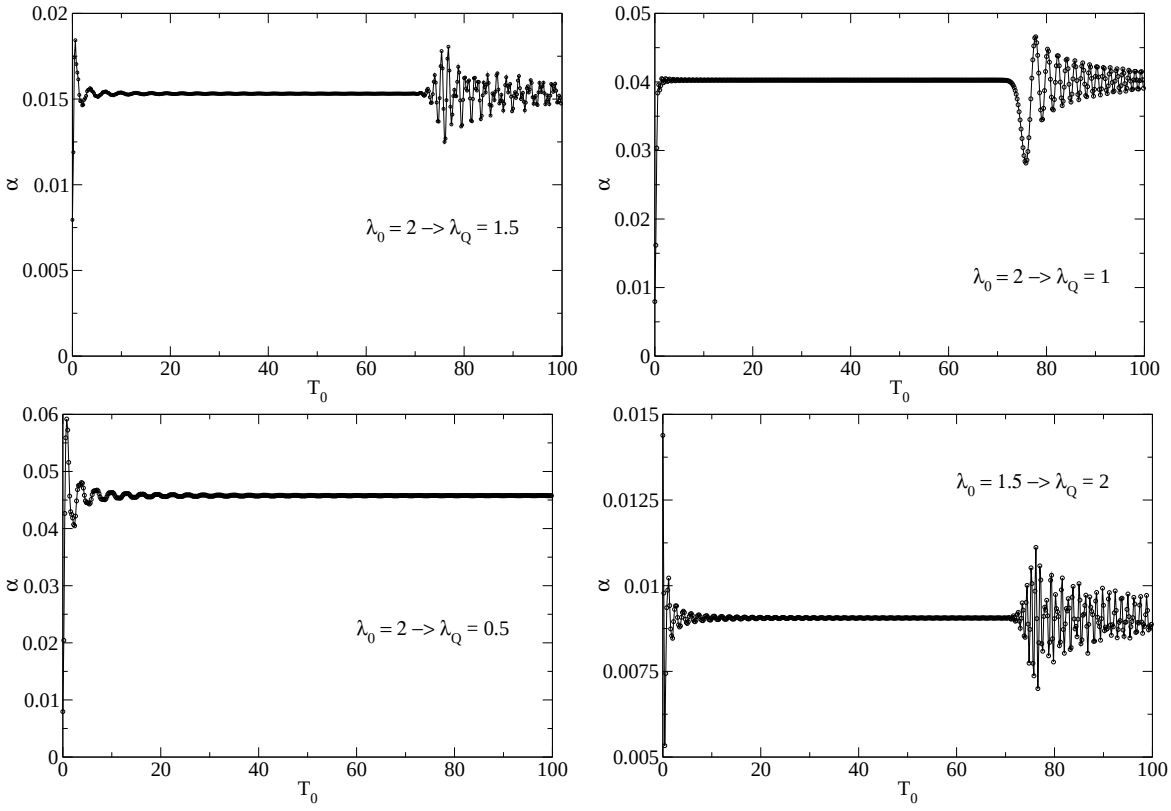

Figure 3.15: Decay parameter α of the Loschmidt echo when coupling a qubit to a transverse-field Ising chain after a quantum quench starting from a paramagnetic ground state the as a function of the waiting time T_0. The lattice size of the bath is $L = 300$. The strong oscillations for $T_0 \gtrsim 70$ are due to finite size effects.

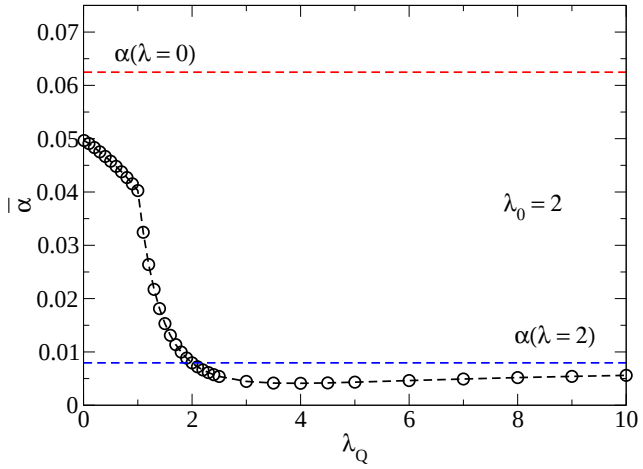

Figure 3.16: Time-averaged decay parameter $\bar{\alpha}$ for quenches starting from a paramagnetic ground state ($\lambda_0 = 2$). Red dashed line: $\alpha(\lambda = 0)$, the maximum value for the ground state bath. Blue dashed line: $\alpha(\lambda = 2)$, the bath without any quench.

by Eq. (3.34), as discussed before. In addition, for $\lambda_Q = \infty$, no decoherence will occur, as before.

Initial state at the critical point

In Fig. 3.17, we depict quenches that start from the critical point ($\lambda_0 = 1$), i.e., the long-time behavior of the Loschmidt echo after the quenches to $\lambda_Q = 0.5, 0.9, 1.1,$ and 2 for different waiting times $T_0 = 0, 10,$ and 100. The Hamiltonians $H(\lambda_Q)$ are within the ferromagnetic phase ($\lambda_Q = 0.5$and 0.9), and the paramagnetic phase ($\lambda_Q = 1.1$and 2). In the figure, as for the cases described before, the Loschmidt echo for different quenches all decay to 0, when low-energy and the high-energy modes are present. The larger quenches still have a shorter decoherence time, compare Fig. 3.17 (a) with Fig. 3.17 (b), and Fig. 3.17 (c) with Fig. 3.17 (d). Notice that even when the quench is very small here, i.e., $\lambda_0 = 1$ and $\lambda_Q = 1.001$, the populated low-energy modes still lead to complete decoherence.

In Fig. 3.18, we plot the Gaussian decay parameter $\alpha(T_0)$ as a function of the waiting time T_0. The deviation of $\alpha(T_0 = 0)$ from $\alpha(\lambda_0)$ in these cases is negligible, as before. The strong oscillations of $\alpha(T_0)$ for $T_0 \gtrsim 70$, see Fig. 3.17 (d), are due to finite-size effects, as before. For long enough times, $\alpha(T_0)$ weakly oscillates around a time-averaged value $\bar{\alpha}$ for $T_0 \gtrsim 35$ after a strong oscillation for $T_0 \lesssim 35$. The phenomena for these cases are similar to those for a ferromagnetic initial state bath and for a paramagnetic initial state bath. Thus, we will omit the detailed discussion of the time-averaged $\bar{\alpha}$ here.

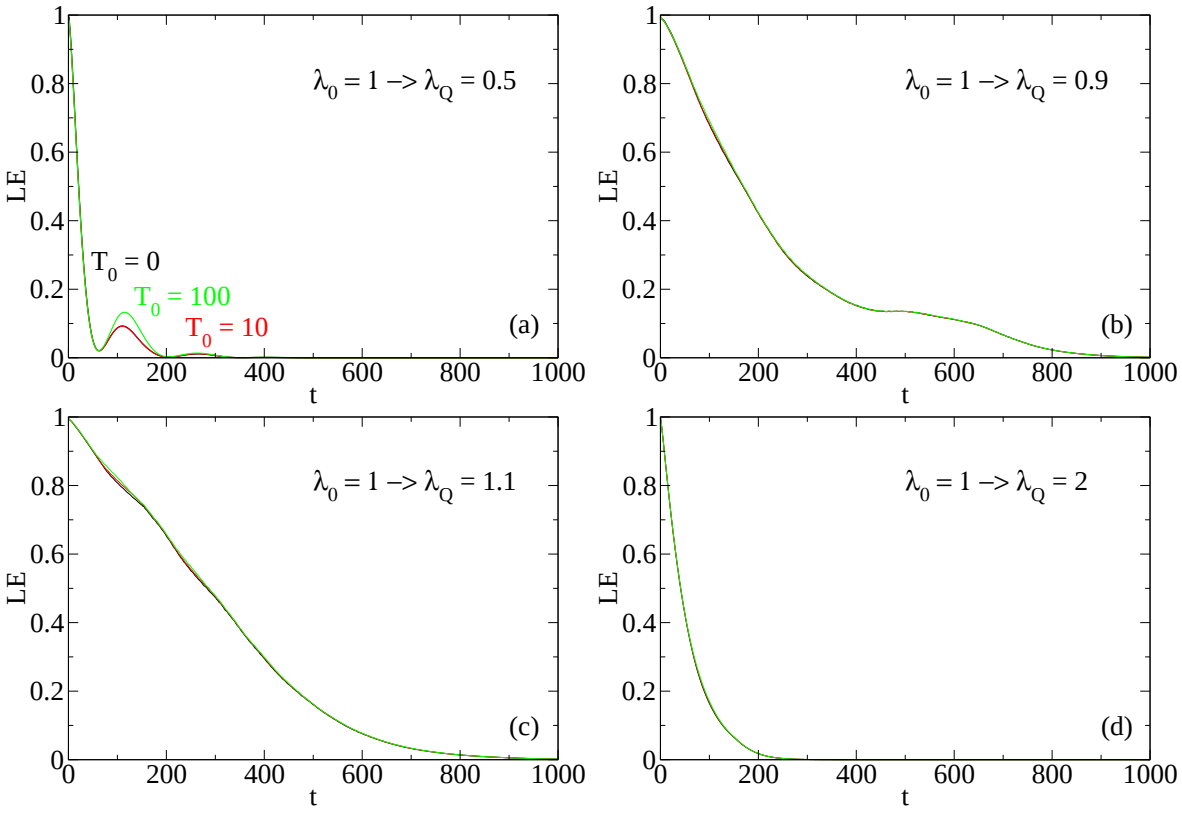

Figure 3.17: Loschmidt echo of a qubit coupled to a transverse-field Ising chain for various quantum quenches from the critical point, and for different waiting times $T_0 = 0$ (black), $T_0 = 10$ (black), and $T_0 = 100$ (green). The lattice size of the bath is $L = 300$. The quench parameters are (a) $\lambda_0 = 1$, $\lambda_Q = 0.5$; (b) $\lambda_0 = 1$, $\lambda_Q = 0.9$; (c) $\lambda_0 = 1$, $\lambda_Q = 1.1$; and (d) $\lambda_0 = 1$, $\lambda_Q = 2$.

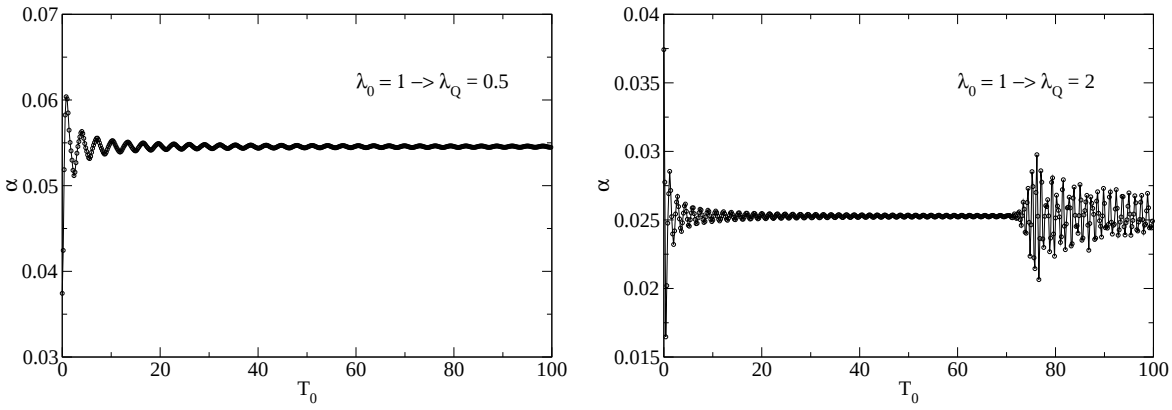

Figure 3.18: Decay parameter α of the Loschmidt echo when coupling a qubit to a transverse-field Ising chain after a quantum quench starting from the critical point ($\lambda_0 = 1$) as a function of the waiting time T_0. The lattice size of the bath is $L = 300$ under PBCs. The strong oscillations for $T_0 \gtrsim 70$ are due to finite-size effects.

In conclusion, complete decoherence occurs in almost all of the various quench scenarios for a transverse-field Ising bath, except when the quench takes place deep in the paramagnetic phase, i.e., when the lowest-energy modes are dominant. The presence of the high-energy modes is crucial for the occurrence of complete decoherence. In addition, for quenches starting from the critical point ($\lambda_0 = 1$), though the lowest-energy modes are dominant, complete decoherence nonetheless occurs. Similar considerations will be important in Sec. 3.4.3. The dynamics of the decoherence is related to the details of the quench. A shorter decoherence time corresponds to a larger quench. For the short-time dynamics of the Loschmidt echo, the Gaussian decay parameter α as a function of the waiting time T_0 will weakly oscillate around a well-defined time-averaged value $\bar{\alpha}$ after a sufficient long T_0 when the bath has evolved to a quasi-stationary state. The time-averaged decay parameter $\bar{\alpha}$ is close to $\alpha(\lambda_Q)$ for $\lambda_Q \in (0, \lambda_0]$ and tends to $\alpha(\lambda_0)$ for $\lambda_Q > 1$. When λ_Q is deep in the paramagnetic phase, $\bar{\alpha}$ will be very close to $\alpha(\lambda_0)$. For $\lambda_Q = \infty$, no decoherence occurs.

3.4.3 XXZ chain after a quantum quench

We now turn to the decoherence induced by quenched states of a more complex bath, the XXZ chain, see Eq. (3.27). We set $J = 1$ and $\epsilon = 0.2$, as in Sec. 3.3.1, in the following discussion. The calculations for this section are based on a bath with lattice size $L = 49$ and OBCs using the adaptive t-DMRG. The calculations are carried out with $\Delta t = 0.001$ in the time evolution, with discarded weight below 10^{-13}, a typical minimum truncated Hilbert space dimension of

$D = 100$, and a typical maximum truncated Hilbert space dimension of $D = 5000$. For lattice size $L \leq 17$, we use Lanczos exact diagonalization with OBCs. In order to minimize the boundary effects, we consider only the case in which the system is coupled to a spin in the middle of the chain, i.e., $j = 25$ for $L = 49$.

Long-time behavior of the Loschmidt echo

We begin the discussion of the results of the long-time behavior of the Loschmidt echo by considering the quenches that start from the antiferromagnetic phase, i.e., with the Hamiltonian $H(\Delta_0 = -5)$. In Fig. 3.19, we display the long-time behavior of the Loschmidt echo as a function of time t after quenches to $\Delta_Q = 0, -1, -1.8, 5, -2.5$ and -10 for different waiting times T_0. The quenched Hamiltonians $H(\Delta_Q)$ are taken to be in the antiferromagnetic phase ($\Delta_Q = -1.8, -2.5$ and -10), in the critical region ($\Delta_Q = 0$), at the critical point ($\Delta_Q = -1$), and in the ferromagnetic phase ($\Delta_Q = 5$). In the figure, the typical behavior of the Loschmidt echo is a smooth decay. The Loschmidt echo decreases with T_0 in all cases. For the quenches that target the critical region or the critical point ($\Delta_Q = -1$), the Loschmidt echo decays almost linearly for long times ($t \approx 1 \sim 4$) after following a Gaussian decay at short times ($t \lesssim 1$), see Fig. 3.19 (a) and (b). For quenches that target the antiferromagnetic phase and the ferromagnetic phase, the decay has a Gaussian form to at least time $t \approx 4$, see Fig. 3.19 (c), (d), (e) and (f).

We now shift our attention to quenches that start from the critical region, i.e., with the Hamiltonian $H(\Delta_0 = -0.5)$, $H(\Delta_0 = -0.25)$, $H(\Delta_0 = 0)$ and $H(\Delta_0 = 0.5)$. In Fig. 3.20, we display the results of the long-time behavior of the Loschmidt echo as a function of time t after various quenches for different waiting times T_0. The quenched Hamiltonians $H(\Delta_Q)$ is taken to be in the antiferromagnetic phase ($\Delta_Q = -5$ and -20), in the critical region ($\Delta_Q = 0.5$), at the critical point ($\Delta_Q = -1$), and in the ferromagnetic phase ($\Delta_Q = 3$). In the figure, the typical behavior of the Loschmidt echo is a smooth decay, as before. For all the quenches, the dependence of the Loschmidt echo on T_0 is small compared to the cases of quenches that start from an antiferromagnetic phase, as before. In Fig. 3.20 (a) and (b), for quenches that target the antiferromagnetic phase, similar to Fig. 3.19 (a) and (b), the Loschmidt echo decays linearly for long times ($t \approx 1 \sim 4$) after following a Gaussian decay at short times ($t \lesssim 1$). In Fig. 3.20 (d), a quench target the ferromagnetic phase, the Loschmidt echo undergoes a Gaussian decay for ($t = 0 \sim 2.5$). In Fig. 3.20 (c) and (e), for quenches that target the critical region or the critical point ($\Delta_Q = -1$), the Loschmidt echo undergoes a Gaussian decay at short-times ($t \lesssim 0.5$) and decays with slow oscillations for at long times ($t \lesssim 0.5 \sim 4$).

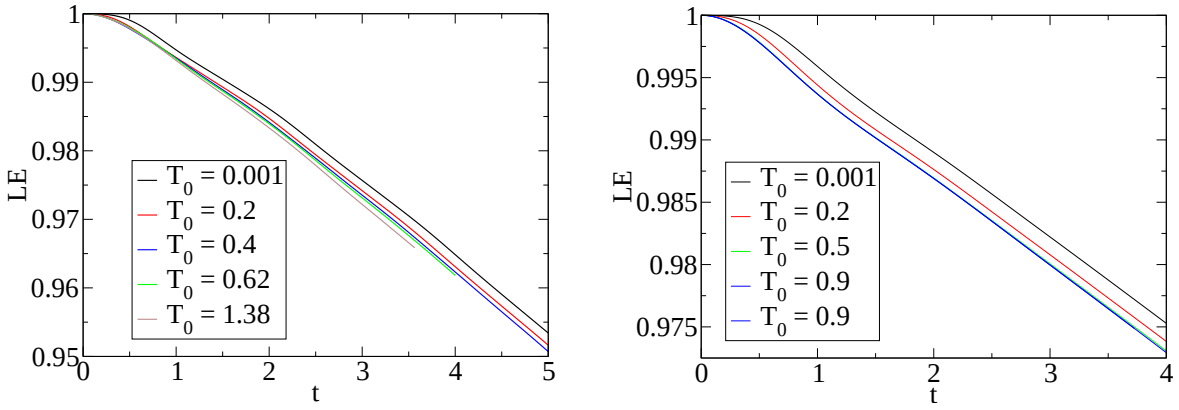

(a) $\Delta_0 = -5, \Delta_Q = 0$

(b) $\Delta_0 = -5, \Delta_Q = -1$

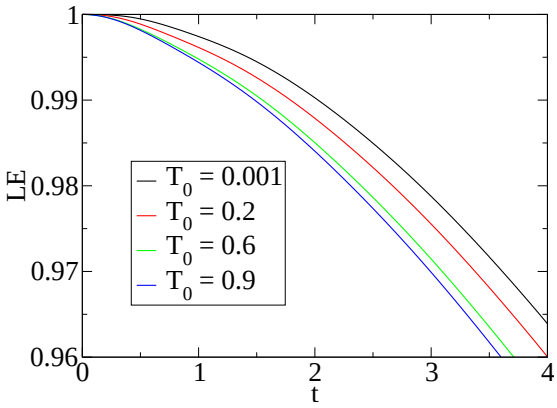

(c) $\Delta_0 = -5, \Delta_Q = -1.8$

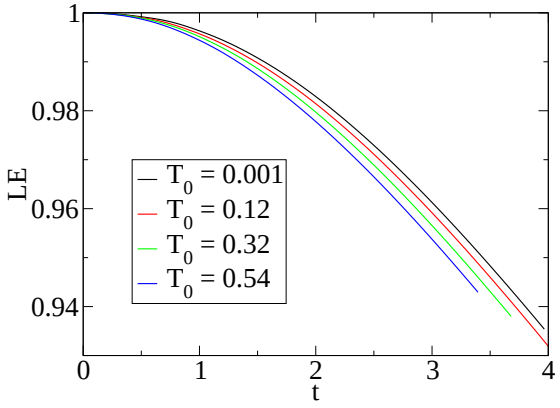

(d) $\Delta_0 = -5, \Delta_Q = 5$

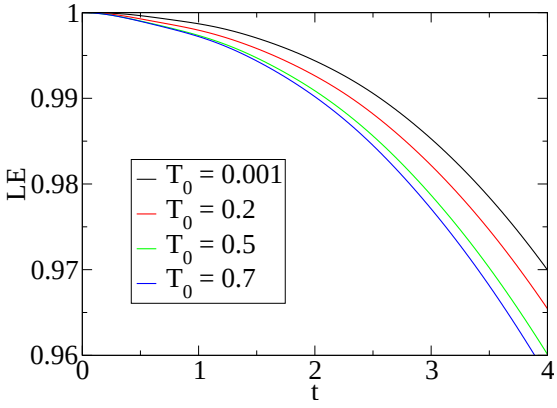

(e) $\Delta_0 = -5, \Delta_Q = -2.5$

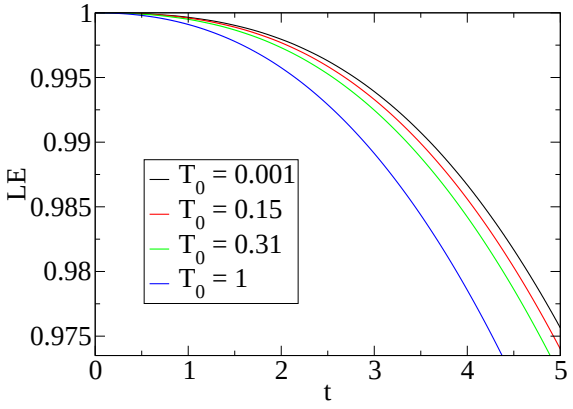

(f) $\Delta_0 = -5, \Delta_Q = -10$

Figure 3.19: Loschmidt echo for a qubit coupled to an XXZ chain for various quantum quenches starting from an antiferromagnetic ground state and for different waiting times T_0. The lattice size of the bath is $L = 49$.

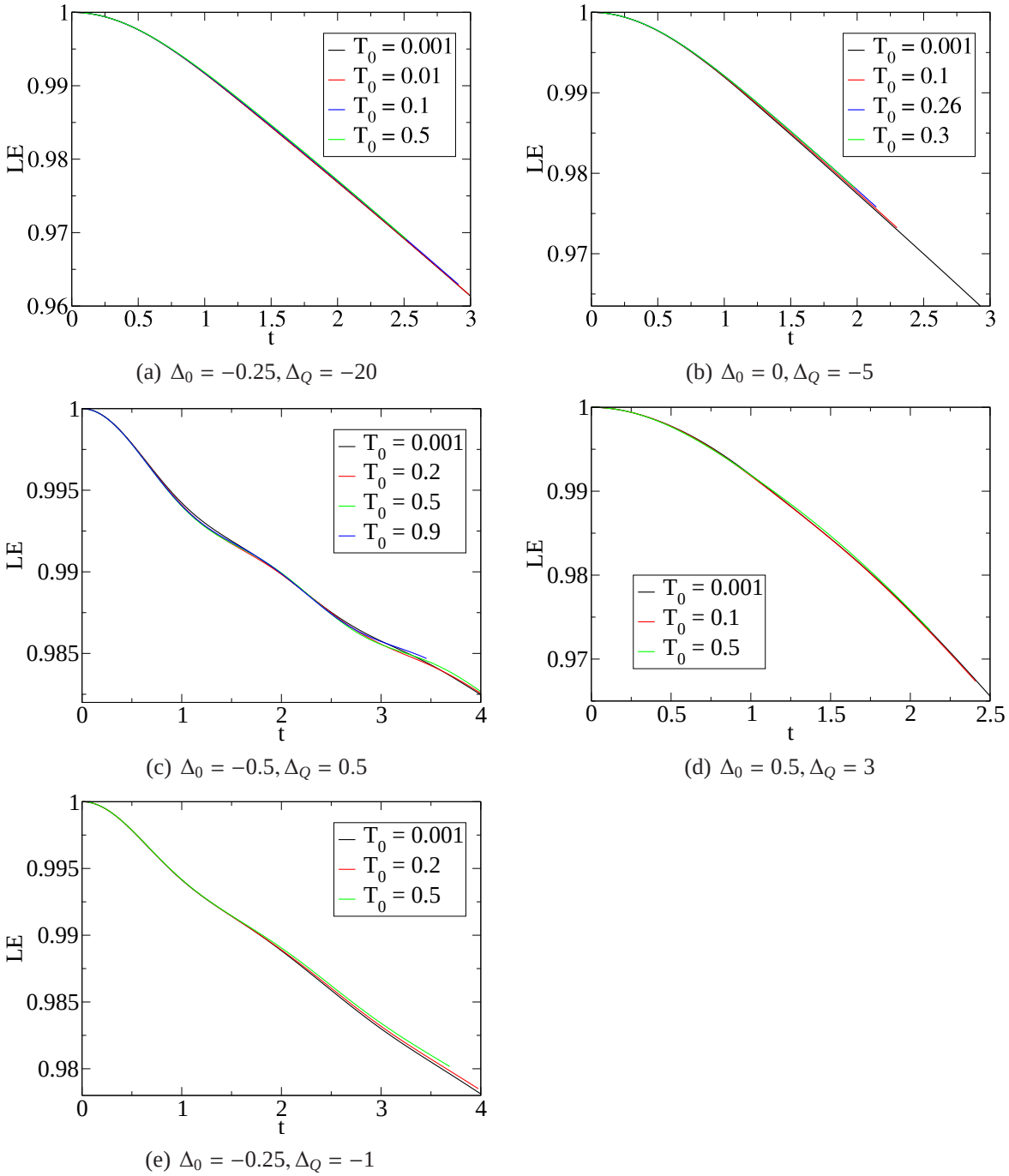

(a) $\Delta_0 = -0.25, \Delta_Q = -20$

(b) $\Delta_0 = 0, \Delta_Q = -5$

(c) $\Delta_0 = -0.5, \Delta_Q = 0.5$

(d) $\Delta_0 = 0.5, \Delta_Q = 3$

(e) $\Delta_0 = -0.25, \Delta_Q = -1$

Figure 3.20: Loschmidt echo for a qubit coupled to an XXZ chain after the indicated quantum quenches starting from the critical region and for different waiting times T_0. The lattice size of the bath is $L = 49$.

As before, it is interesting to calculate the dynamics of the Loschmidt echo for a longer time in order to determine the final value of the Loschmidt echo. However, because of the fast-growing number of states needed in the DMRG calculations, it is difficult to calculate the dynamics of the Loschmidt echo for times longer than $t \approx 5$. In general, for the bath with lattice size $L = 49$, at least 5000 states are necessary to obtain a reasonable result with a discarded weight below 10^{-13}. It is only possible to evaluate the long-time behavior of the Loschmidt echo using ED, which can only treat a small bath. In Fig. 3.21, We display the long-time behavior of the Loschmidt echo for a bath with lattice size $L = 15$ and OBCs as a function of time t after various quenches that start from the antiferromagnetic phase, i.e., with the Hamiltonian $H(\Delta_0 = -5)$, for the waiting times $T_0 = 0, 5,$ and 10. The different quenches target $\Delta_Q = -10, -2.5, -1.8, -1, 0, 1, 5,$ and 50. The quenched Hamiltonian $H(\Delta_Q)$ is taken to be in the antiferromagnetic phase ($\Delta_Q = -10, -2.5,$ and -1.8), at the critical points ($\Delta_Q = -1$ and 1), in the critical region ($\Delta_Q = 0$), and in the ferromagnetic phase ($\Delta_Q = 5$ and 50). The Loschmidt echo oscillates around a finite value, ≈ 0.9 in Fig. 3.21 (a) for $\Delta_Q = -10$, ≈ 0.6 in Fig. 3.21 (b) for $\Delta_Q = -2.5$, and ≈ 0.6 in Fig. 3.21 (h) for $\Delta_Q = 50$. These oscillations are due to the small lattice size. In contrast to these three cases, the Loschmidt echo tends to 0 after a long enough time $t \approx 150 - 200$ when Δ_Q is taken to be in the region that is close to the critical point $\Delta_Q = -1$, in Fig. 3.21 (c) for $\Delta_Q = -1.8$; at the critical points, in Figs. 3.21 (d) and (f) for $\Delta_Q = -1$ and 1; in the critical region, in Fig. 3.21 (e) for $\Delta_Q = 0$; and in the ferromagnetic phase, in Fig. 3.21 (g) for $\Delta_Q = 5$ In Fig. 3.21 (e), the revival of the Loschmidt echo at $t \approx 780$ is a finite-size effect. The very small and high frequency oscillations in the Loschmidt echo in all quenches are finite-size effects and are related to the strength of the coupling constant ϵ.

In Fig. 3.22, we display the long-time behavior of the Loschmidt echo for a bath with lattice size $L = 15$ and OBCs as a function of time t after various quenches that start from the critical region, i.e., with the Hamiltonian $H(\Delta_0 = -0.25)$ and $H(\Delta_0 = 0.5)$ for different waiting times $T_0 = 0, 5,$ and 10. The various quenches target $\Delta_Q = -20$ or 3. The quenched Hamiltonians $H(\Delta_Q)$ is taken to be in the antiferromagnetic phase ($\Delta_Q = -20$) and in the ferromagnetic phase ($\Delta_Q = 3$). In these quenches, the Loschmidt echo tends to 0 after a time $t \approx 50$ in all cases.

In Fig. 3.23, we display the long-time behavior of the Loschmidt echo for a bath with lattice size $L = 15$ and OBCs as a function of time t after various quenches that start form the critical region, i.e., with the Hamiltonians $H(\Delta_0 = -0.5)$ and $H(\Delta_0 = -0.25)$ for different waiting times $T_0 = 0, 5,$ and 10. The quenches target $\Delta_Q = -1$ or 0.5. The quenched Hamilto-

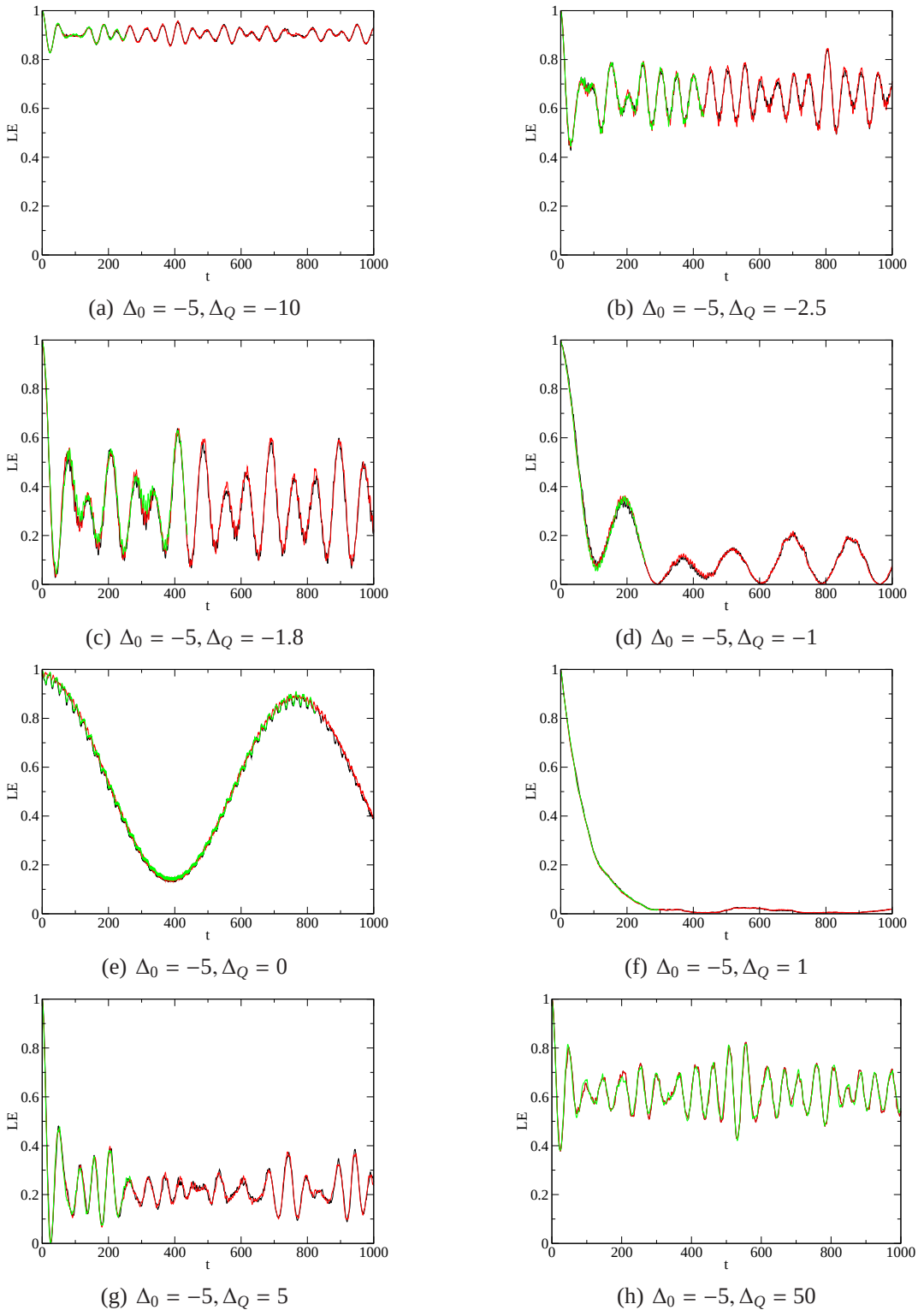

(a) $\Delta_0 = -5, \Delta_Q = -10$ (b) $\Delta_0 = -5, \Delta_Q = -2.5$

(c) $\Delta_0 = -5, \Delta_Q = -1.8$ (d) $\Delta_0 = -5, \Delta_Q = -1$

(e) $\Delta_0 = -5, \Delta_Q = 0$ (f) $\Delta_0 = -5, \Delta_Q = 1$

(g) $\Delta_0 = -5, \Delta_Q = 5$ (h) $\Delta_0 = -5, \Delta_Q = 50$

Figure 3.21: Loschmidt echo for a qubit coupled to an XXZ chain for the indicated quantum quenches starting from the antiferromagnetic phase and for different waiting times $T_0 = 0$ (black), $T_0 = 5$ (red), and $T_0 = 10$ (green) The lattice size of the bath is $L = 15$.

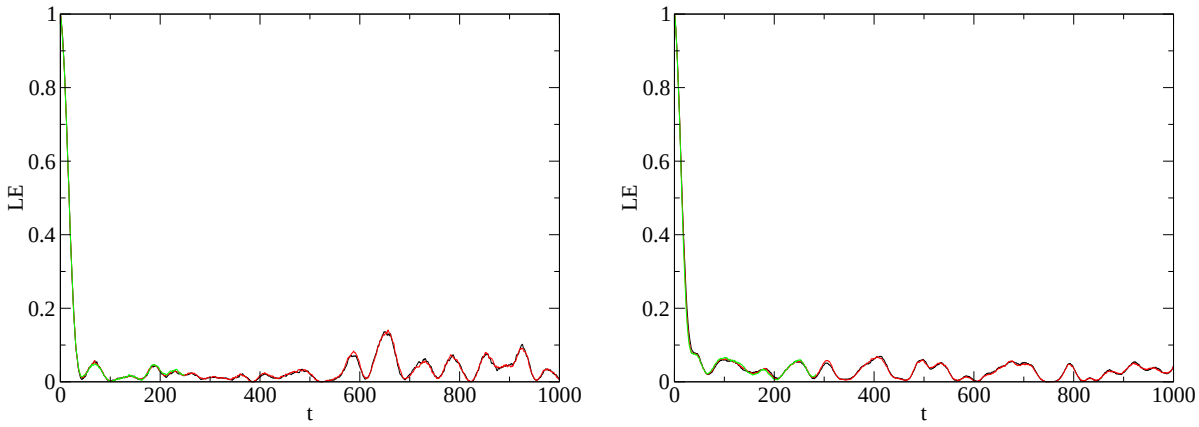

(a) $\Delta_0 = -0.25, \Delta_Q = -20$ (b) $\Delta_0 = 0.5, \Delta_Q = 3$

Figure 3.22: Loschmidt echo for a qubit coupled to an XXZ chain for the indicated quantum quenches from the critical region to (a) the antiferromagnetic phase and (b) the ferromagnetic phase for different waiting times $T_0 = 0$ (black), $T_0 = 5$ (red), and $T_0 = 10$ (green). The lattice size of the bath is $L = 15$.

nians $H(\Delta_Q)$ are taken to be in the critical phase ($\Delta_Q = 0.5$) and at the critical point ($\Delta_Q = 1$). In these quenches, the Loschmidt echo tends to a finite value, ≈ 0.6 in Fig. 3.23 (a) and ≈ 0.8 in Fig. 3.23 (b) for sufficiently long times. The Loschmidt echo decreases with T_0 in both Figs. 3.23 (a) and (b). The very small and high frequency oscillations about the curves of the Loschmidt echo for these quenches are related to the finite-size effects and the strength of the coupling constant ϵ.

In conclusion, an unambiguous complete decoherence occurs for the quenches that start from the antiferromagnetic phase and go to the critical points, to the critical region, to the ferromagnetic phase, and to the region close to the critical point in the antiferromagnetic phase. For quenches that start from the critical region, from the critical points (not shown), and from the region close to the critical point in the antiferromagnetic phase (not shown) and go to the antiferromagnetic phase, or to the ferromagnetic phase, complete decoherence also occurs. In addition, for some large quenches that take place in the critical region, i.e., $\Delta_0 = -0.9$ and $\Delta_Q = 0.9$, small quenches that take place in the critical region close to the critical point $\Delta_c = 1$, i.e., $\Delta_0 = 0.99$ and $\Delta_Q = 0.991$, and quenches that take place between the critical points, complete decoherence also occurs (not shown). In these quenches, low-energy and high-energy modes that are expanded by $|\uparrow\downarrow\uparrow\ldots\downarrow\rangle, |\uparrow\uparrow\downarrow\ldots\downarrow\rangle, \ldots, |\downarrow\uparrow\downarrow\ldots\uparrow\rangle, |\downarrow\downarrow\uparrow\ldots\uparrow\rangle$ are present. For small quenches that occur within the critical region away from the critical point $\Delta_c = 1$, and within the region close to the critical point in the antiferromagnetic phase (not shown), the behavior of the Loschmidt echo is unknown, because it cannot be calculated

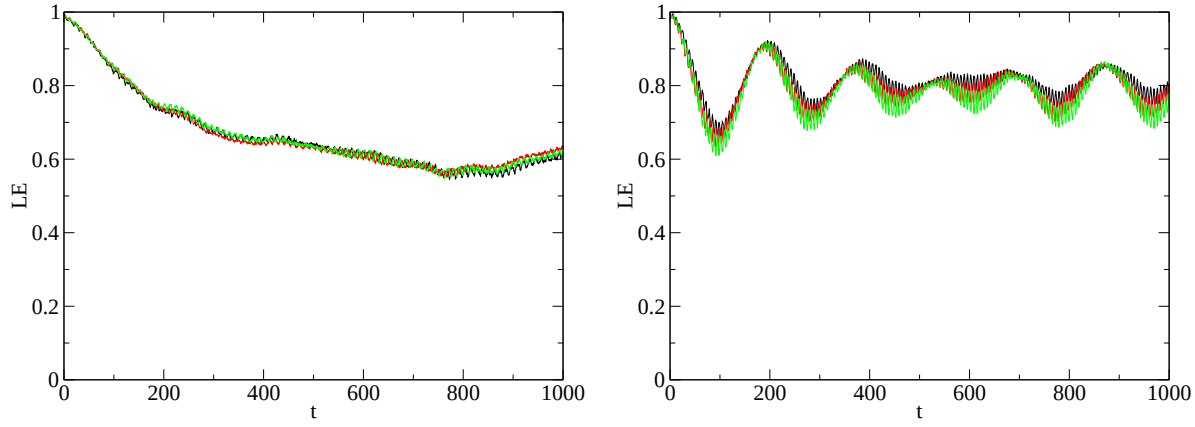

(a) $\Delta_0 = -0.5, \Delta_Q = 0.5$ (b) $\Delta_0 = -0.25, \Delta_Q = -1$

Figure 3.23: Loschmidt echo for a qubit coupled to an XXZ chain for the indicated quantum quenches within the critical region and from the critical region to the critical point for different waiting times $T_0 = 0$ (black), $T_0 = 5$ (red), and $T_0 = 10$ (green) The lattice size of the bath is $L = 15$.

to sufficiently large times for a sufficiently large bath to determine the long-time behavior of the Loschmidt echo. For quenches that occur deep in the antiferromagnetic phase (not shown), no decoherence occurs because only the lowest energy modes, i.e, $|\uparrow\downarrow \ldots \uparrow\downarrow\rangle$, are present. For extremely large quenches that start from the points deep in the antiferromagnetic phase, e.g. $\Delta_0 = -50$, to the points deep in the ferromagnetic phase, e.g., $\Delta_Q = 100$, (not shown), no decoherence also occurs because only the highest energy modes, i.e, $|\uparrow\downarrow \ldots \uparrow\downarrow\rangle$, are present. In addition, if the different between Δ_0 and Δ_Q is extremely small, i.e., $\Delta_0 = 0.1$ and $\Delta_Q = 0.101$, the Loschmidt echo dynamics are effectively those of no quench, $\Delta_0 = \Delta_Q = 0.1$.

Short-time dynamics of the Loschmidt echo

We now focus on the short-time dynamics of the Loschmidt echo. Since the short-time decay of the Loschmidt echo is Gaussian in all cases, see Fig. 3.19 and Fig. 3.20, we will mainly discuss the behavior of the Gaussian decay parameter α with respect to the waiting time T_0. The parameter α is obtained by fitting a Gaussian to data for times $t \lesssim 0.02$. We begin the discussion by considering quenches that start form the antiferromagnetic phase, i.e., with the Hamiltonian $H(\Delta_0 = -5)$ or $H(\Delta_0 = -2)$. We calculate the Gaussian decay parameter $\alpha(T_0)$ of the Loschmidt echo as a function of the waiting time T_0 after various quenches for the bath with the lattice size $L = 49$ (DMRG) and $L = 17$ (ED). Since the number of the states required to maintain accuracy grows quickly in these cases, we only can calculate the results

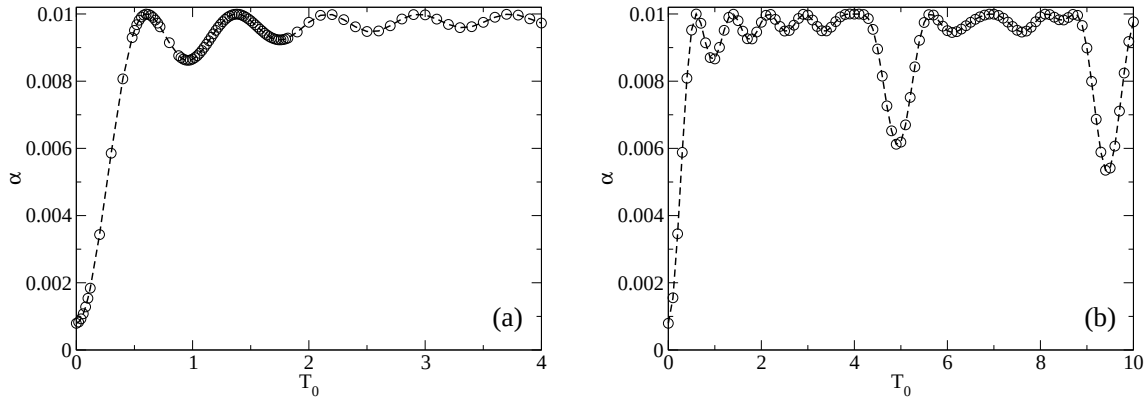

Figure 3.24: Decay parameter α as a function of T_0 for a quench from $\Delta_0 = -5$ to $\Delta_Q = 0$: (a) t-DMRG for $L = 49$, (b) ED for $L = 17$.

for $T_0 \approx 4$ at most.

In Fig. 3.24, we consider the quench from the antiferromagnetic phase, $\Delta_0 = -5$, to the critical region, $\Delta_Q = 0$. In Fig. 3.24 (a), the Gaussian decay parameter $\alpha(T_0)$ for $L = 49$ increases quickly to the maximal value 0.01 at a waiting time $T_0 \approx 0.6$. The initial value $\alpha(T_0 = 0)$ is close to the value of $\alpha(\Delta_0 = -5)$, i.e., the value for a ground-state bath for this lattice size. Subsequently, $\alpha(T_0)$ weakly oscillates around a value 0.01. From Figs. 3.24 (a) and (b), we can see that the qualitative behavior of $\alpha(T_0)$ for $L = 17$ and $L = 49$ is similar for $T_0 \lesssim 4$. In Fig. 3.24 (b), the suddenly deep decays around $T_0 \approx 5$ and $T_0 \approx 9.5$ are finite-size effects.

For the quench from the antiferromagnetic phase, $\Delta_0 = -5$, to the critical point, $\Delta_Q = -1$, Fig. 3.25, $\alpha(T_0)$ quickly increase to the maximal value 0.01, when $T_0 \approx 0.8$ from the initial value $\alpha(T_0 = 0) \approx \alpha(\Delta_0 = -5)$ and retains the value 0.01 in contrast to the oscillatory behavior in the above case. As can be seen in Figs. 3.25 (a) and (b), the qualitative behavior of $\alpha(T_0)$ for $L = 17$ and $L = 49$ is similar for $T_0 \lesssim 3$. In Fig. 3.25 (b), the irregular behavior of $\alpha(T_0)$ after the waiting $T_0 \approx 3$ is a finite-size effect.

For quenches that take place within the antiferromagnetic phase, and when Δ_0 or Δ_Q is at the point in the region close to the critical point, Fig. 3.26 and Fig. 3.27, $\alpha(T_0)$ steadily increases, reaching the maximum value 0.01 at waiting time $T_0 \approx 4$. The qualitative behavior of $\alpha(T_0)$ for $L = 17$ and $L = 49$ is similar for $T_0 \lesssim 2$ for these two quenches. The irregular behaviors of the Loschmidt echo after $T_0 \approx 2$ in Fig. 3.26 (b) and after $T_0 \approx 3$ in Fig. 3.27 (b) are finite-size effects.

For a quench from the antiferromagnetic phase, $\Delta_0 = -5$, to the ferromagnetic phase, $\Delta = 5$, shown in Fig. 3.28, $\alpha(T_0)$ increases from the value $\alpha(T_0) \approx \alpha(\Delta_0)$, to a local maximum

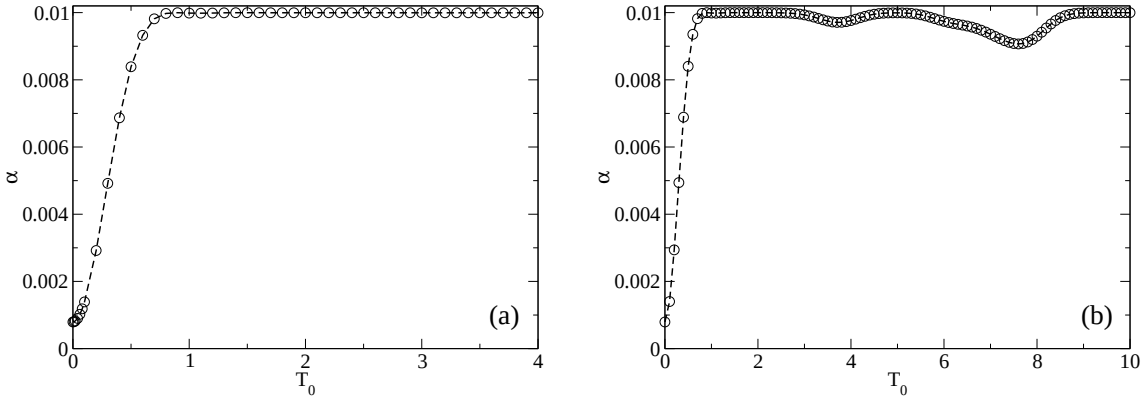

Figure 3.25: Decay parameter α as a function of T_0 for a quench from $\Delta_0 = -5$ to $\Delta_Q = -1$: (a) t-DMRG for $L = 49$, (b) ED for $L = 17$.

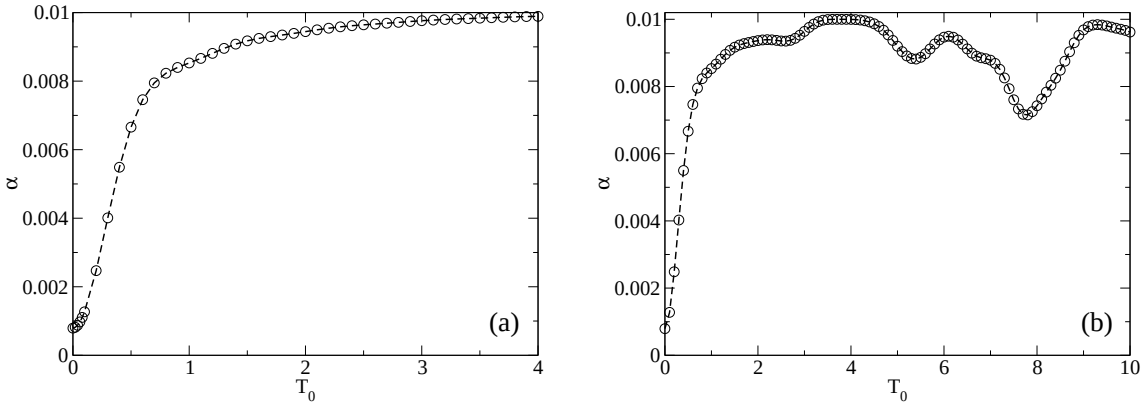

Figure 3.26: Decay parameter α as a function of T_0 for a quench from $\Delta_0 = -5$ to $\Delta_Q = -1.8$: (a) t-DMRG for $L = 49$, (b) ED for $L = 17$.

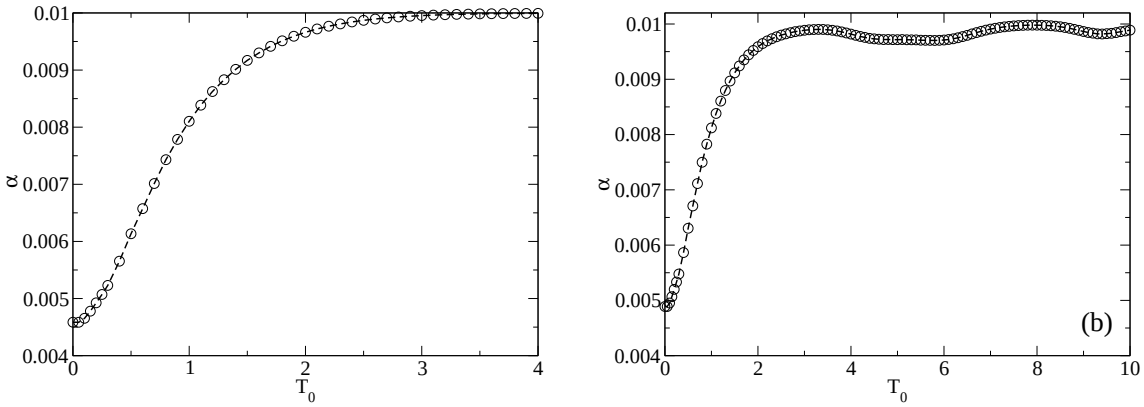

Figure 3.27: Decay parameter α as a function of T_0 for a quench from $\Delta_0 = -2$ to $\Delta_Q = -200$: (a) t-DMRG for $L = 49$, (b) ED for $L = 17$.

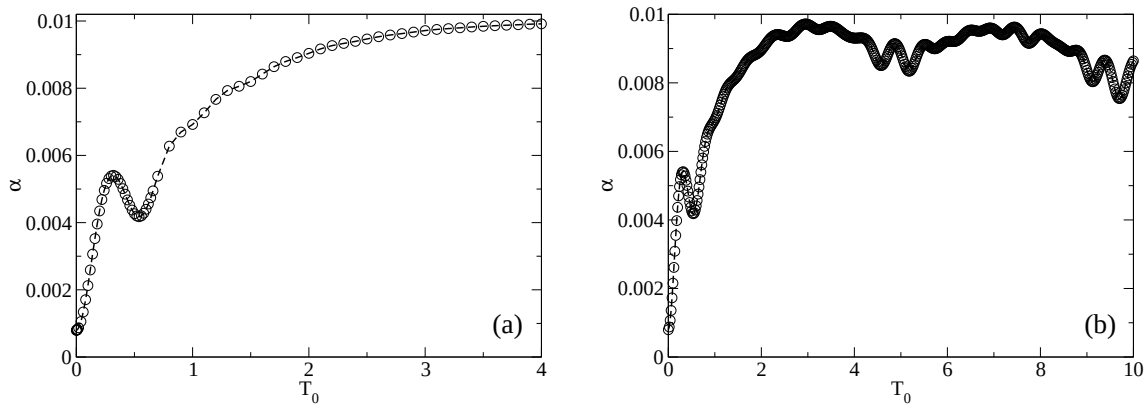

Figure 3.28: Decay parameter α as a function of T_0 for a quench from $\Delta_0 = -5$ to $\Delta_Q = 5$: (a) t-DMRG for $L = 49$, (b) ED for $L = 17$.

value ≈ 0.00541 at $T_0 \approx 0.32$, then decreases to a local minimum value ≈ 0.0042 at $T_0 \approx 0.54$. The position and the number of local minimum values and maximum values is related to the choice the values of Δ_0 and Δ_Q. Finally, it steadily increases to the value 0.01. From Figs. 3.28 (a) and (b), we find that the qualitative behaviors of $\alpha(T_0)$ for $L = 49$ and $L = 17$ are similar for $T_0 \lesssim 2$. In Fig. 3.28 (b), the oscillatory behavior of $\alpha(t_0)$ for $T_0 \gtrsim 2$ is a finite-size effect.

For most quenches that start from the antiferromagnetic phase, $\alpha(T_0)$ reaches the maximal value 0.01. However quenches in the antiferromagnetic phase that are far away from the critical point, $\alpha(T_0)$, in general, do not reach the maximal value 0.01, see Fig. 3.29 and Fig. 3.30. Since we cannot obtain $\alpha(T_0)$ for a very large T_0 using the adaptive t-DMRG, it is hard to determine the the final value of $\alpha(T_0)$ at large enough T_0 when the bath becomes quasi-stationary. However, although it has large finite-size effects, $\alpha(T_0)$ calculated using ED tends to a finite value: $\lesssim 0.008$ for $T_0 \approx 3$, shown in Fig. 3.29 (b) and $\lesssim 0.002$ for $T_0 \approx 3$, shown in Fig. 3.30 (b). As before, we find that the qualitative behavior of $\alpha(T_0)$ for $L = 49$ and $L = 17$ are similar for $T_0 \lesssim 2$ for these two quenches. The big oscillations in 3.29 (b) and Fig. 3.30 (b) for $T_0 \gtrsim 2$ are due to finite-size effects. In addition, for a quench that takes place from the antiferromagnetic phase, i.e., $\Delta_0 = -5$, to a point deep in the ferromagnetic phase, i.e., $\Delta = \pm 100$ (not shown), $\alpha(T_0)$ also does not reach the value 0.01. The explanation is given by Eq. (3.34). For a very large quench, the behavior of $\alpha(T_0)$ is similar to that for the no-quench case.

We now turn our attention to quenches that start from the critical region, i.e., with the Hamiltonians $H(\Delta_0 = -0.5)$, $H(\Delta_0 = -0.25)$, $H(\Delta_0 = 0)$, and $H(\Delta_0 = 0.5)$. We again

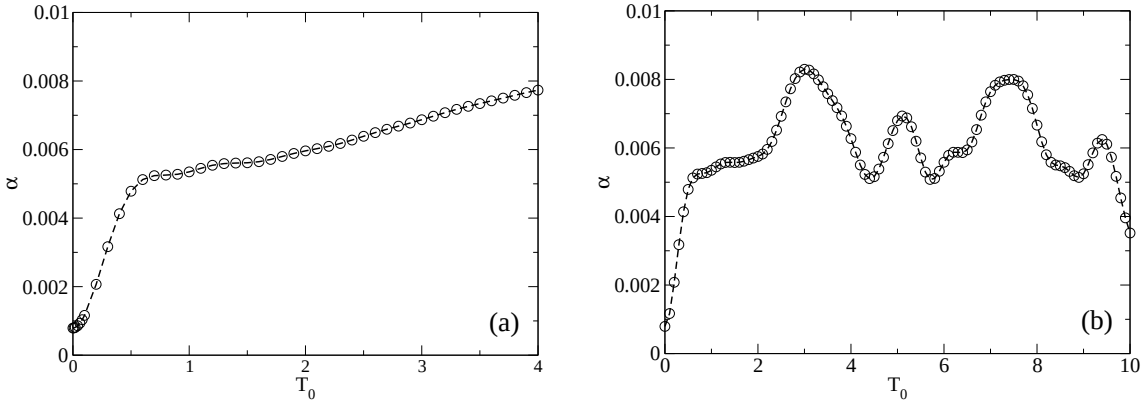

Figure 3.29: Decay parameter α as a function of T_0 for a quench from $\Delta_0 = -5$ to $\Delta_Q = -2.5$: (a) t-DMRG for $L = 49$, (b) ED for $L = 17$.

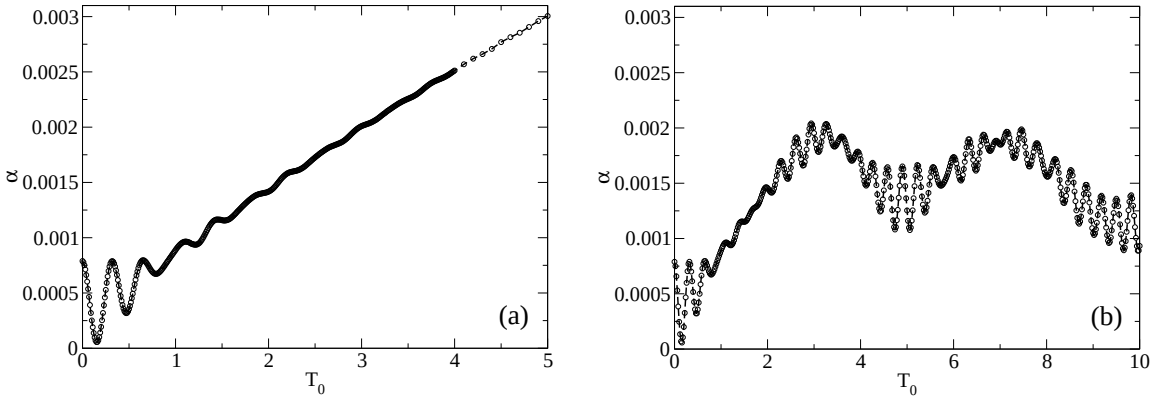

Figure 3.30: Decay parameter α as a function of T_0 for a quench from $\Delta_0 = -5$ to $\Delta_Q = -10$: (a) t-DMRG for $L = 49$, (b) ED for $L = 17$.

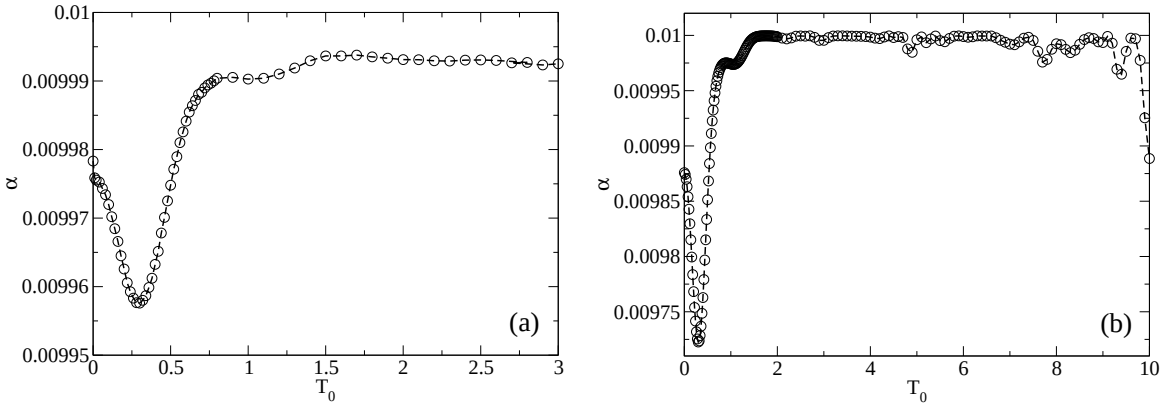

Figure 3.31: Decay parameter α as a function of T_0 for a quench from $\Delta_0 = 0$ to $\Delta_Q = -5$: (a) t-DMRG for $L = 49$. (b) ED for $L = 17$.

calculate the Gaussian decay parameter $\alpha(T_0)$ of the Loschmidt echo as a function of the waiting time T_0 for various quenches of the bath with lattice sizes $L = 49$ (DMRG) and $L = 17$ (ED). Since the initial value $\alpha(T_0 = 0)$ is already very close to 0.01, $\alpha(T_0)$ rapidly increases to the value 0.01 here. Since the number of states required to maintain accuracy grows rapidly with T_0, we only can obtain results to at most $T_0 \approx 3$ for most cases here.

We first consider a quench from the critical region, $\Delta_0 = 0$, to the antiferromagnetic phase, $\Delta_Q = -5$. In Fig. 3.31 (a), for lattice size $L = 49$, $\alpha(T_0)$ decays to a local minimum value $\alpha \approx 0.009958$ at $T_0 \approx 0.3$ from $\alpha(T_0 = 0) \approx \alpha(\Delta_0 = 0)$ the value for a ground-state bath. Subsequently, $\alpha(T_0)$ smoothly increases to the maximum value 0.01 at $T_0 \approx 0.75$ and remains at an almost constant value 0.01 for $T_0 \gtrsim 0.75$. For $L = 17$, Fig. 3.31 (b), the local minimum has a value $\alpha \approx 0.009723$ and also occurs at $T_0 \approx 0.3$. The difference between the initial values of $\alpha(T_0 = 0)$ for $L = 17$ and for $L = 49$ are observable. However, all of the values are very close to 0.01. Aside from the finite-size effects, the qualitative behavior of $\alpha(T_0)$ for $L = 17$ and $L = 49$ are similar for $T_0 \lesssim 3$. For $T_0 \gtrsim 3$, there are large finite-size effects visible for $L = 17$. Similar behavior occurs for a quench from the critical region, $\Delta_0 = -0.25$ to a point deep in the antiferromagnetic phase, $\Delta_Q = -20$. As can be seen in Fig. 3.32 (a), $\alpha(T_0)$ for lattice size $L = 49$ decays from $\alpha(T_0 = 0) \approx \alpha(\Delta_0 = -0.25)$, to four local minimum values and also increases to three local maxima that are much smaller than 0.01. Subsequently, $\alpha(T_0)$ smoothly increases to the maximal value 0.01 at $T_0 \approx 1$ and retains an almost constant value 0.01 for $T_0 \gtrsim 1$. In Fig. 3.32 (b), the qualitative behavior of $\alpha(T_0)$ for $L = 17$ is similar to the case of $L = 49$. Due to finite-sizes effects, $\alpha(T_0)$ has a large jump at $T_0 \approx 9$.

For a quench that takes place within the critical region, $\Delta_0 = -0.5$ and $\Delta_Q = 0.5$,

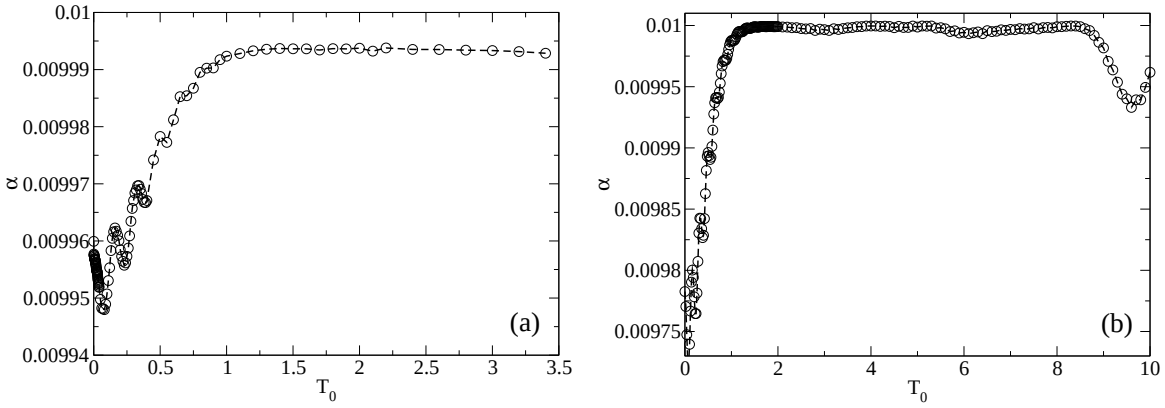

Figure 3.32: Decay parameter α as a function of T_0 for a quench from $\Delta_0 = -0.25$ to $\Delta_Q = -20$: (a) t-DMRG for $L = 49$, (b) ED for $L = 17$.

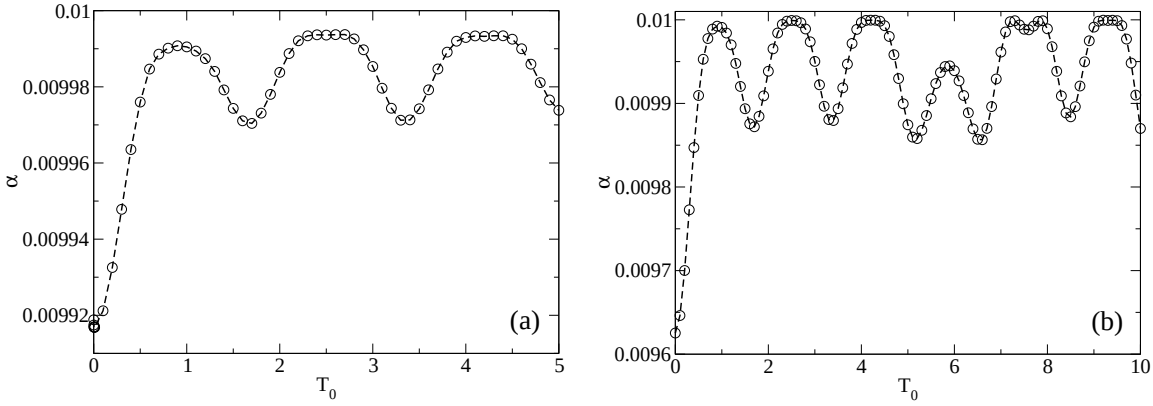

Figure 3.33: Decay parameter α as a function of T_0 for a quench from $\Delta_0 = -0.5$ to $\Delta_Q = 0.5$: (a) t-DMRG for $L = 49$, (b) ED for $L = 17$.

Figs. 3.33 (a) and (b), $\alpha(T_0)$ increases from $\alpha(T_0 = 0) \approx \alpha(\Delta_0 = -0.5)$ to the maximum value 0.01 at $T_0 \approx 0.9$ and then slowly oscillates. The period and the amplitude of the oscillation are related to the values of Δ_0 and Δ_Q and the difference between them. This oscillatory behavior is also related to the fact that the effective quantum number is $S_z = 1/2$ for odd lattice size. For an even sized lattice, the oscillation does not occur. In Fig. 3.33 (b), the qualitative behavior of $\alpha(T_0)$ for $L = 17$ is similar to the case of $L = 49$. Finite-size effects can be observed for $T_0 \gtrsim 4$.

A quench from the critical region, $\Delta_0 = 0.5$, to the ferromagnetic phase, $\Delta_Q = 3$, is shown in Fig. 3.34. In Fig. 3.34 (a), $\alpha(T_0)$ decreases from $\alpha(T_0 = 0) \approx \alpha(\Delta_0)$ to a small value at $T_0 \approx 0.002$, then increases to the maximum value 0.01 at $T_0 \approx 0.5$. It then remains almost constant at values near 0.01. The roughness of the $\alpha(T_0)$ curve is related to the number of data

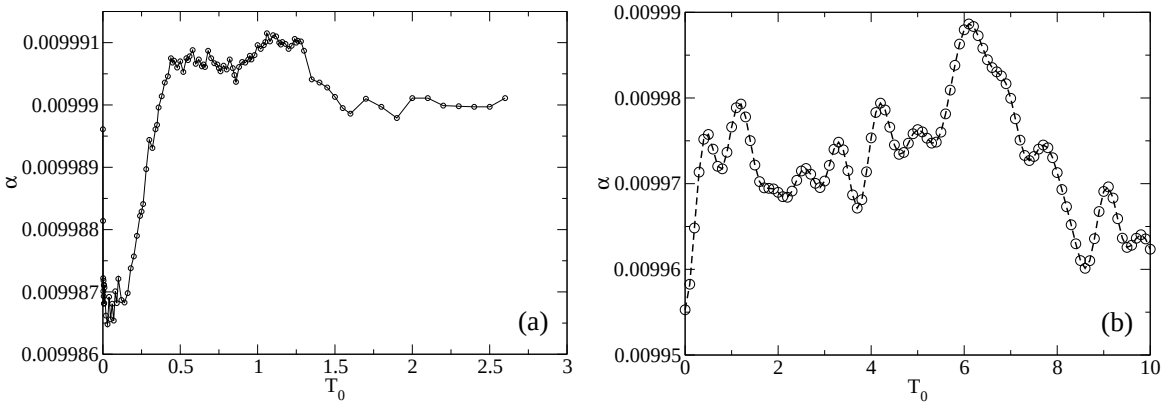

Figure 3.34: Decay parameter α as a function of T_0 for a quench from $\Delta_0 = 0.5$ to $\Delta_Q = 3$: (a) t-DMRG for $L = 49$, (b) ED for $L = 17$.

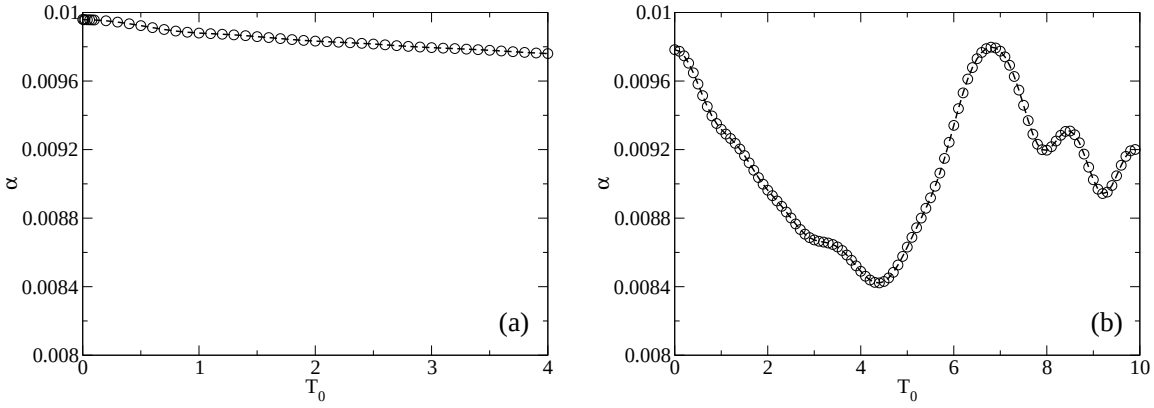

Figure 3.35: Decay parameter α as a function of T_0 for a quench from $\Delta_0 = -0.25$ to $\Delta_Q = -1$: (a) t-DMRG for $L = 49$, (b) ED for $L = 17$.

included in the fit. Including more data generally produces smoother curve. In Fig. 3.34 (b), one can observe that the qualitative behavior of $\alpha(T_0)$ for $L = 17$ is similar to that for $L = 49$. However, there is no initial decrease at $T_0 \approx 0.002$ for the case of $L = 17$. This initial decrease is also related to the number of data included in the fit. This behavior is not observed if one includes more data for times $t \lesssim 0.1$ in the fit.

For a quench from the critical region, $\Delta = -0.25$, to the critical point, $\Delta_Q = -1$, Fig. 3.35 (a), $\alpha(T_0)$ for $L = 49$ decays monotonically but only reaches values slightly less than 0.01 for $T \lesssim 4$. In Fig. 3.35 (b), $\alpha(T_0)$ for $L = 17$ decays to a minimum value ≈ 0.0084 then revives to a value close to 0.01. This revival behavior a finite-size effect. The decay behavior here is related to the odd lattice size and to the effective quantum number $S_z = 1/2$. For an even lattice, i.e., $L = 50$, no decay behavior of $\alpha(T_0)$ occurs (not shown).

Some other quenches still remain to be discussed. For cases of quenches starting form the critical points $\Delta_0 = \pm 1$, to any other phases or to the other critical point, the behavior of $\alpha(T_0)$ is similar to the cases of quenches starting from the critical region: $\alpha(T_0)$ always tends to the maximum value 0.01 (not shown). For cases of quenches starting from a point in the region close to the critical point in the antiferromagnetic phase, e.g., $\Delta_0 = -2$, to a point deep in the antiferromagnetic phase, e.g., $\Delta_Q = -20$, or to the points in the region $-1.3 \lesssim \Delta_Q \leqq 1$, $\alpha(T_0)$ also tends to 0.01 (not shown). An example of such behavior has been shown in Fig. 3.27 ($\Delta = -2$ and $\Delta = -200$).

In conclusion, the decoherence is enhanced relative to the coupling to a ground-state bath for all quenches. For long times, the Loschmidt echo always decays to zero for most quenches that take place between different phases or between different critical points. Quenches that take place deep in the antiferromagnetic phase and that start from a point deep in the antiferromagnetic phase to a point deep in the ferromagnetic phase do not lead to a complete decoherence. For some quenches, the behavior of the Loschmidt echo is unknown. Examples are small quenches occurring in the region close to the critical point $\Delta_c = -1$ and including the critical point: $-2 \lesssim \Delta_0 \leqq -1$ and $-2 \lesssim \Delta_Q \leqq -1$, and small quenches occurring in the critical region away from the critical point $\Delta_c = 1$. While taking the initial state of the bath to be a quenched state leads to more generic behavior, i.e., complete decoherence of the qubit generally occurs, the short-time behavior of the Loschmidt echo nevertheless decays as a Gaussian. The Gaussian decay parameter α for most quenches reach the maximum decay parameter value 0.01 for the qubit-bath coupling $\epsilon = 0.2$. However, quenches deep in the antiferromagnetic phase, quenches from a point deep in the antiferromagnetic phase to a point deep in the ferromagnetic phase, and small quenches occurring in the region close to the critical point $\Delta_c = -1$ and including the critical point: $-2 \lesssim \Delta_0 \leqq -1$ and $-2 \lesssim \Delta_Q \leqq -1$, yield values of α that are smaller than 0.01, for reasons discussed above. In Fig. 3.36, we indicate the quenches that lead to an $\alpha(T_0)$ that tends to the maximum value 0.01 for large enough T_0. The blank region for quenches deep in the antiferromagnetic phase indicate the parameter regime where $\alpha(T_0)$ does not tend to 0.01.

3.5 Conclusion

We have studied the decoherence dynamics of a qubit induced by a coupling it to bath consisting of a transverse-field Ising chain or an XXZ chain initially in a quenched state using an analytical method (Ising case), the adaptive t-DMRG (XXZ case) and ED (XXZ case).

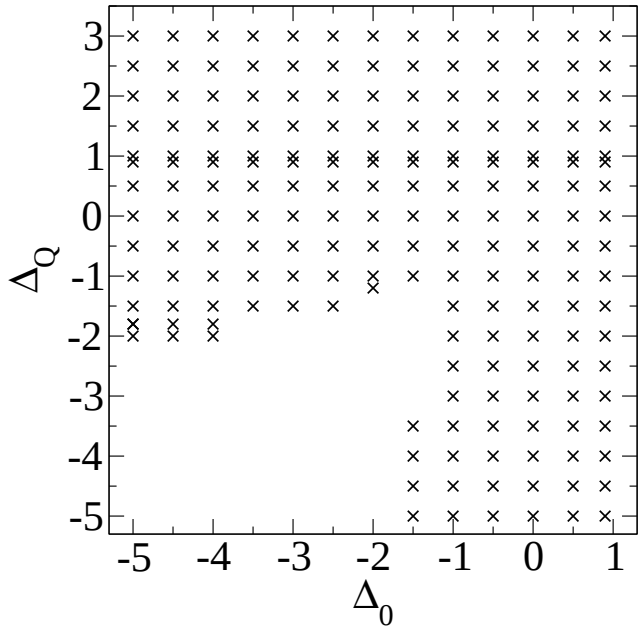

Figure 3.36: Decay parameter α for qubit-bath coupling $\epsilon = 0.2$ for a quenched initial state as a function of the initial anisotropy Δ_0 and the quenched anisotropy Δ_Q of the bath. The symbol $\times$ indicates quenches that $\alpha(T_0)$ tends to the maximum value 0.01 for large enough T_0. Blanks for quenches deep in the antiferromagnetic phase and for small quenches occurring in the region close to the critical point indicate that $\alpha(T_0)$ does not tend to 0.01.

We have also revisited the decoherence dynamics of a qubit induced by a bath initially in the ground states previously studied in Refs. [77, 78] with high accuracy. We find that, for all types of initial states, the Loschmidt echo decays as a Gaussian for short times ($t \lesssim 1$). In the cases we have treated here, a quenched initial state always leads to more generic behavior, i.e., to complete decoherence of the qubit. For quenched states of the transverse-field Ising chain, $\alpha(T_0)$ always slowly oscillates around a time-averaged value $\bar{\alpha}$ after a long waiting time T_0 after which the bath becomes quasi-stationary. For quenched states of an XXZ chain, $\alpha(T_0)$ tends to the maximum value 0.01 for majority of quenches.

Conclusion

In this thesis, we have studied two problems in the field of the one-dimensional interacting quantum systems. The first one provides a new understanding of the effects of the nearest-neighbor antiferromagnetic coupling J_1 in the one-dimensional Hubbard model at half-filling. We also find that some new phases are induced by the addition of a next-nearest-neighbor antiferromagnetic coupling J_2. In the second problem, we have carried out very accurate DMRG calculations of the decoherence of a qubit coupled to a XXZ bath that is initially in a ground state and have found that the decoherence behavior of a qubit coupled to a quenched bath is generic.

In Chapter 2, we have investigated the quantum phase transitions of the one-dimensional half-filled t-U-J_1-J_2 model using the static DMRG and bosonization. We have obtained a sketch of the ground-state phase diagram of the one-dimensional t-U-J_1-J_2 model. Our numerical and analytical results indicate that the ground state has a finite gap for either charge excitations (spin-density-wave phase) or spin excitations (Luther-Emery phase) or both (bond-order-wave phase). For some larger interactions, e.g., $U = 2$, the DMRG finds a strong-coupling bond-order-wave phase which eludes analytical description. Instead, its existence and its properties can be inferred from a strong-coupling expansion of the model in which it is seen that the strong-coupling bond-order-wave phase results from the frustration of the nearest-neighbor coupling J_1 by the next-nearest-neighbor Heisenberg coupling J_2. Our conclusion is that the nearest-neighbor Heisenberg coupling J_1 is not a frustrating interaction for the half-filled Hubbard model because the ground state of the t-U-J_1 model is a spin-density wave for all $J_1 \geq 0$, whereas a frustrating next-nearest-neighbor coupling J_2 is.

It is would also be interesting to study the t-U-J_1-J_2 model away from half-filling in order to understand of its behavior more completely. More realistically, a consideration of the t-U-J_1-J_2 model in a two-dimensional lattice is also important in relation to a possible spin-liquid state and superconductivity. In view of the limitations of the DMRG method in two

dimensions, a quasi-two-dimensional lattice, such as a ladder lattice, could be considered.

In Chapter 3, we have explored the decoherence of a qubit coupled to a one-dimensional XXZ spin bath using the time-dependent DMRG and coupled to a transverse-field Ising bath using analytical methods. We find that, for all types of initial states (a ground state or a quantum quenched state), the Loschmidt echo decays as a Gaussian for short times ($t \lesssim 1$). A quenched initial state always leads to more generic behavior, i.e., to complete decoherence of the qubit. For quenched states of an XXZ chain, the Gaussian decay parameter $\alpha(T_0)$ tends to a maximum value of 0.01 for the qubit-bath coupling strength $\epsilon = 0.2$ for the majority of quenches after a waiting time T_0 (i.e., the evolution time of the bath state after a quench). For quenched states in the transverse-field Ising chain, $\alpha(T_0)$ always slowly oscillates around a time-averaged value $\bar{\alpha}$ after a waiting time T_0 that is long enough to yield quasi-stationary behavior.

In general, the decoherence of a qubit coupled to a interacting spin bath is inevitable. However, the lack of decoherence behavior can occur in other systems. For example, one can consider a two-qubit system coupled to a bath to investigate the possibility of decoherence. In particular, unlike for a single-qubit system, the self-Hamiltonian becomes more relevant to the decoherence dynamic for a two-qubit system (A and B). The structure of a two-qubit system is more complex compared to a single qubit. Correspondingly, the initial state of the two-qubit system can be considered to be a quenched state that has evolved from an arbitrary non-interacting classical state such as $|\uparrow\rangle_A |\downarrow\rangle_B$, by turning on some specific interactions. As a result, the initial state of the two-qubit system could have the form of Bell states or other highly entangled mixed states. A lack of decoherence behavior of the two-qubit system is found for some cases that are related to the interactions between two qubits and between the qubits and the bath, e.g., for the case of two qubits in the singlet state coupled to the same spin of the bath with the same coupling strength. Other decoherence behavior can also be observed. Studying a more general n-qubit system coupled to a bath would be quite interesting; there will likely be strong dependence of the decoherence behavior on the Hamiltonian and the initial state of the n-qubit system.

Appendix A

Exactly solvable models

Here, we investigate the decoherence of a qubit coupled to an XY spin-1/2 bath that is in the ground state or in a quenched state. The interaction between the qubit and the bath is an Ising coupling. In these cases, the Loschmidt echo of a qubit can be exactly calculated using the Jordan-Wigner transformation and the Lieb-Schultz-Mattis method (Sec. A.3) applied to the effective Hamiltonian that we obtained in Chapter 3.

A.1 The one-dimensional XY model in magnetic fields

We treat an effective Hamiltonian describing the one-dimensional XY model. It is composed of a lattice of N spin-1/2 spins with nearest-neighbor interaction and an external magnetic field in the z-direction. It has the form

$$H = -2J \sum_{j=1}^{N} [(1+\gamma) S_j^x S_{j+1}^x + (1-\gamma) S_j^y S_{j+1}^y + (\lambda + \epsilon_j) S_j^z], \tag{A.1}$$

where S_j^x, S_j^y, and S_j^z denote the spin operators of the jth spin site in the chain. The parameter J ($J > 0$) sets the interaction strength in the xy plane with a degree of anisotropy γ ($-1 \leq \gamma \leq 1$). Here λ ($\lambda \geq 0$) is the strength of a uniform external magnetic field in the z-direction, and ϵ_j is a local external magnetic field in the z-direction on site j induced by the Ising coupling between the system (qubit) and the bath. If the qubit uniformly couples to all spins of the bath with a same coupling strength ϵ, $\epsilon_j = \epsilon$, the model is called the central spin model. When $\gamma = 1$, this model reduces to the transverse-field Ising model.

As usual, we first rewrite Hamiltonian (A.1) in the terms of raising and lowering operators,

which are defined by

$$S_i^{\dagger} = S_i^x + iS_i^y \tag{A.2a}$$

and

$$S_i^{-} = S_i^x - iS_i^y. \tag{A.2b}$$

The spin operators can then be written

$$S_i^x = \frac{1}{2}(S_i^{\dagger} + S_i^{-}), \tag{A.3a}$$

$$S_i^y = \frac{1}{2i}(S_i^{\dagger} - S_i^{-}), \tag{A.3b}$$

$$S_i^z = S_i^{\dagger} S_i^{-} - 1/2. \tag{A.3c}$$

These operators partly obey the canonical anticommutation relations,

$$\{S_i^{-}, S_i^{\dagger}\} = 1,\ \{S_i^{\dagger}, S_i^{\dagger}\} = \{S_i^{-}, S_i^{-}\} = 0, \tag{A.4}$$

and partly the canonical commutation relations,

$$[S_i^{-}, S_j^{\dagger}] = [S_i^{-}, S_j^{-}] = [S_i^{\dagger}, S_j^{\dagger}] = 0,\ i \neq j \tag{A.5}$$

After substituting the Eq. (A.3) into Eq. (A.1), the Hamiltonian takes the quadratic form

$$H = -J \sum_{j=1}^{N} [(S_j^{\dagger} S_{j+1}^{-} + \gamma S_j^{\dagger} S_{j+1}^{\dagger} + H.c.) + 2(\lambda + \epsilon_j) S_j^{\dagger} S_j^{-} - (\lambda + \epsilon_j)]. \tag{A.6}$$

Because of the two kinds of different commutation relations for the spin S_i, Hamiltonian (A.6) cannot be directly diagonalized by a linear transformation. This can only be done if all spins S_i at different sites obey the canonical anticommutation relations. The detailed reason is that if we assume S_i that can be linearly transformed by the form $S_i = \sum_k \phi_{ik} \tilde{S}_k$, we obtain $\{\tilde{S}_k, \tilde{S}_{k'}\} = 0$ from Eq. (A.4), but the contradictory result $[\tilde{S}_k, \tilde{S}_{k'}] = 0$ from Eq. (A.5). The canonical transformation $\tilde{S}_k$ is neither fermionic nor bosonic. Fortunately, it is still possible to transform the spins S_i both at the same site and at the diferent sites to a new set of operators that strictly obey the canonical anticommutation relations. The method to do this was firstly introduced by Jordan and Wigner [100].

A.2 The Jordan-Wigner transformation (JWT)

Let

$$c_i = \exp\Big(i\pi \sum_{j=1}^{i-1} S_j^\dagger S_j^-\Big) S_i^-,\ c_i^\dagger = S_i^\dagger \exp\Big(-i\pi \sum_{j=1}^{i-1} S_j^\dagger S_j^-\Big), \tag{A.7}$$

where c_i and $c_i^\dagger$ are the annihilation and creation operators for spinless fermions which obey the canonical anticommutation relations

$$\{c_i, c_j^\dagger\} = \delta_{ij},\ \{c_i, c_j\} = \{c_i^\dagger, c_j^\dagger\} = 0. \tag{A.8}$$

Examining the Eq. (A.7), we can rewrite the operator transformation, Eq. (A.7), as

$$\exp\Big(\pm i\pi \sum_{j=1}^{i-1} S_j^\dagger S_j^-\Big) = \exp\Big(\pm i\pi \sum_{j=1}^{i-1}(S_j^z + \frac{1}{2})\Big) = \Big(\prod_{j=1}^{i-1} \mathrm{e}^{\pm i\pi S_i^z}\Big)\mathrm{e}^{\pm i\pi(i-1)/2}. \tag{A.9}$$

Equation (A.9) implies that the physical meaning of the transform operators is to rotate all spins from $j = 1$ to $i - 1$ by π or $-\pi$ around the z axis. Notice that since $c_j^\dagger c_j = S_j^\dagger S_j^-$, it is easy to form the inverse transformations of transformation (A.7),

$$S_i^- = \exp\Big(-i\pi \sum_{j=1}^{i-1} c_j^\dagger c_j\Big) c_i,\ S_i^\dagger = c_i^\dagger \exp\Big(i\pi \sum_{j=1}^{i-1} c_j^\dagger c_j\Big). \tag{A.10}$$

Observe that $(c_j^\dagger c_j)^n = c_j^\dagger c_j$, and since the $(c_j^\dagger c_j)$'s on different sites commute with each other, the transformation (A.10) can be simplified to

$$\begin{aligned}
\exp\Big(\pm i\pi \sum_{j=1}^{i-1} c_j^\dagger c_j\Big) &= \prod_{j=1}^{i-1} \exp(\pm i\pi c_j^\dagger c_j) = \prod_{j=1}^{i-1}\Big[1 + \sum_{n=1}^{\infty} \frac{(\pm i\pi)^n (c_j^\dagger c_j)^n}{n!}\Big] \\
&= \prod_{j=1}^{i-1}\Big[1 + \sum_{n=1}^{\infty} \frac{(\pm i\pi)^n (c_j^\dagger c_j)}{n!}\Big] = \prod_{j=1}^{i-1}\Big[1 + (e^{\pm i\pi} - 1)(c_j^\dagger c_j)\Big] \\
&= \prod_{j=1}^{i-1}(1 - 2c_j^\dagger c_j).
\end{aligned} \tag{A.11}$$

This implies that

$$\exp\Big(\pm i\pi \sum_{j=1}^{i-1} c_j^\dagger c_j\Big) = \Big[\exp\Big(\pm i\pi \sum_{j=1}^{i-1} c_j^\dagger c_j\Big)\Big]^\dagger, \tag{A.12}$$

where the canonical commutation relation

$$\left[\exp\Big(\pm i\pi\sum_{j=1}^{m-1}c_j^\dagger c_j\Big),\exp\Big(\pm i\pi\sum_{j=1}^{n-1}c_j^\dagger c_j\Big)\right]=0. \tag{A.13}$$

Also notice that since $[c_i^\dagger, 1-2c_j^\dagger c_j]=2\delta_{ij}c_j^\dagger$, $[c_i, 1-2c_j^\dagger c_j]=-2\delta_{ij}c_j$, $\{c_j^\dagger, 1-2c_j^\dagger c_j\}=0$, and $\{c_j, 1-2c_j^\dagger c_j\}=0$, we can obtain

$$\left[c_k^\dagger,\exp\Big(\pm i\pi\sum_{j=1}^{i-1}c_j^\dagger c_j\Big)\right]=\left[c_k,\exp\Big(\pm i\pi\sum_{j=1}^{i-1}c_j^\dagger c_j\Big)\right]=0,\quad k\geq i, \tag{A.14}$$

$$\left\{c_k^\dagger,\exp\Big(\pm i\pi\sum_{j=1}^{i-1}c_j^\dagger c_j\Big)\right\}=\left\{c_k,\exp\Big(\pm i\pi\sum_{j=1}^{i-1}c_j^\dagger c_j\Big)\right\}=0,\quad k<i. \tag{A.15}$$

Similarly, we can conclude that

$$\exp\Big(\pm i\pi\sum_{j=1}^{i-1}S_j^\dagger S_j^-\Big)=\prod_{j=1}^{i-1}(1-2S_j^\dagger S_j^-), \tag{A.16}$$

$$\exp\Big(\pm i\pi\sum_{j=1}^{i-1}S_j^\dagger S_j\Big)=\left[\exp\Big(\pm i\pi\sum_{j=1}^{i-1}S_j^\dagger S_j\Big)\right]^\dagger, \tag{A.17}$$

$$\left[\exp\Big(\pm i\pi\sum_{j=1}^{m-1}S_j^\dagger S_j\Big),\exp\Big(\pm i\pi\sum_{j=1}^{n-1}S_j^\dagger S_j\Big)\right]=0, \tag{A.18}$$

and

$$\left[S_k^\dagger,\exp\Big(\pm i\pi\sum_{1}^{i-1}S_j^\dagger S_j^-\Big)\right]=\left[S_k^-,\exp\Big(\pm i\pi\sum_{1}^{i-1}S_j^\dagger S_j^-\Big)\right]=0,\quad k\geq i, \tag{A.19}$$

$$\left\{S_k^\dagger,\exp\Big(\pm i\pi\sum_{1}^{i-1}S_j^\dagger S_j^-\Big)\right\}=\left\{S_k^-,\exp\Big(\pm i\pi\sum_{1}^{i-1}S_j^\dagger S_j^-\Big)\right\}=0,\quad k<i. \tag{A.20}$$

Thus, we have verified the canonical anticommutation relations for the c's. For a site $i \neq j$,

$$\begin{aligned} c_i c_j^\dagger &= \exp\Big(i\pi \sum_{k=1}^{i-1} S_k^\dagger S_k^-\Big) S_i^- S_j^\dagger \exp\Big(-i\pi \sum_{k=1}^{j-1} S_k^\dagger S_k^-\Big) \\ &= -S_j^\dagger \exp\Big(-i\pi \sum_{k=1}^{j-1} S_k^\dagger S_k^-\Big) \exp\Big(i\pi \sum_{k=1}^{i-1} S_k^\dagger S_k^-\Big) S_i^- \\ &= -c_j^\dagger c_i, \end{aligned} \tag{A.21}$$

Thus,

$$\{c_i, c_j^\dagger\} = 0. \tag{A.22}$$

Similarly,

$$\begin{aligned} c_i c_j &= \exp\Big(i\pi \sum_{k=1}^{i-1} S_k^\dagger S_k^-\Big) S_i^- \exp\Big(i\pi \sum_{k=1}^{j-1} S_k^\dagger S_k^-\Big) S_j^- \\ &= -\exp\Big(i\pi \sum_{k=1}^{j-1} S_k^\dagger S_k^-\Big) S_j^- \exp\Big(i\pi \sum_{k=1}^{i-1} S_k^\dagger S_k^-\Big) S_i^- \\ &= -c_j c_i. \end{aligned} \tag{A.23}$$

Therefore, we obtain

$$\{c_i, c_j\} = 0. \tag{A.24}$$

For the case of $i = j$, it is easy to verify the canonical commutation relations for spins at the same site, $\{c_i, c_i^\dagger\} = 1$ and $\{c_i, c_i\} = 0$. Here we recover the relations (A.8) again. In this method, the most crucial feature is that the JWT translates the canonical commutation relations for the spin operators at different sites into canonical anticommutation relations for the spinless fermionic operators. An additional advantage of the JWT is that it preserves the locality of interacting Hamiltonians.

We now turn to transforming Hamiltonian (A.1) into spin operator form by substituting Eq. (A.7) into Eq. (A.6). Since $c_i^\dagger c_i$ is a particle number operator with eigenvalues of 0 or 1, we obtain

$$\begin{aligned} S_i^\dagger S_{i+1}^- &= c_i^\dagger \exp\Big(i\pi \sum_{j=1}^{i-1} c_j^\dagger c_j\Big) \exp\Big(i\pi \sum_{j=1}^{i} c_j^\dagger c_j\Big) c_{i+1}^\dagger \\ &= c_i^\dagger \exp(-i\pi c_i^\dagger c_i) c_{i+1} = c_i^\dagger c_{i+1}. \end{aligned} \tag{A.25}$$

Notice that $c_i^\dagger \exp(-i\pi c_i^\dagger c_i) = c_i^\dagger = 0$, so that after we apply it to an occupied state, at site i, then a fermion can no longer be present. The anisotropic term in the xy plane in Eq. (A.6) is transformed into

$$\begin{aligned} S_i^\dagger S_{i+1}^\dagger &= c_i^\dagger \exp\Big(i\pi \sum_{j=1}^{i-1} c_j^\dagger c_j\Big) c_{i+1}^\dagger \exp\Big(i\pi \sum_{j=1}^{i} c_j^\dagger c_j\Big) \\ &= c_i^\dagger \exp\Big(-i\pi \sum_{j=1}^{i-1} c_j^\dagger c_j\Big) c_{i+1}^\dagger \exp\Big(i\pi \sum_{j=1}^{i} c_j^\dagger c_j\Big) \\ &= c_i^\dagger \exp(i\pi c_i^\dagger c_i) c_{i+1}^\dagger = c_i^\dagger c_{i+1}^\dagger. \end{aligned} \tag{A.26}$$

For open boundary conditions (OBCs), the transformed effective Hamiltonian in term of fermionic operators is

$$H_{OBC} = -J \sum_{j=1}^{N-1} [(c_j^\dagger c_{j+1} + \gamma c_j^\dagger c_{j+1}^\dagger) + H.c. + 2(\lambda + \epsilon_j) c_j^\dagger c_j - (\lambda + \epsilon_j)]. \tag{A.27}$$

We will discuss this case more fully after deriving the solution for period boundary conditions (PBCs). If we consider PBCs ($S_{N+1}^\dagger = S_1^\dagger$ and $S_{N+1}^- = S_1^-$), the special cyclic boundary term $S_N^\dagger S_{N+1}^- + S_N^\dagger S_{N+1}^\dagger + H.c.$ has the form

$$\begin{aligned} S_N^\dagger S_{N+1}^- = S_N^\dagger S_1^- &= c_N^\dagger \exp\Big(i\pi \sum_{j=1}^{N-1} c_j^\dagger c_j\Big) c_1 = -c_N^\dagger c_1 \exp\Big(i\pi \sum_{j=1}^{N-1} c_j^\dagger c_j\Big) \\ &= -c_N^\dagger c_1 \exp\Big(i\pi \sum_{j=1}^{N} c_j^\dagger c_j\Big) = -c_N^\dagger c_1 \exp(i\pi\Pi), \end{aligned} \tag{A.28a}$$

$$\begin{aligned} S_N^\dagger S_{N+1}^\dagger = S_N^\dagger S_1^\dagger &= c_N^\dagger \exp\Big(i\pi \sum_{j=1}^{N-1} c_j^\dagger c_j\Big) c_1^\dagger = -c_N^\dagger c_1^\dagger \exp\Big(i\pi \sum_{j=1}^{N-1} c_j^\dagger c_j\Big) \\ &= -c_N^\dagger c_1^\dagger \exp\Big(i\pi \sum_{j=1}^{N} c_j^\dagger c_j\Big) = -c_N^\dagger c_1^\dagger \exp(i\pi\Pi), \end{aligned} \tag{A.28b}$$

where

$$\Pi = \sum_{j=1}^{N} c_j^\dagger c_j = \sum_{j=1}^{N} (S_j^z + 1/2), \tag{A.29}$$

finally leading to the transformed effective Hamiltonian in fermionic form,

$$H_{PBC} = -J\sum_{j=1}^{N}[(c_j^\dagger c_{j+1} + \gamma c_j^\dagger c_{j+1}^\dagger + H.c.) + 2(\lambda+\epsilon_j)c_j^\dagger c_j - (\lambda+\epsilon_j)] \\ + J[c_j^\dagger c_N + \gamma c_j^\dagger c_N^\dagger + H.c.](\exp(i\pi\Pi)+1). \tag{A.30}$$

The Hamiltonian H_{PBC} takes on a quadratic form in its leading term (free spinless fermions on a cyclic chain), the first line of Eq. (A.30), which can be diagonalized by a linear transformation. The second line of Eq. (A.30) is a boundary term proportional to $\exp(i\pi\Pi)+1$. Even though $[\Pi, H_{PBC}] \neq 0$ for arbitrary γ, λ and ϵ_i, because of the $c_j^\dagger c_{j+1}^\dagger$ terms, $[\exp(i\pi\Pi), H_{PBC}] = 0$ holds. This means that $\exp(i\pi\Pi)$ can be diagonalized simultaneously with the leading term (the first line of Eq. (A.30)). We will discuss the correction of the boundary effect term after we have diagonalized the leading term. The effective Hamiltonian without the boundary effect term is

$$H = -J\sum_{j=1}^{N}[(c_j^\dagger c_{j+1} + \gamma c_j^\dagger c_{j+1}^\dagger + H.c.) + 2(\lambda+\epsilon_j)c_j^\dagger c_j - (\lambda+\epsilon_j)]. \tag{A.31}$$

We would like to find a unitary transformation to diagonalize this Hamiltonian and calculate the Loschmidt echo. The remainder of this appendix will be organized as follows. In the next section, we will discuss how to diagonalize the Hamiltonian using the Lieb-Schultz-Mattis method [101, 102]. We will then show how to calculate the Loschmidt echo of a qubit coupled to one site of the environment based on the results of the diagonalization. The advantage of this method is that it is easy to be generalize to other cases in which the qubit or qubits couples isotropically or anisotropically to arbitrary sites of the bath with arbitrary coupling strengths. For the sake of completeness, we will also introduce another method to diagonalize the Hamiltonian that is based on transforming the Hamiltonian from real space to momentum space and using the Bogoliubov transformation in the last section. This method has been frequently applied to the so-called central spin model [81, 80] and is more convenient, in some cases, to analyze with the analytical tools which will give additinal physical insight into the problem.

A.3 Lieb-Schultz-Mattis method

The fermionic Hamiltonian (A.31) can be rewritten as

$$H = \sum_{i,j=1}^{N}[(c_i^\dagger A_{ij} c_j + \frac{1}{2}(c_i^\dagger B_{ij} c_j^\dagger + H.c.)] - \frac{1}{2}\sum_{i}^{N} A_{i,i}, \tag{A.32}$$

where

$$[A]_{i,j} = -J(\delta_{i,j+1} + \delta_{j,i+1}) - 2J(\lambda + \epsilon_i)\delta_{i,j}, \tag{A.33}$$

$$[B]_{i,j} = -\gamma J(\delta_{j,i+1} - \delta_{i,j+1}). \tag{A.34}$$

Here **A** is a real Hermitian matrix due to the Hermiticity of H, and **B** is a real antisymmetric matrix due to the anticommutation relations among the c_j's.

To diagonalize the Hamiltonian (A.32), Lieb, Schultz and Mattis introduced the unitary transformation [101]

$$\eta_k = \sum_{i=1}^{N}(g_{ki}c_i + h_{ki}c_i^\dagger),\ \eta_k^\dagger = \sum_{i=1}^{N}(g_{ki}c_i^\dagger + h_{ki}c_i), \tag{A.35}$$

where g_{ki} and h_{ki} are elements of the N-length real vectors $\vec{g}_k$ and $\vec{h}_k$, respectively, which are defined by the linear combinations

$$g_{ki} = (\phi_{ki} + \psi_{ki})/2,\ h_{ki} = (\phi_{ki} - \psi_{ki})/2, \tag{A.36}$$

and the η_k's are fermionic operators which obey canonical anticommutation relations, $\{\eta_k, \eta_{k'}^\dagger\} = \delta_{kk'}$ and $\{\eta_k, \eta_{k'}\} = \{\eta_k^\dagger, \eta_{k'}^\dagger\} = 0$. These relations require that

$$\sum_i (g_{ki}h_{k'i} + h_{ki}g_{k'i}) = 0,\ (k = k',\ k \neq k') \tag{A.37a}$$

$$\sum_i (g_{ki}g_{k'i} + h_{ki}h_{k'i}) = \delta_{k,k'}. \tag{A.37b}$$

Suppose that Hamiltonian (A.32) can be diagonalized as

$$H = \sum_k \Lambda_k \eta_k^\dagger \eta_k + C, \tag{A.38}$$

where C is a constant. The constant C can be determined by analyzing the invariance of tr$H$

under different bases. From Eq. (A.32), one obtain

$$\mathrm{tr}H = 2^{N-1}\sum_{i}^{N} A_{ii} - 2^{N} \times \frac{1}{2}\sum_{i}^{N} A_{ii} = 0. \tag{A.39}$$

On the other hand, one get

$$\mathrm{tr}H = 2^{N-1}\sum_{k_1}^{k_N} \Lambda_k + 2^N C \tag{A.40}$$

from Eq. (A.38). Thus,

$$C = -\frac{1}{2}\sum_{k} \Lambda_k, \tag{A.41}$$

and

$$H = \sum_{k} \Lambda_k (\eta_k^{\dagger}\eta_k - \frac{1}{2}). \tag{A.42}$$

Noticing that the relation $[\eta_k, H] = \Lambda_k \eta_k$ and substituting (A.35) into this relation, we obtain

$$\Lambda_k g_{ki} = \sum_{j} (g_{kj}A_{ji} - h_{ki}B_{ji}), \tag{A.43a}$$

$$\Lambda_k h_{ki} = \sum_{j} (g_{kj}B_{ji} - h_{ki}A_{ji}), \tag{A.43b}$$

which can be simplified using Eq. (A.36), yielding

$$\vec{\phi}_k(\mathbf{A} - \mathbf{B}) = \Lambda_k \vec{\psi}_k, \tag{A.44a}$$

$$\vec{\psi}_k(\mathbf{A} + \mathbf{B}) = \Lambda_k \vec{\phi}_k. \tag{A.44b}$$

This implies that,

$$\vec{\phi}_k(\mathbf{A} - \mathbf{B})(\mathbf{A} + \mathbf{B}) = \Lambda_k^2 \vec{\phi}_k, \tag{A.45a}$$

$$\vec{\psi}_k(\mathbf{A} + \mathbf{B})(\mathbf{A} - \mathbf{B}) = \Lambda_k^2 \vec{\psi}_k. \tag{A.45b}$$

For period boundary conditions, the relevant matrices are

$$\mathbf{A} = -J\begin{bmatrix} 2(\lambda+\epsilon_1) & 1 & & & & 1 \\ 1 & 2(\lambda+\epsilon_2) & 1 & & & \\ & \ddots & \ddots & \ddots & & \\ & & 1 & 2(\lambda+\epsilon_{N-1}) & 1 & \\ 1 & & & 1 & 2(\lambda+\epsilon_N) & \end{bmatrix} \tag{A.46}$$

and

$$\mathbf{B} = -\gamma J\begin{bmatrix} 0 & 1 & & & -1 \\ -1 & 0 & 1 & & \\ & \ddots & \ddots & \ddots & \\ & & -1 & 0 & 1 \\ 1 & & & -1 & 0 \end{bmatrix}. \tag{A.47}$$

From Eq. (A.46) and Eq. (A.47), we can write $(\mathbf{A} - \mathbf{B})$ as

$$(\mathbf{A} - \mathbf{B})_{i,k} = -J(1-\gamma)\delta_{k,i+1} + -J(1+\gamma)\delta_{i,k+1} - 2J(\lambda+\epsilon_i)\delta_{i,k}, \tag{A.48}$$

or, explicitly,

$$(\mathbf{A} - \mathbf{B}) = -J\begin{bmatrix} 2(\lambda+\epsilon_1) & 1-\gamma & & & & 1+\gamma \\ 1+\gamma & 2(\lambda+\epsilon_2) & 1-\gamma & & & \\ & \ddots & \ddots & \ddots & & \\ & & 1+\gamma & 2(\lambda+\epsilon_{N-1}) & 1-\gamma & \\ 1-\gamma & & & 1+\gamma & 2(\lambda+\epsilon_N) & \end{bmatrix}. \tag{A.49}$$

We can write $(\mathbf{A} + \mathbf{B})$ as

$$(\mathbf{A} + \mathbf{B})_{k,j} = -J(1+\gamma)\delta_{j,k+1} + -J(1-\gamma)\delta_{k,j+1} - 2J(\lambda+\epsilon_k)\delta_{k,j}. \tag{A.50}$$

or, explicitly,

$$(\mathbf{A}+\mathbf{B}) = -J\begin{bmatrix} 2(\lambda+\epsilon_1) & 1+\gamma & & & 1-\gamma \\ 1-\gamma & 2(\lambda+\epsilon_2) & 1+\gamma & & \\ & \ddots & \ddots & \ddots & \\ & & 1-\gamma & 2(\lambda+\epsilon_{N-1}) & 1+\gamma \\ 1+\gamma & & & 1-\gamma & 2(\lambda+\epsilon_N) \end{bmatrix}. \tag{A.51}$$

Finally, we obtain the matrix $(\mathbf{A}-\mathbf{B})(\mathbf{A}+\mathbf{B})$,

$$\begin{aligned}(\mathbf{A}-\mathbf{B})(\mathbf{A}+\mathbf{B})_{i,j} = J^2[&(1-\gamma^2)(\delta_{i,j-2}+\delta_{i,j+2}) \\ &+ 2(1-\gamma)(\lambda+\epsilon_i)\delta_{i,j+1} + 2(1-\gamma)(\lambda+\epsilon_j)\delta_{j,i+1} \\ &+ 2(1+\gamma)(\lambda+\epsilon_i)\delta_{j,i+1} + 2(1+\gamma)(\lambda+\epsilon_j)\delta_{i,j+1} \\ &+ [2(1+\gamma^2)+4(\lambda+\epsilon_i)^2]\delta_{i,j}].\end{aligned} \tag{A.52}$$

For the initial state of the bath where there is no coupling to the qubit, $\epsilon_1 = \cdots = \epsilon_N = 0$, $(\mathbf{A}-\mathbf{B})(\mathbf{A}+\mathbf{B})$ is

$$(\mathbf{A}-\mathbf{B})(\mathbf{A}+\mathbf{B}) = J^2\begin{bmatrix} 4\lambda^2+2(1+\gamma^2) & 4\lambda & 1-\gamma^2 & & & 1-\gamma^2 & 4\lambda \\ 4\lambda & 4\lambda^2+2(1+\gamma^2) & 4\lambda & 1-\gamma^2 & & & 1-\gamma^2 \\ 1-\gamma^2 & 4\lambda & 4\lambda^2+2(1+\gamma^2) & 4\lambda & 1-\gamma^2 & & \\ & \ddots & \ddots & \ddots & \ddots & \ddots & \\ & & 1-\gamma^2 & 4\lambda & 4\lambda^2+2(1+\gamma^2) & 4\lambda & 1-\gamma^2 \\ 1-\gamma^2 & & & 1-\gamma^2 & 4\lambda & 4\lambda^2+2(1+\gamma^2) & 4\lambda \\ 4\lambda & 1-\gamma^2 & & & 1-\gamma^2 & 4\lambda & 4\lambda^2+2(1+\gamma^2) \end{bmatrix} \tag{A.53}$$

We will discuss the cases for arbitrary coupling strengths ϵ_j later. It remains to diagonalize the matrix $(\mathbf{A}-\mathbf{B})(\mathbf{A}+\mathbf{B})$ and then choose a set of normal modes for further application. We assume that the eigenvectors are $\phi_{kj} = \alpha_{kj}e^{ikj} + \beta_{kj}e^{-ikj}$, where α_{kj} and β_{kj} are arbitrary real or complex values. If the ϵ_j's on all different sites j are equal ($\epsilon_j = \epsilon$), a set of the normal modes could be given by Ref. [101]. (We will not show the details of choosing the set of ϕ_{kj}.) From Refs. [101] and [102], the simplest form

$$\phi_{kj} = \sqrt{\frac{2}{N}}\sin(kj),\ k>0,\ \phi_{kj} = \sqrt{\frac{2}{N}}\cos(kj),\ k\leqslant 0, \tag{A.54}$$

where

$$\begin{aligned} &k = 2\pi m/N, \\ &m = -\frac{N}{2}, -\frac{N}{2}+1, \ldots, -1, 0, 1, \ldots, \frac{N}{2}-1. \text{ (N even)} \\ &m = -\frac{(N-1)}{2}, -\frac{(N-1)}{2}+1, \ldots, -1, 0, 1, \ldots, \frac{(N-1)}{2}, \text{ (N odd),} \end{aligned} \tag{A.55}$$

with the corresponding eigenvalues

$$\Lambda_k^2 = 4J^2[1 + 2\lambda\cos k + \lambda^2 - (1-\gamma^2)\sin^2 k]. \tag{A.56}$$

We will choose all Λ_k's to be positive due to the particle-hole picture of η's in which the energy of particles below or above the Fermi point are all positive. For $\Lambda_k \neq 0$, the ψ_k's can be calculated from Eq. (A.44a), yielding

$$\begin{aligned} \psi_{kj} &= \Lambda_k^{-1}\phi_{kj}(\mathbf{A}-\mathbf{B})_{jl} \\ &= -J\Lambda_k^{-1}[(1-\gamma)\phi_{k,j+1} + (1+\gamma)\phi_{k,j-1} + 2(\lambda+\epsilon)\phi_{k,j}] \\ &= -J\Lambda_k^{-1}[\cos k\phi_{kj} + 2(\lambda+\epsilon)\phi_{kj} + \gamma\sin k\phi_{-kj}]. \end{aligned} \tag{A.57}$$

If $\lambda = 0$ and $\gamma = 0$ when $N/4$ is a integer, the eigenvalues of $(\mathbf{A}-\mathbf{B})(\mathbf{A}+\mathbf{B})$ $\Lambda_{\pm\frac{\pi}{2}} = 0$. For $\lambda = 1$, as well, the eigenvalues $\Lambda_{-\pi} = 0$. These properties will lead to some degenerate states. In these cases, Eq. (A.43a) and Eq. (A.43b) are equal. Thus, ψ_{kj} is given by

$$\psi_{kj} = \pm\phi_{kj}, \tag{A.58}$$

and the Hamiltonian can still be represented in the form of Eq. (A.42). For simplicity, we will not discuss the details of how to calculate the ground-state energy for the these two special parameter space cases ($\Lambda_k = 0$). One may shift all the k's to symmetrize their distribution around zero point to avoid a zero Λ_k, and then calculate the ground state. For example, one can choose $k = \pm\frac{(2n+1)\pi}{N}$, $n = 0, 1, \ldots, \frac{N}{2}-1$. We will also not consider these special cases in the discussions below.

We define the ground state as a vacuum state of the kth mode for all k, η_k, that is

$$\eta_k|\Psi_0\rangle = 0. \tag{A.59}$$

The corresponding ground state energy is given by Eq. (A.42),

$$E_0 = -\frac{1}{2}\sum_k \Lambda_k. \tag{A.60}$$

Now we turn to discuss the correction of the boundary effect term in Eq. (A.30),

$$J[c_j^\dagger c_N + \gamma c_j^\dagger c_N^\dagger + H.c.](\exp[i\pi\Pi] + 1). \tag{A.61}$$

Notice that the evenness or oddness of Π is invariant under any transformation. Thus, $\exp[i\pi\Pi]$ always has eigenvalues ± 1. Especially, when $N/4$ is not a integer, through the transformation Eq. (A.35), for the ground state and exited states with an even number of elementary excitations, $\exp[i\pi\Pi] = -1$ ($\langle\Pi\rangle$ is odd). Therefore, the correction term gives zero when applied to such states and hence such states are true eigenstates of the original Hamiltonian. Otherwise, for states with an odd number of elementary excitations, the remaining term $(c_N^\dagger c_1 + \gamma c_N^\dagger c_1^\dagger)$ gives a $O(1/N)$ order correction for normal modes and negligible corrections for evaluating physical quantities. Therefore, this correction term can be omitted for sufficiently large systems.

At this point, if we consider the ϵ_j's to be different on every site, the translational invariance is destroyed, and corrections to k, g_{ki}, and h_{ki} with complicated forms arise. Thus, for the sake of convenience, we do not express these corrections exactly. Instead, we directly diagonalize the matrix (A.52) to get all the normal modes ϕ_k''s (eigenvectors of $(\mathbf{A}-\mathbf{B})(\mathbf{A}+\mathbf{B})$) and the Λ_k''s. We then directly apply Eq. (A.44a) to obtain the normal modes ψ_k'.

For open boundary conditions, there are significant boundary effects in finite-size systems. The main purpose here is to check the DMRG and the exact diagonalization using the analytical results.

Without the boundary connections, $\mathbf{A}$ and $\mathbf{B}$ are given by

$$\mathbf{A} = -J\begin{bmatrix} 2(\lambda+\epsilon_1) & 1 & & & & 0 \\ 1 & 2(\lambda+\epsilon_2) & 1 & & & \\ & \ddots & \ddots & \ddots & & \\ & & 1 & 2(\lambda+\epsilon_{N-1}) & 1 & \\ 0 & & & 1 & 2(\lambda+\epsilon_N) & \end{bmatrix} \tag{A.62}$$

and

$$\mathbf{B} = -\gamma J \begin{bmatrix} 0 & 1 & & & 0 \\ -1 & 0 & 1 & & \\ & \ddots & \ddots & \ddots & \\ & & -1 & 0 & 1 \\ 0 & & & -1 & 0 \end{bmatrix}. \tag{A.63}$$

The matrices $(\mathbf{A}-\mathbf{B})$ and $(\mathbf{A}+\mathbf{B})$ are

$$(\mathbf{A}-\mathbf{B}) = -J \begin{bmatrix} 2(\lambda+\epsilon_1) & 1-\gamma & & & 0 \\ 1+\gamma & 2(\lambda+\epsilon_2) & 1-\gamma & & \\ & \ddots & \ddots & \ddots & \\ & & 1+\gamma & 2(\lambda+\epsilon_{N-1}) & 1-\gamma \\ 0 & & & 1+\gamma & 2(\lambda+\epsilon_N) \end{bmatrix} \tag{A.64}$$

$$(\mathbf{A}+\mathbf{B}) = -J \begin{bmatrix} 2(\lambda+\epsilon_1) & 1+\gamma & & & 0 \\ 1-\gamma & 2(\lambda+\epsilon_2) & 1+\gamma & & \\ & \ddots & \ddots & \ddots & \\ & & 1-\gamma & 2(\lambda+\epsilon_{N-1}) & 1+\gamma \\ 0 & & & 1-\gamma & 2(\lambda+\epsilon_N) \end{bmatrix}. \tag{A.65}$$

For the initial state of the bath with $\epsilon_1 = \cdots = \epsilon_N = 0$, the matrix $(\mathbf{A}-\mathbf{B})(\mathbf{A}+\mathbf{B})$ is given by

$$(\mathbf{A}-\mathbf{B})(\mathbf{A}+\mathbf{B}) = J^2 \begin{bmatrix} 4\lambda^2+(1-\gamma)^2 & 4\lambda & 1-\gamma^2 & & & & & 0 \\ 4\lambda & 4\lambda^2+2(1+\gamma^2) & 4\lambda & 1-\gamma^2 & & & & \\ 1-\gamma^2 & 4\lambda & 4\lambda^2+2(1+\gamma^2) & 4\lambda & 1-\gamma^2 & & & \\ & \ddots & \ddots & \ddots & \ddots & \ddots & & \\ & & 1-\gamma^2 & 4\lambda & 4\lambda^2+2(1+\gamma^2) & 4\lambda & 1-\gamma^2 & \\ & & & 1-\gamma^2 & 4\lambda & 4\lambda^2+2(1+\gamma^2) & 4\lambda & \\ 0 & & & & 1-\gamma^2 & 4\lambda & 4\lambda^2+(1+\gamma)^2 & \end{bmatrix} \tag{A.66}$$

In this case, for open boundary conditions, because of the lack of translational invariance, the expressions for the normal modes $\vec{\phi}_k$ and $\vec{\psi}_k$ are relatively complicated. Notice that if the lattice size N is odd and $\lambda = 0$, $\det((\mathbf{A}-\mathbf{B})(\mathbf{A}+\mathbf{B})) = 0$. This leads to zero eigenvalue of $(\mathbf{A}-\mathbf{B})(\mathbf{A}+\mathbf{B})$, which, in turn, generates degenerate eigenstates of the Hamiltonian. However,

because we only consider finite lattice sizes here, any finite value of λ removes this degeneracy of the ground state. So we can consider a lattice of either odd or even size when $\lambda > 0$. We can still numerically diagonalize the matrix $(\mathbf{A}-\mathbf{B})(\mathbf{A}+\mathbf{B})$ and choose a set of normal modes $\vec{\phi_k}$ and $\vec{\psi_k}$ (the eigenvectors or the corresponding linear combinations) and corresponding eigenvalues Λ_k. For $\epsilon_i \neq 0$, analogous to the above procedure, the solution, the normal modes $\vec{\phi_k'}$,$\vec{\psi_k'}$ and the eigenvalues Λ_k', can also be obtained.

For the limiting case of $\lambda = 0$, the solution for $(\mathbf{A}-\mathbf{B})(\mathbf{A}+\mathbf{B})$ is

$$\phi^I = A_k \begin{pmatrix} 0 \\ \sin 2k \\ 0 \\ \sin 4k \\ \vdots \\ 0 \\ \sin Nk \end{pmatrix}, \quad \psi^I = -A_k\delta_k \begin{pmatrix} \sin Nk \\ 0 \\ sin(N-2)k \\ 0 \\ \vdots \\ \sin 2k \\ 0 \end{pmatrix}, \tag{A.67}$$

with

$$\begin{aligned} A_k &= \left(\sqrt{\sum_{n=1}^{N/2} \sin^2 2nk} \right)^{-1} \\ &= \left(\sqrt{\frac{N}{4} - \frac{1}{4}\Big(\sum_{n=-N/2}^{N/2} e^{i4nk} - 1\Big)} \right)^{-1} \\ &= 2\left(\sqrt{N+1-\frac{\sin 2(N+1)k}{\sin 2k}} \right)^{-1}. \end{aligned} \tag{A.68}$$

Here δ_k denotes the sign of $\cos(N+1)k$. The eigenvalues are

$$\Lambda_k^2 = 1 - (1-\gamma^2)\sin^2 k. \tag{A.69}$$

The k's are the solutions of

$$\frac{\sin(N+2)k}{\sin Nk} = \frac{\gamma-1}{\gamma+1}. \tag{A.70}$$

Another solution of $(\mathbf{A}-\mathbf{B})(\mathbf{A}+\mathbf{B})$ is

$$\phi^{II} = A_k \begin{pmatrix} \sin Nk \\ 0 \\ \sin(N-2)k \\ 0 \\ \vdots \\ \sin 2k \\ 0 \end{pmatrix}, \quad \psi^{II} = -A_k \delta_k A_k \begin{pmatrix} 0 \\ \sin 2k \\ 0 \\ \sin 4k \\ \vdots \\ 0 \\ \sin Nk \end{pmatrix}, \tag{A.71}$$

with the same A_k, δ_k, and Λ_k as before. Here the k's are the solutions of

$$\frac{\sin(N+2)k}{\sin Nk} = \frac{\gamma+1}{\gamma-1}. \tag{A.72}$$

Notice that one of the solutions for k is complex here.

For the limiting case $\gamma = 0$, i.e., the transverse-field Ising model, the solution for $(\mathbf{A}-\mathbf{B})(\mathbf{A}+\mathbf{B})$ is

$$\phi = B_k \begin{pmatrix} \sin k \\ \frac{\sin k}{\lambda} + \sin 2k \\ \vdots \\ \frac{\sin(N-2)k}{\lambda} + \sin(N-1)k \\ \frac{\sin(N-1)k}{\lambda} + \sin Nk \end{pmatrix}, \tag{A.73}$$

with $B_k = \left(\sqrt{\sum_{n=1}^{N}(\frac{\sin(n-1)k}{\lambda} + \sin nk)^2}\right)^{-1}$ and $\psi_i = \Lambda_k^{-1}(2\phi_{i-1} + 2\lambda\phi_i)$, where the excitation spectrum is given by

$$\Lambda_k^2 = 4J^2(1+\lambda^2+2\lambda\cos k). \tag{A.74}$$

The k's are the roots of

$$\frac{\sin Nk}{\sin(N+1)k} = -\lambda. \tag{A.75}$$

Notice that k has a complex solution for $0 \le \lambda < 1$.

A.4 Single-coupling scheme

So far, we have carried out the Hamiltonian diagonalization. Now the Loschmidt echo can be calculated. We assume that the system (qubit) couples to only one bath site, which we take to

be the central spin (at the position $N/2$). Therefore, the qubit-bath coupling strength ϵ_i is set to $\epsilon_{N/2} = \epsilon,\ \epsilon_i = 0\ (i \neq N/2)$ in Hamiltonian (A.32). The next step is to rewrite the perturbed Hamiltonian in the form [77]

$$H = \frac{1}{2}\Psi^\dagger \mathbf{C}\Psi - \sum A_{i,i}, \tag{A.76}$$

where $\Psi^\dagger = (c_1^\dagger, \ldots, c_N^\dagger, c_1, \ldots, c_N)$, $\Psi = (c_1, \ldots, c_N, c_1^\dagger, \ldots, c_N^\dagger)^T$, and

$$\mathbf{C} = \sigma^z \mathbf{A} + i\sigma^y \mathbf{B} = \begin{pmatrix} \mathbf{A} & \mathbf{B} \\ -\mathbf{B} & -\mathbf{A} \end{pmatrix} \tag{A.77}$$

due to the canonical anti-communication relationship of fermions. Here the c_i's denotes spinless fermions.

The Loschmidt echo (3.15) corresponding to case that the bath is initially in the ground state can be evaluated by means of the formula [103, 104, 105]

$$LE(t) = \left|\langle e^{-it\sum_{i,j} C_{i,j}\Psi_i^\dagger \Psi_j}\rangle\right| = \left|\det\left(1 - \mathbf{r} + \mathbf{r}\, e^{-i\mathbf{C}t}\right)\right|, \tag{A.78}$$

and the Loschmidt echo (3.31) corresponding to case that the bath is initially in a quenched state is given by

$$\begin{aligned} LE^Q(t) &= \left|\langle e^{i(T_0+t)\sum_{i,j} C^Q_{i,j}\Psi_i^\dagger \Psi_j} e^{-it\sum_{i,j} C^{Q\prime}_{i,j}\Psi_i^\dagger \Psi_j} e^{-iT_0\sum_{i,j} C^Q_{i,j}\Psi_i^\dagger \Psi_j}\rangle\right| \\ &= \left|\det\left(1 - \mathbf{r} + \mathbf{r} e^{i\mathbf{C}^Q(t+T_0)} e^{-i\mathbf{C}^{Q\prime}t} e^{-i\mathbf{C}^Q T_0}\right)\right|, \end{aligned} \tag{A.79}$$

where $\mathbf{C}$,$\mathbf{C}^{Q\prime}$, and $\mathbf{C}^Q$ are derived from H^G, $H^{Q\prime}$, and H^Q, respectively. The elements of the $2N \times 2N$ two-point correlation matrix $\mathbf{r}$ are $r_{ij} = \langle\psi_0|\Psi_i^\dagger \Psi_j|\psi_0\rangle$ ($\Psi_i^\dagger \equiv c_i^\dagger, \ldots, \Psi_{2N}^\dagger \equiv c_N$), and $|\psi_0\rangle$ is the ground state of bath. We will begin by evaluating the Loschmidt echo $LE(t)$ (A.78). It is easy to be extended to evaluate $LE^Q(t)$ (A.79).

First, the explicit expression for the two-point correlation matrix $\mathbf{r}$ in terms of spinless

fermionic operators is

$$\mathbf{r} = \begin{pmatrix} \langle c_1^\dagger c_1\rangle & \dots & \langle c_1^\dagger c_N\rangle & \langle c_1^\dagger c_1^\dagger\rangle & \dots & \langle c_1^\dagger c_N^\dagger\rangle \\ \vdots & \ddots & \vdots & \vdots & \ddots & \vdots \\ \langle c_N^\dagger c_1\rangle & \dots & \langle c_N^\dagger c_N\rangle & \langle c_N^\dagger c_1^\dagger\rangle & \dots & \langle c_N^\dagger c_N^\dagger\rangle \\ \langle c_1 c_1\rangle & \dots & \langle c_1 c_N\rangle & \langle c_1 c_1^\dagger\rangle & \dots & \langle c_1 c_N^\dagger\rangle \\ \vdots & \ddots & \vdots & \vdots & \ddots & \vdots \\ \langle c_N c_1\rangle & \dots & \langle c_N c_N\rangle & \langle c_N c_1^\dagger\rangle & \dots & \langle c_N c_N^\dagger\rangle \end{pmatrix}_{(2N\times 2N)} . \tag{A.80}$$

We can evaluate the matrix $\mathbf{r}$ by transforming all c_i's into η_k's which are the eigenmodes of the initial bath Hamiltonian. By inverting Eq. (A.35), we obtain

$$c_i = \sum_{k=k_1}^{k_N} (g_{k,i}\eta_k + h_{k,i}\eta_k^\dagger),\ c_i^\dagger = \sum_{k=k_1}^{k_N} (g_{k,i}\eta_k^\dagger + h_{k,i}\eta_k). \tag{A.81}$$

Notice that we define the ground state as a vacuum state without any excitations of the η_k mode, that is $\langle \eta_k | \eta_{k'}^\dagger\rangle = \delta_{k,k'}$. We can directly evaluate $\mathbf{r}$ using

$$\mathbf{r} = \sum_{k=k_1}^{k=k_N} \begin{pmatrix} h_{k,1}h_{k,1} & \dots & h_{k,1}h_{k,N} & h_{k,1}g_{k,1} & \dots & h_{k,1}g_{k,N} \\ \vdots & \ddots & \vdots & \vdots & \ddots & \vdots \\ h_{k,N}h_{k,1} & \dots & h_{k,N}h_{k,N} & h_{k,N}g_{k,1} & \dots & h_{k,N}g_{k,N} \\ g_{k,1}h_{k,1} & \dots & g_{k,1}h_{k,N} & g_{k,1}g_{k,1} & \dots & g_{k,1}g_{k,N} \\ \vdots & \ddots & \vdots & \vdots & \ddots & \vdots \\ g_{k,N}h_{k,1} & \dots & g_{k,N}h_{k,N} & g_{k,N}g_{k,1} & \dots & g_{k,N}g_{k,N} \end{pmatrix}_{(2N\times 2N)} . \tag{A.82}$$

Second, we can evaluate $e^{i\mathbf{C}t}$ by diagonalizing the perturbed Hamiltonian (A.76),

$$H' = \frac{1}{2}\Psi^\dagger \mathbf{C}\Psi = \frac{1}{2}\mathbf{\Gamma}^\dagger \mathbf{U}\mathbf{C}\mathbf{U}^\dagger \mathbf{\Gamma} = \frac{1}{2}\mathbf{\Gamma}^\dagger \mathbf{D}\mathbf{\Gamma}, \tag{A.83}$$

where $\mathbf{\Gamma}^\dagger = (\eta_{k_1}^{(\prime)\dagger} \dots \eta_{k_N}^{(\prime)^\dagger} \eta_1^{(\prime)} \dots \eta_N^{(\prime)})$ and $\mathbf{\Psi}^\dagger = \mathbf{\Gamma}^\dagger \mathbf{U}$. Here $\mathbf{U}$ is a unitary transformation matrix

defined by

$$\mathbf{U} = \begin{pmatrix} g^{(\prime)}_{k_1,1} & \cdots & g^{(\prime)}_{k_1,N} & h^{(\prime)}_{k_1,1} & \cdots & h^{(\prime)}_{k_1,N} \\ \vdots & \ddots & \vdots & \vdots & \ddots & \vdots \\ g^{(\prime)}_{k_N,1} & \cdots & g^{(\prime)}_{k_N,N} & h^{(\prime)}_{k_N,1} & \cdots & h^{(\prime)}_{k_N,N} \\ h^{(\prime)}_{k_1,1} & \cdots & h^{(\prime)}_{k_1,N} & g^{(\prime)}_{k_1,1} & \cdots & g^{(\prime)}_{k_1,N} \\ \vdots & \ddots & \vdots & \vdots & \ddots & \vdots \\ h^{(\prime)}_{k_N,1} & \cdots & h^{(\prime)}_{k_N,N} & g^{(\prime)}_{k_N,1} & \cdots & g^{(\prime)}_{k_N,N} \end{pmatrix}_{(2N\times 2N)} . \tag{A.84}$$

Obviously, $\mathbf{D} = \mathbf{U}\mathbf{C}\mathbf{U}^\dagger$ is a diagonal matrix whose elements are the eigenvalues of $(\mathbf{A}-\mathbf{B})(\mathbf{A}+\mathbf{B})$ and their negatives,

$$\mathbf{D} = \begin{pmatrix} \mathbf{\Lambda}' & \mathbf{0} \\ \mathbf{0} & -\mathbf{\Lambda}' \end{pmatrix}_{(2N\times 2N)} . \tag{A.85}$$

Also notice that $\mathbf{C} = \mathbf{U}^\dagger\mathbf{D}\mathbf{U}$, from which one can easily evaluate the exponential $e^{-i\mathbf{C}t}$. Similarly, by replacing H' with H_Q or $H_{Q\prime}$, we can also evaluate $e^{-i\mathbf{C}^Q t}$ or $e^{-i\mathbf{C}^{Q\prime}t}$. The final task is to numerically evaluate the determinant (A.78) or (A.79) to get the Loschmidt echo.

A.5 Central spin model

Hamiltonian (A.31) can be diagonalized in momentum space. We write

$$\begin{aligned} c_j &= \frac{1}{\sqrt{N}}\sum_k e^{-ikj}c_k, \qquad (A.86)\\ k &= \frac{2\pi n}{N}, \quad n = -\frac{N}{2}, -\frac{N}{2}+1, \ldots, 0, \ldots, \frac{N}{2}-1, \quad (\text{N even})\\ k &= \frac{2\pi n}{N}, \quad n = -\frac{N-1}{2}, -\frac{N-3}{2}, \ldots, 0, \ldots, \frac{N-1}{2}, \quad (\text{N odd}). \end{aligned}$$

Substituting Eq. (A.86) into Eq. (A.31), we obtain

$$\begin{aligned} H_k &= -J\sum_k [2(\lambda+\cos k)c_k^\dagger c_k + i\gamma \sin k(c_{-k}^\dagger c_k^\dagger + c_{-k}c_k) - \lambda],\\ &\Rightarrow -2J\sum_{k>0}[(\lambda+\cos k)(c_k^\dagger c_k + c_{-k}^\dagger c_{-k}) + i\gamma\sin k(c_{-k}^\dagger c_k^\dagger + c_{-k}c_k) - \lambda]. \end{aligned} \tag{A.87}$$

Notice that for calculating the ground state energy, the omitted terms $c_{-\pi}^\dagger c_{-\pi}$ and $c_0^\dagger c_0$ can be picked back up later. However, they are negligible when evaluating the Loschmidt echo.

Either in the thermodynamic limit or on a finite size lattice, such terms do not contribute to the Loschmidt echo, see below.

We then use the Bogoliubov transformation to map the c_k's onto a new set of fermionic η_k's:

$$\eta_k = u_k c_k - i v_k c_{-k}^\dagger, \quad \eta_k^\dagger = u_k c_k^\dagger + i v_k c_{-k}. \tag{A.88}$$

The inverse of (A.88) is

$$c_k = u_k \eta_k + i v_k \eta_{-k}^\dagger, \quad c_k^\dagger = u_k \eta_k^\dagger - i v_k \eta_{-k}, \tag{A.89}$$

where u_k and v_k are real numbers satisfying $u_k^2 + v_k^2 = 1$ and $u_{-k} = u_k$, $v_{-k} = -v_k$, and η_k obeys the canonical fermion anticommutation relations

$$\{\eta_k, \eta_{k'}^\dagger\} = \delta_{k,k'}, \ \{\eta_k^\dagger, \eta_{k'}^\dagger\} = 0. \tag{A.90}$$

We insert Eq. (A.89) into Eq. (A.87) and choose $u_k = \cos(\theta_k/2)$, $u_k = \sin(\theta_k/2)$. We then set all the coefficients of the terms with $\eta_k \eta_{-k}$ and $\eta_k^\dagger \eta_{-k}^\dagger$ to 0. We finally diagonalize the Hamiltonian (A.87), resulting in

$$H_k = \sum_k \Lambda_k (\eta_k^\dagger \eta_k - 1/2) \Rightarrow \sum_{k>0} \Lambda_k (\eta_k^\dagger \eta_k - \eta_{-k} \eta_{-k}^\dagger), \tag{A.91}$$

where

$$\Lambda_k = 2J \sqrt{(\cos k + \lambda)^2 + \gamma^2 \sin^2 k}. \tag{A.92}$$

Here, we take all the Λ_k to be positive. Eq. (A.56) is then recovered. The ground state is defined as a vacuum state of every eigenmode, $\eta_k |\Psi_0\rangle = 0$, and the ground state energy is expressed as $E_0 = -1/2 \sum_k \Lambda_k$. The Bogoliubov coefficients satisfy

$$\tan \theta_k = \frac{\gamma \sin k}{\cos k + \lambda}. \tag{A.93}$$

For a set of initial values, J, λ and γ, we can obtain the eigenmodes η^G and the corresponding eigenvalues Λ_k^G, as well as the Bogoliubov transformation coefficients u_k^G and u_k^G of the initial Hamiltonian. The effective Hamiltonian H^Q for the quantum quench and the effective Hamiltonian $H^{Q\prime}$ containing the coupling between the qubit and the bath are can also be diagonalized in a similar way. For the case of the central spin model [81, 80], the effect of the coupling is essentially a quantum quench because the qubit couples to every site of the bath.

Below, we will compute the Loschmidt echo for a ground state bath first, and then analyze the Loschmidt echo for the case of a quenched bath.

Using a Bogoliubov transformation, we can connect the eigenmodes of the different Hamiltonians,

$$\eta_k^G = U_k \eta_k^Q - iV_k \eta_{-k}^{Q\dagger}, \tag{A.94}$$

where

$$U_k = u_k^G u_k^Q + v_k^G v_k^Q = \cos((\theta_k^Q - \theta_k^G)/2) = \cos(\alpha_k), \tag{A.95}$$

$$V_k = u_k^G v_k^Q - v_k^G u_k^Q = \sin((\theta_k^Q - \theta_k^G)/2) = \sin(\alpha_k). \tag{A.96}$$

Hence $\eta_k^G|\Psi_0^G\rangle = (U_k\eta_k^Q - iV_k\eta_{-k}^{Q\dagger})|\Psi_0^G\rangle = 0$, and the formal solution of $|\Psi_0^G\rangle$ is possible to relate the ground state $|\Psi_0^Q\rangle$ of H^Q as

$$|\Psi_0^G\rangle = \prod_{k>0}(\cos\alpha_k + i\sin\alpha_k \eta_k^{Q\dagger}\eta_{-k}^{Q\dagger})|\Psi_0^Q\rangle. \tag{A.97}$$

The BCS-like state $|\Psi_0^G\rangle$ is automatically normalized, $\langle\Psi_0^G|\Psi_0^G\rangle = 1$. Applying the time evolution operator to this state, we obtain

$$e^{-iH^Q t}|\Psi_0^G\rangle = e^{-iH^Q t}\prod_{k>0}(\cos\alpha_k + i\sin\alpha_k \eta_k^{Q\dagger}\eta_{-k}^{Q\dagger})|\Psi_0^Q\rangle = \prod_{k>0}(e^{i\Lambda_k^Q t}\cos\alpha_k + e^{-i\Lambda_k^Q t} i\sin\alpha_k \eta_k^{Q\dagger}\eta_{-k}^{Q\dagger})|\Psi_0^Q\rangle. \tag{A.98}$$

The Loschmidt echo can then be evaluated in a simple form as

$$LE(t) = |\langle\Psi_0^G|e^{-iH^Q t}|\Psi_0^G\rangle|^2 = |\prod_{k>0}(e^{i\Lambda_k^Q t}\cos^2\alpha_k + e^{-i\Lambda_k^Q t}\sin^2\alpha_k)|^2 = \prod_{k>0}[1 - \sin^2(2\alpha_k)\sin^2(\Lambda_k^Q t)]. \tag{A.99}$$

Eq. (A.99) can be directly evaluated.

From now on, we take a quenched state as the initial state of the bath. The effect of the coupling between the qubit and the bath is in fact another quantum quench of the bath. We can also connect the eigenmodes $\eta_k^{Q'}$ of the Hamiltonian $H^{Q'}$ to the eigenmodes η_k^Q of the Hamiltonian H^Q with

$$\eta_k^{Q'} = X_k \eta_k^Q - iY_k \eta_{-k}^{Q\dagger}, \tag{A.100}$$

where

$$X_k = u_k^{Q\prime} u_k^Q + v_k^{Q\prime} v_k^Q = \cos((\theta_k^Q - \theta_k^{Q\prime})/2) = \cos(\beta_k), \tag{A.101}$$

$$Y_k = u_k^{Q\prime} v_k^Q - v_k^{Q\prime} u_k^Q = \sin((\theta_k^Q - \theta_k^{Q\prime})/2) = \sin(\beta_k). \tag{A.102}$$

We then need to express the Hamiltonian $H^{Q\prime}$ in terms of the eigenmodes η_k^Q of the Hamiltonian H^Q, giving

$$\begin{aligned} H^{Q\prime} &= \sum_{k>0} \Lambda_k^{Q\prime} (\eta_k^{Q\prime\dagger} \eta_k^{Q\prime} - \eta_{-k}^{Q\prime} \eta_{-k}^{Q\prime\dagger}) \\ &= \sum_{k>0} \Lambda_k^{Q\prime} [\cos(2\beta_k) \eta_k^{Q\dagger} \eta_k^Q - \cos(2\beta_k) \eta_{-k}^Q \eta_{-k}^{Q\dagger} + i \sin(2\beta_k) \eta_{-k}^Q \eta_k^Q - i \sin(2\beta_k) \eta_k^{Q\dagger} \eta_{-k}^{Q\dagger}]. \end{aligned} \tag{A.103}$$

Thus, we can directly apply the time evolution operator $e^{-iH^{Q\prime}t}$ to the quenched state. Assuming the waiting time after the quantum quench is T_0, we obtain

$$\begin{aligned} e^{-iH^{Q\prime}t} e^{-iH^Q T_0} |\Psi_0^G\rangle &= e^{-iH^{Q\prime}t} \prod_{k>0} (e^{i\Lambda_k^Q T_0} \cos\alpha_k + e^{-i\Lambda_k^Q T_0} i \sin\alpha_k \eta_k^{Q\dagger} \eta_{-k}^{Q\dagger}) |\Psi_0^Q\rangle \\ &= \prod_{k>0} (A + B \eta_k^{Q\dagger} \eta_{-k}^{Q\dagger})) |\Psi_0^Q\rangle, \end{aligned} \tag{A.104}$$

where

$$\begin{aligned} A &= \cos(\alpha_k) \cos(\Lambda_k^{Q\prime} t) e^{i\Lambda_k^Q T_0} \\ &\quad + i \cos(\alpha_k) \cos(2\beta_k) \sin(\Lambda_k^{Q\prime} t) e^{i\Lambda_k^Q T_0} + i \sin(\alpha_k) \sin(2\beta_k) \sin(\Lambda_k^{Q\prime} t) e^{-i\Lambda_k^Q T_0}, \end{aligned} \tag{A.105}$$

$$\begin{aligned} B &= i \sin(\alpha_k) \cos(\Lambda_k^{Q\prime} t) e^{-i\Lambda_k^Q T_0} \\ &\quad + \sin(\alpha_k) \cos(2\beta_k) \sin(\Lambda_k^{Q\prime} t) e^{-i\Lambda_k^Q T_0} - \cos(\alpha_k) \sin(2\beta_k) \sin(\Lambda_k^{Q\prime} t) e^{i\Lambda_k^Q T_0}. \end{aligned} \tag{A.106}$$

Thus,

$$\langle \Psi_0^G | e^{iH^Q(T_0+t)} e^{-iH^{Q\prime}t} e^{-iH^Q T_0} |\Psi_0^G\rangle = \prod_{k>0} \left[A \cos(\alpha_k) e^{-i\Lambda_k^Q (T_0+t)} - i \sin(\alpha_k) e^{i\Lambda_k^Q (T_0+t)} B \right]. \tag{A.107}$$

Finally, we obtain the Loschmidt echo

$$LE(t) = \prod_{k>0} \left[|A|^2 \cos^2(\alpha_k) + |B|^2 \sin^2(\alpha_k) - iA^* B \sin(2\alpha_k) e^{2i\Lambda_k^Q (T_0+t)}/2 + iB^* A \sin(2\alpha_k) e^{-2i\Lambda_k^Q (T_0+t)}/2 \right]. \tag{A.108}$$

We can then directly evaluate the Loschmidt echo (A.108). This coupling scheme, a qubit coupled uniformly to all the spins of the bath may drive a quantum phase transition of the bath in some situations. It does not lead to a physically interesting bath. A global quantum quench can cause a quick evolution of the bath. For this reason, people have turned to treating local couplings between the qubit and the bath, although many studies of this central spin model have been carried out.

Appendix B

Numerical error in t-DMRG calculations of the Loschmidt echo

In this appendix, we use examples to analyze numerical error in the adaptive time-dependent DMRG (t-DMRG) calculations (using a second-order Suzuki-Trotter decomposition) of the Loschmidt echo (the XXZ bath) by comparing with analytical results for a system (qubit) coupled to a ground-state bath through Ising coupling in Fig. B.1, exact diagonalization (ED) results for a system coupled to a quenched bath with Ising coupling in Fig. B.2 and for a system coupled to a ground-state bath through Heisenberg coupling in Fig. B.3.

We begin our analysis by comparing the analytical results and the t-DMRG results. As mentioned in Appendix A, the Loschmidt echo of a system coupled to a ground-state XXZ chain ($\Delta = 0$) through Ising coupling can be analytically evaluated. We consider the system coupled to a XXZ chain with lattice size $L = 50$. The coupling constant of the XXZ chain, Eq. (3.27), is $J = 1$. The system couples to a spin in the middle of the lattice at the position $j = 25$ with strength $\epsilon = 0.2$. In Fig. B.1 (a), we treat systems with OBCs using t-DMRG calculations with $\Delta t = 0.001, 0.005$ and 0.01 for the time evolution and discarded weight below 10^{-13}. It can be seen that all the t-DMRG results of the Loschmidt echo numerically coincide with the analytical results. The relative error of the Loschmidt echo for the different calculations is always below 1.2×10^{-6}. We find that the required number of the states increases to a maximal value ($M = 330$) and retains this value after the time $t \approx 7.5$. Here the DMRG truncation errors are dominant for the calculations of the Loschmidt echo. More states kept in the calculations lead to better results. The calculations for $\Delta t = 0.001$ keep less states ($M \approx 330$) than those of the cases of $\Delta t = 0.005$ and $\Delta t = 0.01$ and are accordingly less accurate. In Fig. B.1 (b), we show t-DMRG calculations with fixed numbers of states

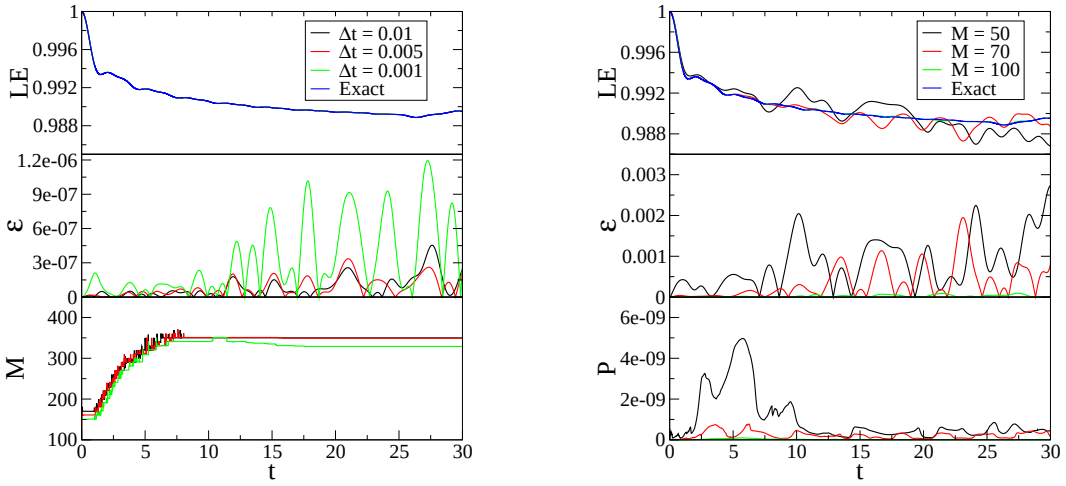

Figure B.1: Comparison of analytical results and t-DMRG results for the Loschmidt echo (LE) of a qubit coupled to a spin-1/2 XXZ chain ($\Delta = 0$) with lattice size $L = 50$ and OBCs. The Ising-type qubit-bath interaction strength is $\epsilon = 0.2$. The initial state of the bath is a ground state. (a) t-DMRG calculations with a discarded weight below $P = 10^{-13}$ for time intervals $\Delta t = 0.001, 0.005,$ and 0.01. (b) t-DMRG calculations with fixed numbers of states $M = 50, 70,$ and 100 with time interval $\Delta t = 0.001$.

$M = 50, 70,$ and 100 with $\Delta t = 0.001$. We find that only the calculation keeping $M = 100$ states. provides numerically accurate results. Thus, keeping the discarded weight below 10^{-13} ensures that the t-DMRG calculations are numerical accurate. In fact, we do almost all the calculations using $\Delta t = 0.001$ with a maximal discarded weight $P = 10^{-13}$. For the case of the XXZ chain with $\Delta \neq 0$, we cannot obtain analytical results in general. Thus, we can only compare the t-DMRG results to the ED results. We will not show this comparison because this situation is contained in the case of the quenched bath below.

We test our t-DMRG results for the case of a quenched XXZ bath with lattice size $L = 11$ and OBCs by comparing with ED results. The quench is form $\Delta_0 = -0.25$ to $\Delta_t = -20$. The initial quenched bath state is at waiting time $T_0 = 5$ after the quench. The coupling constant J of the XXZ chain and the Ising qubit-bath coupling strength are chosen as before. The qubit couples to one spin in the middle of the lattice at the position $j = 6$. In Fig. B.2, using t-DMRG calculations with $\Delta t = 0.001$ for the time evolution and discarded weight below 10^{-13}, we treat systems with OBCs. Here the t-DMRG results of the Loschmidt echo numerically coincide with the ED results. The relative error of the Loschmidt echo is always below 2.4×10^{-5}. We find that the required number of the states increases from $M = 50$ to a maximal value of $M = 53$ and retains this value after the time $t \approx 0.4$.

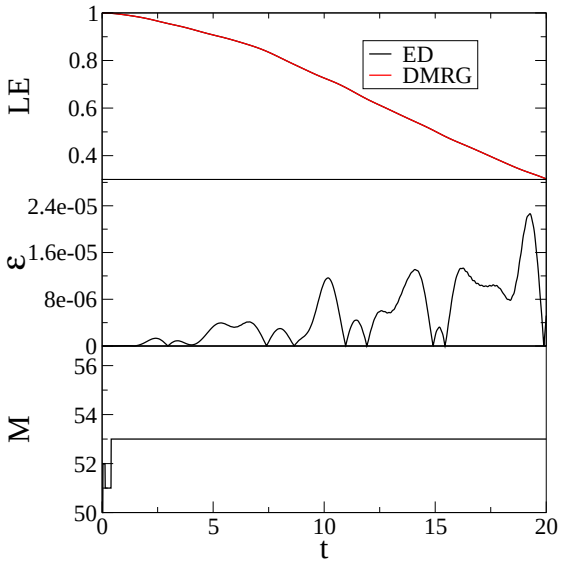

Figure B.2: Comparison of ED results and t-DMRG results for the Loschmidt echo (LE) of a qubit coupled to a quenched spin-1/2 XXZ bath with lattice size $L = 11$ and OBCs. The Ising type qubit-bath interaction strength is $\epsilon = 0.2$. The quench is from $\Delta_0 = -0.25$ to $\Delta_t = -20$ and the waiting time after the quench is $T_0 = 5$.

Finally, we test our t-DMRG calculations for the case of a Heisenberg qubit-bath coupling by comparing with ED results. We consider only an initial state that is a ground state. The XXZ bath has a lattice size $L = 12$ and OBCs. The coupling constant J of the XXZ chain is chosen as before. The strength of Heisenberg qubit-bath coupling is $\varepsilon^x = \varepsilon^y = \varepsilon^z = 0.2$. The qubit couples to one spin in the middle of the lattice at the position $j = 6$. In Fig. B.3, using t-DMRG calculations with $\Delta t = 0.001$ for the time evolution, discarded weight below 10^{-13}, we treat systems with OBCs. We find that the t-DMRG results of the Loschmidt echo numerically coincide with the ED results. The relative error of the Loschmidt echo is always below 4×10^{-7}. We find that the required number of the states increases from $M = 42$ to a maximal value of $M = 91$ and retains this value after the time $t \approx 3.1$.

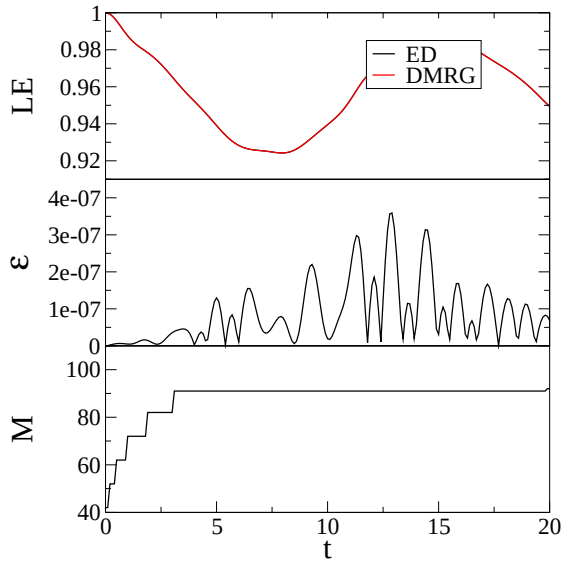

Figure B.3: Comparison of ED results and t-DMRG results for the Loschmidt echo (*LE*) of a qubit coupled to a spin-1/2 XXZ chain with lattice size $L = 12$ and OBCs. The initial state of the bath is a ground state. The coupling constants of the XXZ chain are $J = 1$ and $\Delta = -0.5$. The qubit couples to the middle site of the bath-environment ($j = 6$) with Heisenberg coupling strength $\varepsilon^x = \varepsilon^y = \varepsilon^z = 0.2$.

Appendix C

Finite size effects in the Loschmidt echo

In this appendix, corresponding to Sec. 3.4.2, we illustrate the finite-size effects in the Loschmidt echo for the case of a transverse-field Ising bath with a quenched initial state ($\lambda_0 = 2$ and $\lambda_Q = 1$). The coupling constant $J = 1$ of the bath and the qubit-bath coupling $\epsilon = 0.5$ are the same as those in Sec. 3.4.2. In addition, we also discuss the finite-size effects for the maximum T_0 treated for the same quench in the investigation of the Gaussian decay parameter $\alpha(T_0)$.

In Fig. C.1, we show the Loschmidt echo for lattice sizes $L = 50, 100,$ and 300 after waiting times $T_0 = 0, 10,$ and 100. All decay to 0, but have some revivals in the curves of the Loschmidt echo. The curves of the Loschmidt echo for different T_0 deviate from each other. The first revival times of the Loschmidt echo are linearly dependent on the lattice size. We do not explicitly consider what happens to the first revival of the Loschmidt echo for $T_0 = 10$ and 100, because the finite-size effects in the long-time dynamics of the Loschmidt echo are more serious for long waiting times T_0. For simplicity, we only consider the case of $T_0 = 0$. The values of the first minimum of the Loschmidt echo for $T_0 = 0$ are dependent on the lattice size: $LE_{min}(L = 50) \approx 0.907$, $LE_{min}(L = 100) \approx 0.824$, $LE_{min}(L = 200) \approx 0.679$, and $LE_{min}(L = 300) \approx 0.559$. We conjecture that the Loschmidt echo for $T_0 = 0$ should decay smoothly to 0 without any revivals when the lattice size tends to thermodynamic limit. Notice that there is no obvious lattice size dependence of the time at which the Loschmidt echo reaches 0, see Fig. C.1.

In Fig. C.2, the Gaussian decay parameter $\alpha(T_0)$ weakly oscillates around the time-average value $\bar{\alpha} = 0.04026$ for lattice sizes $L = 50, 100,$ and 300. A weak oscillation starts at $T_0 = 1.3$ and then turns into a strong oscillation after a maximum time for quasi-stable behavior $T_0 = 10.2$ for $L = 50$, $T_0 = 20.6$ for $L = 100$, and $T_0 = 72.2$ for $L = 300$. The maximum time

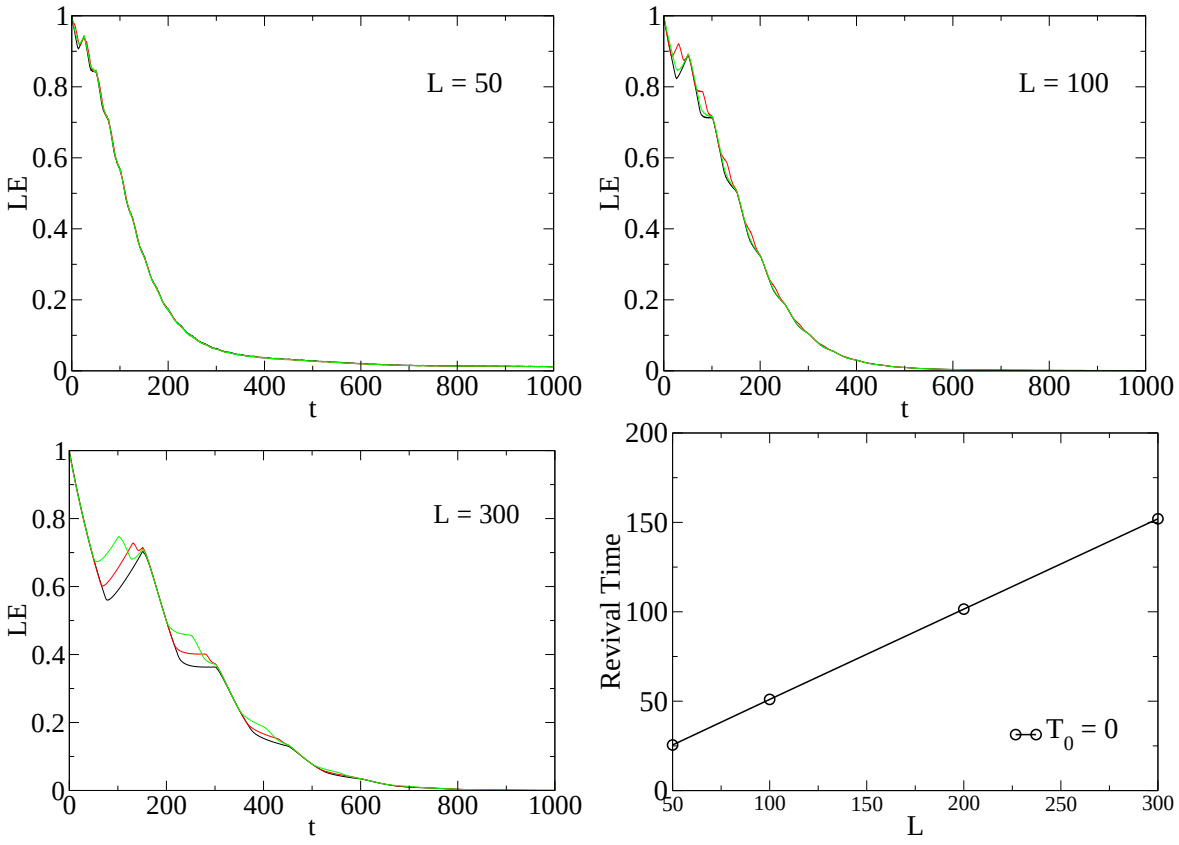

Figure C.1: Finite-size effects in the Loschmidt echo of a qubit coupled to a transverse-field Ising chain with different lattice sizes for the quantum quench form $\lambda_0 = 2$ to $\lambda_Q = 1$ after waiting times $T_0 = 0$ (black), $T_0 = 10$ (black), and $T_0 = 100$ (green).

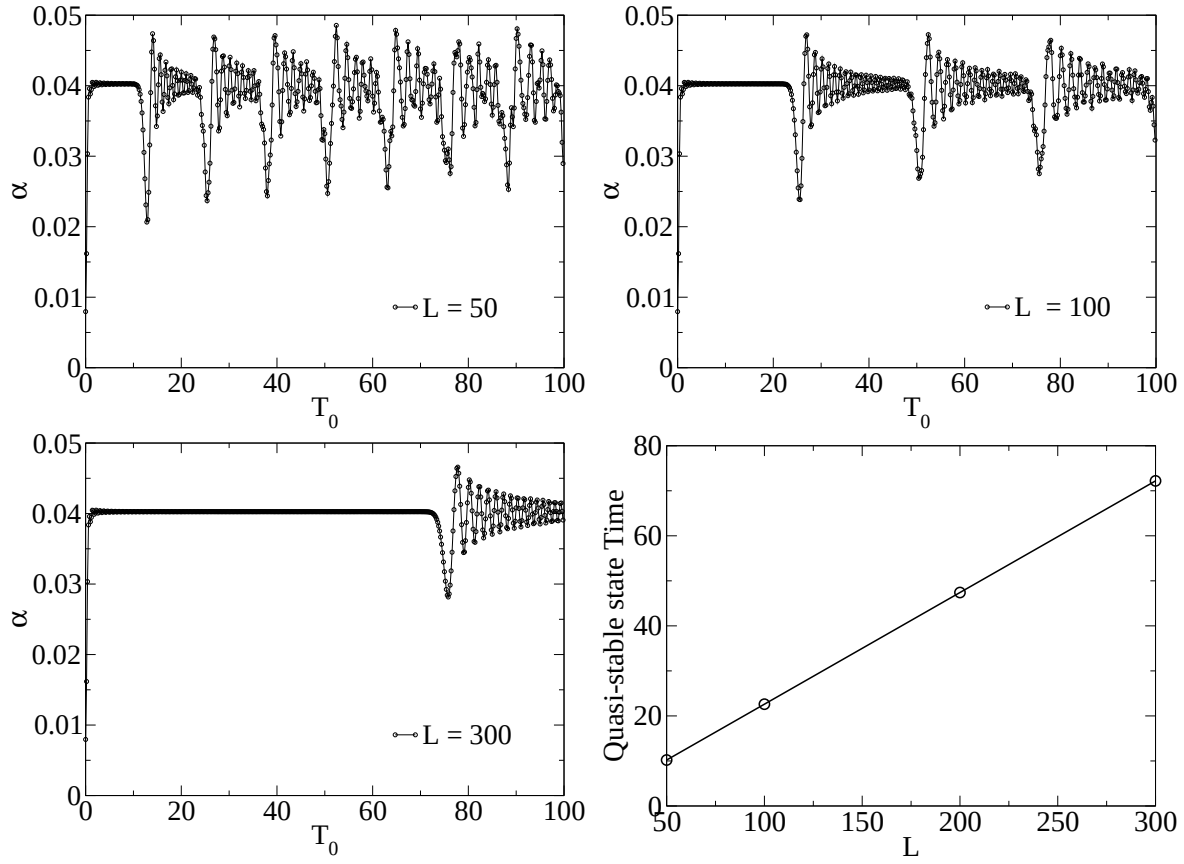

Figure C.2: Finite-size effects in the Gaussian decay parameter $\alpha(T_0)$ of a qubit coupled to a transverse-field Ising chain with different lattice sizes for the quantum quench form $\lambda_0 = 2$ to $\lambda_Q = 1$.

for quasi-stable behavior is linearly dependent on the lattice size.

Bibliography

[1] A. A. Abrikosov, L. P. Gorkov, and I. E. Dzyaloshinski. Methods of Quantum Field Theory in Statistical Mechanics (Dover Publications, 1975).

[2] H. Bruus and K. Flensberg, Many-Body Quantum Theory in Condensed Matter Physics: An Introduction (Oxford University Press, 2004).

[3] F. D. M. Haldane, J. Phys. C: Solid State Phys. **14**, 2585 (1981); F. D. M. Haldane, Phys. Rev. Lett. **45**, 1358 (1980).

[4] X. G. Wen, Phys. Rev. B **41**, 12838 (1990).

[5] T. Giamarchi, Quantum Physics in One Dimension (Oxford University Press, 2004).

[6] J. Jain, Composite Fermions (Cambridge University Press, 2007).

[7] F. H. L. Essler, H. Frahm, F. Göhmann, A. Klümper, and V. E. Korepin, The One-Dimensional Hubbard Model (Cambridge University Press, 2005).

[8] P. Schlottmann, Phys. Rev. B **36**, 5177 (1987).

[9] F. H. L. Essler and V. E. Korepin, Phys. Rev. B **46**, 9147 (1992).

[10] A. Gogolin, A. Nersesyan,and A. Tsvelik, Bosonization and Strongly Correlated Systems (Cambridge University Press, 1998).

[11] S. R. White, Phys. Rev. Lett. **69**, 2863 (1992); Phys. Rev. B **48**, 10345 (1993).

[12] I. Peschel, X. Wang, M. Kaulke, and K. Hallberg, eds., Density Matrix Renormalization - A New Numerical Method in Physics (Springer Verlag, Berlin, 1999).

[13] U. Schollwöck, Rev. Mod. Phys. **77**, 259 (2005).

[14] S. Sachdev, Quantum Phase Transitions (Cambridge University Press, 1999).

[15] M. Greiner, O. Mandel, T.ZW. Hänsch, and I. Bloch, Nature (London) **419**, 51 (2002).

[16] T. Kinoshita, T. Wenger, and D. S. Weiss, Nature (London) **440**, 900 (2006).

[17] L. E. Sadler, J. M. Higbie, S. R. Leslie, M. Vengalattore, and D. M. Stamper-Kurn, Nature (London) **443**, 312 (2006).

[18] C. N. Weiler, T. W. Neely, D. R. Scherer, A. S. Bradley, M. J. Davis, and B. P. Anderson, Nature (London) **455**, 948 (2008).

[19] P. Calabrese and J. Cardy, Phys. Rev. Lett. **96**, 136801 (2006).

[20] P. Calabrese and J. Cardy, J. Stat. Mech. P06008 (2007).

[21] S. R. White and A. E. Feiguin, Phys. Rev. Lett. **93**, 076401 (2004).

[22] A. J. Daley, C. Kollath, U. Schollwöck, and G. Vidal, J. Stat. Mech. P04005 (2004).

[23] W. H. Zurek, arXiv: quant-ph/0306072.

[24] W. H. Zurek, Phys. Rev. D **26**, 1862 (1982).

[25] W. H. Zurek, Rev. Mod. Phys **75**, 715 (2003).

[26] K. G. Wilson, Rev. Mod. Phys. **47**, 773 (1975).

[27] H.R. Krishna-murthy, J.W. Wilkins and K.G. Wilson, Phys. Rev. B **21**, 1044 (1980).

[28] J. W. Bray and S. T. Chui, Phys. Rev. B **19**, 4876(1979).

[29] T. Xiang and G. A. Gehring, Phys. Rev. B **48**, 303 (1993).

[30] S. R. White and R. M. Noack, Phys. Rev. Lett. **68**, 3487 (1992).

[31] W. Hofstetter, Phys. Rev. Lett. **85**, 1508 (2000).

[32] G. Vidal, J. I. Latorre, E. Rico, and A. Kitaev, Phys. Rev. Lett. **90**, 227902(2003).

[33] J. I. Latorre, E. Rico, G. Vidal, Quant. Inf. Comput. **4**, 48 (2004).

[34] P. Calabrese and J. Cardy, J. Stat. Mech. P06002 (2004).

[35] J. Cardy, O. A. Castro-Alvaredo and B. Doyon, J. Stats. Phys. **130**, 129 (2008).

[36] M. Srednicki, Phys. Rev. Lett. **71**, 666 (1993).

[37] J. Eisert, M. Cramer and M. B. Plenio, Rev. Mod. Phys. **82**, 277 (2010).

[38] I. P. McCulloch and M. Gulácsi, Europhys. Lett. **57**, 852 (2002).

[39] S. R. White, Phys. Rev. Lett. **77**, 3633 (1996).

[40] S. Östlund and S. Rommer, Phys. Rev. Lett. **75**, 3537 (1995).

[41] T. D. Kühner and S. R. White, Phys. Rev. B **60**, 335 (1999).

[42] E. Jeckelmann, Phys. Rev. B **66**, 045114 (2002).

[43] M. Cazalilla and B. Marston, Phys. Rev. Lett. **88**, 256403 (2002).

[44] William H. Press, Saul A. Teukolsky, William T. Vetterling, Brian P. Flannery, Numerical Recipes 3rd Edition: The Art of Scientific Computing (Cambridge University Press, 2007).

[45] H. G. Luo, T. Xiang and X. Q. Wang, Phys. Rev. Lett. **91**, 049701 (2003).

[46] P. Schmitteckert, Phys. Rev. B **70**, 121302 (2004).

[47] A. E. Feiguin and S. R. White, Phys. Rev. B **72**, 020404R (2005).

[48] G. Vidal, Phys. Rev. Lett. **91**, 147902 (2003).

[49] G. Vidal, Phys. Rev. Lett. **93**, 040502 (2004).

[50] S. R. Manmana, A. Muramatsu, R. M. Noack, AIP Conf. Proc. **789**, 269 (2005).

[51] S. R. White and I. Affleck, Phys. Rev. B **77**, 134437 (2008).

[52] E. Forest and R. D. Ruth, Physica D **43**, 105 (1990).

[53] I. P. Omelyan, I. M. Mryglod, and R. Folk, Comput. Phys. Commun. **146**, 188 (2002).

[54] E. H. Lieb and F. Y. Wu, Phys. Rev. Lett. **20**, 1445 (1968); **21**, 192(E) (1968).

[55] H. Kiess, ed., Conjugated conducting polymers, vol. 102 of Springer Series in Solid-State Sciences (Springer, Berlin, Heidelberg, 1982).

[56] Y.-J. Kim, J. P. Hill, H. Benthien, F. H. L. Essler, E. Jeckelmann, H. S. Choi, T. W. Noh, N. Motoyama, K. M. Kojima, S. Uchida, et al., Phys. Rev. Lett. **92**, 137402 (2004).

[57] H. Benthien, F. Gebhard, and E. Jeckelmann, Phys. Rev. Lett. **92**, 256401 (2004).

[58] M. Nakamura, J. Phys. Soc. Jpn. **68**, 3123 (1999); Phys. Rev. B **61**, 16377 (2000).

[59] A. W. Sandvik, L. Balents, and D. K. Campbell, Phys. Rev. Lett. **92**, 236401 (2004).

[60] M. Fabrizio, A. O. Gogolin, and A. A. Nersesyan, Phys. Rev. Lett. **83**, 2014 (1999).

[61] S. R. Manmana, V. Meden, R. M. Noack, and K. Schönhammer, Phys. Rev. B **70**, 155115 (2004).

[62] M. Fabrizio, Phys. Rev. B **54**, 10054 (1996).

[63] S. Daul and R. M. Noack, Phys. Rev. B **61**,1646 (2000).

[64] P. W. Anderson, Phys. Rev. **124**, 41 (1961).

[65] B. A. Bernevig, R. B. Laughlin, and D. I. Santiago, Phys. Rev. Lett. **91**, 147003 (2003).

[66] L. Arrachea and D. Zanchi, Phys. Rev. B **71**, 064519 (2005).

[67] G. I. Japaridze and E. Müller-Hartmann, Phys. Rev. B **61**, 9019 (2000).

[68] J. Dai, X. Feng, T. Xiang, and Y. Yu, Phys. Rev. B **70**, 064518 (2004).

[69] X. Feng, Z. Xu, and J. Dai, J. Phys.: Condens. Matter **16**, 4245 (2004).

[70] X. Huang, E. Szirmai, F. Gebhard, J. Sóyom, and R. M. Noack, Phys. Rev. B **78**, 085128 (2008).

[71] V. J. Emery, in Highly Conducting One-Dimensional Solids, edited by J. Devreese, R. Evrard, and V. van Doren (Plenum, New York, 1979).

[72] J. Sólyom, Adv. Phys. **28**, 201 (1979).

[73] M. Tsuchiizu and A. Furusaki, Phys. Rev. Lett. **88**, 056402 (2002); Phys. Rev. B **69**, 035103 (2004).

[74] A. A. Ovchinnikov, Zh. Eksp. Teor. Fiz. **57**, 2137 (1969) [Sov. Phys. JETP 30, 1160 (1970)].

[75] S. Eggert, Phys. Rev. B **54**, R9612 (1996).

[76] K. Okamoto and K. Nomura, Phys. Lett. A **169**, 433 (1992).

[77] D. Rossini, T. Calarco, V. Giovannetti, S. Montangero, and R. Fazio, Phys. Rev. A **75**, 032333 (2007).

[78] C. Lai, J. Hung, C. Mou and P. Chen, Phys. Rev. B **77**, 205419 (2008).

[79] F. M. Cucchietti, J. P Paz, and W. H. Zurek, Phys. Rev. A **72**, 052113 (2005).

[80] F. M. Cucchietti, S. Fernandez-Vidal, and J. P Paz, Phys. Rev. A **75**, 032337 (2007).

[81] H. T. Quan, Z. Song, X. F. Liu, P. Zanardi, and C. P. Sun, Phys. Rev. Lett. **96**, 140604 (2006).

[82] Z. Wang, B. Wang, and Z. Su, Phys. Rev. B **78**, 054433 (2008).

[83] W. W.Cheng and J. M. Liu, Phys. Rev. A **79**, 052320 (2009).

[84] H. T. Quan and F. M. Cucchietti, Phys. Rev. E **79**, 031101(2009).

[85] C. Cormick and J. P. Paz, Phys. Rev. A **78**, 012357 (2008).

[86] S. Yuan, M. I. Katsnelson and H. De. Raedt, Phys. Rev. B **77**, 184301 (2008).

[87] A. Peres, Phys. Rev. A **30**, 1610 (1984).

[88] J. des Cloizeaux and M. Gaudin, J. Math. Phys. **7**, 1384 (1966).

[89] H. J. Schulz, G. Cuniberti, and P. Pieri, in Field Theories for Low-dimensional Condensed Matter Systems: Spin Systems and Strongly Correlated Electrons, edited by G. Morandi, P. Sodano, A. Tagliacozzo, and V. Tognetti (Springer Verlag, Berlin, 2000).

[90] J. L. Roberts, N. R. Claussen, James P. Burke, Jr., Chris H. Greene, E. A. Cornell, and C. E. Wieman, Phys. Rev. Lett. **81**, 5109 (1998).

[91] T. Loftus, C. A. Regal, C. Ticknor, J. L. Bohn, and D. S. Jin, Phys. Rev. Lett. **88**, 173201 (2002).

[92] M. Rigol, V. Dunjko, V. Yurovsky, and M. Olshanii, Phys. Rev. Lett. **98**, 050405 (2007).

[93] M. A. Cazalilla, Phys. Rev. Lett. **97**, 156403 (2006).

[94] C. Kollath, A. M. Läuchli, and E. Altman, Phys. Rev. Lett. **98**, 180601 (2007).

[95] S. R. Manmana, S. Wessel, R. M. Noack, and A. Muramatsu, Phys. Rev. Lett. **98**, 210405 (2007).

[96] T. Barthel and U. Schollwöck, Phys. Rev. Lett. **100**, 100601 (2008).

[97] M. Moeckel and S. Kehrein, Phys. Rev. Lett. **100**, 175702 (2008).

[98] S. R. Manmana, S. Wessel, R. M. Noack, and A. Muramatsu, Phys. Rev. B **79**, 155104 (2009).

[99] A. Silva, Phys. Rev. Lett. **101**, 120603 (2008).

[100] P. Jordan and E. Wigner, Z. Phys. **47**, 631 (1928).

[101] E. Lieb, T. Schultz, and D. Mattis, Ann. Phys. **16**, 407 (1961).

[102] P. Pfeuty, Ann. Phys. **57**, 79 (1970).

[103] L. S. Levitov, H. W. Lee, and G. B. Lesovik, J. Math. Phys. **37**, 4845 (1996).

[104] D. A. Ivanov, H. W. Lee, and L. S. Levitov, Phys. Rev. B **56**, 6839 (1997).

[105] I. Klich, in Quantum Noise in Mesoscopic Physics, edited by Yu. V. Nazarov, Vol. 97 of NATO Advanced Science Series (Kluwer Academic Press, Dordrecht, 2003).

Acknowledgement

I am indebted to many people who gave me invaluable supports and many assistances during my PhD studies.

First of all, I would like to thank my supervisor Prof. Dr. Reinhard M. Noack for his supervision and many interesting discussions. I owe him my deepest gratitude for teaching me many aspects of DMRG and sharing his physical intuitions with me in my PhD works. Moreover, I deeply appreciate his patience and encouragement during the time I was writing my thesis and also thanks for his careful reading and detailed comments of my thesis. I also would like to thank Prof. Dr. Florian Gebhard who gave me the opportunity to collaborate with him in studying the t-U-J_1-J_2 model.

I am grateful also to Dr. Salvatore Manmana for the useful discussions of the time-dependent problem and the decoherence problem and also to Dr. Leonildo Tincani for teaching me how to use the computer cluster and other computer skills.

I want to express my gratitude to my beloved parents for their support and great confidence in me all through these years. Yan I thank you for all the time with you, for waiting me patiently when I was very busy and for convincing me so strongly to study physics. I also thank my friends and teachers in China and other countries who encouraged me to continue to study physics.

Last, but not least, I acknowledge the financial support by the European Graduate College / DFG-OTKA International Research Training Group “Electron-Electron Interactions in Solids” in Marburg and Budapest and three months financial support by the STIBET program of the “Deutscher Akademischer Austauschdienst” (DAAD) for a completion grant of an international PhD candidate. Finally, I would like to express my gratitude to all the people in our groups who provide a good learning environment and a strongly academic atmosphere.

Curriculum Vitae

Personal

Name:	Xiaoxuan Huang
Nationality:	Chinese
Date of birth:	March 9, 1981
Place of birth:	Lanxi, Zhejiang, China

Education

2006.12-2011.5 Ph.D. in Theoretical physics, Philipps-Universität Marburg, Germany
Thesis: *Explicit Exchange Interaction and Decoherence Dynamics in One-Dimensional Quantum Systems*
Supervisor: Prof. Reinhard M. Noack

2004.9-2006.6 Master of Science in Theoretical Physics, Zhejiang University, China
Thesis: *Numerical Studies of Quantum Phase Transitions in One-Dimensional Electron Systems*
Supervisor: Prof. Jianhui Dai

1999.9-2003.6 Bachelor of Science in Physics, Zhejiang University, China
Thesis: *Quantum Transport Effects in a Single Electron Transistor*
Supervisor: Prof. Jianhui Dai